Ph.D. Program in Earthquake Engineering and Structural Dynamics

Soil-Structure Interaction in the Performance-Based Seismic Design of Reinforced-Concrete Buildings

Doctoral thesis by:

Juan Sebastián Baquero Mosquera

Thesis advisor:

Jesús Miguel Bairán Garcia, Dr.

Thesis co-advisor:

Alberto Ledesma Villalba, Dr.

Department of Civil and Environmental Engineering

Barcelona, April 2023

To God,
to my beloved family,
and to my supporting love…
Everything is possible when you are by my side.

Acknowledgments

None of this work would have been possible without the help and support of the people that walked by my side during these years.

To Prof. Jesús Bairán and Prof. Alberto Ledesma as supervisors of this thesis, my sincere gratitude for their motivation and advice to develop such a valuable research work. Their experience was essential to overcome academic situations that would have resulted in dead ends for me.

To the Universitat Politècnica de Catalunya, BarcelonaTECH (UPC), for becoming a figurative fortress and more than a home. There I met wonderful people struggling with the same battle I did.

To the Secretaria Nacional de Educacion Superior, Ciencia, Tecnología e Innovación, SENESCYT, and the Instituto de Fomento al Talento Humano, IFTH, both in Ecuador. For their aid in accomplishing this step in my academic development through the Convocatoria Abierta 2017.

To my *Alma Mater* University, Pontificia Universidad Católica del Ecuador (PUCE), which, more than ever, has become an essential player in my academic and research development.

Not less important is the support and motivation received by my family. To my dad, Patricio Baquero; my mom, María Teresa Mosquera; my sisters, María José and Salomé and my little nieces Emilia, Martina, and Aitana. Your love was the most potent fuel throughout these years. My girl, Esther, who joined me in good and bad times. To my friends, Mike, Andrés, Samar, Arash, Joseph, John, Lilibeth, Esther Gallego, Ana, Reina, and Vanessa, the list can keep going. Thank you all for everything!

Juan Sebastián Baquero Mosquera
Barcelona, 2023

Abstract

When analyzing structures for seismic design and performance assessment purposes, it has been common to assume that the ground motions or their equivalent representations through design and response spectra, respectively, correspond to that of the *free-field* characteristics. Implicit in this assumption was the reduced or no understanding of how the behavior of the soil beneath the studied structures modifies their global dynamic response and that of the foundation-level ground itself to a certain extent. While employing the free-field criteria to the seismic demand could closely reflect the actual response of structures found over firm and stiff soils, poorer soil characteristics indeed change how ground motions are propagated throughout the soil medium, mainly given the presence of a structure. Moreover, changes in the foundation-level ground motions don't come alone, but the structural responses are also modified due to the reduced support capacities of a soft soil. The reason for these alterations in the response is that the soft soil must be considered part of the analyzed soil-structure system (SSS), somewhat increasing its deformability. The combined system behavior and its repercussions regarding its dynamic response have been studied approximately since the second half of the twentieth century. From then on, this phenomenon's understanding and comprehensive knowledge have constantly grown to the point of nowadays becoming a broad research area devoted to studying the so-called *soil-structure interaction* (SSI) effects. Even though the most considerable advances in better describing and understanding the soil-structure interaction effects were made in the 1970s to address the need to ensure the safety of nuclear power plants being built at that time, in the last decades, efforts have been made to reach a thorough comprehension of this phenomenon aided by the fast improvement in computing capabilities and the growth of new technologies.

Among the topics addressed worldwide to complement the information regarding the soil-structure interaction effect are studies devoted to explaining both the elastic and inelastic structural response using either simplified single-degree of freedom (SDOF), multiple-degree of freedom (MDOF) systems that consider uncoupled linear equivalent representations of the nonlinear soil behavior and even fully coupled nonlinear 3D structural mathematical models aiming to fulfill the same goal: to understand the influence of SSI effects in the structural response. In addition, different structural systems have been studied throughout this research path ranging from nuclear and dam facilities to building structures—the latter of particular interest for the research work presented in this document. Advances in this type of structure allow us today to have a variety of analysis and design aids that have been developed and improved as academic and research studies come to light. In this regard, it has gradually become more common to find specialized chapters in design standards around the world dedicated to giving guidelines for the seismic design of buildings with interaction effects considerations. Within the North American scope, for instance, the *Minimum Design Loads and Associated Criteria for Buildings and Other Structures* (ASCE-7), and the *Seismic Evaluation and*

Retrofit of Existing Structures (ASCE-41) standards prescribe, respectively, seismic design and performance assessment requirements that account for the SSI effects for their corresponding individual purposes. However, the requirements and recommendations in such standards still rely on the outcomes of oversimplified linear equivalent models of the structure and supporting soil. It is worth mentioning that such simplifications are not just a matter of simple will but because of the complex and intricate nature of a more rigorous analysis of the soil-structure interaction phenomenon using more elaborated models.

Such prescribed recommendations are focused only on reflecting the beneficial effects of the SSI phenomenon, even though it is well-known from studies carried out around two decades ago, that the soil-structure interaction can also induce detrimental effects in the structural response. Quoting Anestis Veletsos, "*With the methods of analysis and the computer programs now available, it is in principle possible to evaluate the dynamic response of any structure-foundation system to any excitation of the base. Such evaluations, however, can be no better than the assumptions underlying the analyses.*" A statement made back in 1992 but still applicable these days in concern to the standards' simplifications.

In light of this brief background, the study presented in this document acquires relevance based on two primary goals. First, focusing our attention on the seismic assessment of the structural performance, we look for a correlation model that allows professionals to calculate the actual performance outcomes that consider the SSI effects based on the obtained seismic performance indicators from buildings modeled both accounting for and neglecting such interaction effects while employing various analysis procedures available in ASCE-41 standard. Second, supported by such performance indicators, a pair of factors dedicated to modifying the seismic design demand and the expected inelastic deformations are recommended to improve the building design outcomes in terms of measured performance. Thus, α-factor and α_{C_d} are called to meet the needs of improving strength and stiffness characteristics, respectively, of buildings achieving adequate Life Safety and Collapse Prevention structural performance levels. Moreover, these factors consider not only the beneficial effects of the SSI phenomenon but the detrimental ones, seeking to change the current paradigms of the code-prescribed provisions for assessment and design practices. To help accomplish these goals, a reinforced concrete buildings database is constructed considering high seismicity design criteria of the ACI-318 standard for the design requirements of reinforced concrete structures, neglecting and accounting for soil-structure interaction effects. Then, all buildings in the so-built database are assessed through the guidelines described in the ASCE-41 standard to compare their performance indicators and find the sought relationship mentioned above for different structural performance levels. Finally, the same indicators are employed to generate estimation models for the α- and α_{C_d} factors through regression analysis methods. Advanced computational tools such as OpenSeesPy, embedded in the Python environment, for the design and assessment of the buildings in the database

and machine-learning regression techniques for generating the estimation models, are used to ease the development of the tasks involved in the process described above.

It is demonstrated that the generated correlation models can translate the performance indicators obtained through simple analysis procedures and models to those determined using more complex counterparts. This means, for instance, that it is possible to assess a building with or without flexible base conditions using either the modal response spectrum analysis (MRSA) or the pushover nonlinear static procedure (NSP) and transform its performance indicators to those that would be obtained from a flexible base model analyzed through the nonlinear time history analysis (NLTHA). The latter is deemed the analysis procedure giving the closest to actual performance indicators. This represents a leap forward in the performance assessment process since the time-consuming NLTHA can be skipped using a less complex model and analysis procedures. In addition, α and α_{C_d} values proved to successfully produce sound building designs that achieve expected structural performance levels while considering SSI effects, something that has been demonstrated unlikely to accomplish just by following the current code-prescribed recommendations.

Supported by the achievement of the stated goals and the rational development of the procedures in making it possible, this document is expected to represent a valuable tool for practitioners involved in earthquake engineering design and a step forward in developing the soil-structure interaction research field.

Keywords: *soil-structure interaction effects, performance-based seismic design, seismic structural assessment, performance estimation, artificial intelligence, classical regression analysis, machine-learning-based regression, seismic design recommendations*.

Resumen

Cuando se analizan estructuras con fines de diseño y evaluación del desempeño sísmicos, ha sido común suponer que los movimientos del terreno o sus representaciones equivalentes a través de los espectros de diseño y respuesta, respectivamente, corresponden a las características de *campo libre*. Implícito en esta suposición estaba la reducida o nula comprensión de cómo el comportamiento del suelo debajo de las estructuras estudiadas modifica la respuesta dinámica global de éstas y, en cierta medida, la del suelo a nivel de fundación de los elementos de cimentación. Si bien el empleo de los criterios de *campo libre* para la demanda sísmica podría reflejar con cierta precisión la respuesta real de las estructuras que se encuentran sobre suelos firmes y rígidos, suelos con características más pobres cambian la forma en que se propagan los movimientos del suelo en todo el medio circundante, principalmente dada la presencia de una estructura. Además, los cambios en los movimientos del suelo a nivel de cimentación no vienen solos, sino que las respuestas estructurales también se modifican debido a la reducida capacidad de soporte presente en un suelo blando. La razón de estas alteraciones en la respuesta es que el suelo blando tiene que ser considerado parte del sistema suelo-estructura analizado (SSS por sus siglas en inglés), aumentando de alguna manera su deformabilidad. El comportamiento del sistema combinado y sus repercusiones respecto a la respuesta dinámica han sido estudiados aproximadamente desde la segunda mitad del siglo XX. A partir de entonces, la comprensión y el conocimiento integral de este fenómeno ha ido en constante crecimiento hasta convertirse en la actualidad en una amplia área de investigación dedicada al estudio de los así llamados *efectos de interacción suelo-estructura* (SSI por sus siglas en inglés). Si bien los avances más importantes para describir y comprender mejor los efectos de la interacción suelo-estructura se realizaron en la década de 1970 para abordar la necesidad de garantizar la seguridad de las centrales nucleares que se construían en ese momento, en las últimas décadas se han realizado esfuerzos para llegar a una comprensión cabal de este fenómeno ayudados por las rápidas mejoras en capacidades de cómputo y nuevas tecnologías.

Entre los temas abordados a nivel mundial para complementar la información sobre el efecto de la interacción suelo-estructura se encuentran estudios dedicados a explicar la respuesta estructural tanto elástica como inelástica utilizando sistemas simplificados de un solo grado de libertad (SDOF por sus siglas en inglés) o de múltiples grados de libertad (MDOF por sus siglas en inglés) que consideran representaciones equivalentes lineales desacopladas del comportamiento no lineal del suelo e incluso modelos matemáticos estructurales 3D no lineales totalmente acoplados con el enfocados en cumplir el mismo objetivo: comprender la influencia de los efectos SSI en la respuesta estructural. Además, a lo largo de esta rama de investigación se han estudiado diferentes sistemas estructurales que van desde instalaciones nucleares y de represas hasta estructuras de edificios; estas últimas de particular interés para el trabajo de investigación presentado en este documento.

Los avances en este tipo de estructura nos permiten hoy tener una variedad de ayudas de análisis y diseño que se han desarrollado y mejorado a medida que salen a la luz estudios académicos y de investigación. En este sentido, gradualmente se ha vuelto más común encontrar capítulos especializados en estándares de diseño alrededor del mundo dedicados a dar pautas para el diseño sísmico de edificios con consideraciones de efectos de interacción. Dentro del ámbito norteamericano, por ejemplo, las normas *Minimum Design Loads and Associated Criteria for Buildings and Other Structures* (ASCE-7) y *Seismic Evaluation and Retrofit of Existing Structures* (ASCE-41), se enfocan respectivamente en el diseño y en la evaluación del desempeño sísmicos; ambas permitiendo tomar en cuenta los efectos de la interacción suelo-estructura. Sin embargo, los requisitos y recomendaciones en dichas normas aún se basan en los resultados de modelos equivalentes lineales simplificados de la estructura y el suelo de soporte. Vale la pena mencionar que tales simplificaciones no son el producto de una decisión arbitraria, sino debido a la naturaleza compleja e intrincada de un análisis más riguroso del fenómeno de interacción suelo-estructura utilizando modelos más elaborados. Dadas las series de supuestos requeridos para generar las recomendaciones de dichas normas, éstas se enfocan únicamente en reflejar los efectos benéficos del fenómeno SSI, aunque es bien sabido por estudios realizados hace aproximadamente dos décadas, que la interacción suelo-estructura también puede inducir efectos perjudiciales en la respuesta estructural. Citando a Anestis Veletsos, "*Con los métodos de análisis y los programas informáticos ahora disponibles, en principio es posible evaluar la respuesta dinámica de cualquier sistema estructura-cimentación sujeto cualquier excitación de la base. Tales evaluaciones, sin embargo, no pueden ser mejores que las suposiciones que subyacen a los análisis*". Una declaración hecha en 1992 pero aún aplicable en estos días en relación con las simplificaciones de las normas citadas anteriormente.

A la luz de estos breves antecedentes, el estudio presentado en este documento adquiere relevancia a partir de dos objetivos principales. Primero, centrando nuestra atención en la evaluación sísmica del desempeño estructural, buscamos un modelo de correlación que permita a los profesionales calcular resultados *reales* del desempeño que consideran los efectos SSI en función de los indicadores de desempeño sísmico obtenidos en los edificios modelados tanto que consideren o no dichos efectos de interacción a la vez que se utilizan los procedimientos de análisis disponibles en la norma ASCE-41. En segundo lugar, con el apoyo de dichos indicadores de desempeño, se recomienda un par de factores dedicados a modificar la demanda de diseño sísmico y las deformaciones inelásticas esperadas para mejorar los resultados del diseño de edificios en términos del desempeño medido. De esta manera, los factores α y α_{C_d} están llamados a satisfacer las necesidades de mejorar respectivamente las características de resistencia y rigidez con el fin de que las estructuras alcancen niveles adecuados de desempeño estructural de Seguridad de Vida (Life Safety) y Prevención de Colapso (Collapse Prevention). Además, estos factores consideran no solo los efectos beneficiosos del fenómeno de SSI, sino también los perjudiciales, buscando cambiar los paradigmas actuales de las

disposiciones prescritas por el código para las prácticas de evaluación y diseño. Para ayudar a lograr estos objetivos, se construye una base de datos de edificios de hormigón armado considerando los criterios de diseño para zonas de alta sismicidad del código ACI-318 para los requisitos de diseño de estructuras de hormigón armado, tanto despreciando como teniendo en cuenta los efectos de interacción suelo-estructura. Luego, todos los edificios en la base de datos se evalúan a través de las pautas descritas en el estándar ASCE-41 para comparar sus indicadores de desempeño y encontrar la relación buscada mencionada anteriormente para diferentes niveles de desempeño estructural. Finalmente, los mismos indicadores se emplean para generar modelos de estimación para los factores α y α_{C_d} a través de métodos de análisis de regresión. Herramientas computacionales avanzadas como OpenSeesPy, embebido en el entorno Python, para el diseño y evaluación de los edificios en la base de datos y técnicas de regresión basadas aprendizaje autónomo para generar los modelos de estimación se utilizan para facilitar el desarrollo de las tareas involucradas en el proceso descrito arriba.

Se demuestra que los modelos de correlación generados pueden traducir los indicadores de desempeño obtenidos a través de procedimientos y modelos de análisis simples hacia aquellos determinados usando contrapartes más complejas. Esto significa, por ejemplo, que es posible evaluar un edificio con o sin condiciones de base flexible utilizando el Análisis Modal Espectral (MRSA en inglés) o el procedimiento estático no lineal, Pushover (NSP en inglés) y transformar sus indicadores de rendimiento a los que se obtendrían a partir de un modelo de base flexible analizado a través del Análisis Tiempo-Historia Nolineal (NLTHA en inglés). Este último se considera el procedimiento de análisis que proporciona los indicadores de desempeño más cercanos a los reales. Esto representa un avance en el proceso de evaluación del desempeño, ya que el NLTHA, que demanda mucho tiempo, es reemplazado por un modelo y procedimientos de análisis menos complejos. Además, los valores de α y α_{C_d} demostraron con éxito que producen diseños de edificios seguros, logrando los niveles de desempeño estructural esperados mientras se consideran los efectos SSI, algo que se ha demostrado que es poco probable conseguir simplemente siguiendo las recomendaciones actuales prescritas por el código.

Apoyado en el logro de las metas planteadas y el desarrollo racional de los procedimientos para hacerlo posible, se espera que este documento llegue a representar una herramienta valiosa para los profesionales involucrados en el diseño sísmico y también como un paso firme en el desarrollo del campo de investigación del fenómeno de interacción suelo-estructura.

Palabras clave: *efectos de interacción suelo-estructura, diseño sísmico basado en desempeño, evaluación sísmica de estructuras, estimación del desempeño, inteligencia artificial, análisis de regresión clásico, análisis de regresión basado en aprendizaje automatizado, recomendaciones de diseño*.

Table of Contents

List of Tables

List of Figures

List of Symbols and Abbreviations

Latin Alphabet

a	site class factor determined according to Eq. [3.7].
$\hat{a}, \hat{b}$	scaling parameters calculated per Eq. [4.17]
a_o	dimensionless frequency parameter calculated for the fixed-base structure.
$\tilde{a}_o$	dimensionless frequency parameter calculated for the flexible-base structure.
A	area of the element's cross-section. foundation area in Eq. [2.17].
A_{base}	area of the foundation footprint measured in ft^2.
A_g	Area of the element's cross-section.
A_v	shear reinforcement.
$A_{v,min}$	minimum shear reinforcement.
b_e	effective foundation size calculated in feet units.
B	total width of the foundation footprint.
B_{bsa}	base-slab averaging factor.
B_e	end-region length of the foundation width.
B_{SSI}	modification factor allowing a response spectrum to be constructed considering a system's damping ratio different than 5%.
c_{rd}	radiation damping coefficient in the soil vicinity of the foundation.
c_s	soil cohesion parameter.
C_0	Modification factor that relates the spectral displacement of an SDOF system to the control node displacement of the building's MDOF system.
C_1	modification factor for translating the obtained elastic displacement from the linear analysis to the maximum expected inelastic displacement according to ASCE-41
C_2	modification factor that accounts for the complex effects of pinched hysteresis behavior shapes, cyclic stiffness degradation, and strength deterioration that linear elastic sections cannot display.
C_d	deflection amplification factor for the seismic design of buildings according to ASCE-7.
C_d^{theo}	theoretical deflection amplification factor for the seismic design of buildings according to ASCE-7.
C_d^{real}	real amplification factor for the seismic design of buildings calculated with the α_{C_d}.
C_m	effective mass factor as per ASCE-41.
C_t	building approximate period coefficient depending on the structure type.

$C_{R-V}^{K_{ii}}$	rotational stiffness deficit ratio.
C_s	seismic response coefficient for the fixed-base structure according to ASCE-7.
$\tilde{C}_s$	seismic response coefficient for the flexible-base structure according to ASCE-7.
C_{units}	Unit transformation factor equals 1.0 when f_c' introduced in [MPa] for Eq. [3.19].
dA_i	foundation's tributary area that is supported by the i^{th}-zero-length element.
d_b	the diameter of longitudinal reinforcement.
D_f	foundation depth.
D_r	relative density of the soil.
E_c	modulus of elasticity of the concrete.
E_{cE}	modulus of elasticity of the concrete calculated using expected material properties.
$ft.$	feet units.
f_c'	concrete compressive strength at the age of 28 days.
f_{cE}'	expected concrete compressive strength.
f_{cL}'	lower-bound concrete compressive strength.
f_y	reinforcement steel yield strength.
f_{yE}	expected reinforcement steel yield strength.
f_{yL}	lower-bound reinforcement steel yield strength.
F_a	site coefficient affecting the short-period spectral pseudo acceleration parameter.
F_v	site coefficient affecting the 1.0s period spectral pseudo acceleration parameter.
FS_v	the vertical factor of safety for the soil bearing capacity calculation.
g	Acceleration of gravity.
G	strain-compatible shear modulus of the soil, modified due to large-strain effects.
G_o	small-strain or maximum shear modulus of the soil.
h^*	first-mode effective building height.
h_n	total building height.
h_i	inter-story height.
I_a	Arias intensity energy measure.
I_g	moment of inertia of the gross concrete section about the centroidal axis.
I_y	elements' cross-section inertia about the local y-axis.
I_z	elements' cross-section inertia about the local z-axis.
I_{xx}	rotational moment of inertia about the xx-axis of the foundation element.
I_{yy}	rotational moment of inertia about the yy-axis of the foundation element.
I_e	importance factor related to earthquake actions as per ASCE-7.
J	force-delivery reduction factor affecting the seismic demand as per ASCE-41.

J_{xx}	torsional polar moment of the elements' cross-section about the local x-axis.
k_{end}	end-region surface-distributed stiffness of the soil-foundation system.
k_{mid}	mid-region surface-distributed stiffness of the soil-foundation system.
k_{region}	any region surface-distributed stiffness of the soil-foundation system.
k_{xx}	surface-distributed stiffness of the soil-foundation system about the xx-axis.
k_{yy}	surface-distributed stiffness of the soil-foundation system about the yy-axis.
k_z	surface-distributed stiffness of the soil-foundation system in the vertical direction.
K_e	effective lateral stiffness of the building in the direction of analysis, obtained from the idealized force-displacement curve in the NSP analysis procedure.
K_{ii}	rotational stiffness of the soil-foundation system about a general ii-degree-of-freedom.
K_{mem}	rotational stiffness of the member's cross-section.
$K_{mem(mod)}$	modified rotational stiffness of the member's cross-section.
K_{ph}	rotational stiffness of the plastic hinge region of an element's cross-section.
K_{xx}	rotational stiffness of the soil-foundation system about the global xx-axis.
K_{yy}	rotational stiffness of the soil-foundation system about the global yy-axis.
K_z	translational stiffness of the soil-foundation system in the global vertical direction.
K^i	generic soil-foundation system stiffness applied to the i^{th}-zero-length element.
K^i_{region}	generic soil-foundation system stiffness applied to the i^{th}-zero-length element within a foundation region that could be end- or mid-regions.
K^*	the relative stiffness measured as the stiffness ratio of the *SSIDs*-designed to the *convDs*-designed structure in Section 2.6.
l_p	plastic length calculated as per Eq. [3.18].
L	total length of the foundation footprint.
L_e	end-region length of the foundation length.
m-factor	element demand modification factor as per ASCE-41.
M	Moment action in a cross-section.
M_u	LRFD design moment action. ultimate moment capacity of a cross-section.
M_w	seismic moment magnitude.
M_y	yield moment capacity of a cross-cross section.
$\overline{M}$	effective modal mass for the fundamental vibration mode in the analysis direction under consideration.
M^*	the relative mass measured as the mass ratio of the *SSIDs*-designed to the *convDs*-designed structure in Section 2.6. the relative mass measured as the mass ratio of the originally designed structure with SSI effects considerations as per ASCE-7 to the mass of the structure designed using α and α_{C_d} proposed modification factors in Section 6.2.

n	member stiffness modification factor for concentrated plasticity hinges modeling.
N	number of Lobatto integration points within the nonlinear beam-column element object.
N_c, N_q, N_γ	bearing capacity factors.
N_{UG}	imposed gravitational axial load acting on an element.
p	the number of predictors selected in regression analysis.
p_a	athmospheric pressure.
P	axial load action in a cross-section.
P_u	LRFD design axial force action.
q_i	bearing capacity ordinate of the parabolic distribution at the extreme ends of the foundation surface, calculated as per Eq. [3.29].
q_L	surface-distributed Live Load applied to slab surfaces during design and assessment.
q_{L_r}	surface-distributed roof Live Load applied to slab surfaces during design and assessment.
q_{SD}	surface-distributed Dead Load different from the self-weight. (Super-Dead Load).
$q_{ult}(x)$	location-dependent ultimate soil stress capacity calculated per Eq. [3.27].
$q_\gamma(x)$	term of the unit-weight contribution to the ultimate soil stress capacity defined in Eq. [3.28].
Q_{CE}	element's capacity considering expected material properties.
Q_{CL}	element's capacity considering lower-bound material properties.
Q_D	actions in elements induced by the dead loads.
Q_E	actions in elements induced by seismic loads.
Q_G	actions in elements induced by the gravity loads system.
Q_L	actions in elements induced by the live loads.
Q_{max}	maximum cross-section strength for a determined action.
Q_{res}	residual strength of a cross-section for a determined action.
Q_{UD}	deformation-controlled demand on an element.
Q_{UF}	force-controlled demand on an element.
Q_{ult}^i	ultimate soil bearing capacity modeled through the i^{th}-zero-length element.
Q_y	yield strength of a cross-section for a determined action.
Q^i	soil's vertical bearing capacity represented in the i^{th}-zero-length element.
R	Response Modification Factor for building design according to ASCE-7.
R_d	Strength-ductility Reduction Factor.
R^2	determination coefficient for measuring the efficiency of the estimation model.
R_{adj}^2	determination coefficient for measuring the efficiency of the estimation model, adjusted to the number of degrees-of-freedom of the model.
s	units of seconds.

s_z	translational displacement degree-of-freedom of foundation elements in the z-direction.
S_a	5%-damped spectral design acceleration parameter for the fixed-base structure.
$\tilde{S}_a$	5%-damped spectral design acceleration parameter for the flexible-base structure.
S_{ax}	x%-damped spectral assessment acceleration parameter for the fixed-base structure.
$\tilde{S}_{ax}$	x%-damped spectral assessment acceleration parameter for the flexible-base structure.
S_n	cross-section generalized nominal strength.
S_1	mapped MCE_R, 5% damped, spectral response acceleration parameter at a period of 1.0s as per ASCE-7.
S_s	mapped MCE_R, 5% damped, spectral response acceleration parameter at short periods as per ASCE-7.
S_{MS}	MCE_R, 5% damped, spectral response acceleration parameter at short periods adjusted for site-class effects as per ASCE-7.
S_{M1}	MCE_R, 5% damped, spectral response acceleration parameter at a period of 1.0s adjusted for site-class effects as per ASCE-7.
S_{DS}	design, 5% damped, spectral response acceleration parameter at short periods as per ASCE-7.
S_{D1}	design, 5% damped, spectral response acceleration parameter at a period of 1.0s as per ASCE-7.
S_{xs}	assessment short-period spectral acceleration parameter corresponding to an X-SHL for a damping ratio β_x different to 5%.
S_{x1}	assessment 1.0s-period spectral acceleration parameter corresponding to an X-SHL for a damping ratio β_x different to 5%.
t_{ult}	ultimate frictional capacity stress of the soil.
T_a	approximate fundamental period of the building.
T_e	effective fundamental period of the building in the analysis direction when assessing the fixed-base structure through the NSP.
$\tilde{T}_e$	effective fundamental period of the building in the analysis direction when assessing the flexible-base structure through the NSP.
T_{min}	lower bound period range limit for scaling ground motion records.
T_{max}	upper bound period range limit for scaling ground motion records.
T_n	the fundamental period of vibration of the fixed-base building.
T_o	lower period limit of the constant acceleration region in the design response spectrum.
T_s	upper period limit of the constant acceleration region in the design response spectrum.
T_L	mapped long-period transition limit as per ASCE-7.
T_{xx}	fundamental rotational period of the soil-structure system about the weak axis.
T_y	fundamental translational period of the soil-structure system along the weak direction.
T_{ult}^i	ultimate frictional sliding capacity of the soil modeled through the i^{th}-zero-length element.

T_x^i	soil's frictional sliding capacity in the x-direction modeled in the i^{th}-zero-length element.
T_y^i	soil's frictional sliding capacity in the y-direction modeled in the i^{th}-zero-length element.
$\tilde{T}_n$	fundamental period of vibration of the flexible-base building.
$\left(\tilde{T}_n/T\right)_{eff}$	effective period lengthening that depends on the expected ductility demand.
u_x	translational degree-of-freedom in the soil-foundation system along the x-direction.
u_y	translational degree-of-freedom in the soil-foundation system along the y-direction.
U	generalized majored action for cross-section design.
v_s	effective shear wave velocity of the soil modified to account for large-strain levels.
v_{so}	shear wave velocity of the soil beneath the foundation at small-strain levels.
$\bar{v}_{so}$	average shear wave velocity of the soil beneath the foundation at small-strain levels
V	total design lateral force or shear at the base of a fixed-base structure. shear force action at a cross-section.
V_d	lateral strength of the building measured at the target displacement, δ_t.
V_e, V_E	shear force developed at the base of a structure, assuming it behaves elastically when subjected to the design level.
V_t	design value of the seismic base shear of the fixed-base structure, determined through the MRSA analysis procedure.
V_u	LRFD design shear force action.
V_y	yield or maximum lateral strength of the fixed-base structure.
$\tilde{V}$	total design lateral force or shear at the base of a flexible-base structure.
$\tilde{V}_t$	design value of the seismic base shear of the flexible-base structure, determined through the MRSA analysis procedure.
$\tilde{V}_y$	yield or maximum lateral strength of the flexible-base structure
w_i, b	weights and bias transferred from one neuron layer to another.
W	effective seismic weight of the structure.
$\overline{W}$	effective seismic weight of the structure for the SSI design type.
x	building approximate period coefficient depending on the structure type.
X_i	i^{th} predictor variable for regression analyses.
z	distance from the critical section of maximum curvature and the element point of contraflexure.
z_{50}	displacement at which 50% of Q_{ult}^i is mobilized in monotonic loading.

Greek Alphabet

α	coefficient that accounts for the modification in design base shear caused by foundation damping due to SSI effects. According to ASCE-7, this modification implies a reduction, as explained in Section 5.2.
α_{C_d}	correction factor to translate from C_d^{theo} to C_d^{real}.
$\alpha_{(X_i)}$	proposed coefficient for the modification in design base shear caused by foundation damping due to SSI effects that either amplifies or reduces the design demand. It depends on its relationship with predictors X_i.
α_{obs}	observed value of α stored in the dataset.
α_{pred}	predicted value of α results from the regression analysis.
α_{xx}	surface level stiffness modifier applied to rotational stiffness and damping, adapted from (Pais & Kausel, 1988).
α_1	slope fraction of K_e for constructing the idealized force-displacement curve through the NSP.
α_2	negative slope fraction of K_e for constructing the idealized force-displacement curve through the NSP.
β	the effective viscous damping ratio of the structure, taken as 5% for design purposes and 3% for performance assessment.
β_f	the effective viscous damping ratio relating to the soil-foundation interaction.
β_i	estimated regression coefficients.
β_o	the effective viscous damping ratio of the soil-structure system.
β_{rd}	radiation damping ratio.
β_s	soil hysteretic damping ratio.
β_x	translational foundation damping ratio in the x-direction.
β_{yy}	rotational foundation damping ratio about the yy-axis.
B_i	regression coefficients.
γ	load factor regarding the relative importance of the element's action capacity for structural integrity. Used in Eq. [3.17].
γ_s	unit weight of the soil.
Γ_1	first modal mass participation factor.
δ	inelastic story drift ratio or inelastic deflections.
δ_E	elastic story drift ratios or elastic deflections calculated assuming the structure remains elastic at the design level demand.
δ_p	plastic deformation beyond the yield limit of the cross-section for a determined action.
δ_{pc}	effective post-capping deformation of the cross-section for a determined action.
δ_t	NSP (pushover) target displacement for the control node.
δ_u	ultimate deformation of the cross-section for a determined action.
δ_y	yield deformation of the cross-section for a determined action.

Δ_a	allowable story drift ratio.
Δ_d	Roof displacement measured at the maximum lateral strength or the target displacement, δ_t; whichever gives the least displacement.
Δ_{max}	maximum calculated story drift ratio obtained from the analysis.
ΔV	design base shear variation due to SSI effects.
Δ_y	control node displacement at the yield point in the idealized force-displacement curve obtained through the NSP.
ε	random error of the equation approximating the response variable in the classical regression analysis.
ϑ	strain-related factor used to simplify Eq. [2.27].
θ	Generic cross-section rotation.
$\theta_{p,cyclic}$	plastic rotation beyond the yield limit of the cross-section for the cyclic backbone moment-rotation relationship.
$\theta_{pc,cyclic}$	effective post-capping rotation of the cross-section for the cyclic backbone moment-rotation relationship.
$\theta_{p,monotonic}$	plastic rotation beyond the yield limit of the cross-section for the monotonic envelope moment-rotation relationship.
$\theta_{pc,monotonic}$	effective post-capping rotation of the cross-section for the monotonic envelope moment-rotation relationship.
θ_u	ultimate rotation capacity of a cross-section.
θ_y	yield rotation capacity of a cross-section.
κ	knowledge factor that accounts for the geometrical and mechanical data collection uncertainties reducing elements' strength during performance assessment according to ASCE-41
λ_{str}	structure's slenderness ratio.
μ	expected ductility demand.
$\mu_{strength}$	ratio of the elastic strength demand to the yield strength of the building.
ν	axial load ratio for use in Eqs. [3.19] and [3.20].
ν_s	soil's Poisson ratio.
ρ	Redundancy Factor applicable to structures assigned to the SDCs D, E, and F.
ρ_{sh}	area ratio of transverse reinforcement in the plastic hinge region.
σ	the standard deviation of a set of values.
σ_{OB}	overburden pressure.
σ_{SSI}	wave-parameter measuring the influence of SSI effects.
ϕ	section strength reduction factor in LRFD design. Chapter 2.
ϕ_{cs}	critical state frictional angle of the soil.
$\phi_{1,r}$	ordinate of the first mode shape obtained at the roof of the building.
ϕ_s	the angle of internal friction of the soil.
χ	factor used for adjusting the demand induced by the seismic response for the SPL being evaluated.

Ψ	the ratio of the demand-capacity ratio acceptance criteria values employed to approximate the actual structural seismic performance of a building.
$\widetilde{\omega}_n$	fundamental angular frequency of the flexible-base structure.
Ω	overstrength of a structure.
Ω_o	overstrength factor as per ASCE-7.
$\widetilde{\Omega}_{(T_n)}$	actual estimated overstrength of the building considering SSI effects.

Abbreviations

5-95SD	significant duration of a ground motion record defined in Section 3.4.3
ACI	American Concrete Institute
AI	Artificial-Intelligence
AP	analysis procedures
ASCE	American Society of Civil Engineers
BNWF	Beam-on-Nonlinear-Winkler-Foundation
BPON	Basic Performance Equivalent to New Building Standards.
BSA	base-slab averaging kinematic interaction effects
BSC	base support condition
BSE-XN	basic safety earthquake equivalent to new buildings for X- seismic hazard level
convDs	conventional design
CP	collapse prevention
CR	Classical Regression Analysis Method
DCR	demand-capacity ratio
$DCR_{(ac)}$	demand-capacity ratio acceptance criteria
DNN	Deep Neural Network
DOF	degree of freedom
DRS	design response spectrum
DT	design type
ELF	Equivalent Lateral Force
FS	Forward Selection strategy
GMs	ground motion acceleration histories
GBCT	Gradient-Boosting Classification-Tree
GBRT	Gradient-Boosting Regression-Tree
GRS	general response spectrum
IDs	inelastic deformations
IF	importance factor
ISDR	inelastic story drift ratio
IMKDM	Ibarra-Medina-Krawinkler deterioration model
IO	immediate occupancy
LDP	Linear Dynamic Procedure
LS	life safety
LSP	Linear Static Procedure

LTHA	Linear Time-History Analysis
MAPE	Mean Absolute Percentage Error
MCE_R	risk-targeted maximum considered earthquake
MDOF	multiple degrees of freedom
MDS	maximum direction spectrum
ML	Machine-Learning
MRSA	Modal Response Spectrum Analysis
NbaysX	number of bays in the global X-direction
NbaysZ	number of bays in the global Y-direction
NDP	Nonlinear Dynamic Procedure
NPL	nonstructural performance level
NSP	Nonlinear Static Procedure
NStrs	number of stories in a building of the database
PO	Pushover analysis.
RC	reinforced concrete
RMSE	Root Mean Squared Error
PGA	peak ground acceleration of a ground motion record
PGV	peak ground velocity of a ground motion record
RRS_{bsa}	ratio of response spectra factor due to base-slab averaging kinematic effects.
RSN	record serial number of the PEER Ground Motion NGA-West database
s.c.-w.b.	strong column – weak beam
SC	Site Class
SDC	Seismic Design Category
SDOF	Single degree of freedom
SHL	Seismic Hazard Level
SPL	Structural Performance Level
SRSS	Square Root of the Sum of the Squares
SSI	soil-structure interaction
SSIDs	soil-structure interaction design type
SSI-MDRS	soil-structure interaction modified design response spectrum
SSI-MGDRS	soil-structure interaction modified general design response spectrum
SSS	soil-structure interaction system

1. Introduction

1.1. Background and Motivation

Soil-structure interaction (SSI) regards to the study of the influence of the soil behavior on the structure's and vice versa; the structures that may be prone to SSI include buildings, bridges, tunnels, and other civil engineering infrastructure. The behavior of the soil beneath a structure affects the structural response. In turn, this structural response affects that of the soil and how the actions imposed by machinery or ground motions are propagated being affected by such an interaction. The SSI phenomenon is complex due to the nonlinear behavior of the soil-structure system (SSS), i.e., the superstructure (part of the system that is located above ground) and the substructure (the soil and foundation elements below ground level) responses get modified primarily because of the nonlinear force-deformation relationships representing their behavior.

From the early beginnings of this phenomenon's study, researchers, motivated by strong ground motion events and the damage they caused to infrastructure (Ohsaki, 1966), found out that the structural response and the induced damage depend not only on the characteristics of the superstructure but also on the substructure and the seismic (or any dynamic) demand. Moreover, some noticed that the effects of soil-structure interaction could be significant, especially in areas with high seismic activity or soft soils. Regarding the latter, the poor bearing capacity of the soil and its inelastic deformability potential can induce different effects on the SSS; two of the most predominant are (ATC, 2012; Kausel, 2010; Stewart, Fenves, et al., 1999; Stewart, Seed, et al., 1999):

- *Inertial Interaction*. The inertia developed in the structure due to its vibrations induces base shear and moment actions, which in turn generate displacement of the foundation relative to the free-field. These displacements and rotations are possible because of the flexibility of the soil and foundation elements, which highly contribute to the flexibility of the whole SSS. The most appreciable effects of the inertial interaction are the increase in the building period of vibration due to the SSS augmented flexibility and additional energy dissipation through the radiation damping and hysteretic soil damping. Overall, the inertial interaction effects are responsible for affecting the period of vibration and the damping ratio of the SSS.
- *Kinematic Interaction*. Stiff foundation elements placed at or below the ground surface cause foundation motions to deviate from free-field motions due to effects known as base slab averaging, wave scattering, and embedment effects in the absence of structure and foundation inertia. This means that this interaction effect is induced only by the change in the stiffness of the medium the ground motion waves have to pass through.

Different approaches and computational methods have been used to evaluate the effects of the SSI phenomenon on the structural response. For instance, the substructuring approach considers the soil and the superstructure separately as two systems to be solved independently. The final seismic response obtained for the SSS is calculated as the superposition of individual actions. As such, one can think that equivalent linear representations of the superstructure and the soil should be used for this approach. However, the SSI problem has been solved through equivalent-linear and nonlinear numerical models of the soil domain using the Beam-on-Nonlinear Winkler Foundation (BNWF) for shallow foundations (Raychowdhury, 2008) and nonlinear spring models for pile foundations (Boulanger et al., 1999). To solve the SSI phenomenon through the substructuring approach, three main steps are followed (Kramer & Stewart, 2004): 1) The Foundation Input Motion (FIM) is determined starting from the converted Free-Field Motion (FFM) using transfer functions that reflect the effects of the kinematic interaction, neglecting the inertial counterparts, 2) evaluating the frequency-dependent foundation impedance functions are used to define the stiffness and damping characteristics of the soil-foundation interaction. Such stiffness and damping are modeled through springs and dashpots that are used as support elements for the superstructure, and 3) calculate the seismic response of the structure thus modeled employing either the Modal Response Spectrum Analysis (MRSA) or any of the Time History Analyses (THA). In this last step, the inertial interaction is taken into account. A graphical representation of the substructuring approach is shown in **Figure 1.1**.

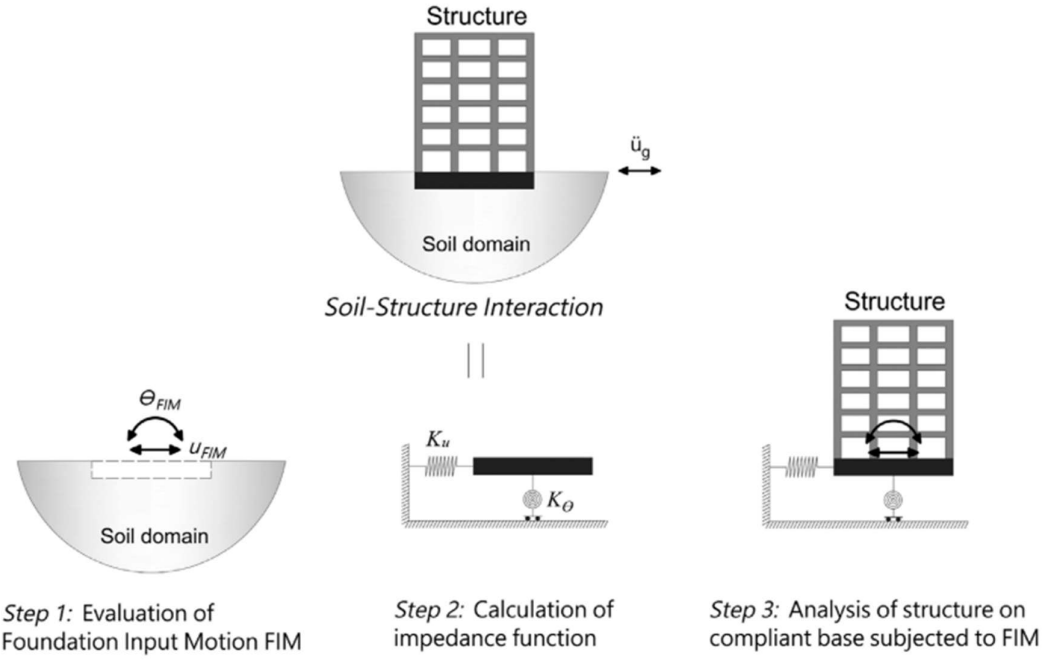

Figure 1.1. Substructuring approach schematization. After (Kramer & Stewart, 2004).

On the other hand, the direct approach is a more rigorous approach to solving the SSI phenomenon problem. In this case, the soil and the superstructure are modeled and analyzed simultaneously by solving the governing equations of motion expressed in [1.1]

$$[M]\ddot{u} + [C]\dot{u} + [K]u = -[M]\ddot{u}_g \qquad [1.1]$$

Where $[M]$, $[C]$, and $[K]$ are the mass, damping, and stiffness matrices, $\ddot{u}$, $\dot{u}$, and u are the acceleration, velocity, and displacement vectors of the system, respectively, and $\ddot{u}_g$ is the ground motion acceleration used as input. Despite being a powerful method for solving complex problems regarding the system geometry and nonlinearities, this approach is rarely used because it is time-consuming, and generating an adequate model could be challenging. The soil is represented as a continuum and connected to the foundation through interface elements. In addition, boundary conditions must be adequately defined to avoid wave reflection and other unwanted phenomena induced by the modeling technique. A schematization of this approach is shown in **Figure 1.2**.

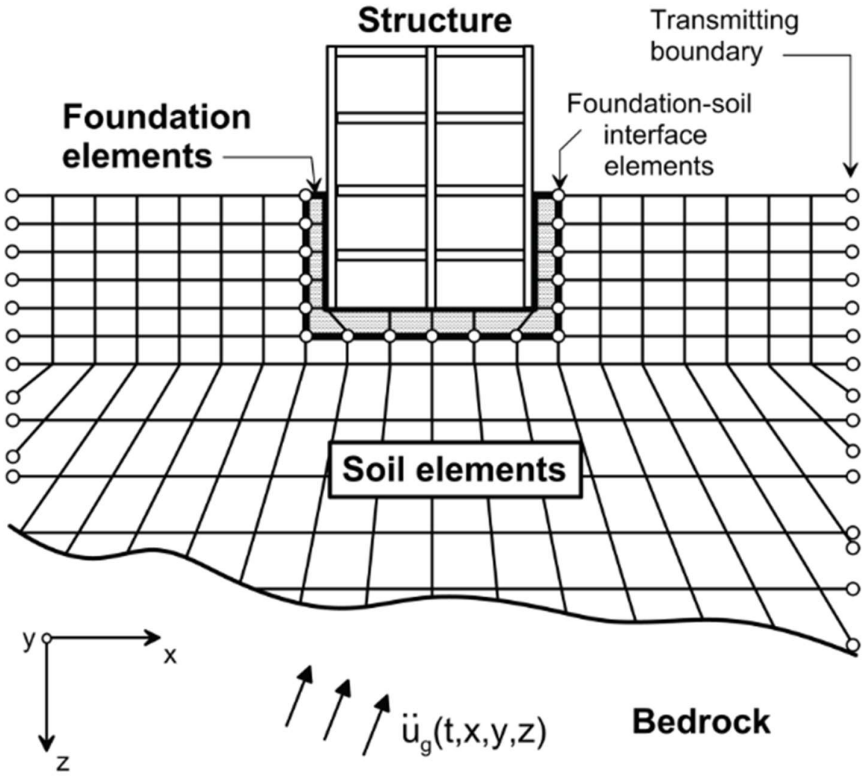

Figure 1.2. Direct approach schematization. After (ATC, 2012).

Several studies have been conducted employing either of the approaches mentioned above for evaluating the SSI effects in the structural response of linear or nonlinear 2D and 3D representations of the soil-structure system. A wide range of conclusions have been drawn from the studies on SSI effects, and its role in the seismic response of structures is still under debate, even though it is well known so far that the interacting effects can lead to beneficial and detrimental structural responses

depending on the SSS characteristics. To name a few of the research work that came out with detrimental effects, there are the studies carried out by (Abdel Raheem et al., 2015; Reza Tabatabaiefar et al., 2013), indicating that an increase in the ductility demand could be expected mostly in lower stories. On the other hand, in (Bhattacharya & Dutta, 2004; Kraus & Džakić, 2013), an increase in lateral displacements and story drifts was found to be common in reinforced-concrete moment frames. Similarly, an increase in deformation in inelastic deformations of structural members (Fatahi et al., 2018; Hokmabadi, 2014), in punding impact for adjacent structures (Ghandil & Behnamfar, 2017), and foundation rocking and settlements (Girault, 1987), have also been identified.

Additional information regarding the soil-structure interaction phenomenon from different points of view can be found in state-of-the-art and literature review published documents. For instance, (Kausel, 2010; Roesset, 2013) consolidate information regarding the historical evolution of the static and dynamic evaluations of SSI effects. Regarding the techniques employed to assess the SSI effects in the structural response, simplified idealizations and their effectiveness in explaining this phenomenon are summarized in (Dutta & Roy, 2002) to name one. Relative to numerical and analytical approaches in evaluating the SSI effects, on the other hand, review articles such as those of (Dhadse et al., 2021; Lou et al., 2011) are available. In addition, comparisons made on techniques with different levels of sophistication are also presented in more recent review studies, such as in (Anand & Satish Kumar, 2018; Far, 2019). In other more general state-of-the-art documents, where an overall evaluation of the consequences generated by the SSI effects is carried out, a review of techniques and approaches employed for different modeling strategies and their adoption in code prescriptions can be found elsewhere (Awchat et al., 2022; Bapir et al., 2023; Darbandsari & Kashani, 2018).

The compilation of the broad and spread information product of research carried out so far in the SSI phenomenon field allows us to have a variety of analysis and design aids that have been developed and improved as academic and research studies come to light. In this regard, it has gradually become more common to find specialized chapters in design standards around the world dedicated to giving guidelines for the seismic design of buildings with interaction effects considerations. However, most of the prescriptive guidelines related to the SSI effects in codes worldwide (when considered) consist of a simple recommendation for taking into account these effects, but no detailed methodologies are indicated. This is the case of Eurocode 8 (EN 1998-5, 2004), the Indian Standard (IS 1893, 2016), the Japanese guidelines (JSCE, 2007), and the New Zealand standards (NZS 1170.5, 2004).

Within the North American scope, on the other hand, the *Minimum Design Loads and Associated Criteria for Buildings and Other Structures* (ASCE-7) (American Society of Civil Engineers, 2017a), and the *Seismic Evaluation and Retrofit of Existing Structures* (ASCE-41) (American Society of Civil Engineers, 2017b) standards prescribe, respectively, seismic design and performance assessment

requirements that account for the SSI effects for their corresponding individual purposes accompanied by a detailed methodology. However, the requirements and recommendations in such standards still rely on the outcomes of oversimplified linear equivalent models of the structure and supporting soil. It is worth mentioning that such simplifications are not just a matter of simple will but because of the complex and intricate nature of a more rigorous analysis of the soil-structure interaction phenomenon using more elaborated models.

Such prescribed recommendations are focused only on reflecting the beneficial effects of the SSI phenomenon, even though it is well-known from studies carried out around two decades ago, that the soil-structure interaction can also induce detrimental effects in the structural response. Quoting Anestis Veletsos, "*With the methods of analysis and the computer programs now available, it is in principle possible to evaluate the dynamic response of any structure-foundation system to any excitation of the base. Such evaluations, however, can be no better than the assumptions underlying the analyses.*" A statement made back in 1992 but still applicable these days in concern to the standards' simplifications.

In light of this brief background, the study presented in this document acquires relevance based on two primary goals. First, focusing our attention on the seismic assessment of the structural performance, we look for a correlation model that allows professionals to calculate the actual performance outcomes that consider the SSI effects based on the obtained seismic performance indicators from buildings modeled both accounting for and neglecting such interaction effects while employing various analysis procedures available in ASCE-41 standard. Second, supported by such performance indicators, a pair of factors dedicated to modifying the seismic design demand and the expected inelastic deformations are recommended to improve the building design outcomes in terms of measured performance. Thus, these modification factors are called to meet the needs of enhancing strength and stiffness characteristics, respectively, of buildings achieving adequate Life Safety and Collapse Prevention structural performance levels. Moreover, these factors consider not only the beneficial effects of the SSI phenomenon but the detrimental ones, seeking to change the current paradigms of the code-prescribed provisions for assessment and design practices. To help accomplish these goals, a reinforced concrete buildings database is constructed considering high seismicity design criteria of the ACI-318 standard for the design requirements of reinforced concrete structures, neglecting and accounting for soil-structure interaction effects. Then, all buildings in the so-built database are assessed through the guidelines described in the ASCE-41 standard to compare their performance indicators and find the sought relationship mentioned above for different structural performance levels. Finally, regression analysis methods employ the same indicators to generate estimation models for the design modification factors. Advanced computational tools such as OpenSeesPy, embedded in the Python environment, for the design and assessment of the buildings

in the database and machine-learning regression techniques for generating the estimation models, are used to ease the development of the tasks involved in the process described above.

It is demonstrated that the generated correlation models can translate the performance indicators obtained through simple analysis procedures and models to those determined using more complex counterparts. This means, for instance, that it is possible to assess a building with or without flexible base conditions using either the modal response spectrum analysis (MRSA) or the pushover nonlinear static procedure (NSP) and transform its performance indicators to those that would be obtained from a flexible base model analyzed through the nonlinear time history analysis (NLTHA). The latter is deemed the analysis procedure giving the closest to actual performance indicators. This represents a leap forward in the performance assessment process since the time-consuming NLTHA can be skipped using a less complex model and analysis procedures. In addition, the modification factor values proved to successfully produce sound building designs that achieve expected structural performance levels while considering SSI effects, something that has been demonstrated unlikely to accomplish just by following the current code-prescribed recommendations.

Supported by the achievement of the stated goals and the rational development of the procedures in making it possible, this document is expected to represent a valuable tool for practitioners involved in earthquake engineering design and a step forward in developing the soil-structure interaction research field.

1.2. Aims and Objectives

The soil-structure interaction (SSI) phenomenon may condition the structural response of buildings subjected to seismic demands; such an interaction could lead to either beneficial or detrimental effects on the response. Nevertheless, currently available performance assessment and design codes within the North American scope prescribe guidelines considering only the silver lining part of this interaction phenomenon. The aim of this thesis is twofold: a) estimate the *actual* seismic structural performance of reinforce-concrete moment-frame buildings, and b) propose suitable modifications to the seismic design prescriptions that allow buildings to reach the expected structural performance levels. Both aims are oriented to include the ambivalent SSI effects known to induce in the structural response instead of relying only on current guidelines. In addressing the former aim, estimation models based on regression analysis were generated after studying the existing correlation between the actual and the approximate structural performance obtained from the assessment of 3D-flexible-base-nonlinear building mathematical models and less complex ones, respectively. As for the latter aim, novel reliable factors are deduced to scale (amplify or reduce) design demand forces and expected inelastic deformations generally employed in the seismic design of buildings using linear dynamic analysis procedures.

The aims described above are met by addressing specific objectives as will be described in the following lines. They are segmented according to each stated aim, starting with those devoted to accomplishing the first of them.

1) Identify the geometrical and mechanical characteristics of the building and the supporting soil, leading to soil-structure systems where the SSI effects are appreciable according to the available literature.
2) Generate a database of reinforced-concrete moment-resisting frame buildings designed according to the geometry and soil considerations required for the SSI to be evidentiated, following the design guidelines for two base support conditions (BSC), fixed-base and flexible-base conditions.
3) Compare the design results of buildings in the database with flexible-base support conditions against those of the fixed-base counterparts to gain a first insight into the different outcomes that the SSI effects induce regarding the design.
4) Identify the most appropriate linear and nonlinear force-deformation relationships for elements of the superstructure and the soil, to develop mathematical models of the buildings designed for constructing the database. Fixed- and flexible-base support conditions are considered to be assessed using the analysis procedures proposed in ASCE-41 standard.
5) Establish, qualitatively, the Structural Performance Levels (SPL) that the buildings should reach when subjected to the accordingly defined Seismic Hazard Levels (SHL) to examine the accomplishment of the corresponding Performance Objective.
6) Determine the seismic demand to be used in the assessment of buildings part of the database in terms of Generalized Response Spectra (GRS) and a suite of eleven pairs of Ground Motion Histories (GMs) for the analysis through linear dynamic (LDP) or nonlinear static procedures (NSP), and time-history analysis procedures (LTHA or NLTHA), respectively.
7) Assess and compare the achieved performance levels of buildings in the database with and without SSI effects considerations to understand the influence of this phenomenon in the structural performance evaluation.
8) Identify the soil-structure system (SSS) parameters that influence and explain the ambivalent effects of the interaction phenomenon in the performance assessment outcomes.
9) Generate an estimation model based on regression analysis methods and the SSS parameters of influence that allows approximating the actual seismic performance of a building, including SSI effects.

As for the second sought aim, it is fulfilled by addressing the following specific objectives:

1) Review the current SSI-oriented code prescriptions for the design of buildings to understand the ground knowledge upon which they are based.

2) Identify the actual seismic demand magnitude that buildings in the database should be prepared to withstand at the design level in order to compare it against the currently prescribed design forces.
3) Evaluate the SSS parameters that better explain the correlation between the currently prescribed non-SSI-dedicated design forces (forces for conventional design) and the actual SSI-dependent seismic demand at the design level to make evident the differences between both criteria.
4) Propose a correction factor that modifies (amplifies or reduces) the conventional design force that implicitly takes into account the soil-structure interaction effects and produces buildings performing as expected, in terms of strength, for the SPLs established at the previous aim.
5) Examine the magnitude of inelastic story drift ratios (ISDR) calculated at the Life Safety SPL, equivalent to the design demand level, to evaluate whether the structural stiffness provided during the prescription-based design process is enough to control excessive inelastic deformations.
6) Evaluate the SSS parameters that better explain the increase or decrease of the obtained ISDR relative to the expected inelastic deformation limits prescribed in the current design code to understand the consequences of lacking adequate stiffness when considering SSI effects.
7) Propose a correction factor that modifies (amplifies or reduces) the currently prescribed deflection amplification factor, C_d, in charge of estimating the expected inelastic deformations while designing a building through any linear procedure. Such a correction factor implicitly takes into account the soil-structure interaction effects and produces buildings performing as expected, in terms of stiffness, for the SPLs established at the previous aim.

1.3. Methodology overview

The previous section introduces the aims and objectives to concisely describe what is sought throughout this document and why; yet, the how requires a somewhat more extended explanation. Thus, this section attempts to give a detailed description of the methodology employed, the design and assessment standards, and the computational tools that were used to carry out this research. It is worth mentioning that the order in which the methodology is described in this section follows that of this thesis' structure.

Evaluating the available literature (Bielak, 1971; Jennings & Bielak, 1973; Veletsos & Meek, 1974), it is acknowledged that some dimensionless parameters were found to be significant for explaining the soil-structure interaction effects in the structural response. These parameters are, for instance, the wave parameter, σ_{SSI}, the slenderness ratio, λ_{str}, the dimensionless frequency parameter, a_o, and the footprint aspect ratio, B/L, to name the most important. Based on this information, a database of

buildings was created by designing them from scratch to have at our disposal several structures to be further assessed. Such a database is generated in this Thesis according to the following considerations:

- The geometrical and mechanical characteristics of the buildings and the soil were chosen to induce noticeable soil-structure interaction effects.
- By analyzing the behavior of the wave parameter σ_{SSI} relative to the variation in the building's height, h_n, and the shear wave velocity of the soil, v_{so}, a series of possible combinations of these last two parameters were defined, ensuring that $\sigma_{SSI} < 20$. In that manner, the presence of SSI effects was guaranteed.
- 9 discrete values of the h_n parameter were selected within the range that complies with the σ_{SSI} condition but expressed in terms of the number of building stories. Hence, the chosen number of stories is defined as $NStr = [4,5,6,7,8,9,10,11,12]$.
- In accounting for the B/L geometrical parameter, a different number of bays in the principal orthogonal directions of the building were defined. For the global X direction, 9 discrete bays were defined as $NbaysX = [4,5,6,7,8,9,10,11,12]$. As for the number of bays in the global Z direction, a constant number was specified, i.e., $NbaysZ = 4$.
- 9 discrete values of the shear wave velocity were also defined, thus, $v_{so} = [130,155,175,200,235,266,300,335,365]$ in m/s units. Additional soil mechanical properties such as the relative density, D_r, the angle of internal friction, ϕ_s, the Poissons modulus, ν_s, the cohesion parameter, c_s, and the self-weight, γ_s, are defined according to (Coduto, 1998; Day, 2010; Hough, 1969; Tokimatsu & Seed, 1987; Wolf, 1985).
- According to the building's geometry and the soil shear wave velocities, a total of 729 different configurations were used in the design process.
- These structures were designed following the design requirements detailed by ASCE-7 (American Society of Civil Engineers, 2017a) for determining the gravitational and seismic demands, and the prescriptions included in (ACI Committee 318, 2019) for providing adequate strength and stiffness to the buildings' elements.
- In addition to the 729 configurations described earlier, 2 base support conditions (BSC) were considered: a fixed-base BSC to generate conventionally designed buildings (*convDs*), i.e., without SSI effects considerations, and a flexible-base BSC (*SSIDs*) for addressing their design counterparts. Hence, two design types (DT) were considered.
- The total number of designed structures that make up the building database, thus, reached up to 1,458.
- Design considerations regarding the flexible-base building to consider the SSI effects were established in Chapter 19 of the ASCE-7 standard. These guidelines were strictly applied for this purpose.

- The Modal Response Spectrum Analysis (MRSA) was the design-oriented analysis procedure. This analysis procedure was selected to make the most familiar to the average ground knowledge of professionals.
- A high seismicity level was identified within the North American pacific coast, so the elements were designed as part of *special* structural systems.
- OpenSees (McKenna et al., 2010), through its enhanced capabilities in the embedded Python environment (OpenSeesPy (Zhu et al., 2018)), was selected as the modeling and analysis engine for the design process in this thesis. This combination of computational tools was chosen because of the practicality of pre- and post-processing data inputs and outputs during the analysis procedure. It is worth mentioning that the algorithms used during the analysis and design processes were written from scratch for this research aiming to automatize the task of designing such a considerable number of buildings in the database.
- In generating the flexible-base building mathematical models, the sub-structuring method was used. It considers the soil linear or nonlinear force-deformation relationship concentrated in zero-length elements at the foundation-soil interface. The spatial distribution and their behavioral relationships were defined according to the recommendations of (Applied Technology Council, 1996) and (Harden et al., 2005). This flexible-base modeling method was preferred over the so-called direct approach, in which the soil medium is entirely modeled and fully coupled to the superstructure because it is less time-consuming than the latter. Given the large number of buildings to be designed, this decision was the most appropriate regarding time efficiency.
- The results obtained from the design process for both BSC considerations were compared to understand the different influence that SSI code prescriptions exert on the design outcomes relative to those of the conventional design guidelines. This comparison was made by calculating the relative mass and stiffness of the structures designed accounting for SSI effects and their conventionally designed counterparts.

After completing the design process, the generated buildings for the database were subjected to a performance assessment. As detailed above, this process involved additional steps to those executed for the design that permits the building seismic evaluation and, based on the outcomes, generate estimations of the actual response. The procedures are:

- The *Seismic Evaluation and Retrofit of Existing Buildings*, ASCE-41 standard, was chosen for applying their guidelines regarding the seismic performance assessment of the structures designed for the database. This standard is appropriate for evaluating structures that have been designed following the north American standards design prescriptions mentioned earlier.

- In assessing the performance of buildings, a Basic Performance Objective (BPO) was established based on the recommendations in ASCE-41. Considering the structures in the database as *New Buildings* since current design prescriptions were employed in such design process, the BPO was selected accordingly. The BPO equivalent to new buildings (BPON) requires a pair of Seismic Hazard Levels (SHL) and their corresponding Structural Performance Levels (SPL) to be selected. **Table 3.1** shows the two SPL-SHL combinations used during the performance assessment.
- The performance assessment implied subjecting the structures in the database to seismic demands adjusted to the SHLs selected while establishing the performance objective. How these demands were specified depended on the Analysis Procedure used. In that sense, linear and nonlinear, static and dynamic procedures are suggested by ASCE-41. The *Equivalent Lateral Force* (ELF) procedure is recommended as the linear static procedure (LSP), and *Linear Time-History Analysis* (LTHA) or Modal Response Spectrum (MRSA) analyses can be selected as the linear dynamic procedure (LDP). In contrast, *Pushover* (PO) and the *Nonlinear Time-History Analysis* (NLTHA) procedures of analysis are included for *Nonlinear Static* (NSP) and *Nonlinear Dynamic* (NDP) procedures, respectively. Every APs but the LSP was used to assess structures since it is not permitted based on geometric limitations present in the buildings in the database.
- The demand was specified for the MRSA (LDP) and the Pushover (NSP) analysis procedures by constructing a General Response Spectrum (GRS). It is called *General* because it can be defined for damped spectral responses different from the 5% recommended in ASCE-7 for conventionally designed structures. However, for the GRSs used in assessing flexible-base building models, the GRS in ASCE-41 is the same as the one recommended by Chapter 19 of ASCE-7 for other damping ratios.
- For the LTHA (LDP) and the NLTHA (NDP) analysis procedures, though, the demand was specified as a suite of 11 eleven pairs of orthogonal horizontal Ground Motion History Records (GMs). In addition, these GMs were first signal-processed and then modified to reach the specified SHL through scaling procedures.
- The signal-processing of the GMs was carried out by trimming the signal accounting for the Significant Duration (5-95SD), a base-line signal correction, filtering the signal using a band-pass filter model, and finally, smoothening the signal with a Tukey window model and zero padding at the end of the earthquake record for evaluating the free-vibration response of the building.
- The scaling process involved the progressive amplification or reduction of the GMs ordinates' magnitude until the mean of the Maximum Direction Spectrum (MDS) (David M. Boore, 2010) of all GMs in the suite represents no less than 90% of a target GRS.

- Also linked to the selected APs were the modeling requirements that had to be fulfilled. For instance, nonlinear 3D models of the superstructure and the soil should be used while analyzing buildings through the NSP and the NDP. At the former, a monotonic representation of the force-displacement behaviors in elements' sections and for soil elements (when flexible-base conditions were considered), while cyclic counterparts for the latter AP.
- In modeling the nonlinear behavior superstructure elements, concentrated plasticity models were used for the moment-rotation relationship in beam ends through the Modified Ibarra-Median-Krawinkler deterioration model with peak-oriented hysteresis response (Ibarra & Krawinkler, 2005) according to the recommendations of (Curt B. Haselton et al., 2008; Curtis B. Haselton & Deierlein, 2007). Fiber model sections were selected for columns to describe the P-M-M interaction in the nonlinear response straightforwardly.
- As for the nonlinear representation of the soil force-deformation relationship, the *QzSimple* and *TzSimple* (Boulanger et al., 1999) materials were used. The former is in charge of the vertical bearing deformation-capacity relationship, and the latter is for the frictional-sliding counterpart.
- In applying linear analysis procedures (LTHA and MRSA), the same modeling criteria used in the design process were followed.
- To evaluate the accomplishment of the selected BPON, structural responses such as forces and deformations in elements induced by the seismic demand were compared against the section's element capacity to withstand the same actions (i.e., forces or deformations). The ratio of the exerted demand to the sections' capacity was calculated and compared against acceptance criteria as required in ASCE-41 to obtain the so-called $DCR_{(ac)}$. This performance indicator helps to identify whether a section (and ultimately a building) is capable of withstanding the demands to which they are subjected at a certain SHL.
- Using the $DCR_{(ac)}$ indicators, the performance achieved in buildings in the database considering SSI effects during the design process and both fixed-base and flexible-base support conditions during the assessment process were compared to those traditionally-designed buildings to draw conclusions regarding the differences in the performance when applying currently available design and evaluation guidelines.
- Assuming that the performance indicators obtained from buildings evaluated with flexible-base considerations analyzed through the NDP analysis procedure are the closest to the actual performance in real scenarios, a relationship was sought to translate $DCR_{(ac)}$ indicators obtained from other BSC-AP combinations to that of the actual *flexBase*-NDP.
- The translation of performance indicators, as described in the previous point, was meant to be done by a simple product operation using the expression:

$$DCR_{(ac)NDP:SPL}^{DT:flex} = \Psi \times DCR_{(ac)AP:SPL}^{DT:BSC} \quad [1.2]$$

Where Ψ is the translation term explaining the relationship between the starting and target performance indicators shown in the above equation.

- A list of SSS parameters was believed to influence the relationship sought for such a translation; they were detailed in **Table 4.1**. These parameters were used as predictor variables in the regression analysis performed through Classical Regression (CR) and two machine learning (ML)-based techniques, namely, Deep Neural Network regression (DNN) and the Gradient Boosting Regression Trees (GBRT).
- Using the regression methods detailed above, estimation models of Ψ translation factor in the form of equations (for the CR) and computational models (for the ML-based regression techniques) were generated to approximate the actual performance indicator. Every obtained model was presented and evaluated against each other to identify and recommend the best model in this thesis.

The first aim of this thesis was accomplished by completing the procedures carried out in the previous points. Regarding the second aim, the structural outcomes from the performance assessment were employed, especially those corresponding to the Life Safety (LS) SHL, because it equals the design demand level, as mentioned earlier.

The following procedures listed below were performed to propose suitable modifications to the seismic design prescriptions that allow buildings to reach the expected structural performance levels.

- The basis of the prescriptive seismic design of buildings was examined, focusing first on those related to determining the design demands (base shear design forces) calculated when the SSI effects are considered. Due to the interaction effects, these demands can be reduced according to ASCE-7. Nevertheless, it has been mentioned that SSI effects could lead to even an increment in the response of buildings subjected to LS seismic demands.
- Four different analysis procedure-based scenarios were established, one per each AP employed in the performance assessment to evaluate the base shear seismic forces induced when subjecting the buildings in the database to the LS SHL. The base shear forces so determined were compared against those used in designing the structure, considering a fixed-base support model to identify the actual increase or decrease in force magnitude that can be expected.
- This comparison was carried out through the definition of a ratio factor expressed as $\alpha = \tilde{V}/V$. The numerator in the ratio represents the actual base shear demand for the flexible-base structure that would be rather used instead of the fixed-base structure base shear design force, V (in the denominator). The factor α, thus, can theoretically be used in increasing or

decreasing the prescribed seismic design demand, along with modeling the building with flexible-base considerations, to account for the SSI effects in the design process.

- After analyzing the four scenarios mentioned earlier, the NDP analysis procedure scenario was taken as the one giving responses closer to the actual ones since α values calculated employing this AP reflect the beneficial and detrimental effects of the interaction phenomenon.
- A relationship between α factor and the same predictors listed in **Table 4.1** was sought again through regression analysis based on the CR, DNN, and GBRT methods, and estimation models were generated. These models were likewise presented in the form of equations for the CR and computational objects for the ML-based techniques to approximate the values of α and further determine a more realistic design base shear force that considers the ambivalent characteristics of the SSI phenomenon.
- The process was repeated this time though evaluating the Inelastic Story Drift Ratios (ISDR) obtained from the NDP AP scenario for the LS SPL (δ_{NDP}). These inelastic deformations were compared to the limit specified by ASCE-7, the allowable drift ratio Δ_a/ρ. When performing a design-oriented analysis through linear procedures such as the MRSA used in this study, the obtained elastic deformations, δ_e, must be multiplied by the Deflection Amplification Factor, C_d, to approximate them to an expected inelastic deformation. The lateral stiffness of the building is then adjusted until $C_d\delta_e \leq \Delta_a/\rho$. Theoretically, the term $C_d\delta_e$ should be equivalent to δ_{NDP} obtained from the NDP-LS combination; this is why the latter was compared against Δ_a/ρ.
- A factor denominated as α_{C_d} was defined by the ratio $\delta_{NDP}/(\Delta_a/\rho)$, which represents a correction factor to modify the theoretical value of C_d given by ASCE-7 and generate better estimations of expected inelastic deformations based on elastic responses.
- The same predictors and regression methods were used to generate estimation models to approximate the α_{C_d} factor as a function of the most influencing SSS parameters. With the estimated α_{C_d} factors the product operation $\alpha_{C_D} \times C_d$ can be calculated to determine a more realistic deflection amplification factor, C_d^{real}, valuable for design purposes.

Once both α and α_{C_d} factor models were generated and used in a validation example to determine which estimation model is the most appropriate for developing buildings showing adequate expected performance levels and avoiding creating uneconomical structures.

1.4. Document organization

This thesis document has been organized so that the objectives and the points described methodology overview are progressively addressed and thoroughly explained.

Chapter 1. Introduction

This chapter begins by briefly contextualizing how the SSI effects have been studied over the last decades and how it was applied in real-case scenarios. It is recognized how challenging it is to be understood and used by typical professionals when the original raw basis of the phenomenon is examined. Then, it describes how the terminology in the SSI effects context was unified to be portrayed in assessment and design frameworks within the North American scope and the advantage it represented to performance-based earthquake engineering design taking into account these effects. Despite the decades dedicated to refining the ground knowledge regarding the SSI phenomenon, the authors still identify a gap expected to be closed through this study.

The aims are later stated, and the objectives are enumerated. A description of the methodologies and tools used in addressing the objectives and fulfilling the aims of this thesis are detailed in a structured fashion. Finally, by the end of the chapter, the organization of the document is portrayed.

Chapter 2. Structural Design

The design process for constructing a building database of buildings is explained in Chapter 2. According to the literature, some parameters define the SSI effects affecting the structural response. Based on the combined behavior of these parameters, a range of values for the geometrical and mechanical characteristics of the building and the supporting soil are defined, for which the interaction effects are appreciable. The design seismicity level, two base support conditions for accounting and neglecting the SSI effects, and the mathematical models' description are also presented in this chapter. The design outcomes regarding the differences between the mass and stiffness of buildings designed with SSI effects considerations and their fixed-base counterparts are examined.

Chapter 3. Seismic Performance Assessment

The designed buildings in the database are assessed to evaluate their performance according to ASCE-41 standards, and the results are presented in this chapter. According to the prescribed guidelines, the performance assessment can be done by analyzing the buildings through different linear and nonlinear static and dynamic analysis procedures (APs). For this study, four APs are used for this purpose, and mathematical models of the buildings are generated accordingly to compare their results to define the one AP that gives outcomes closest to the actual response that a building could develop. By the end of the chapter, a hypothesis is stated regarding the possibility of approximating the actual performance of buildings considering SSI effects based on the assessment using less complex models and less time-consuming analysis procedures employing a translation factor denominated as Ψ.

Chapter 4. Estimation of Structural Performance

In this chapter, the behavior of the translation factor Ψ relative to some selected SSS parameters is studied to estimate the actual performance. For this purpose, some SSS parameters are believed to explain the relationship between the actual performance and Ψ factor, so they are selected and listed. Using the classical regression method and machine learning techniques, estimation models for Ψ are generated, considering the chosen parameters as predictors and the translation factor as the response variables. A detailed explanation of how the predictors are processed before using them in regression analysis is presented, and finally, an evaluation of the more significant predictors is described. It is shown that the machine learning-generated estimation models efficiently approximate the actual performance of buildings through Ψ.

Chapter 5. Recommended Modifications on the Prescriptive Seismic Design with considerations of SSI Effects

This chapter first examines the basis for building seismic design considering SSI effects in currently available code prescriptions and the flaws encountered. Nowadays, design guidelines only acknowledge the beneficial effects of the SSI phenomenon, and the expected inelastic displacements induced are accounted for by generating a flexible-base model. Hence, using the same responses obtained from the performance assessment in Chapter 3 related to the design hazard level along with the selected predictors, estimation models are generated to estimate the increase in both design forces and expected inelastic deformations that would be rather used in the seismic design of buildings. Two factors are proposed for achieving this goal, α and α_{C_d}. The former is a correction factor focused on the design forces, and the latter is on the expected inelastic deformation in a SSS. These novel factors attempt to ease the design process with interaction effects considerations while improving the seismic structural performance of the buildings so designed.

Chapter 6. Verification: RC Building Design Based on Estimations

As stated in the chapter´s description, the design modifications proposed in Chapter 5 through the use of α and α_{C_d} factors are verified. An example building chosen from the database is designed considering the values of such factors calculated employing every α and α_{C_d} estimation model, and then subjected to a performance assessment. The outcomes from these procedures indicate that the proposed design modification factors successfully produce buildings better prepared for withstanding the design seismic hazard level and a more demanding one. Nevertheless, one $\alpha - \alpha_{C_d}$ combination is finally recommended for designing buildings that not only perform adequately but avoiding the overestimation of SSI demands.

Chapter 7. Conclusions and Recommendations for Future Work

Chapter 7 is a closing section with a brief recap of this study and conclusions drawn from every preceding chapter. In addition, some recommendations for future work are exhibited, hoping that the efforts made to bring this thesis to light help professionals and researchers expand the knowledge regarding the SSI phenomenon even further.

Appendices

Six appendices were needed to complement the procedures and outcomes from the seven chapters described above. Appendix A gives additional information regarding the assessment process and some important guidelines data recommended by the ASCE-41 standard. On the other hand, Appendix B shows a set of closed-form equations used in this research study to calculate the yielding and ultimate moment-rotation couples for the nonlinear modeling of reinforced concrete elements (Monti & Petrone, 2015). Then, Appendix C is in charge of graphically portraying the signal-processing and scaling procedures outcomes for the ground motion histories selected to carry out the time-history analysis APs. Appendix D graphically complements the performance assessment outcomes for every DT-BSC-AP-SPL (design type – base support condition – analysis procedure – structural performance level) combination. Appendix E presents the correlation between the predictor variables and the performance translation factor, Ψ, through scatter plots and Pearson correlation matrices. Finally, Appendix F details a short analysis of the overstrength factor and its dependence on the soil-structure interaction effects.

2. Structural Design

2.1. Overview

This section defines the geometrical characteristics of structures used in the study, the soil properties beneath them, and the seismicity level used during the design process. A short yet meaningful analysis is first developed in Section 2.2 to get a suitable building database for which soil-structure interaction (SSI) effects are noticeable enough to be evaluated. Then, based on past studies, referenced in the corresponding sections and on an assumed geographical location, soil properties are defined to establish their behavior applied to the mathematical model in Section 2.3. The number of buildings that comprise the database and the soil mechanical properties used in the design process are based on the above-mentioned sections.

Next, also through the same geographical location assumption that lets us define the soil mechanical properties, the seismicity level is determined in Section 2.4. Once the previous definitions are established, Section 2.5 explains some general and specific aspects of the design process to make the reader aware of how SSI effects are considered in this step. It is recalled that the design requirements followed throughout this study are based on North American standards; namely, ASCE-7 (American Society of Civil Engineers, 2017a) for preliminary load definitions and SSI modeling considerations, and ACI-318 (ACI Committee 318, 2019) for providing adequate strength to elements' sections.

Lastly, 2.6 briefly reviews the design outcomes in terms of the dynamical properties of the buildings part of the study database.

2.2. Definition of building suite geometry

It is well known that the response of soil-structure systems (SSSs) depends on the geometrical and mechanical properties of the foundation elements, the supporting soil, the superstructure, and some excitation characteristics. Past research works, such as (Bielak, 1971; Jennings & Bielak, 1973; Veletsos & Meek, 1974), first found that dimensionless parameters involving these properties better express the behavior of such structural response. Three of these parameters are formulated in Eqs. [2.1] to [2.3] corresponding to the wave parameter, σ_{SSI}; the structure's slenderness ratio, λ_{str}; and the dimensionless frequency, a_o.

$$\sigma_{SSI} = \frac{v_{so} T_n}{h^*} \quad [2.1]$$

$$\lambda_{str} = \frac{2h^*}{B} \quad [2.2]$$

$$a_o = \frac{\tilde{\omega}_n B}{2v_{so}} \quad [2.3]$$

Where v_{so}, T_n, h^*, B, and $\widetilde{\omega}_n$ stand for the shear-wave velocity at small soil-strain levels, the fundamental period of the fixed-base structure, the first-mode effective height, the foundation's width, and the flexible-base structure's fundamental angular frequency, respectively. The relevance of the apparent correlation between these parameters and the structural response lies in their dependence on both structure and soil characteristics, mainly σ_{SSI} and a_o. For instance, the former may be considered a soil-to-structure stiffness ratio. On the other hand, the latter has the physical interpretation of being the ratio of the foundation half-width to a fraction of the seismic wavelength of an excitation having the same frequency as the flexible-base structure (American Society of Civil Engineers, 2017a; ATC, 2012). Taking advantage of the premise mentioned above, researchers devoted part of their work to evaluate how the variation of these parameters affects the behavior of flexibly supported structures and, at the same time, finding limit values that may anticipate when SSI effects are negligible.

Let us consider the wave parameter σ_{SSI}. Studies analyzing single-degree-of-freedom (SDOF) linear and nonlinear systems over linear representations of flexible soil, (Lin et al., 2008; Moghaddasi et al., 2012; Veletsos & Meek, 1974; Wu et al., 2001), agree that: when $\sigma_{SSI} < 20$, SSI effects on the structural response *may deserve* consideration. In addition, a more specific research work related to nonlinear reinforced concrete (RC) framed structures developed by (H. R. Tabatabaiefar & Massumi, 2010) concludes that it is *essential* to consider SSI effects when $\sigma_{SSI} < 10$, agreeing with the recommendations given in (Stewart et al., 2004). These limiting values are now acknowledged in practical guidelines for analyzing and designing buildings considering SSI effects. For instance, documents (ATC, 2012) and (Applied Technology Council, 2020) use the wave parameter as a rule-of-thumb test to determine whether the interacting effects are likely to be significant. Thus, it is evident that certain combinations of building periods (or heights) and soil shear wave velocities represent SSSs whose σ_{SSI} value indicates the presence of SSI effects.

Regarding the period of vibration, we would establish that RC-framed buildings making up the study database are designed following prescriptions in ASCE-7 (American Society of Civil Engineers, 2017a) and ACI-318 (ACI Committee 318, 2019). According to the former standard, the fundamental period of buildings can be approximated using the expression in Eq. [2.4].

$$T_a = C_t h_n^{\,x} \qquad [2.4]$$

Where C_t and x are building period coefficients that depend on the type of structure and h_n is the total building height. Specifically for RC buildings, C_t and x adopt values of 0.0466 and 0.90 for the metric system, respectively. These coefficients were obtained from constrained regression analyses developed by Goel and Chopra (Goel & Chopra, 1997) and correspond to the-best fit -1σ (reads, best fit minus one standard deviation) as a conservative pair of values to use in Eq. [2.4]. Therefore, it is considere that periods approximated with these coefficients will deliver conservative spectral

demands. However, recalling that one of the main consequences of taking into account foundation flexibility in the building system is the period elongation, it may be reasonable to use the best-fit coefficients instead of those adopted in (American Society of Civil Engineers, 2017a), aiming to obtain larger values of T_n. Chopra and Goel in (Chopra & Goel, 2000) showed that $C_t = 0.0524$ (0.018 in the original $ft.$-units expression) for the best-fit regression when constrained to $x = 0.90$.

Combining Eq. [2.1] with Eq. [2.4] and assuming that $h^* = 0.70h_n$, Eq. [2.5] is obtained.

$$h_n = \left(1.43 C_t \frac{v_{so}}{\sigma_{SSI}} \right)^{\frac{1}{1-x}} \qquad [2.5]$$

In its general form, this simple yet helpful expression relates the shear wave velocity, the wave parameter, and the period coefficients to the building height. On the other hand, Eq. [2.6] provides a similar relationship specific to RC buildings. Here C_t and x coefficients have been replaced by their best-fit regression values.

$$h_n = \left(0.075 \frac{v_{so}}{\sigma_{SSI}} \right)^{10} \qquad [2.6]$$

Eq. [2.6] allows us to find an $h_n - v_{so}$ pair for a fixed σ_{SSI}, making it easier to select appropriate soil and building characteristics in this study while ensuring the presence of SSI effects in the response. **Figure 2.1** depicts the relationship between h_n and v_{so} of Eq. [2.6] for fixed values of $\sigma_{SSI} = 10$ (dashed curves), 20 (dotted curves), and 15 (solid curves). Also, two vertical lines are shown in the graph. The blue one at $182 m/s$, represents the v_{so} limit value for site class E (SC-E), and the pink line at $365 m/s$, represents the same for site class D (SC-D), according to ASCE-7 standard. As mentioned before, when σ_{SSI} gets values below 10 or 20 indicates that SSI effects would either be *essential* to consider or *may deserve* consideration, respectively. The value of 15 was included as the mean value between both limits.

Consequently, **Figure 2.1** shows in shaded areas the $h_n - v_{so}$ space for which whatever combination of values of both characteristics in a SSS would reflect interacting effects in the response. Notice that, for any building higher than $20m$ and resting over SC-E soil, the need to evaluate SSI effects results as *essential*. On the other hand, a structure of the same height founded on SC-D soil *may* show signs of these effects depending on the magnitude of v_{so}.

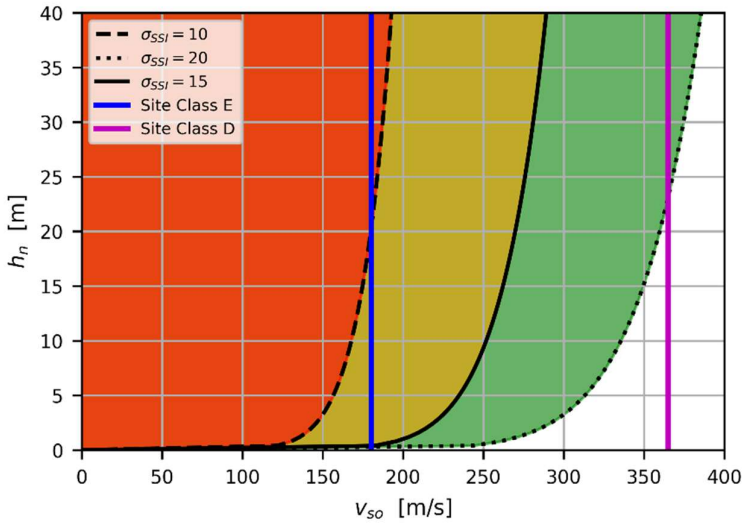

Figure 2.1. $h_n - v_{so}$ relationship for fixed values of σ_{SSI}.

In light of the brief analysis developed in previous paragraphs, the characteristics of buildings and the supporting soil in terms of v_{so} are defined and enumerated in the following lines. Refer to **Figure 2.2** for a graphical description of the terminology used below.

- 1 constant number of bays in the Z direction for all buildings; $NbaysZ = 4$.
- 9 different numbers of bays in the X direction; $NbaysX = [4,5,6,7,8,9,10,11,12]$.
- 9 different values of shear wave velocity; $v_{so} = [130,155,175,200,235,266,300,335,365] m/s$, corresponding to SC-D and SC-E soils.
- 9 different numbers of stories with a constant interstory height of $h_i = 3.0m$ are considered: $NStrs = [4,5,6,7,8,9,10,11,12]$.

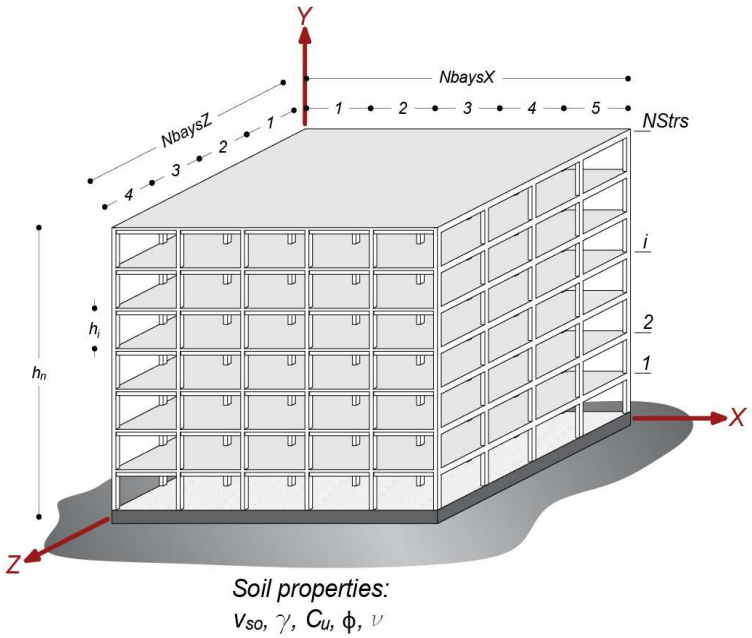

Figure 2.2. Graphical description of building and soil characteristics.

It is worth noting that the amount of buildings considering the above definitions is 729. Still, as further explained in Section 2.5, the total number of designed structures doubles that amount. It is no less important to declare that all buildings in the constructed database are assumed to have shallow foundation systems stiff enough to consider them as rigid diaphragms.

2.3. Definition of seismicity level

According to ASCE-7, structures can be assigned to different *Seismic Design Categories* (SDC) identified by letters from SDC-A to -F depending on the site seismic hazard, the relative importance of the structure (translated to a *Risk Category* classification), and the site soil classification (or *Site Class*). Category A reflects the absence of generalized seismic affectations on the structural system. Conversely, category F indicates that seismic demands are considerably high on a relatively important structure founded on soils whose properties tend to increase these demands. This section exhibits the selection of a determined seismicity level based on the aims of this study.

To conjugate the building SDCs classification with actual design requirements, Chapter 18 of ACI-318, devoted to seismic design, identifies three types of structural systems or structural elements: "*ordinary*," "*intermediate*," and "*special*" denominations. **Table 2.1** shows the relationship between the SDCs, the recommended structural type, and a qualitative description of the expected seismicity.

In general terms, it can be noted from **Table 2.1** that buildings assigned to SDC-D, -E, and -F are treated by ACI-318 in the same way. *Special* elements are recommended for assembling the structural system within that SDC design framework, where "*special*" means more astringent limitations in the design requirements.

Table 2.1. SDC relationships with structural type denomination

Seismic Design Category (SDC)	Recommended structural type	Expected seismicity
A	No need to fulfill seismic design requirements	**No** ground motion movements
B	***Ordinary*** moment-resisting frames	**Slight** ground motions at long time intervals
C	Combination of ***ordinary*** structural walls or pre-fabricated ***intermediate*** walls with ***intermediate*** moment-resisting frames	**Moderately strong** ground motions
D, E, and F	***Special*** moment-resisting frames, ***special*** structural walls, or a combination of both	Might be subjected to **strong** ground motions

Let us recall that it was stated in the introductory chapter (Chapter 1) that this study aims to evaluate the structural performance of buildings when subjected to *high* seismic demand levels while taking into account SSI effects in the response. Thus, given that the definition of seismicity level depends on the geographical location selected for the building database implantation, an adequate one fulfilling this objective shall be established.

Following the recommendations made by the ASCE-7 standard, the identification of seismic intensity (i.e., seismicity level) starts by determining the relative distance between the building's implantation and a known active fault. In this regard, one can classify a site as a *Near-Fault* or *Far-Fault Site*. The former refers to a site within $15km$ or $10km$ from the surface projection of a known active fault capable of producing $M_w 7$ or $M_w 6$ or more significant events, respectively. For this study, *Far-Field Site* conditions are assumed in the design and the assessment process (the latter, addressed in Chapter 3). The main reason for this decision is that the Near-Field Site conditions imply an additional evaluation and processing of the pulse-like ground motion records and the design spectra. Information regarding the study of the response of buildings considering SSI effects subjected to Near-Fault Site ground motions can be found elsewhere (Brunelli et al., 2021; Cao, 2021; Chouw & Hao, 2008a, 2008b; Dabaghi & Der Kiureghian, 2018; Fatahi et al., 2014; Galal & Naimi, 2008; Ghandil & Behnamfar, 2017; Güllü & Karabekmez, 2017; Masaeli et al., 2018; Minasidis et al., 2014; Sudret et al., 2014; S. H. R. Tabatabaiefar et al., 2013; Taghizadeh et al., 2021; Vicencio & Alexander, 2018; Yeganeh & Fatahi, 2019).

The next step in defining the seismicity level is determining the mapped response spectral accelerations for 5% damped structures according to the geographical location. These acceleration response parameters are identified as S_s and S_1 and expressed in terms of expected acceleration values in units of $[g]$ for systems having short vibration periods ($T_n = 0.20s$) and $1.0s$ periods, respectively. These acceleration values are consistent with the Risk-Targeted Maximum Considered Earthquake (MCE_R) ground motion response acceleration. The MCE_R acceleration parameters represent the most severe earthquake effects for the orientation that results in the largest maximum response to horizontal ground motions, adjusted for a uniform targeted risk (American Society of Civil Engineers, 2017a).

Figure 2.3 displays a map showing the assumed location for the buildings in the suite whose acceleration response parameters are $S_S = 1.50g$ and $S_1 = 0.817g$. The values for these parameters were obtained from the mapped values in Chapter 22 of ASCE-7 Standard. The site and the parameters described in previous lines correspond to a high seismicity level. Nevertheless, it will be further demonstrated in Section 3 that the combination of acceleration response parameters described in the current section, the soil properties defined in Section 2.4, and the selected relative importance of the buildings result in a Level of Seismicity defined as **High**.

Figure 2.3. Building suite assumed location.

At the beginning of this section, it was explained that assigning a structure to a determined SDC depends not only on the definition of the seismic hazard but on the *Risk Category* and the *Site Class*. How the acceleration response parameters (S_s and S_1) already introduced are processed and conjugated with these other classifications to define the seismic demand for the design is addressed in more detail in Section 2.5.

2.4. Definition of suite's soil properties

Even though Section 2.2 introduced the general soil property definition through the shear-wave velocity, v_{so}, there are additional characteristics that may be helpful to determine in advance. First, let's recall that in creating the building suite database, a space $h_n - v_{so}$ was found in which SSI effects are worthy of accounting for. During the design process, as explained in the subsequent section, only the soil parameter v_{so} is needed to represent the mathematical model of the supporting media. However, **Table 2.2** lists five other characteristics for each of the nine soil v_{so} values selected while creating the database. Features in the table include the shear-wave velocity at small soil strain levels, v_{so}, consistent with ASCE-7 *Site Class* classification, the average unit weight, γ_s, the Poisson's ratio, v_s, the cohesion parameter, c_s, the relative density, D_r, and the angle of internal friction, ϕ_s.

The additional characteristics in **Table 2.2** are essential to generate a simplified mathematical nonlinear model of the soil for the performance assessment procedures of Chapter 3. It is important to mention that the shear-wave velocity values and amount were selected to provide a wide range of appreciable responses generated by the influence of SSI effects. Other parameters, such as D_r has been adopted from (Tokimatsu & Seed, 1987), the angle of internal friction, ϕ_s, from recommendations described in (Hough, 1969), and the rest from topic-related texts such as (Coduto, 1998; Day, 2010; Wolf, 1985).

Table 2.2. Soil characteristics for the created database.

Site Class	v_{so} [m/s]	γ_s [kN/m^3]	υ_s [-]	c_s [kPa]	D_r [-]	ϕ_s [°]
E (*soft soil*)	130.0	17.0	0.45	18.0	0.0	10
	155.0	18.0	0.45	20.0	0.0	10
	175.0	20.0	0.45	35.0	0.0	10
	200.0	21.0	0.45	75.0	0.0	10
D (*stiff soil*)	235.0	21.0	0.30	150.0	0.0	10
	266.0	22.0	0.30	0.0	65.0	32
	300.0	22.0	0.30	0.0	80.0	34
	335.0	22.0	0.30	0.0	80.0	34
	365.0	22.0	0.30	0.0	90.0	36

All these parameters have been selected to adjust the characteristics of typical soil conditions in sites nearby the one defined in Section 2.3, taking into account site studies (Borcherdt, 1994; Borcherdt & Glassmoyer, 1992; Crouse & McGuire, 1996).

2.5. Design considerations

2.5.1. General aspects

As mentioned previously, RC framed structures are designed following ASCE-7 provisions for determining design loads and ACI-318 requirements for providing adequate strength for the structural elements. Overall recommendations for calculating the seismic demand to be applied to buildings designed conventionally (without SSI effects considerations) are issued in Chapters 11 and 12 of ASCE-7; these specific requirements are addressed in Section 2.5.2 of this document. On the other hand, the procedures for calculating the adjusted demands affected by SSI effects are depicted in Chapter 19 of the same standard. The latter are treated in Section 2.5.3 of this work.

The current research considers two *Design Types* (DT) in creating the complete building database. 729 buildings were first conventionally designed using the base shear demand calculated per Chapter 12 of ASCE-7 ($DT = convDs$). In addition, the same number of structures are designed considering provisions of Chapter 19 for soil-structure interaction seismic design ($DT = SSIDs$), totaling 1,458 designed buildings. The database constructed in this manner is helpful for a straightforward comparison of the seismic performance of the same building designed using both DTs (carried out in Section 4).

Independently of the DT, some essential definitions remain constant. For instance, the SDC introduced in Section 2.3 is considered the same for both the fixed-base and flexible-base buildings design. Implied in the description of the SDC is the definition of the *Risk Category*. The criteria for selecting a category regards to structural and occupancy considerations. The classification of these categories reflects a progression of the anticipated seriousness of the consequences of failure of a specific structure to risk of human life. In that sense, ASCE-7 discretizes *Risk Categories* from the

lowest to the highest in terms of *Risk Category I* to *Risk Category IV*, respectively. A rational basis for determining the seismic design-oriented Risk Category classification is based primarily on the number of persons whose lives would be endangered in the event of a failure, or "lives at risk" for short. This concept encompasses the risk of persons occupying the structure in question, and those who are outside and prone to suffer the consequences of falling objects part of the structure or the structure itself. In this regard, ASCE-7 delivers a visual aid for approximately relating the number of persons at risk and the category to be selected. This graphical description is shown in **Figure 2.4**, taken from the standard mentioned above and replicated here for convenience.

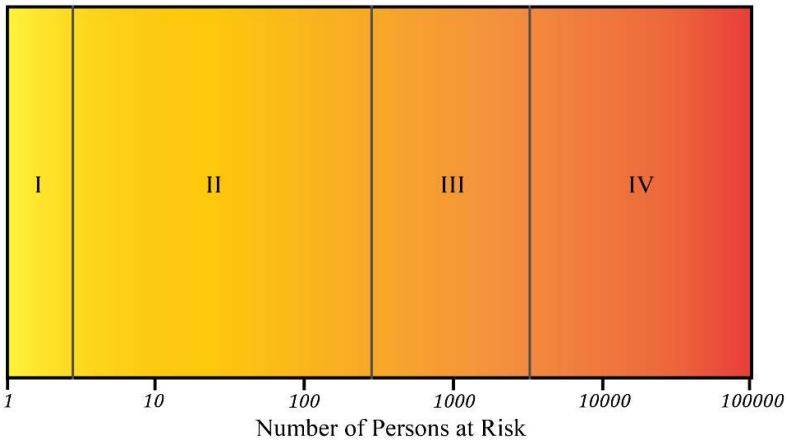

Figure 2.4. Approximate relationship between the number of lives placed at risk by a failure and occupancy category. Replicated from *Fig. C1.5-1* in ASCE-7 (American Society of Civil Engineers, 2017a).

In the figure, *Risk Category II* is applicable for the vast majority of structures projected as residential, commercial, or industrial buildings. Thus, the buildings in the database are assigned to ***Risk Category II***. Useful for the design process, it is essential to define an *Importance Factor* (IF) that is linked to the classification of the building into a *Risk Category* and is at the same time related to specific statistical characteristics of environmental loads. For the development of this study, the IF that interests the most is the one focusing on seismic loads, as may seem evident. Then the *Importance Factor*, I_e, is selected according to *Table 1.5-2* of ASCE-7 Standard and quantitatively adopts a unit value, i.e., $\boldsymbol{I_e = 1.0}$. As a quantitative entity, it is used throughout the design standard to increase the required yielding strength of the building to reduce the ductility demand and the possibly induced related damage.

Regarding the application of gravitational loads, on the other hand, the same magnitude of live and dead loads was considered for the $convDs$ and the $SSIDs$ DTs. **Table 2.3** shows the values of gravitational loads used throughout the design process, where q_L, q_{L_r}, and q_{SD} correspond to the general surface-distributed Live Load, Roof Live Load, and Surcharge Dead Load, respectively. Surcharge Dead Load is the permanent load applied to a building by additional objects different from those conforming to the structure (non-structural and mechanical elements). The magnitude of q_{SD}

has been defined by engineering judgment and former personal experiences in the design of RC buildings.

Table 2.3. Gravitational loads used for design.

q_{SD} $[kN/m^2]$	q_L $[kN/m^2]$	q_{Lr} $[kN/m^2]$
7.15	2.00	0.70

Concerning the design process, it is intended to be executed most familiarly to practicing engineering professionals. In that sense, the Modal Response Spectrum Analysis procedure (MRSA) is used to determine force and deformation demands. The substructuring approach is selected to model SSSs when $DT = SSIDs$, and the superstructure is modeled as fixed at ground level when $DT = convDs$. Since a linear procedure is employed to determine demands for design, linear-elastic sections with reduced stiffness are implemented in beam-column elements, and linear-elastic springs represent soil flexibility when needed. OpenSees (McKenna et al., 2010), through its enhanced capabilities in the embedded Python environment (OpenSeesPy (Zhu et al., 2018)), was selected as the modeling and analysis engine for the design process in this work.

The building seismic design process is an iterative process usually performed in two parts. Especially for high seismicity level locations, design is mainly controlled by the allowable lateral deformation the building shall be prepared to withstand. Hence, dimensions for the elements' cross-section are first calculated to accommodate the needed lateral stiffness; then, elements are provided with the code-prescribed strength. The flowchart in **Figure 2.5** depicts the design strategy described in the following points.

a. *First iterative process: initial sizing.*

   For a first analysis run, minimum dimensions are assigned to beams and columns cross-sections. The maximum interstory drift ratio, Δ_{max}, is obtained and compared to the allowable drift ratio, Δ_a, specified in ASCE-7; if $\Delta_{max} \geq \Delta_a$, cross-section dimensions are increased. A new analysis is executed, interstory drift ratios are verified, and sizes are increased every time until this lateral deformation limit is fulfilled for each orthogonal direction of analysis.

b. *Second iterative process: tuning of cross-section dimensions and strength provision.*

   Element actions (i.e., shear, flexure, and axial forces) are calculated using cross-section dimensions obtained in the previous step. Columns are first checked against shear actions; a minimum amount of transversal shear reinforcement is provided and iteratively increased until shear strength exceeds demand or reinforcement steel reaches the maximum quantity recommended for the cross-section area. If the latter occurs, the section area is enlarged, and the shear design is repeated until adequate strength is granted. After tuning column dimensions for shear design, beams, and columns are designed for flexure and flexure-axial

force interaction, respectively. Minimum longitudinal reinforcement is provided to the cross-section of both element types and increased iteratively until two conditions are met: 1) the strength is greater than demand; 2) the strong-column-weak-beam principle is warranted. The second condition may require an additional increase of cross-section dimensions in border and corner columns.

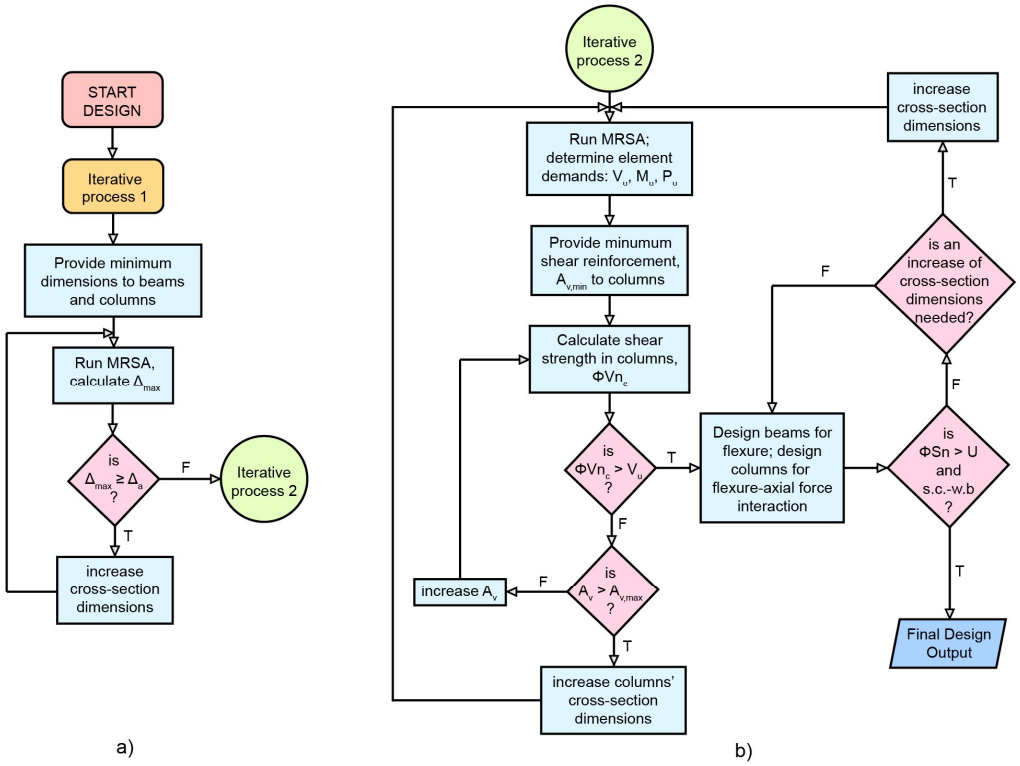

Figure 2.5. Design process flowchart.

This study accounts for two different base support conditions (BSC) for modeling the buildings during the design (and performance assessment) process. *fixBase* and *flexBase* nomenclature are used when dealing with fixed- and flexible-base BSCs, respectively.

The following sub-sections are devoted to introducing the reader to the elements (beams, columns, and soil representation) modeling criteria and the specific demand definition for the *fixBase* model design (Section 2.5.2) and the *flexBase* model design (Section 2.5.3). It is important to emphasize that the design's modeling criteria for linear section behavior may also be replicated during the assessment process explained in Chapter 3 of this work when applicable. Similarly, the seismic demand calculated during design may, in part, help establish the seismic demand for the assessment process. These similarities or differences will be explained in the corresponding section.

2.5.2. Conventional design: fixed-base design

2.5.2.1. Modeling of elements

It has been mentioned before that linear MRSA is used as the analysis methodology during the design process. This section describes the procedures followed to generate mathematical models that fulfill the needs of linear analysis procedures by introducing the superstructure and substructure elements in the *fixBase* model.

Regarding the beam and column elements, in general, the *forcebeamColumn* element from OpenSeesPy is used to model beam and column elements because of the ease of defining linear and nonlinear sections to describe the member's behavior. As for the mechanical properties of the materials, $f_c' = 35MPa$ is used for the concrete compressive strength and $f_y = 420MPa$ for the steel yielding stress.

Beams and columns modeled as *forceBeamColumn* elements use the Gauss-Lobatto integration rule implemented through the *Lobatto* object with five integration points ($N = 5$) to obtain the responses at various stations of the elements' length. To specify the linear elastic behavior in each integration point, an *Elastic* section object was defined in terms of the mechanical and geometrical properties of the RC element section, assuming it has a reduced stiffness due to prior deformations at construction stages and service levels according to ACI-318. Local axes and a schematic view of beam and column elements are depicted in **Figure 2.6**.

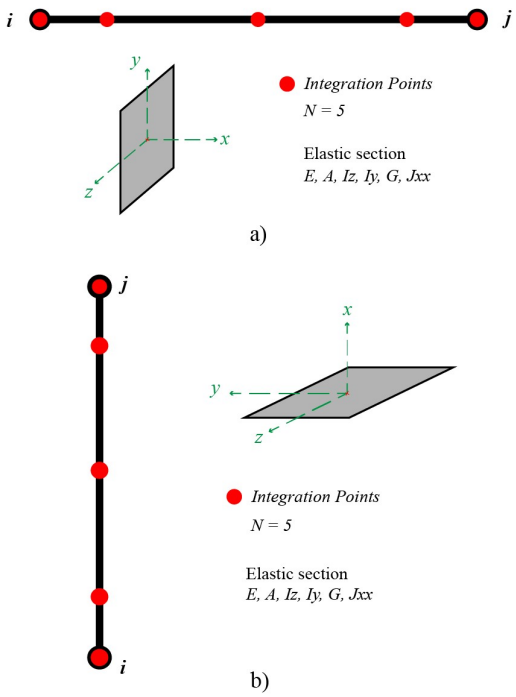

Figure 2.6. Linear elastic *forceBeamColumn* element. Schematic representation for: a) beams; b) columns.

Relative to the BSC of the *fixBase* model, its name is self-explanatory. Buildings modeled with this BSC are assumed to be fixed at their base (refer to **Figure 2.7**), and soil properties effects are neglected.

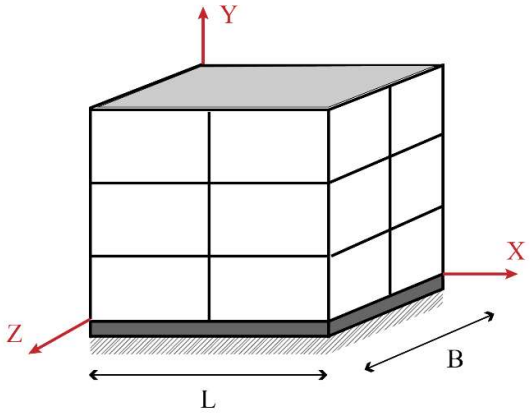

Figure 2.7. General schematization of a building with *fixBase* BSC.

2.5.2.2. Specific seismic demand

This section shows the calculations and procedures for defining the seismic demand for the design of structures in the database considering *fixBase* BSC.

According to the ASCE-7 standard, when a response spectrum is required, the Design Response Spectrum (DRS) shall be developed as indicated in Section 11.4.6 of the standard mentioned earlier. The development of the DRS consists of constructing the prescriptive spectrum depicted in **Figure 2.8**. Such a spectrum helps determine the acceleration, S_a, a building with a fundamental period of vibration, T_n, will be subjected to.

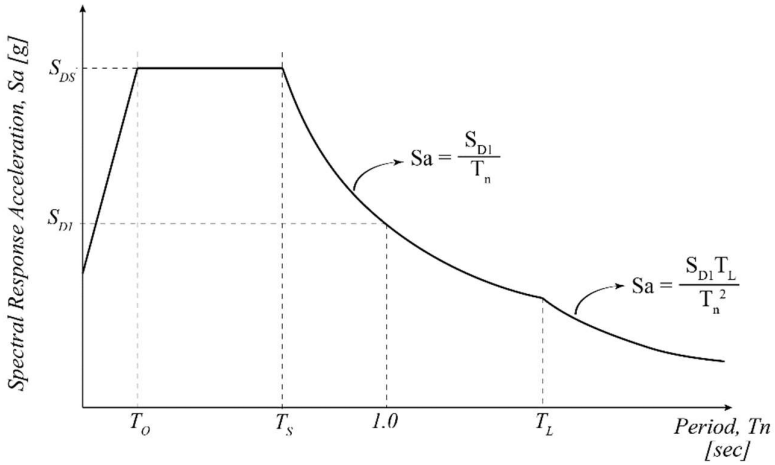

Figure 2.8. Design Response Spectrum as per ASCE-7 (American Society of Civil Engineers, 2017a).

The parameters shown in the figure to build the spectrum are described as follows: T_o the period limit at which the constant acceleration region begins, T_s is the period limit at which the constant

acceleration region in the spectrum ends, T_L is the long-period transition period included graphically in ASCE-7. S_{DS} and S_{D1} are the design spectral response acceleration parameters at short period and at a 1.0s period, respectively.

The branch of the S_a spectrum for T_n values below T_o is calculated using Eq. [2.7], while other spectral acceleration values are determined as indicated in **Figure 2.8**.

$$S_a = S_{DS}\left(0.40 + 0.60\frac{T_n}{T_o}\right) \quad [2.7]$$

Employing Eqs. [2.8] and [2.9], the upper and lower limit periods for the constant acceleration region are calculated.

$$T_o = 0.2\frac{S_{D1}}{S_{DS}} \quad [2.8]$$

$$T_S = \frac{S_{D1}}{S_{DS}} \quad [2.9]$$

On the other hand, for calculating the design spectral acceleration parameters, Eqs. [2.10] and [2.11] are recommended in ASCE-7.

$$S_{DS} = \frac{2}{3}S_{MS} \quad [2.10]$$

$$S_{D1} = \frac{2}{3}S_{M1} \quad [2.11]$$

Notice that the design acceleration parameters correspond to a fraction of the MCE_R spectral response acceleration parameters for short periods and at 1.0s, adjusted for Site Class effects, S_{MS} and S_{M1}, respectively. The adjustment for obtaining these acceleration parameters is made by multiplying S_s and S_1 by the site coefficients F_a and F_v, respectively, as described in Eqs. [2.12] and [2.13].

$$S_{MS} = F_a S_S \quad [2.12]$$

$$S_{M1} = F_v S_1 \quad [2.13]$$

Since the mapped acceleration response parameters S_s and S_1 are applicable for sites with an average shear wave velocity $\bar{v}_s = 760m/s$, they must be adjusted for other site conditions. In this sense, ASCE-7 adopted the Site Class coefficients from work undertaken by (D. M. Boore et al., 2014; Kami et al., 2013; Stewart & Seyhan, 2013). Values for site coefficients F_a and F_v are tabulated in the ASCE-7 standard (*Table 11.4-1* and *Table 11.4.2*, respectively), varying relative to the Site Class definition and parameters S_s and S_1. Since only one seismicity level (in terms of the acceleration parameters)

was defined in Section 2.3, and two Site Class definitions were made according to **Table 2.2**, just two different values for each site coefficient shall be calculated.

Table 2.4 shows the calculated values for the site coefficients on both site classes E and D, along with the spectral acceleration parameters described in Eqs. [2.10] through [2.13]. Notice how the spectral acceleration is amplified to a bigger amplitude for the case of the soil with poor characteristics, i.e., SC-E reflecting the site effect addressed through F_a and F_v coefficients.

Table 2.4. Values for site coefficients F_a and F_v.

Site Class	F_a [-]	F_v [-]	S_{MS} [g]	S_{M1} [g]	S_{DS} [g]	S_{D1} [g]
E (*soft soil*)	1.18	1.87	1.77	1.53	1.18	1.02
D (*stiff soil*)	1.00	1.60	1.50	1.30	1.00	0.87

Values have been calculated using $S_s = 1.5g$ and $S_1 = 0.817g$.
$T_L = 12s$ is obtained from *FIGURE 22-14* in ASCE-7 standard.

All values that are shown in **Table 2.4** and limit periods in Eqs. [2.8] and [2.9] are used to build the DRS of **Figure 2.9**. As an additional valuable parameter, mapped $T_L = 12$ is obtained from *Fig. 22-14* of the ASCE-7 standard.

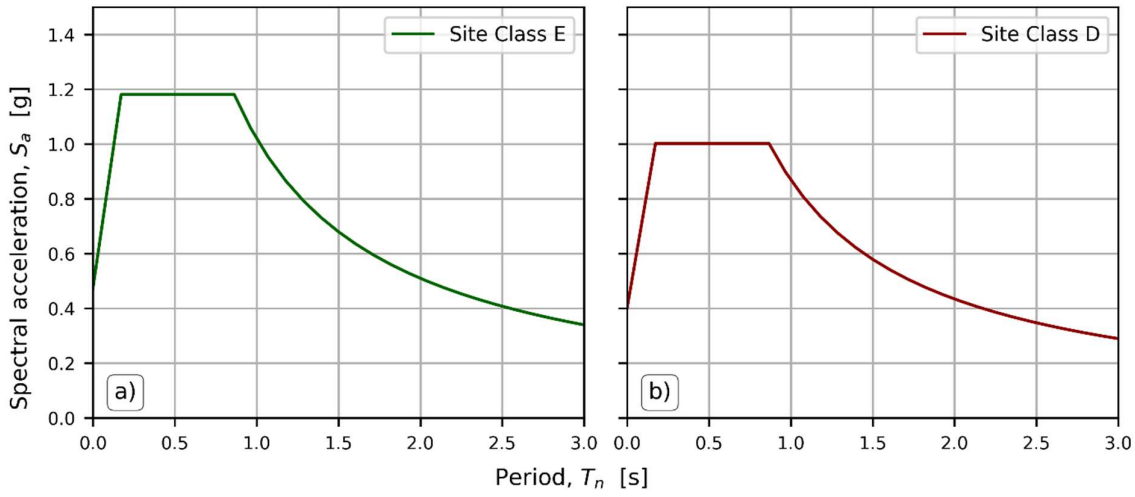

Figure 2.9. DRS used for the design of buildings in the database. a) DRS for Site Class E-located buildings; and b) DRS for Site Class D-located buildings.

In **Figure 2.9**, it can be noticed how the maximum period shown in the DRS is limited to a value of $T_n = 3.0s$, and the parameter T_L is not considered to be in a range relevant to the design. This is because by evaluating Eq. [2.4] and applying geometry definitions (i.e., the maximum number of stories, $\max(NStrs) = 12$ with a $3.0m$ story height) for the buildings in the database made in Section 2.2, a maximum *fixBase* approximate vibration period of $T_a = 0.0466(36m)^{0.9} = 1.17s$ can be expected. Nevertheless, greater actual values of T_n can be obtained through modal analysis; thus, the $T_n = 3.0s$ upper vibration period limit in the spectra is employed. **Figure 2.9a** depicts the DRS

devoted to designing buildings in SC-E. It shows how these structures are subjected to a more considerable magnitude of spectral acceleration, as was stated before while introducing F_a and F_v site coefficients.

Once the DRS of the preceding figure has been constructed in the way explained above, the MRSA analysis procedure can be executed. This implies calculating the value for each design parameter involved in the process detailed in **Figure 2.5**, i.e., the story drifts and individual member forces for each response mode. These force-related parameters shall be divided by the ratio R/I_e. The Response Modification Coefficient, R, intends to reduce the demand determined while assuming an elastic response of the structure to target the development of the first significant yield. In other words, it reduces the demand by taking advantage of the structures' expected ductility and inelastic behavior capacity. The purpose of the IF, I_e, was introduced in Section 2.5.1. Similarly, the values of displacement-related quantities are affected by the ratio C_d/I_e. In the last expression, C_d is the deflection amplification factor for estimating the deformations that would occur in the structure in the event of the design earthquake while behaving inelastically.

The responses of the analyzed independent modes are combined through the square root of the sum of the squares (SRSS) rule, ensuring that the considered modes let us obtain a combined modal mass participation of at least 90% of the actual mass in each orthogonal horizontal direction of response considered in the mathematical model.

Finally, when needed, forces and drifts calculated using the MRSA procedure are scaled following the recommendations of Section 12.9 in the ASCE-7 standard, depending on the magnitude of the base shear obtained from the modal combination denominated as V_t. This scaling process shall be executed by calculating a relative increment of the base shear demand determined through the Equivalent Lateral Force (ELF) procedure, V, and V_t using the ratio V/V_t.

2.5.3. SSI design: flexible-base design

2.5.3.1. Modeling of elements

For modeling linear elastic beam and column elements, the same considerations as for Section 2.5.2.1 apply.

On the other hand, a more elaborated modeling procedure is required relative to the soil representation at the *flexBase* BSC. In this case, the soil becomes part of the evaluated system; consequently, its properties are of significance for the overall SSS response. For this BSC, *zeroLength* element objects are distributed over the footprint surface for modeling the sub-structure employing the so-called Beam-On-Nonlinear-Winkler-Foundation (BNWF) approach, as depicted in **Figure 2.10a**. Zero-length elements (*zeroLength* element type in OpenSees) help simulate force-displacement relationships by connecting two points located at the exact coordinates and developing

the behavior of a uniaxial material (*uniaxialMaterial* object in OpenSees) on the local degree of freedom of interest. In featuring soil force-displacement relationships, it is common practice to use different representations in agreement with the required mechanics (i.e., whether the section behaves linear or nonlinear). For instance, linear springs are suitable for simulating such behavior when applying a linear analysis methodology as the MRSA during the design process.

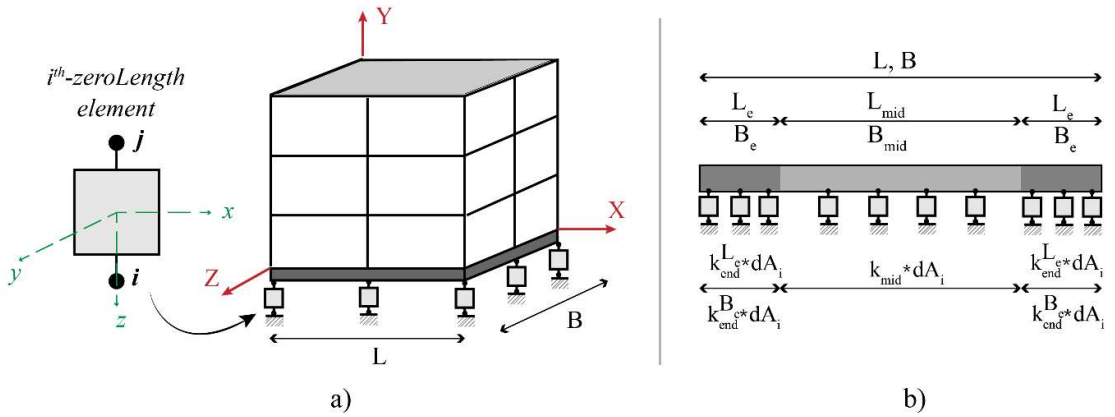

Figure 2.10. General schematization of a building with *flexBase* BSC. a) *zeroLength* elements located at the base of columns; and b) region definition along the foundation's length and width.

When using the BNWF approach, ATC-40 (Applied Technology Council, 1996) suggests a simple procedure to implicitly provide the system with the soil rotational stiffness while considering its coupling to the vertical one. It first consists of transforming the vertical and rotational stiffnesses, K_z and K_{ii} (rotational $ii-DOF$), to the vertical stiffness intensities written in Eqs. [2.14] to [2.16].

$$k_z = \frac{K_z}{LB} \quad [2.14]$$

$$k_{yy} = \frac{K_{yy}}{I_{yy}} \quad [2.15]$$

$$k_{xx} = \frac{K_{xx}}{I_{xx}} \quad [2.16]$$

Where $k_z, k_{yy}, k_{xx}, I_{yy}, I_{xx}$, and L are the vertical stiffness intensity relative to the $z-$axis, the vertical stiffness intensity relative to rotation about $yy-$ and $xx-$axis, the rotational moment of inertia about $yy-$ and $xx-$axis, and the foundation's length, respectively. Then, the foundation surface is divided into two regions: end- and middle-region, as shown in **Figure 2.10b**. In the former region, the stiffness intensity magnitude is increased relative to that of the middle-region to account for rotational stiffness effects using vertically oriented elements alone.

Recommendations regarding the length of the end-region, L_e (or B_e) and the stiffness intensity magnitudes for that and the middle-region are also found in ATC-40. This standard supports the stiffness intensity magnitude expressions on the valuable work by George Gazetas in the early 1990s

detailed in (Gazetas, 1991b, 1991a). However, a more refined group of expressions suggested by (Harden et al., 2005) are employed in calculating these parameters.

Refer to Eqs. [2.17] to [2.19] for the definition of rotational stiffness deficit ratio, $C_{R-V}^{K_{ii}}$, L_e, B_e, vertical stiffness intensity for the middle-region, k_{mid}, and vertical stiffness intensity for the end-region, k_{end}, respectively.

$$C_{R-V}^{K_{ii}} = \frac{\left(K_{ii} - \frac{K_z}{A} I_{ii}\right)}{K_{ii}} \qquad [2.17]$$

$$L_e = 0.50L - L\left[\frac{1}{8}\left(1 - C_{R-V}^{K_{yy}}\right)\right]^{\frac{1}{3}}$$
$$B_e = 0.50B - B\left[\frac{1}{8}\left(1 - C_{R-V}^{K_{xx}}\right)\right]^{\frac{1}{3}} \qquad [2.18]$$

$$k_{mid} = \frac{K_z}{LB}$$
$$k_{end}^{L_e} = k_{mid} + \frac{K_{yy}}{I_{yy}} C_{R-V}^{K_{yy}} \qquad [2.19]$$
$$k_{end}^{B_e} = k_{mid} + \frac{K_{xx}}{I_{xx}} C_{R-V}^{K_{xx}}$$

Where A is the foundation area, the subscript ii refers to one of the three rotational degrees of freedom, and all other parameters have already been introduced. Vertical and rotational stiffnesses are calculated using the equations obtained in the study held by Pais and Kausel (Pais & Kausel, 1988) and detailed in **Table 2.5**.

It is worth mentioning that once the global vertical stiffness intensities are calculated, individual zero-length element stiffness magnitudes are determined by computing: $K_{region}^{i} = k_{region} \times dA_i$. For instance, an individual vertical stiffness of zero-length elements located in the middle-region shall be calculated as $K_{mid}^{i} = k_{mid} \times dA_i$ (see **Figure 2.10b**). dA_i is the foundation tributary area supported by the i^{th} −zero-length element.

Thus, the soil force-displacement relationship is represented by an equivalent linear spring with stiffness K^i, obtained following the procedures given in previous paragraphs and using soil properties compatible with the strain levels associated with the Seismic Hazard Level (SHL). In this case, the SHL corresponds to the design level, as will be explained in Section 2.5.3.2. The strain-compatible shear wave velocity, v_s, and the strain-compatible shear modulus, G (both modified due to large strain effects), are involved in calculating the stiffness magnitudes shown in **Table 2.5**. To

calculate v_s and G, small-strain shear wave velocity and maximum shear modulus, v_{so} and G_o are modified as per ASCE-7 Chapter 19 recommendations according to the site class designation and the expected effective peak acceleration, $S_{DS}/2.5$.

Table 2.5. Elastic solutions for static stiffness of rigid shallow foundations.

Degree of freedom	Stiffness magnitude	Schematization
Vertical translation, z-axis	$K_z = \frac{GB}{2(1-\nu)}\left[3.1\left(\frac{L}{B}\right)^{0.75} + 1.6\right]$	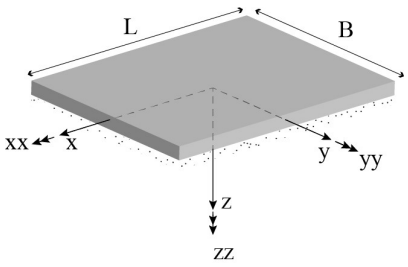
Horizontal translation, y-axis	$K_y = \frac{GB}{2(2-\nu)}\left[6.8\left(\frac{L}{B}\right)^{0.65} + 0.8\left(\frac{L}{B}\right) + 1.6\right]$	
Horizontal translation, x-axis	$K_x = \frac{GB}{2(2-\nu)}\left[6.8\left(\frac{L}{B}\right)^{0.65} + 2.4\right]$	
Torsion, z-axis	$K_{zz} = \frac{GB^3}{8}\left[4.25\left(\frac{L}{B}\right)^{2.45} + 4.06\right]$	
Rotation, y-axis	$K_{yy} = \frac{GB^3}{8(1-\nu)}\left[3.73\left(\frac{L}{B}\right)^{2.4} + 0.27\right]$	
Rotation, x-axis	$K_{xx} = \frac{GB^3}{8(1-\nu)}\left[3.2\left(\frac{L}{B}\right) + 0.8\right]$	

Notes:
Axes should be oriented such that $L \geq B$.
G and ν are the effective soil shear modulus reduced due to large strain effects and the soil Poisson's modulus, respectively.
A more detailed table can be found in NIST GCR 12-917-21 (ATC, 2012).

In the latter expression, S_{DS} is the spectral response acceleration parameter at short periods for the design SHL. K^i values so determined are simulated through uniaxial material objects in OpenSees and linked to the i^{th} −zero-length element local $z - DOF$, as depicted in **Figure 2.11**. In this figure, the terms Q^i, T_x^i, T_y^i correspond to the soil's vertical bearing force and the soil's horizontal frictional sliding capacity in the $x-$ and $y-$ direction, respectively. In addition, s_z, u_x and u_y stand for the displacements in the z −vertical (settlement), $x-$ and y −horizontal (sliding) degrees of freedom.

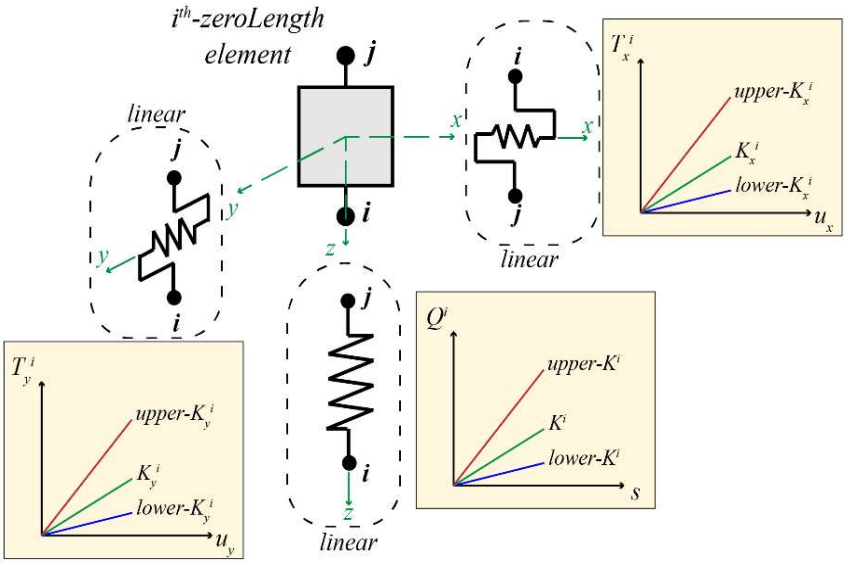

Figure 2.11. Linear soil element representation.

On the other hand, for the lateral force-displacement behavior, K_x and K_y stiffnesses magnitudes are taken directly from the expression in **Table 2.5**, modeled through the uniaxial material object, and linked to the horizontal DOFs (local x and y) of the same i^{th} −zero-length element. In addition, to consider various sources of uncertainties or the natural variability of soil conditions, lower- and upper-bounds are established for K^i stiffnesses, as shown in **Figure 2.11**. Suggested in ASCE-7 is the approach of taking half and twice the initially calculated stiffness to determine lower and upper bounds, respectively.

2.5.3.2. Specific seismic demand

Relative to determining the seismic design considering the SSI effects in the response, ASCE-7 requires that the analytical model incorporates, in some manner, the foundation flexibility. Such requirements are addressed by employing the modeling approaches indicated in the preceding section and the procedures included in the current section.

When using a linear dynamic analysis procedure such as MRSA to analyze buildings, one alternative in accounting for SSI effects is to modify the DRS constructed in accordance with the guidelines shown in Section 2.5.2.2 for *fixBase* models for a *convDs* design type. The modifications recommended by ASCE-7 Standard can be found in its Chapter 19, devoted to Soil-Structure Interaction for Seismic Design. Regarding this modification, an SSI Modified General Design Response Spectrum (SSI-MGDRS) shall be constructed following the standard's recommendations, which include the inherent changes in the damping of the SSS ultimately reflected in the spectral acceleration.

Refer to **Figure 2.12** for a graphical insight into the SSI-MGDRS according to ASCE-7 Standard. Notice that the modified spectral acceleration to account for the SSI effects is now denominated as $\tilde{S}_a$ and

its modification consists of dividing the conventionally determined spectral acceleration, S_a, by the factor B_{SSI}.

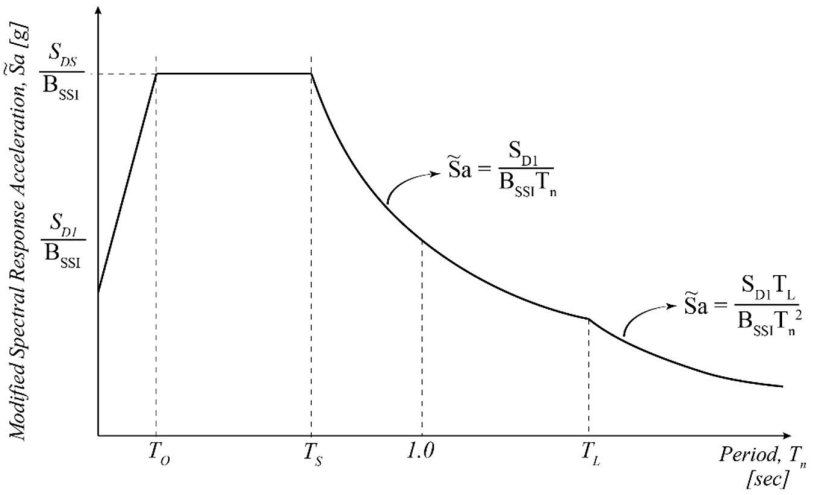

Figure 2.12. SSI Modified General Design Response Spectrum as per ASCE-7 (American Society of Civil Engineers, 2017a).

For constructing the branch of the spectrum in **Figure 2.12** for values of T_n between zero and T_o, Eq. [2.20] shall be used.

$$\tilde{S}_a = \left[\left(\frac{5}{B_{SSI}} - 2\right)\frac{T_n}{T_S} + 0.4\right] S_{DS} \qquad [2.20]$$

The factor B_{SSI} allows a response spectrum to be constructed considering a system's damping ratio different than 5%. Moreover, as can be appreciated in Eq. [2.21], this factor accounts for the change in the SSS damping ratio induced by the SSI, specifically the inertial soil-structure interaction.

$$B_{SSI} = \frac{4}{\left[5.6 - \ln\left(100\beta_o\right)\right]} \qquad [2.21]$$

In the equation above, β_o is the effective viscous damping ratio of the SSS expressed in Eq. [2.22]. This expression consolidates the understanding of how the effective viscous damping of the structure alone, β, participates along with the effective viscous damping ratio of the foundation-soil sub-system, β_f, to alter the damping ratio of the whole.

$$\beta_o = \beta_f + \frac{\beta}{\left(\frac{\tilde{T}_n}{T_n}\right)_{eff}^2} \leq 0.20 \qquad [2.22]$$

From Eq. [2.22], it can be noticed that β is affected by the effective period-lengthening ratio $\left(\tilde{T}_n/T_n\right)_{eff}$, which is considered to be one of the main evident consequences of the SSI effects on the

seismic response of buildings (Applied Technology Council, 2020; ATC, 2005, 2012; Wolf, 1985). The latter term is calculated using Eq. [2.23], shown below.

$$\left(\frac{\tilde{T}_n}{T_n}\right)_{eff} = \left\{1+\frac{1}{\mu}\left[\left(\frac{\tilde{T}_n}{T_n}\right)^2 - 1\right]\right\}^{0.5} \quad [2.23]$$

Where μ, is the expected ductility demand calculated for design purposes as the ratio R/Ω_o; R has already been introduced, and Ω_o is the overstrength factor recommended by ASCE-7 Standard for the selected structural type. In addition, notice that the numerical value obtained from this equation is restrained to a maximum of 20%.

The foundation-soil effective viscous ratio, on the other hand, is calculated using Eq. [2.24]. This expression contains two additional terms involved in the inertial interaction of the foundation-soil sub-system. Namely, the soil hysteretic damping ratio, β_s, and the radiation damping ratio, β_{rd}.

$$\beta_f = \left[\frac{\left(\tilde{T}_n/T_n\right)^2 - 1}{\left(\tilde{T}_n/T_n\right)^2}\right]\beta_s + \beta_{rd} \quad [2.24]$$

Regarding β_s, it is tabulated in Chapter 19 of ASCE-7 Standard and depends on the *Site Class* and a so-called effective peak acceleration defined as $S_{DS}/2.5$. In the case of β_{rd}, its calculation relies on Eq. [2.25].

$$\beta_{rd} = \frac{1}{\left(\tilde{T}_n/T_y\right)^2}\beta_y + \frac{1}{\left(\tilde{T}_n/T_{xx}\right)^2}\beta_{xx} \quad [2.25]$$

In the former equation, β_y and β_{xx} are the effective damping ratios for translation and rotation at and around the structure's weak plane, respectively. T_y, and T_{xx}, stand for the periods of vibration related to the same translational and rotational DOFs of β_y and β_{xx}. Eqs. [2.26] to [2.29] detail the expressions recommended for their calculation.

$$\beta_y = \left[\frac{4(L/B)}{\left(2K_y/GB\right)}\right]\left[\frac{\tilde{a}_o}{2}\right] \quad [2.26]$$

$$\beta_{xx} = \left[\frac{(4.9/3)(L/B)\tilde{a}_o^2}{\left(\frac{8K_{xx}}{GB^3}\right)\left[\left(2.2-\frac{0.4}{(L/B)^3}\right)+\tilde{a}_o^2\right]}\right]\left[\frac{\tilde{a}_o}{2\alpha_{xx}}\right] \quad [2.27]$$

$$T_y = 2\pi\sqrt{\frac{\bar{M}}{K_y}} \qquad [2.28]$$

$$T_{xx} = 2\pi\sqrt{\frac{\bar{M}\left(h^*\right)^2}{\alpha_{xx}K_{xx}}} \qquad [2.29]$$

Further, the group of Eqs. [2.30] are auxiliary expressions that complement the previous ones in defining the SSI-MGDRS construction.

$$\begin{cases} K_y = \dfrac{GB/2}{2-\nu}\left[6.8\left(\dfrac{L}{B}\right)^{0.65} + 0.8\left(\dfrac{L}{B}\right) + 1.6\right] \\ K_{xx} = \dfrac{G\left(B/2\right)^3}{1-\nu}\left[3.2\left(\dfrac{L}{B}\right) + 0.8\right] \\ \tilde{a}_o = \dfrac{\pi B}{\tilde{T}_n v_s} \\ \vartheta = \sqrt{\dfrac{2\left(1-\nu\right)}{\left(1-2\nu\right)}} \le 2.5 \\ \alpha_{xx} = 1.0 - \left[\dfrac{\left(0.55 + 0.01\sqrt{\left(L/B\right)-1}\right)\tilde{a}_o^2}{\left(2.4 - \dfrac{0.4}{\left(L/B\right)^3}\right) + \tilde{a}_o^2}\right] \end{cases} \qquad [2.30]$$

These expressions contain additional terms that are enlisted below:

- $\bar{M}$ is the effective modal mass for the fundamental vibration mode in the direction under consideration.
- K_y and K_{xx} are stiffness magnitudes already introduced in **Table 2.5**.
- $\tilde{a}_o$ is the dimensionless frequency introduced in Eq. [2.3], but this time, considering the large-strain shear wave velocity, v_s, instead of the small-strain velocity, v_{so}.
- α_{xx} is a surface stiffness modifier applied to rotational stiffness and damping adapted from (Pais & Kausel, 1988).
- ϑ is a strain-related factor helpful to simplify the expressions and limited to an upper bound value of 2.5.

Considering all the above prescriptions, the SSI Modified Design Response Spectra (SSI-MDRS) are constructed to obtain the modified spectral acceleration $\tilde{S}_a$ to be employed in the design-oriented analysis using MRSA. As may be evident by looking at the expressions in Eqs. [2.21] to [2.30], there are not only two different design response spectra for the *SSIDs,* as was the case for *convDs* demands in Section 2.5.2.2. Besides the *Site Class* selection, the construction of SSI-MDRS relies upon dynamic characteristics of the soil-structure system, namely, the *fixBase* and *flexBase* periods of vibration and the foundation-soil sub-system damping ratios of the building in question. Hence, there will be a specific SSI-MDRS for each building in the database to the extent that their dynamic characteristics differ. In that concern, **Figure 2.13a** and **Figure 2.13b** depict the SSI-MDRS specific to an example building and all the spectra for each structure in the database, respectively.

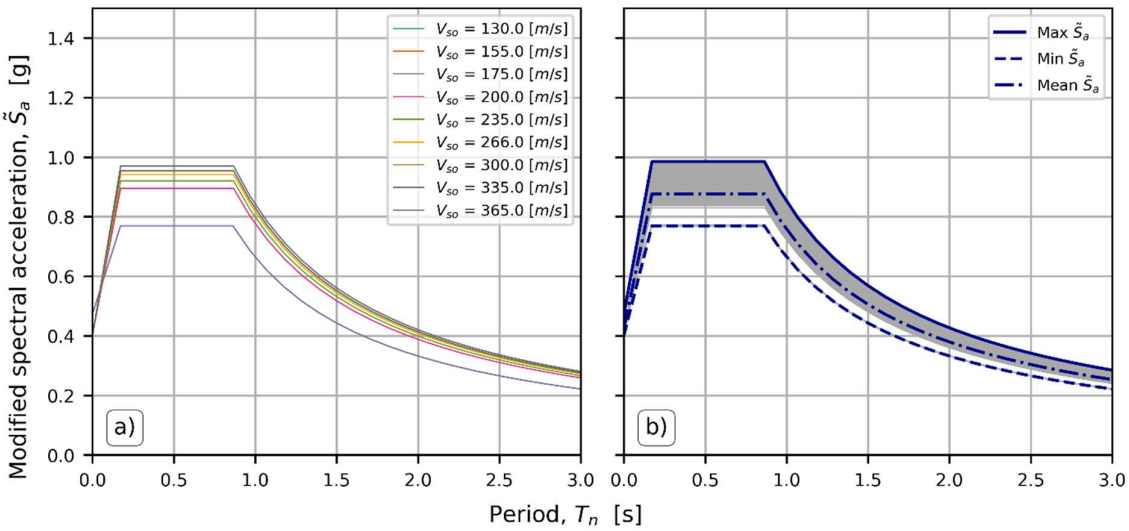

Figure 2.13. SSI Modified Response Spectra for *SSIDs*. a) Specific SSI-MDRS for a 4-bays in X-direction, 10-story height building considering all possible v_{so} values, and b) SSI-MDRS for every building in the database.

Notice from **Figure 2.13a** that there are about six different identifiable spectrum lines, from which the ones delivering the highest value of $\tilde{S}_a$ are those corresponding to higher shear wave velocity values. This fact reflects the basis on which ASCE-7 Standard leans regarding the design considering SSI effects; interacting effects are only deemed beneficial, so seismic demand is reduced during the design process. This criterion is demonstrated to be not entirely accurate and addressed in more detail in Chapter 5.

Let us observe **Figure 2.13b**, where SSI-MDRS are plotted for each building in the database. The broader range of spectral acceleration can affect the building design depending on the dynamic characteristics of each structure for *SSIDs* compared with the case of *convDs*.

From these calculations, as for the conventional design of *fixBase* buildings, the resulting response spectral acceleration shall be divided by the ratio R/I_e. On the other hand, if needed, the base shear design force for the *flexBase* building is scaled using the ratio of the ELF calculated base shear

magnitude to that obtained using MRSA, $\tilde{V}/\tilde{V}_t$. In the latter ratio expression, the curly symbol "~" above each term means that those quantities were determined for *flexBase* BSC.

The *flexBase* base shear design force, $\tilde{V}_t$, is obtained from the MRSA procedure employing the SSI-MDRS constructed as explained in previous paragraphs. On the other hand, for calculating the *flexBase* base shear design force obtained through the ELF procedure, $\tilde{V}$, ASCE-7 recommends the following procedure.

The conventionally determined value of V is permitted to be modified (i.e., reduced) when accounting for SSI effects, according to Eq. [2.31].

$$\tilde{V} = V - \Delta V \geq \alpha \qquad [2.31]$$

Where ΔV is a decrement value for the magnitude of V, and α is a limiting coefficient that accounts for the reduction in base shear caused by the foundation damping. These terms are calculated using Eqs. [2.32] and [2.33], respectively.

$$\Delta V = \left(C_s - \frac{\tilde{C}_S}{B_{SSI}} \right) \bar{W} \qquad [2.32]$$

$$\alpha = \begin{cases} 0.7 & for \quad R \leq 3 \\ 0.5 + R/15 & for \quad 3 < R < 6 \\ 0.90 & for \quad R \geq 6 \end{cases} \qquad [2.33]$$

In Eq. [2.32], C_s is the seismic response coefficient determined with the expression $S_{a(T_n)}/(R/I_e)$. $\tilde{C}_s$ on the other hand, uses a similar expression but with the *flexBase* design spectral acceleration, $\tilde{S}_{a(\tilde{T}_n)}/(R/I_e)$. Notice that $\tilde{C}_s$ assumes the flexibility of the structural base at the foundation-soil sub-system and uses $\tilde{T}_n$ as the fundamental period of the structure. $\bar{W}$ is the weight caused by the effective modal mass in the fundamental mode.

The factor α in Eq. [2.33] depends on the value of R but ranges between 0.70 and 0.90. This implies that for buildings designed in the database ($R = 8$), there can be a maximum reduction of 10% in V to get $\tilde{V}$. The implications and accuracy of these recommendations are also studied in Chapter 5.

2.6. Review and discussion of design results

Due to the large number of buildings comprising the database, it is not easy to present an in-depth description of the design outcomes for each independent structure. Instead, **Figure 2.14** is used to grasp them through a brief analysis of two fundamental structural characteristics. **Figure 2.14a** and **Figure 2.14b** show, respectively, the behavior of the mass ratio, M^*, and stiffness ratio, K_x^* as a function of T_n where each point in the scatter plots portrays a building in the database. These ratios

represent the relationship of the specific structural characteristic, either M or K_x of the *SSIDs* designed building to that of the *convDs* one; i.e., $M^* = M_{SSIDs}/M_{convDs}$ and $K_x^* = K_{x_{SSIDs}}/K_{x_{convDs}}$.

In that sense, M^* and K_x^* indicate whether an *SSIDs*-designed building is heavier or stiffer than a *convDs*-designed one if ratios are greater than 1.0, or lighter and more flexible otherwise. To evaluate this behavior, linear trends depending on the building's slenderness ratio, λ_{str}, are also plotted. Notice how M^* and K_x^* values increase as T_n increases for any λ_{str}, getting values first below and then above unity. It may suggest that although *SSIDs* buildings are initially lighter and more flexible than their *ConvDs* counterpart, they gradually become heavier and stiffer as the *fixBase* structure fundamental period rises. It is worth mentioning, however, that the slopes of the slenderness ratio trends are steeper for K_x^* than for M^*, reflecting the need for rapidly controlling the augmented displacement demands induced by the period elongation of the SSS during the design process.

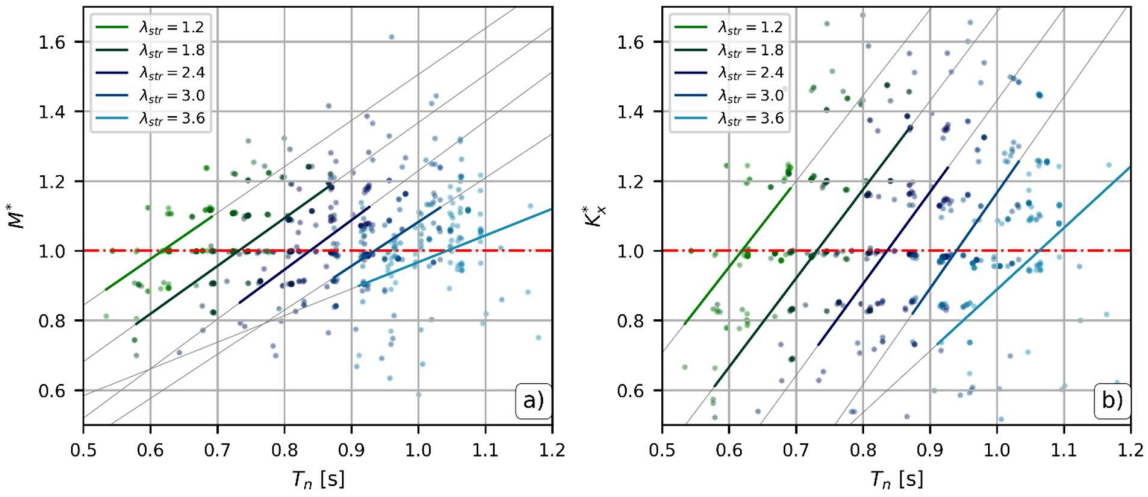

Figure 2.14. Building database design review.

Finally, it is also important to notice that the linear trends representing λ_{str} in **Figure 2.14a,** passes through the unitary axis at approximately the same T_n value as their corresponding lines do in **Figure 2.14b**. This points out that the buildings designed using either of the two DTs for specific periods of vibration result in the same design outcome. This period is higher for higher slenderness ratios.

3. Seismic Performance Assessment

3.1. Overview

Let us recall that one of the objectives of this study is to evaluate the seismic performance of the buildings in the database while considering the effects of soil-structure interaction. Thus, the seismic assessment of buildings from the database is performed using the approved evaluation methodology after ASCE-41 (American Society of Civil Engineers, 2017b). The core aim of this standard is to identify deficiencies in buildings that prevent them from achieving a particular performance objective. For that purpose, a recommended *Analysis Procedure* (AP) is used to calculate demands (forces or deformations) while subjecting the building to a prescribed *Seismic Hazard Level* (SHL). Then, demands are compared to elements' strengths to verify if the expected *Structural Performance Level* (SPL) is reached.

Regarding the APs, linear and nonlinear, static and dynamic procedures are available in ASCE-41. The *Equivalent Lateral Force* (ELF) procedure is recommended as the linear static procedure (LSP), and *Linear Time-History Analysis* (LTHA) or Modal Response Spectrum (MRSA) analyses can be selected as the linear dynamic procedure (LDP). In contrast, *Pushover* (PO) and the *Nonlinear Time-History Analysis* (NLTHA) procedures of analysis are included for *Nonlinear Static* (NSP) and *Nonlinear Dynamic* (NDP) procedures, respectively.

On the other hand, SHL-SPL combinations making up performance objectives depend on whether the assessed buildings are new or existing structures. Since buildings in the study database are designed as detailed in Section 2, they are considered new; hence, the hazard-performance level pairs described in **Table 3.1** apply.

Table 3.1. SPL and SHL pairs used during the performance assessment.

SPL	SHL	Hazard details
S-5 : Collapse Prevention (CP)	BSE-2N	Consistent with MCE_R[a] in ASCE-7
S-3 : Life Safety (LS)	BSE-1N	Matches the design earthquake ground motion[b].

[a] MCE_R: risk-targeted maximum considered earthquake
[b] design earthquake ground motion as two-thirds of MCE_R.

BSE-1N and BSE-2N are the names used in ASCE-41 for *Basic Safety Earthquake* (BSE) equivalent to *New* buildings at hazard levels 1 and 2, respectively. These hazard levels correspond to the hazard details also described in **Table 3.1**.

In connection with the explanation above, the following points summarize the goals of analyses performed in this chapter that help reach the study's aims:

a) *To measure the performance*: LDP employing MRSA, NSP, and NDP are the selected procedures to assess the performance of buildings included in the database. According to

ASCE-41, it is accomplished by calculating demand-capacity ratios (DCR) and comparing them to specific acceptance criteria (ac).

b) *To compare the performance*: the performance assessment results obtained using the earlier APs are contrasted. Since linear and nonlinear procedures measure demands and capacities using different structural response parameters (the former uses forces while the latter uses inelastic deformations), it is not expected to obtain the same DCR values in a particular building analyzed with different APs. To address these differences and evaluate their behavior, a new dimensionless factor, Ψ, is introduced in Section 3.6. As further explained, Ψ is defined as the ratio of the DCR value obtained from a building analyzed using NDP to the DCR value of the same building analyzed using either LDP or NSP.

c) *To estimate the performance*: parametric models explaining the behavior of factor Ψ are determined by regression analysis in Section 4. These can be used to obtain the actual performance of a building by simply multiplying the estimated/predicted value of Ψ by the DCR value of the same building analyzed with either LDP (either with the MRSA or the LTHA procedure) or NSP.

This chapter focuses on fulfilling the goals regarding points a) and b) enlisted earlier. First, Section 3.2 details the code-prescribed recommendations to measure the seismic performance of a building subjected to different levels of demand. Then, Section 3.3 is devoted to showing the criteria followed in modeling superstructure elements and the soil representation for both linear and nonlinear behavior. Section 3.4, on the other hand, defines the prescribed demand utilized through the analysis process for the performance assessment depending on the AP employed for this purpose.

The 1,458 buildings designed in Section 2 (729 *convDs*-designed and 729 *SSIDs*-designed buildings) are used for developing the seismic performance assessment. Each building is independently evaluated for two base-support conditions, fixed- and flexible-base support conditions, denominated as *fixBase* and *flexBase*, respectively. Each building with its corresponding BSC, in turn, is analyzed employing the four analysis procedures mentioned in previous paragraphs for the two SHLs shown in **Table 3.1**.

Figure 3.1 portrays an infographic summarising the information described above, i.e., there are 729 idealized structures defined in Section 2.2 and later designed as per Section 2.5 for *convDs* and *SSIDs* design types. The design process generates a total of 1,458 buildings. These buildings are analyzed for two BSC, namely, *fixBase* and *flexBase*; in this regard, denomination ***convDs:flexBase***, for instance, refers to the analysis of a building that has been designed with no considerations of SSI effects (*convDs*) but analyzed taking into account their effects by modeling a *flexBase* BSC. As mentioned before, four APs were used to analyze each building, thus totaling 23,328 analyses executed ($1{,}458\ Buildings \times 2\ BSCs \times 2\ SHLs \times 4\ APs$) for presenting the study's results in the current chapter.

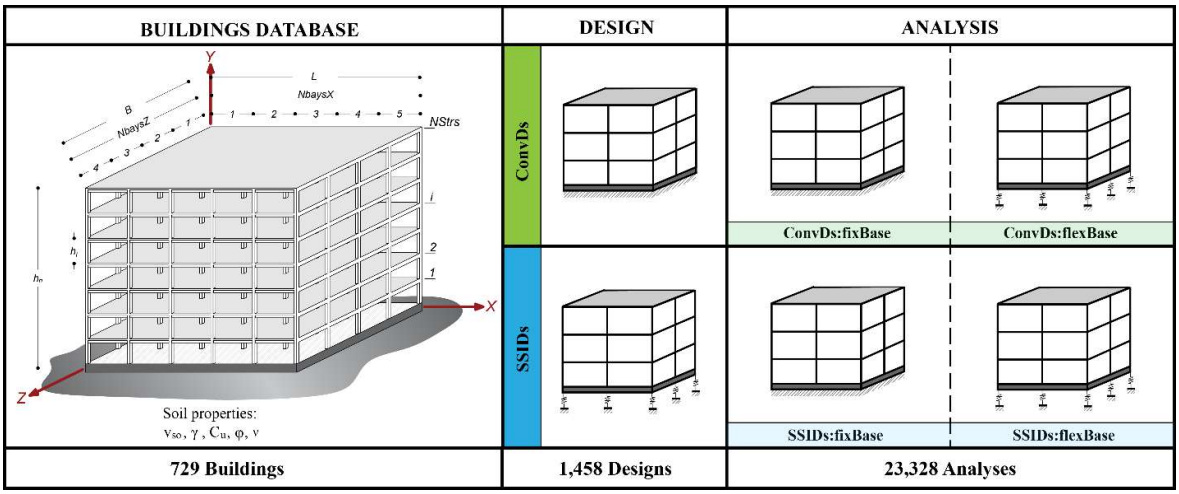

Figure 3.1. Schematization of buildings' database; base-support conditions for design and analysis

Finally, Sections 3.5 and 3.6 give an insight into the general conclusions driven by the performance assessment results and also introduce the aforementioned dimensionless factor Ψ to be later estimated in Chapter 4 for fulfilling point c) of the goals described earlier in this section.

3.2. Code Prescriptions for the Seismic Performance Assessment

The prescribed recommendations for the seismic performance assessment of buildings are carried out through the utilization of ASCE 41-17 *Seismic Evaluation and Retrofit of Existing Buildings* (American Society of Civil Engineers, 2017b) standard, referred to herein as ASCE-41. This standard describes the rationale for demonstrating that a specific building complies with or achieves a selected or expected *Performance Objective*. Selecting a Performance Objective implies the definition of one or more pairings of Seismic Hazard Levels (SHL) linked to a Target Structural Performance Level (SPL) and a Target Nonstructural Performance Level (NPL). Since the aims of this study are focused on the performance of the structural components alone, only the SPL is defined throughout the development of this section.

Considering that the structures to be assessed were previously designed and corresponded to the database created for this research, these buildings are deemed *new*. The meaning of *new* building refers to the type of standard employed for the design process. As mentioned in the corresponding section, later versions of ASCE-7 and ACI-318 were used in the design process to generate the building database. In this regard, ASCE-41 recommends the selection of the Performance Objective according to what is detailed in **Table 3.2**. This table shows the *Basic Performance Objective Equivalent to New Building Standards* (BPON), describing the Seismic Hazard Level the buildings shall be subjected to, the Structural Performance Level the buildings shall achieve, and all this related to the Risk Category defined in the design process.

Table 3.2. Basic Performance Objective Equivalent to New Building Standards[a].

Risk Category	Seismic Hazard Level	
	BSE-1N	**BSE-2N**
I and II	Life Safety Structural Performance	Collapse Prevention Structural Performance
III	Damage Control Structural Performance	Limited Safety Structural Performance
IV	Immediate Occupancy Structural Performance	Life Safety Structural Performance

[a] Adapted from ASCE-41 standard, Table 2-3.

Notice that **Table 3.1**, introduced earlier in the overview of this section, is an extract of **Table 3.2**, the latter including the correspondence of the Risk Category with the Performance Objective. As explained in the former table, buildings assigned to Risk Category II (as is the case of buildings in the database) shall achieve two of the discrete SPLs included in ASCE-41, the Life Safety (LS) and the Collapse Prevention (CP) SPLs.

Life Safety, or Performance Level S-3, is defined as a post-earthquake damage state of a building in which some structural components are damaged but do not compromise any local or global integrity and retains a safety margin against the collapse. On the other hand, Collapse Prevention, or Performance Level S-5, relates to a post-earthquake damage state in which a structure has damaged structural components, managing to sustain gravity loads but with no margin against the building's collapse.

Each of the above referred SPLs shall be achieved when subjecting the structures to a corresponding SHL, i.e., *BSE-1N* and *BSE-2N* have to be applied, respectively. Further, Section 3.4 addresses the determination of these SHLs and also describes their relationship with the seismic demand applicable for each AP. The following subsections specify the general and specific requirements for the analysis procedures recommended by ASCE-41 employed in this study and define the acceptance criteria used in judging the seismic performance of the assessed buildings.

3.2.1. General to all Analysis Procedures

ASCE-41 standard specifies some requirements common to linear and nonlinear procedures separately. Gravity loads (Q_G), for instance, must be applied to structural elements using the combinations written in Eqs. [3.1] and [3.2] when executing any of the available linear procedures. In combination with seismic actions, the former equation is used when the effects of these actions are additive. On the other hand, the latter equation is used in combining gravity loads and seismic effects when they are counteracting each other.

$$Q_G = 1.1\left(Q_d + Q_L\right) \quad [3.1]$$

$$Q_G = 0.9Q_D \quad [3.2]$$

In the case of nonlinear APs, the gravity load combination follows Eq. [3.3] when their effects are considered along with the seismic effects.

$$Q_G = Q_D + Q_L \quad [3.3]$$

In Eqs. [3.1] to [3.3], the terms Q_D and Q_L correspond to the actions caused by the dead loads and to the 25% of the unreduced live load, respectively.

Regarding the mathematical model to be evaluated, a three-dimensional one is recommended, but alternatively, a two-dimensional model is also valid if it agrees with some limitations. The buildings of this study, however, are evaluated employing a full three-dimensional model, as emphasized in Section 3.3. It is worth mentioning that all elements of the three-dimensional model are considered to be *Primary Components*. This denomination refers to the elements' (components') ability to withstand deformations and forces induced by the earthquake and gravitational effects. In assessing the performance through nonlinear procedures, the elements' section behavior explicitly reflects the strength and stiffness degradation, as will be exposed in subsequent sections of this chapter.

As recommended by ASCE-41, a 3% target elastic damping ratio is used for the nonlinear dynamic procedure (i.e., for the NLTHA). On the other hand, for the linear dynamic and nonlinear static procedures, 2% damped response spectra are constructed. Further in this chapter, modifications affecting the system damping regarding the consideration of SSI effects are detailed. The 2% damped response spectral accelerations ordinates, for instance, are reduced according to the SSS's global damping due to SSI inertial and kinematic (if allowed) effects. The inherent target elastic damping ratio of nonlinear superstructure models is combined with the soil-foundation system hysteretic and radiation damping that is implicitly considered in the soil-foundation interface elements.

It is well known that buildings should be prepared to withstand seismic action in any horizontal direction. In this concern, the performance assessment process shall include the effects of applying the seismic demand along two orthogonal directions of the building, according to the descriptions in **Table 3.3**. Notice from the table that forces and deformations must be combined in the MRSA procedure when evaluating the elements in each principal orthogonal direction. For the Pushover analysis in NSP, unlike the previous AP, only (30% of the) forces of the secondary orthogonal direction of analysis are combined with the principal direction to determine the total concurrent seismic effect. On the other hand, when evaluating the effects of the seismic demand on the elements using any time-history analysis procedure, since the model is conceived as a full three-dimensional model, effects are directly related to the responses resulting from the application of the selected

ground motions suite (refer to Section 3.4.3). It is worth mentioning that the vertical seismic effects are not considered for the performance assessment of the buildings in the database.

Table 3.3. Application of multidirectional seismic effects.

Analysis Procedure	Concurrent Seismic Effects	
	X-Axis	**Y-Axis**
LDP : MRSA	100% X-direction forces and deformations + 30% Y-direction forces and deformations	30% X-direction forces and deformations + 100% Y-direction forces and deformations
NSP : PO	100% X-direction forces and deformations + 30% Y-direction forces only	30% X-direction forces only + 100% Y-direction forces and deformations
LDP : LTHA NDP : NLTHA	Elements are evaluated for forces and deformations associated with the application of the selected suite of ground motions (Section 3.4.3)	

Continuing with the general prescriptions dedicated to assessing buildings regarding the SSI effects, ASCE-41 recommends evaluating these effects when an increase in spectral accelerations results from their consideration. However, it has been recognized in previous studies referenced in the introductory chapter of this document that the SSI effects are always present. The understanding and derivation of SSI-related code prescriptions so far (i.e., ASCE-7 and ASCE-41) are founded on the outcomes of evaluating elastic systems or strongly simplified nonlinear models. In this study, the interaction effects are always considered. Nonlinear three-dimensional models are assessed to close the gap of the traditional understanding detailed above and address the research needs raised in documents such as (FEMA, 2020) regarding the SSI effects on the seismic design of buildings.

3.2.2. Specific to Linear Dynamic Procedures

For any of the LDP APs, the elements that make up the mathematical model must reflect a linear elastic force-deformation relationship. Section 3.3.1.1 shows the modeling criteria for the elements with these characteristics. The linear APs permitted in assessing the performance of buildings are the MRSA and the LTHA. As will be explained later in Sections 3.4.2 and 3.4.3, for performing the analysis, a response spectrum and a suite of ground motion acceleration histories are defined for the MRSA and the LTHA procedures, respectively.

As usual, when executing a linear dynamic analysis using the MRSA procedure, enough modes of vibration are used to determine the peak responses to mobilize at least 90% of the participating mass of the building in each orthogonal direction. These peak responses are combined by the SRSS rule, considering the multidirectional seismic effects criteria of **Table 3.3**. The LTHA requires all ground

motions in the selected suite to be applied during analysis. Since three-dimensional models are used for all APs, the multidirectional seismic effects are accounted for by simultaneously applying the two horizontal components of the recorded ground motions. Proceeding in this way, forces and deformations in structural elements can be determined from the analyses and later used for the performance assessment.

Forces and deformation obtained using any of the linear dynamic procedures are multiplied by the factors C_1 and C_2 expressed in Eqs. [3.4] and [3.5] before being used to assess the achieved performance.

$$C_1 = 1 + \frac{\mu_{strength} - 1}{aT_n^2} \quad [3.4]$$

$$C_2 = 1 + \frac{1}{800}\left(\frac{\mu_{strength} - 1}{T_n}\right)^2 \quad [3.5]$$

C_1 is a modification factor capable of translating the obtained elastic displacement from the linear analysis to the maximum expected inelastic displacement. C_2, meanwhile, is a modification factor that accounts for the complex effects of pinched hysteresis behavior shapes, cyclic stiffness degradation, and strength deterioration that linear elastic sections cannot display. ASCE-41 presents some limitations to the values that these factors can adopt depending on the natural vibration period of the structure T_n (or $\tilde{T}_n$ if considering SSI effects). Additional terms including in C_1 and C_2 expressions are the ratio of the elastic strength demand to the yield strength, $\mu_{strength}$, and the site class factor, a. Both terms are expressed in Eqs. [3.6] and [3.7], where W is the effective seismic weight of the building and C_m is an effective mass factor taken as $C_m = 0.90$ for any building with fundamental period of vibration less than $1.0s$ and $C_m = 1.00$ otherwise (refer to Table 7-4 in ASCE-41). S_a on the other hand, is the spectral acceleration and depends also on T_n (or $\tilde{T}_n$ if considering SSI effects).

$$\mu_{strength} = \frac{S_a}{V_y/W} C_m \quad [3.6]$$

$$a = \begin{cases} 130 & \text{for site Class A or B} \\ 90 & \text{for site Class C} \\ 60 & \text{for site Class D, E, or F} \end{cases} \quad [3.7]$$

It is essential to mention that when analyzing *flexBase* buildings for considering SSI effects, the term T_n is replaced by $\tilde{T}_n$ in Eqs. [3.4] through [3.7] or in their period-dependent terms, if applicable.

3.2.3. Specific to Nonlinear Static Procedure

The Pushover analysis is used for the NSP recommended in ASCE-41. Specific considerations in executing this AP consist of guidelines concerning the modeling criteria of nonlinear element sections

for the mathematical model, the determination of the *target displacement* to which a *control node* within the evaluated structure shall reach, and to which the induced force and deformation actions in the elements must be determined, and finally, how these actions are taken in the evaluation of the final performance of a building.

Regarding the first consideration, Section 3.3.1.2 shows the general nonlinear force-displacement backbone curve adopted in modeling the elements' section representing the strength degradation explicitly included in the model.

The mathematical model thus generated should be capable of reflecting the responses (forces and deformations) induced in the elements due to monotonically increasing lateral loads representing inertia forces in an earthquake until a target displacement, δ_t, is reached. Gravitational loads combined as detailed in Section 3.2.1, along with the aforementioned lateral forces, are applied in both positive and negative directions at each orthogonal direction of analysis, and only the maximum seismic effects are considered for calculating the achieved performance. As a result of the Pushover analysis procedure, a curve with the relation between the induced base shear and the lateral displacement of the *control node* is obtained, as portrayed in **Figure 3.2**.

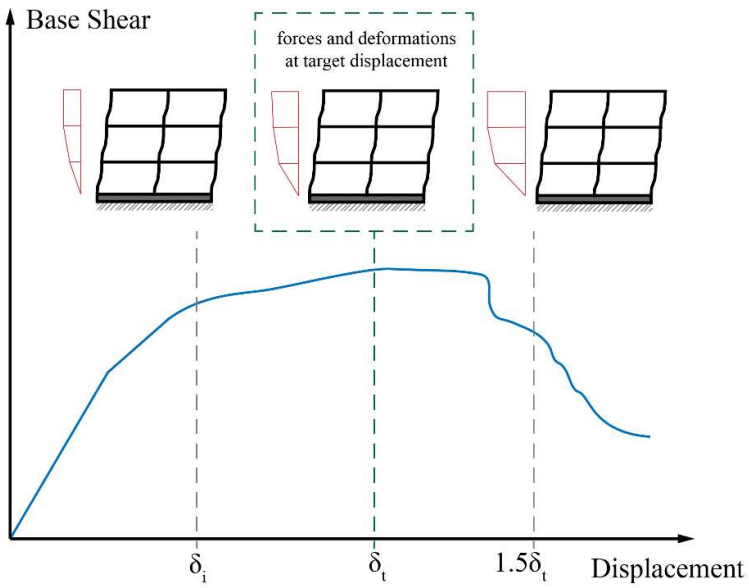

Figure 3.2. Typical shear force – deformation curve. Target displacement identification.

Notice from the figure that, during analysis, the curve is recorded up to a displacement 1.5 times δ_t as recommended by the standard. The target displacement represents a mean displacement value for the SHL being evaluated in the performance assessment, and there is a considerable scatter about this mean value. In this regard, the ASCE-41 standard encourages subjecting the buildings to higher target displacements than the calculated δ_t, aiming to create awareness of the likely performance of a building beyond the selected SHL. Note also that the *control node* shown in **Figure 3.2** is located on the roof of a building, specifically in its center of mass. Also, even though the figure depicts a *fixBase*

structure, *flexBase* models are assessed too. Lastly, it is worth mentioning that the vertical distribution of the lateral seismic forces is proportional to the shape of the fundamental mode in the analysis direction.

The expression in Eq. [3.8] is used to calculate the target displacement as per ASCE-41.

$$\delta_t = C_0 C_1 C_2 S_a \frac{T_e^2}{4\pi^2} g \qquad [3.8]$$

Where C_0 is a modification factor that relates the spectral displacement of an SDOF system to the control node displacement of the building's MDOF system. It was calculated by the expression in Eq. [3.9] as the first mode mass participation factor multiplied by the ordinate of the first mode shape at the control node. In the equation, $\phi_{1,r}$ is ordinate of the first mode shape obtained at the roof of the building, and the fractional term is the first modal mass participation factor, Γ_1.

$$C_0 = \phi_{1,r} \frac{\{\phi_1\}^T [M] \{1\}}{\{\phi_1\}^T [M] \{\phi_1\}} \qquad [3.9]$$

T_e (or $\tilde{T}_e$ if SSI effects are considered), is the effective fundamental period of the building in the direction of analysis, and g is the acceleration of gravity. All other factors in Eq. [3.8] were introduced before.

In determining the effective fundamental period T_e, the actual force-deformation curve resulting from the Pushover analysis is used for constructing an *idealized force-displacement curve,* as portrayed in **Figure 3.3**.

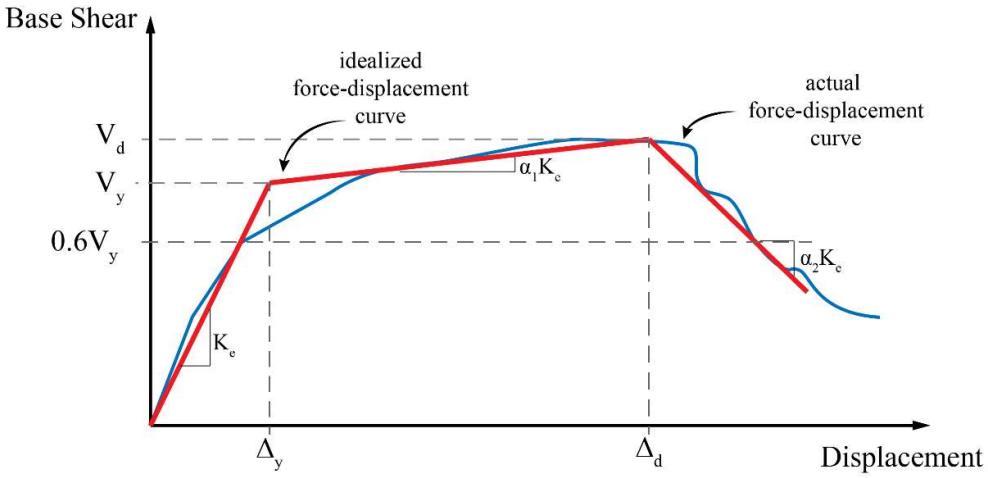

Figure 3.3. Idealized force-displacement curve derived from the actual pushover curve. Adapted from ASCE-41 (American Society of Civil Engineers, 2017b)

In the figure, notice that the idealized curve comprises three segments. The first spans from the origin to the point of coordinates (Δ_y, V_y) with a slope value of K_e. The second segment goes from this point

to another with coordinates (Δ_d, V_d) and its slope is $\alpha_1 K_e$. Lastly, the third segment begins at the point (Δ_d, V_d) and continues with a negative slope $\alpha_2 K_e$. The endpoints of the segments described before are characteristic ordered pairs in the idealized force-deformation curve that are graphically derived from the actual curve. (Δ_d, V_d), for instance, corresponds to the point in the actual curve located at the target displacement, δ_t, or at the displacement corresponding to the maximum base shear, whichever is least. The point (Δ_y, V_y), on the other hand, is defined by intersecting the first and second segments so that the areas above and below the actual curve are approximately balanced. In performing this graphical procedure, two things shall be considered: a) the effective yield strength, V_y, shall not be greater than the maximum base shear in the actual curve, and b) the effective lateral stiffness, K_e, has to be considered as the sectant stiffness of a point in the actual curve whose V value corresponds to a 60% of V_y. Regarding the slope of the second segment, $\alpha_1 K_e$, represents the positive post-yield stiffness of the building. The slope $\alpha_2 K_e$ of the third segment, on the other hand, is the negative post-yield stiffness. The latter slope is also graphically determined by joining (Δ_d, V_d) and the point in the actual curve in which the actual degraded base shear force reaches back 60% of V_y.

Based on the idealized curve, the effective lateral stiffness can now be employed to determine the effective fundamental period, T_e, with the following equation.

$$T_e = T_i \sqrt{\frac{K_i}{K_e}} \qquad [3.10]$$

Where T_i is the fundamental elastic period of the building for the direction of analysis calculated using an elastic dynamic analysis, and K_i is the elastic lateral stiffness measured in the same direction of analysis. Once T_e is calculated, the target displacement applicable to each direction of analysis can be obtained back with Eq. [3.8].

Finally, for assessing the performance of the building through the NSP, element forces, and deformations at a state in which the control node has reached or exceeded δ_t are evaluated.

3.2.4. Specific to Nonlinear Dynamic Procedure

The Nonlinear Time-History Analysis procedure is employed to obtain forces and deformations in elements that can be subjected to the performance assessment. A nonlinear mathematical model capable of representing the nonlinear force-displacement relationship in elements' sections is essential for this nonlinear analysis procedure. In this regard, Section 3.3.1.2 details the nonlinear modeling criteria considering that the section's complex behavior shall include the pinched hysteresis characteristics, the cyclic stiffness degradation, and the strength deterioration that models employed in previously described APs (i.e., MRSA, LTHA, NSP) can only approximate through the factor C_2 (Eq. [3.5]). Moreover, the same nonlinear behavior reflected in the inelastic displacement

and deformation responses neglects the need for modification factors C_0 and C_1, so important to the aforementioned linear (and NSP) procedures.

In determining the response forces and deformations for the performance assessment, these parameters are calculated for each ground motion record in the selected suite. A discretized response history of forces and deformations is recorded for each ground motion in the suite. Then, since the orthogonal components of a ground motion are simultaneously applied to the model, the average of the maximum responses of the response histories (for both forces and deformations) is considered the response parameter of the NDP analysis. The performance assessment is performed using these average responses.

3.2.5. Performance Acceptance Criteria

Generally speaking, performance acceptance criteria can be defined as numerical indicators of the achievement of a performance objective based on a demand-capacity ratio (DCR). The demand relates to the actions (axial, shear, or flexure forces) imposed on an element or component after applying a selected SHL. The capacity results from the ability of the same element or component to resist such a demand related to the corresponding action. In that sense, Eq. [3.11] describes the acceptance criteria based on the aforementioned demand-capacity ratio in a generic way.

$$DCR_{(ac)} = \frac{demand^{SHL}}{capacity} \qquad [3.11]$$

It shall be recalled that throughout this work, different APs are used in assessing the performance of buildings, and two performance objectives are required to be evaluated following the recommendations of ASCE-41, according to **Table 3.2**. In addition, structures designed following conventional and SSI-related code prescriptions (introduced earlier as DTs) are analyzed with two BSCs. Thus, the $DCR_{(ac)}$ outcomes from the assessment carried out in this section will be more specifically described with the expression in Eq. [3.12].

$$DCR_{(ac)}{}^{DT:BSC}_{AP:SPL} = \frac{demand^{SHL}}{capacity} \qquad [3.12]$$

In the latter equation, $DCR_{(ac)}{}^{DT:BSC}_{AP:SPL}$ refers to the demand-capacity ratio acceptance criteria obtained for a structure designed according to $DT = [convDs, SSIDs]$, modeled for the analysis considering one of $BSC = [fixBase, flexBase]$, analyzed using one of the $AP = [LDP, NSP, NDP]$, to one of the structural performance levels in $SPL = [LS, CP]$. As may seem evident, when this ratio gets values below 1.0 indicates that element successfully withstands the exerted demand. On the contrary, if $DCR_{(ac)}{}^{DT:BSC}_{AP:SPL}$ values exceed 1.0, it would point out a failure in achieving the required performance objective.

In determining the demands and capacities for calculating the demand-capacity ratio, ASCE-41 establishes separate guidelines depending on the element or component type, the type of action evaluated, and if the AP is a linear or nonlinear analysis procedure. Regarding the element type, it was noted in Section 3.2.1 that all elements within the designed structures are deemed *Primary Components*.

On the other hand, actions exerted on these elements can be classified as *deformation-controlled* or *force-controlled* actions. The former is an internal force or deformation with an associated deformation that can exceed the yielding condition. The latter, on the contrary, is an internal force that is not allowed to exceed the nominal strength of the evaluated element. It is worth mentioning that the definition of deformation- or force-controlled actions is independent of the AP used for the assessment. It is more related to the actual nonlinear nature of an element's action than to how it is determined, even though such nonlinear action has been evaluated using a linear procedure.

In **Table 3.4** are displayed the criteria used to determine whether an action is considered deformation-controlled or force-controlled in this study. Note that moment forces are the only actions deemed deformation-controlled in both beams and columns. Note also that the behavior of beam-column joints is not accounted for in the table. It is because their behavior is not explicitly included in the mathematical model but implicitly adjusting the centerline representation of the joint with rigid offsets, as detailed later in Section 3.3.

Table 3.4. Considerations on deformation- and force-controlled action for elements in moment frames.

Element	Deformation-Controlled Action	Force-Controlled Action
Beams	Moment (M)	Shear (V)
Columns	Moment (M)	Axial Load (P), Shear (V)

Lastly, the following sections show the specific guidelines for calculating $DCR_{(ac)}$ depending on the AP employed to determine the demands.

3.2.5.1. Acceptance criteria for linear procedures

When elements' forces and deformations considered ***deformation-controlled*** actions are calculated using linear analysis procedures, the demand-capacity ratio acceptance criteria are determined using Eq. [3.13].

$$DCR_{(ac)}^{DT:BSC}{}_{AP:SPL} = \frac{Q_{UD}}{m\kappa Q_{CE}} \qquad [3.13]$$

In the equation above, Q_{UD} is the deformation-controlled demand calculated with the expression in Eq. [3.14], where Q_G for linear procedures was already introduced in Eqs. [3.1] and [3.2], and Q_E is the demand caused by the response to the evaluated SPL.

$$Q_{UD} = Q_G + Q_E \quad [3.14]$$

Back in Eq. [3.13], m is an element demand modification factor reducing the magnitude of Q_{UD}. It accounts for the expected ductility associated with the deformation-controlled actions that would have been obtained from a nonlinear procedure and depends on the element type and the evaluated SPL. **Table A-1** and **Table A-2** in **Appendix A** show the values m-factors adopt and its dependencies[1]. On the other hand, κ is the *knowledge-factor* that accounts for the uncertainty in the geometrical and mechanical data collection used to reduce the element capacity, Q_{CE}. Since no laboratory testes were considered in constructing the database of designed buildings, no uncertainty in the data collection can be present. Hence, values of κ for all every element is assumed to be 1.0.

The expected capacity or strength of the element's deformation-controlled action, Q_{CE}, is determined for any element section by the mechanics of materials fundamentals, considering the expected properties of the materials making up the element (i.e., concrete and reinforcement steel). To define the expected material properties, ASCE-41 recommends multiplying the nominal material strength values by the factors shown in **Table 3.5**.

Table 3.5. Factors to translate nominal to expected strength material properties.

Material Property	Factor
Concrete compressive strength	1.50
Steel reinforcement tensile and yield strength	1.25
Connector steel yield strength	1.50

In Section 2.5.2, it was mentioned that the nominal material strength employed during the design is $f'_c = 35\ [MPa]$ and $f_y = 420\ [MPa]$ for the concrete and the reinforcement steel, respectively. Employing the factor detailed in **Table 3.5**, the expected material strength properties are $f'_{c_E} = 52.5\ [MPa]$ and $f_{y_E} = 525\ [MPa]$.

When elements' forces and deformations considered ***force-controlled*** actions are calculated using linear analysis procedures, the demand-capacity ratio acceptance criteria are determined using Eq. [3.15].

[1] For the sake of the extension of Sections 3.2.5.1 and 3.2.5.2, information regarding m-factors, modeling criteria for nonlinear deformation-controlled actions and their acceptance criteria are presented in Appendix A.

$$DCR_{(ac)}^{DT:BSC}{}_{AP:SPL} = \frac{Q_{UF}}{\kappa Q_{CL}} \quad [3.15]$$

In this equation, Q_{UF} is the force-controlled demand calculated according to Eq. [3.16], where χ is a facter used for adjusting the demand caused by the seismic response for the SPL being evaluated, J is the force-delivery reduction factor also affecting the seismic demand Q_E and is taken as $J = 2.0$ for zones with high levels of seismicity. All other terms in Eq. [3.16] were already introduced earlier.

$$Q_{UF} = Q_G \pm \frac{\chi Q_E}{C_1 C_2 J} \quad [3.16]$$

Conversely to what was established for calculating the elements' strength for *deformation-controlled* actions, for force-controlled actions, a *lower-bound* elements' strength shall be calculated and denominated as Q_{CL}. The same mechanics of materials fundamentals can be used to determine a cross-section strength, but this time, the lower-bound material properties are used instead of the expected strength. According to ASCE-41, the nominal material properties can be assumed to be lower-bound values. Hence, for evaluating the demand-capacity ratios acceptance criteria for the force-controlled actions in an element or component, the properties used are $f'_{c_L} = 35\ [MPa]$ and $f_{y_L} = 420\ [MPa]$. This criterion helps define a security margin for determining the capacity in force-controlled actions that are not allowed nor capable of sustaining demands beyond their maximum elastic strength.

3.2.5.2. Acceptance criteria for nonlinear procedures

When calculating the demand-capacity ratio acceptance criteria for ***deformation-controlled*** actions in structures evaluated using nonlinear procedures, the elements' forces and deformations responses are obtained directly from the analysis results, regardless of the AP employed. As detailed in **Table 3.4**, the only deformation-controlled action is the moment (M). The rotations obtained as responses from the AP selected are compared against the acceptance criteria for beams and columns shown in **Table A-3** and **Table A-4** in **Appendix A**. it means that the deformation demands from analyses should not exceed the inelastic deformation capacities recommended in the tables referred earlier depending on the SPL being evaluated. Again a deeper insight into this topic can be found in **Appendix A**.

On the other hand, calculating the demand-capacity ratio acceptance criteria for ***force-controlled*** actions using nonlinear APs implies using Eq. [3.17].

$$DCR_{(ac)}^{DT:BSC}{}_{AP:SPL} = \frac{\gamma\chi\left(Q_{UF} - Q_G\right) + Q_G}{Q_{CL}} \quad [3.17]$$

Where all terms but γ have been introduced, it is a load factor regarding the relative importance of the element's action capacity for structural integrity. For instance, the failure of a column due to

unexpected and fragile shear or axial force would result in a more extended global failure than if any beam action fails to reach the desired (or maximum limit) capacity. Thus, one could expect that γ factor increases the magnitude of demands for an element essential in sustaining global structural integrity. This is the case, as said before, for shear (V) and axial force (P) demand actions in columns. **Table 3.6** shows values for the γ-factor depending on the action type within an element.

Table 3.6. Load factor for force-controlled actions.

Action Type	γ
Critical	1.3
Ordinary	1.0
Noncritical	1.0

3.3. Modeling Criteria for the Soil-Structure System

An adequate definition of the mathematical model is a crucial step in the performance evaluation of any structure. Such a model should be detailed enough to obtain accurate responses after the analysis but simultaneously avoid being too complex to become time-consuming; especially when assessing extensive databases as in this research work.

Classifying element actions into deformation- or force-controlled helps make decisions regarding the criteria selected to develop the mathematical model, especially in creating the nonlinear model. As specified in **Table 3.4**, the only action deemed deformation-controlled is the moment force (M) in beams and columns. Thus, the nonlinear representation of this action is carefully addressed in Section 3.3.1.2, while all other actions' behavior -even in nonlinear models- are accounted for with linear characteristics. Modeling criteria regarding both deformation- and force-controlled nature of actions for linear models are detailed in Section 3.3.1.1. Concerning the soil modeling criteria, both linear and nonlinear elements included in the *flexBase* BSC models are described in Section 3.3.2.

This section describes the procedures followed to generate models that fulfill the needs of both linear and nonlinear analysis procedures by introducing the superstructure and sub-structure elements separately. The modeling and analysis process is again carried out through the OpenSeesPy environment. The modeling objects representing the force-deformation behavior of the elements are expressed in the following sections following the commands (names) used in OpenSeesPy.

3.3.1. Representation of superstructure elements (beams and columns)

3.3.1.1. Modeling criteria specific to LDPs

Executing the performance assessment using linear analysis procedures requires the mathematical model of the system generated for that purpose to include linear elastic components. In Section 2.5.2.1, the modeling criteria adopted for linear elements during the design process were introduced;

the same guidelines apply to the modeling process of linear elements in the performance assessment with LDPs.

One additional consideration to account for, though, is that ASCE-41 recommends that linear elastic effective stiffnesses of element sections should be derived assuming a behavior at or near yield level. In that concern, the mentioned standard suggests that the stiffnesses shown in **Table 3.7** should be used to describe the proportionality of forces and deformations for the linear behavior of elements.

Table 3.7. Effective Stiffness values

Component	Flexural Rigidity	Shear Rigidity	Axial Rigidity
Beams	$0.30E_{c_E}I_g$	$0.40E_{c_E}A_w$	-
Columns with compression caused by design gravity loads $\geq 0.50A_g f'_{c_E}$ [a]	$0.70E_{c_E}I_g$	$0.40E_{c_E}A_w$	$E_{c_E}A_g$
Columns with compression caused by design gravity loads $\leq 0.10A_g f'_{c_E}$ or with tension [a]	$0.30E_{c_E}I_g$	$0.40E_{c_E}A_w$	$E_{c_E}A_g$ (comp.) $E_{c_E}A_s$ (tension)

[a] For columns with axial compression falling between the limits provided, flexural rigidity shall be determined by linear interpolation. If interpolation is not performed, the more conservative stiffnesses shall be used. An imposed axial load N_{UG} is permitted to be used for stiffness evaluations.

In the table above, E_{c_E} is the Young's modulus of the concrete calculated assuming the expected material property f'_{c_E}. I_g is the moment of inertia of the gross concrete section about the centroidal axis, neglecting reinforcement.

3.3.1.2. Modeling criteria specific to NSP and NDP

Nonlinear elements are modeled using the same element type as for linear ones. This time, though, the Modified Hinge-Radau integration rule (Scott & Fenves, 2006) is used instead for the member response evaluation. For **beams**, this integration method allows us to consider concentrated plasticity in a determined length, l_p, at both extreme ends of the member while keeping linear elastic properties at the central segment as shown in **Figure 3.4**.

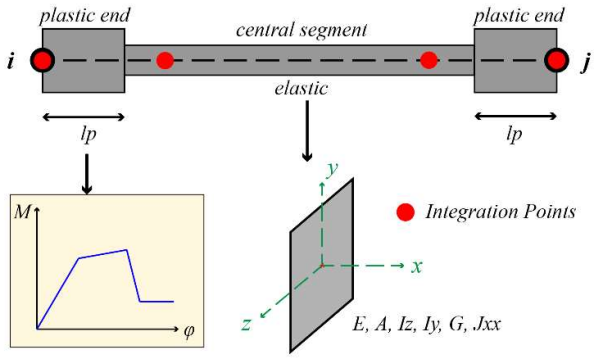

Figure 3.4. Nonlinear elements. Schematic representation for beams.

The plastic length is calculated with the expression shown in Eq. [3.18] as recommended by (Paulay & Priestley, 1992), where z is the distance from the critical section of maximum curvature and the element point of contraflexure, d_b is the diameter of longitudinal reinforcement and f_y its yielding stress.

$$l_p = 0.08z + 0.022d_b f_y \quad [3.18]$$

The nonlinear behavior representation through concentrated plasticity should reflect different characteristics depending on the analysis procedure. For the NSP, where a monotonically increasing lateral seismic load is applied, the concentrated plasticity element representing this behavior shall show a force-deformation *envelope curve* of the expected nonlinear relationship. On the contrary, when using an NDP (say, NLTHA), the cyclic characteristics of the seismic actions should be reflected in the nonlinear response of the concentrated plasticity element. Thus, the force-deformation relationship is represented through a *backbone curve* of the behavior, and the modeling object should be capable of exhibiting complex characteristics such as stiffness, strength, and cyclic degradation.

Although both the backbone and the envelope curves for the behavior of the concentrated plastic hinges for beams in models created for the NSP and NDP differ one from the other, they can be represented in OpenSeesPy using the same material object. However, as explained later in this section, different input parameters are calculated depending on the AP used during the analysis.

Concentrated moment-rotation plasticity in beams is accounted for by employing the Modified Ibarra-Medina-Krawinkler deterioration model (IMKDM) with peak-oriented hysteretic response described in (Ibarra & Krawinkler, 2005), and input arguments for this model were determined as recommended by (Curt B. Haselton et al., 2008; Curtis B. Haselton & Deierlein, 2007). A graphical representation of the behavior of this plastic hinge element model is shown in **Figure 3.5** for a generic action-deformation $Q - \delta$ relationship. On this figure, Q_{max} and Q_y represent the maximum strength and the yielding strength for action Q. Q_{res} is the residual strength for the generic action, K_e is the initial elastic stiffness for the linear segment. Regarding generic deformations, δ_y, δ_p, δ_{pc}, and δ_u are the yielding deformation, the plastic deformation beyond yielding limit and before strength capping, the effective post-capping deformation and the ultimate deformation, respectively.

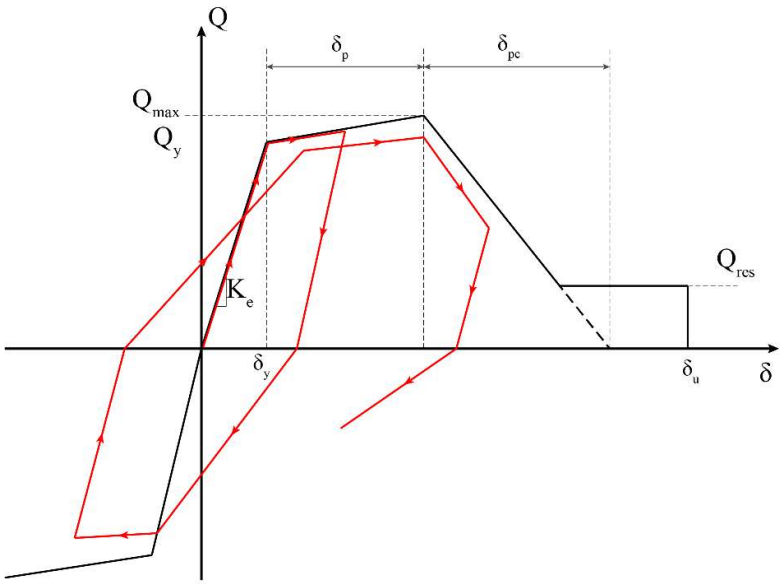

Figure 3.5. Illustration of concentrated plastic-hinge element backbone model with degradation.

Even though the backbone curve shown in **Figure 3.5** is dedicated to modeling the cyclic behavior destinated to NDP procedures, the envelope curve can also be modeled through the same Modified-Ibarra-Medina-Krawinkler object in OpenSeesPy, in which the input parameters that are established, differ from each other. Based on the recommendations detailed in (Applied Technology Council, 2017b), the cyclic and monotonic behavior can be defined according to the parameters depicted in **Figure 3.6**.

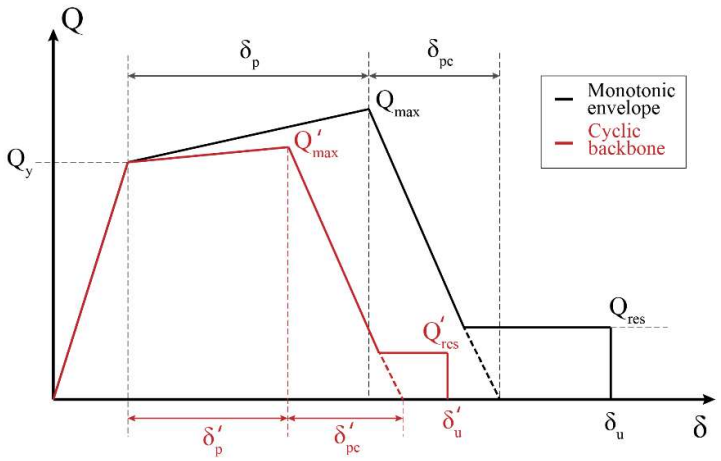

Figure 3.6. Generic cyclic and monotonic curves and corresponding parameters.

The apostrophe (′) over each parameter indicates its correspondence with the cyclic backbone curve with reduced magnitudes due to the degradation responses under cyclic actions. Let us recall that the actions modeled through the IMKDM are flexural forces; the force and deformation parameters correspond to moment (M) and rotation (θ), respectively. Thus, the construction of the force-deformation relationship is related to a moment-rotation behavior of the elements' sections. Some

researchers have focused on defining expressions to help calculate each parameter to determine the conduct of such plastic rotation elements. Documents consolidating the necessary information for this purpose are (Applied Technology Council, 2017a, 2017b); Eqs. [3.19] to [3.23] show the expressions recommended to explain such behavior.

Regarding the rotations, Eqs. [3.19] and [3.20] show the plastic and the post-capping rotation magnitudes employed for the monotonic envelope curve.

$$\theta_p = 0.155(0.16)^{v}\left(0.02+40\rho_{sh}\right)^{0.43}(0.54)^{0.01C_{units}f_c'} \quad [3.19]$$

$$\theta_{pc} = (0.76)(0.031)^{v}\left(0.02+40\rho_{sh}\right)^{1.02} \leq 0.10 \quad [3.20]$$

Where v is the axial load ratio $P/A_g f_c'$. P is the axial load applied to the element section. ρ_{sh} is the area ratio of transverse reinforcement in the plastic hinge region, C_{units} is a unit transformation factor that equals 1.0 for f_c' measured in $[MPa]$.

Eqs. [3.21] describes the recommended correlation between the monotonic envelope parameters and their cyclic backbone parameters counterpart.

$$\begin{aligned}\theta_{p,cyclic} &= 0.70\theta_{p,monotonic}\\ \theta_{pc,cyclic} &= 0.50\theta_{pc,monotonic}\end{aligned} \quad [3.21]$$

In concern with the moment magnitudes, Eq. [3.22] recommends that the maximum resisting moment be adopted as 13% greater than the yielding moment, M_y. The residual flexural strength (residual moment), on the other hand, is considered as 20% of the M_y magnitude in Eq. [3.23].

$$M_{\max} = 1.13M_y \quad [3.22]$$

$$M_{res} = 0.20M_y \quad [3.23]$$

In addition, the yield and ultimate moment-rotation coordinates, i.e., θ_y, θ_u, M_y, and M_u, are calculated using closed-form equations for reinforced concrete sections derived in the study carried out by (Monti & Petrone, 2015). These equations are presented in **Appendix B** for the sake of this section extension. It is worth noting that the results in the closed-form equations correspond to moment-curvature pairs. In modeling the above elements, these curvatures are multiplied by the plastic length (l_p) in Eq. [3.18] to obtain the desired rotation magnitudes.

Finally, to avoid numerical issues during the response integration during the NLTHA, a modified stiffness is defined for the elastic and the plastic portion (concentrated plastic hinge) of the beam members. This modification implies using a factor n, which adopts a value of $n = 10$. Based on (Ibarra

& Krawinkler, 2005), modified stiffnesses of the hinge and the rest of the member are determined according to Eqs. [3.24] and [3.25], respectively.

$$K_{ph} = (n+1)K_{mem} \quad [3.24]$$

$$K_{mem(\mathrm{mod})} = \frac{(n+1)}{n}K_{mem} \quad [3.25]$$

For **columns**, on the other hand, the same element object and integration rule from OpenSeesPy are used to evaluate the response of fiber sections located in the earlier defined l_p to take into account P-M-M interaction. The fiber sections are comprised of nonlinear uniaxial materials representing concrete and reinforcement steel using expected or lower-bound material properties when needed. Regarding the former material, unconfined and confined concrete behavior is modeled utilizing the *Concrete02* Kent-Scott-Park model OpenSeesPy object. A factor to increase the compressive strength due to confinement is calculated per (Mander et al., 1988). The reinforcement steel behavior is modeled through the *SteelMPF* Menegotto-Pinto material model extended by Filippou (Filippou et al., 1983) to include isotropic strain hardening effects. **Figure 3.7** shows a schematic of the nonlinear column elements described in previous lines.

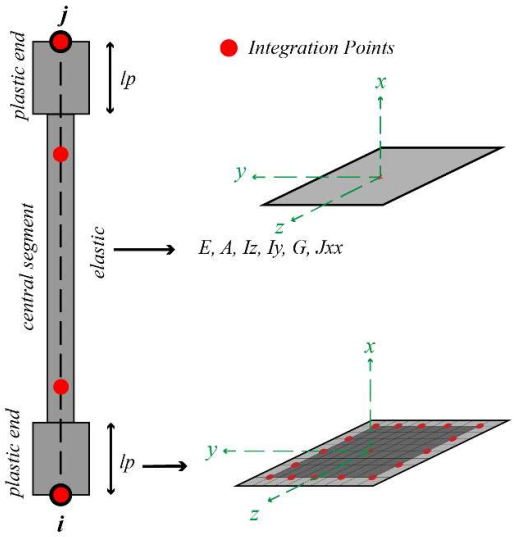

Figure 3.7. Nonlinear elements. Schematic representation for columns.

3.3.2. Representation of substructure elements (soil)

3.3.2.1. Modeling criteria specific to LDP

Regarding the modeling criteria followed for the performance assessment of linear models for LDPs, the guidelines exposed in Section 2.5.3.1 are followed. Please refer to the mentioned section for in-depth details about the OpenSeesPy objects and materials representing the stiffnesses and the linear force-deformation behavior employed.

3.3.2.2. Modeling criteria specific to NSP

A nonlinear representation of the soil force-displacement relationship is now needed for the NSP. This behavior is characterized by stiffness and capacity parameters, contrasting with what was defined for LDP. An equivalent elastoplastic representation is considered acceptable for the vertical and lateral DOFs behavior according to ASCE-41 when applying a monotonically increasing lateral seismic load. Therefore, for calculating the stiffness magnitude K^i as explained for the LDP modeling criteria, it is necessary to define the soil-bearing capacity force, Q_{ult}^i, to shape the vertical elastoplastic behavior of the i^{th} zero-length element, ultimately. In the case of lateral elastoplastic behavior, K_x and K_y stiffness magnitudes are again taken directly from **Table 2.5**. At the same time, the lateral capacity is limited to the determination of the frictional sliding capacity, T_{ult}^i, neglecting the effects of passive earth pressure since all buildings are assumed to be supported by shallow foundations.

In calculating the bearing capacity force, Q_{ult}^i, for the individual zero-length element, Eq. [3.26] is used.

$$Q_{ult}^i = q_{ult}(x) \times dA_i \quad [3.26]$$

Where $q_{ult}(x)$ is the ultimate soil stress capacity calculated according to Eq. [3.27], considering a parabolic contact pressure distribution reflecting the foundation system's ultimate load state (Harden et al., 2005).

$$q_{ult}(x) = cN_c + \gamma N_q D_f + q_\gamma(x) \quad [3.27]$$

From Eq. [3.27], c, γ, and D_f are the cohesion, soil unit weight, and foundation depth; N_c and N_q are the bearing capacity factors affecting the cohesive intercept and the surcharge terms, respectively. In addition, $q_\gamma(x)$, stands for the term of the unit weight contribution to the ultimate soil stress capacity from which the parabolic distribution is taken according to Eqs. [3.28] and [3.29].

$$q_\gamma(x) = q_i + \frac{6}{B^2}\left(\frac{1}{2}\gamma B N_\gamma - q_i\right)\left(\frac{B^2}{4} - x^2\right) \quad [3.28]$$

$$q_i = 0.50\left(\tan\phi + \frac{1}{FS_v}\right)\left(\frac{1}{2}\gamma B N_\gamma\right) \quad [3.29]$$

Where N_γ is the bearing capacity factor affecting the unit weight term, ϕ is the effective friction angle, FS_v is the vertical safety factor, and q_i is the bearing capacity ordinate of the parabolic distribution at the extreme ends of the foundation surface as a function of FS_v, ϕ and the unit weight term itself.

As for the frictional sliding capacity force, T_{ult}^i, for the i^{th} zero-length element, Eq. [3.30] is used.

$$T_{ult}^{i} = t_{ult} \times dA_i \qquad [3.30]$$

In this equation, t_{ult} is the ultimate frictional capacity stress of the soil determined by employing Eq. [3.31].

$$t_{ult} = c + \sigma_{OB} \tan \phi_{cs} \qquad [3.31]$$

Defining σ_{OB} as the overburden pressure and ϕ_{cs} is the critical state friction angle after (Bolton, 1986), calculated using Eq. [3.32].

$$\phi_{cs} = \phi - 3\left[D_r \left(10 - \ln \frac{q_{ult}(x)}{p_a} \right) - 1 \right] \qquad [3.32]$$

Where D_r and p_a, respectively, correspond to the soil's relative density and the atmospheric pressure.

Uncertainties are considered in the same manner as specified for the LDP criteria. In this case, though, not only stiffnesses are affected but also capacities. Refer to **Figure 3.8** for a graphical description of the model.

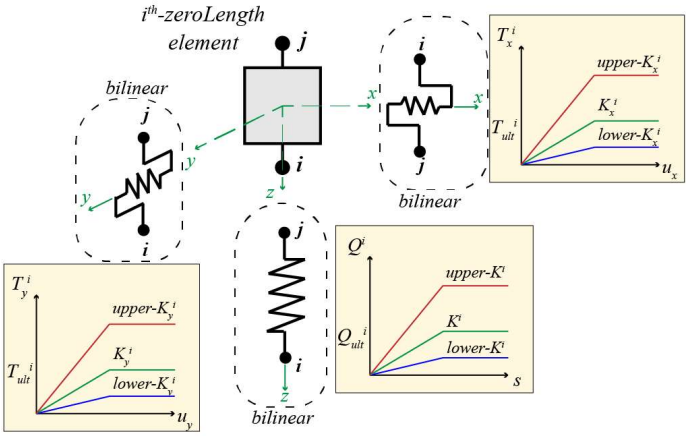

Figure 3.8. Bilinear soil-element representation.

3.3.2.3. Modeling criteria specific to NDP

A more sophisticated representation of the soil force-displacement relationship assigned to the vertical and lateral components of the i^{th} zero-length element is used in NDP, namely, *QzSimple* and *TzSimple* materials. These materials were developed by Boulanger and described in (Boulanger et al., 1999) and implemented for the OpenSeesPy environment to model the behavior of a pile tip subjected to cyclic loading (*QzSimple*) and its skin resistance (*TzSimple*). Nevertheless, several studies have demonstrated the suitability of these materials in broader SSI applications related to the evaluation of systems supported by shallow foundations (Gaja et al., 2008; Gajan et al., 2010; Harden et al., 2006; Raychowdhury & Hutchinson, 2009). The input parameters to model these

materials include a boolean argument to define whether the soil is sand or clay and the soil bearing capacity force, Q_{ult}^{i}, calculated as per Eq. [3.26], the displacement at which 50% of Q_{ult}^{i} is movilized in monotonic loading, z_{50}, using Eq. [3.33] and the radiation damping coefficient, c_{rd}, by Eq. [3.34] for the *QzSimple* OpenSeesPy material. For the *TzSimple* material, on the other hand, the frictional sliding capacity force, T_{ult}^{i}, of Eq. [3.30] and z_{50}^{fr} employing Eq. [3.35] shall be determined.

$$z_{50} = 1.39\frac{Q_{ult}^{i}}{K^{i}};\ \text{for sands}$$
$$z_{50} = 0.525\frac{Q_{ult}^{i}}{K^{i}};\ \text{for clays} \qquad [3.33]$$

$$c_{rd} = \frac{2K^{i}\beta_{rd}}{\tilde{\omega}_{n}} \qquad [3.34]$$

$$z_{50}^{fr} = 2.05\frac{T_{ult}^{i}}{K_{x,y}};\ \text{for sands}$$
$$z_{50}^{fr} = 0.708\frac{T_{ult}^{i}}{K_{x,y}};\ \text{for clays} \qquad [3.35]$$

Where $K_{x,y}$ are the local x or y stiffness magnitudes calculated as per **Table 2.5** depending on the zero-length element local DOF being treated. In addition, β_{rd} is the radiation damping ratio determined under the ASCE-7 standard using Eq. [2.25] and accompanying equations already introduced in Section 2.5.3.2. Finally, it is worth noting that uncertainties are treated similarly to NSP. See Figure 11, where the element modeling is depicted.

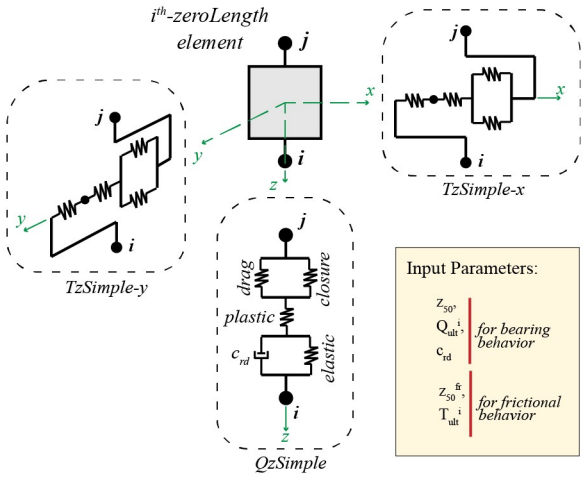

Figure 3.9. Mechanical representation of nonlinear soil elements *QzSimple*, *TxSimple-x*, and *TzSimple-y* using zero-length elements according to the NDP.

3.4. Seismic Demand Definition for the Performance Assessment

3.4.1. General Aspects

The seismic demand is again characterized by the seismic hazard used in the analysis process. During the design-focused analysis using the MRSA, the design hazard was reflected in the Design Response Spectra (DRS) when *convDs* was executed and in the SSI-Modified Response Spectra (SSI-MDRS) for its *SSIDs* DT counterpart. For the performance assessment carried out in this study, however, it can be characterized either by ground motion acceleration histories (GMs) or general response spectra (GRS), depending on the AP used in the assessment process according to ASCE-41.

The GRS, for instance, allows us to determine spectral accelerations, S_a, affecting each vibration mode in the MRSA for calculating forces and displacements. In the NSP, the GRS also helps determine a S_a value to calculate the target displacement, δ_t, through Eq. [3.8]. Regarding the linear and nonlinear time-history analysis procedures, the GRS is used as a target level of spectral accelerations to which the GMs' spectra should be scaled. Thus, as may seem evident, the construction of the GRS is imperative during the performance assessment process of buildings regardless of the APs used.

On the other hand, GMs are used exclusively as seismic inputs to models evaluated using any time-history analysis (linear or nonlinear). These GMs, as said before, are modified to accommodate the required hazard level described by the GRS. Hence, unlike GRS, GMs are not as imperative to be determined for all APs as the former.

In this regard, the fundamental parameters defining the hazard caused by ground shaking are the 5% damped response spectrum ordinates for short ($T_n = 0.2s$) and long ($T_n = 1.0s$) periods in the direction of maximum horizontal response, $S_{s(SHL)}$ and $S_{1(SHL)}$, respectively. Note their dependency on the SHL to which the assessment is performed. Recall that the performance objective was established in Section 3.2.1 based on **Table 3.1** and **Table 3.2**. The performance objective suggested that the buildings shall achieve an LS-SPL while subjected to a seismic demand corresponding to the BSE-1N SHL. On the other hand, a CP-SPL is desired when seismic demand corresponds to the BSE-2N SHL. Ultimately, $S_{s(SHL)}$ and $S_{1(SHL)}$ respectively should agree with the two SHLs included in the performance objective and also with the local soil conditions before being used to verify the achievement of the corresponding SPLs.

To do this, ASCE-41 requieres that , $S_{s(SHL)}$ and $S_{1(SHL)}$ to be adjusted by F_a and F_v factors present in Eqs. [2.12] and [2.13] and determined following the guidelines introduced in Section 2.5.2.2. Proceeding in this way, the *assessment* response spectrum ordinates can be defined with Eqs. [3.36] and [3.37].

$$S_{XS} = F_a S_{S_{(SHL)}} \qquad [3.36]$$

$$S_{X1} = F_v S_{1_{(SHL)}} \quad [3.37]$$

Where S_{XS} and S_{X1}, are the assessment spectral acceleration parameters corresponding to an X-SHL and constructed accounting for a damping ratio β_x that could differ from the 5% damped fundamental spectral ordinates.

According to ASCE-41, BSE-2N is an SHL consistent with the risk-targeted maximum considered earthquake level (MCE_R) for which spectral ordinates are found tabulated in ASCE-7. BSE-1N, on the other hand, corresponds to the design-earthquake ground motion level deemed as two-thirds of the MCE_R. **Table 3.8** summarizes the information presented in the previous lines in a tabulated fashion.

Table 3.8. Spectral assessment parameters and their SHL-correspondence

SHL	Fundamental Acceleration Parameters		Assessment Acceleration Parameters	
	$S_{S(SHL)}$	$S_{1(SHL)}$	S_{XS}	S_{X1}
BSE-2N	$1.5g$	$0.817g$	$1.5F_a$	$0.817F_v$
BSE-1N 2/3(BSE-2N)	$1.0g$	$0.544g$	$1.0F_a$	$0.544F_v$

Note from the table above that S_{XS} and S_{X1} are expressed in terms of the site coefficients F_a and F_v and are left in this way to be more specifically addressed later. The assessment acceleration parameters are used in the following section to build the adequate GRS for the selected APs in this study.

3.4.2. Spectral Demand: General Response Spectrum

The generation of the General Response Spectrum follows the same guidelines as for the SSI-MGRS in Section 2.5.3.2, which was graphically introduced in **Figure 2.12**. The difference lies in the terminology employed since S_{DS} and S_{D1} (design spectral acceleration parameters) are replaced by the assessment acceleration parameters S_{XS} and S_{X1}, respectively. Besides, although the SSI-MGRS is employed during the design process to account for the increase of the SSS effective damping product of SSI effects, its construction procedure still corresponds to that of a GRS employed during the performance assessment according to ASCE-41. It shall be recalled that in Section 3.2, it was noted that different effective damping ratios are permitted to be adopted for structures depending on the selected APs; the possibility of constructing the GRS employing the spectrum in Figure 2.12 obeys this particularity.

For convenience, the GRS shape recommended by ASCE-41 is shown in **Figure 3.10** using the appropriate terminology for the rest of this section. In this figure S_{ax} is the spectral acceleration response obtained from the GRS for a specific SHL and effective damping ratio, and B_1 is described by Eq. [3.38].

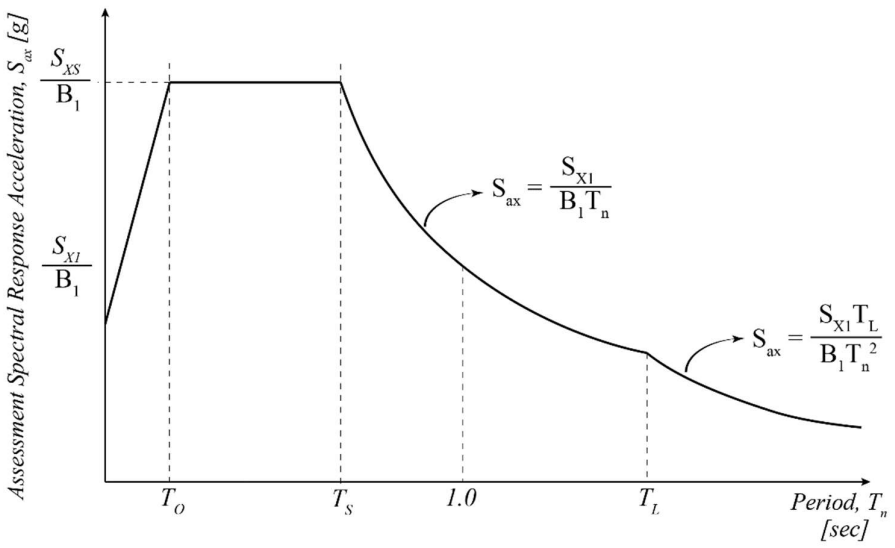

Figure 3.10. General Response Spectrum according to ASCE-41.

When assessing the performance of *flexBase* buildings, the GRS shown in **Figure 3.10** is also applicable. The modification to the assessment spectral accelerations to obtain $\tilde{S}_{ax}$ are carried out in the same fashion as was made for the *SSIDs* through the inclusion of factor B_{SSI}, which in turm depends on the effective viscous damping of the SSS, β_o.

$$B_1 = \frac{4}{\left[5.6 - \ln(100\beta)\right]} \qquad [3.38]$$

Notice in Eq. [3.38] that if β -effective viscous damping ratio for the *fixBase* system- is replaced by β_o, it turns into B_{SSI} modification factor introduced in Eq. [2.21].

Figure 3.11 shows some plots related to the construction of GRS. **Figure 3.11a** depicts 3% damped GRS for assessing *fixBase*-BSC structures considering the two site class categories SC-D and SC-E for the BSE-1N seismic hazard level. **Figure 3.11b** shows the GRS for buildings with the same BSC characteristics and damping but for the BSE-2N seismic hazard level. **Figure 3.11c**, on the other displays a family of GRS for all buildings in the database assessed with *flexBase*-BSC and for the BSE-1N seismic hazard level. A family is presented here because the effective damping ratio of the SSS, β_o, varies depending on the dynamic characteristics of each building and the soil below, thus, there will be a different GRS for each independent building. Also, the maximum, mean, and minimum spectral representations for this family are shown in the same plot. Regarding **Figure 3.11d**, it shows the same family of GRS but for the BSE-2N seismic hazard level. It can be noticed from the plots in this figure the difference between maximum spectral ordinates. **Figure 3.11b** and **Figure 3.11d** consider the highest SHL; hence their ordinates are greater than those shown in **Figure 3.11a** and **Figure 3.11c**. Also, In **Figure 3.11c** and **Figure 3.11d,** the SSI-modified spectral accelerations, $\tilde{S}_{ax}$, can be

read and is evident how β_o decreases the spectral ordinates of the *fixBase* counterparts in **Figure 3.11a** and **Figure 3.11b**.

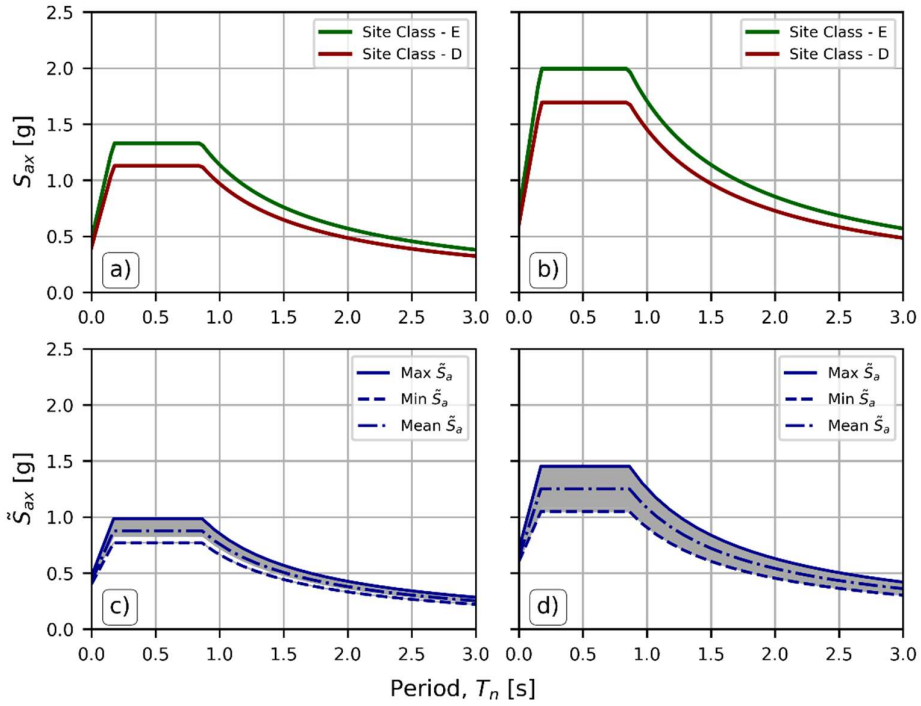

Figure 3.11. General response spectra for a) *fixBase*-BSC, site classes D and E, *BSE-1N* seismic hazard level, 3% damped; b) *fixBase*-BSC, site classes D and E, *BSE-2N* seismic hazard level, 3% damped; c) spectra family for *flexBase*-BSC, for each structure in the database with its corresponding soil and SSS effective damping characteristics for *BSE-1N* seismic hazard level; and d) spectra family for *flexBase*-BSC, for each structure in the database with its corresponding soil and SSS effective damping characteristics for *BSE-2N* seismic hazard level.

It is worth mentioning that the spectra shown in the figure above are permitted to be used in LDPs (i.e., MRSA and LDTHA) and in the NSP without any further modifications. In the MRSA procedure, for instance, S_{ax} and $\tilde{S}_{ax}$ taken directly from the GRS considering each independent modal period of vibration for calculating modal forces and deformations when evaluating *fixBase* and *flexBase* BSC buildings. The same assessment spectral accelerations are employed in NSP for determining the target displacement in the pushover analysis for the two BSC considerations. In LTHA, the shapes of GRS are used as the target spectra for scaling purposes. Regarding the *flexBase* families of GRS in **Figure 3.11c,d** for the use in this latter AP is essential to say that, since the linear buildings cannot include the SSS effective damping ratio implicitly, the SSI-related modification of the spectral ordinates due to β_o is mandatory. It is not the case when assessing the performance of *flexBase* BSC buildings with the NLTHA procedure.

About the use of the GRS as target spectra for scaling ground motions to be used in NLTHA, it is essential to note that the ones shown in **Figure 3.11a** and **Figure 3.11b** are adequate when *fixBase*-BSC buildings are evaluated. However, when SSI effects are considered through a *flexBase* model, it shall be recalled that the damping-generation mechanisms are already included in the nonlinear soil

elements. For instance, the damping coefficient c_{rd} accounts for the radiation damping through the action of an equivalent viscous damper embedded in the OpenSeesPy *QzSimple*-element. On the other hand, the hysteretic behavior of the modeling element itself is in charge of reflecting the hysteretic damping component of the soil-foundation system. In this regard, the definition of the target spectrum to which ground motion records shall be scaled before executing the NLTHA differs from those employed in the same task for the LTHA. This is explained since the model generated for an NDP implicitly considers the soil-foundation damping effects as described before. In contrast, no linear model is capable of displaying such complex behavior.

Hence, when SSI effects are considered, the target spectrum employed in the NLTHA shall include only the recommendations regarding the kinematic interaction effects. The reduction in spectral acceleration magnitudes relates to the base-slab averaging and the embedment effects. However, since all buildings are assumed to be founded over shallow foundations, only base-slab averaging kinematic interaction (BSA) is present. **Figure 3.12** shows the GRS for the *fixBase*-BSC for SC-D and SC-E and both BSE-1N (a) and BSE-2N (b) SHLs. Accompanying these GRS are the BSA-modified family of spectra for each SC. Note that the modifications due to this interaction effect are negligible for all structures in the database. Since the BSA-modified GRS are practically the same as those for *fixBase* conditions, the only evident consequence of SSI effects will be reflected in the inelastic responses, and the mechanisms of radiation and hysteretic damping described earlier.

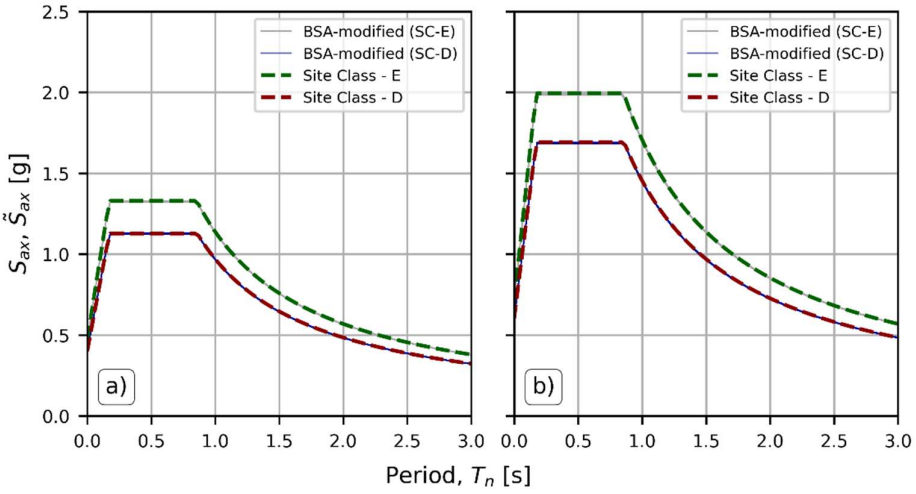

Figure 3.12. General response spectra for *flexBase*-BSC buildings modified considering base-slab averaging (BSA) kinematic interaction effects for: a) BSE-1N seismic hazard level; and, b) BSE-2N seismic hazard level.

For the modification of GRS due to BSA, the recommendations of ASCE-41 are followed. These consist of multiplying each assessment acceleration ordinate by a ratio of response spectra factor, RRS_{bsa}, calculated using Eq. [3.39].

$$RRS_{bsa} = 0.25 + 0.75\left\{\frac{1}{b_0^2}\left[1-\exp\left(-2b_0^2\right)B_{bsa}\right]\right\}^{1/2} \quad [3.39]$$

Where,

$$B_{bsa} = \begin{cases} 1 + b_0^2 + b_0^4 + \dfrac{b_0^6}{2} + \dfrac{b_0^8}{4} + \dfrac{b_0^{10}}{12} & \text{for } b_0 \le 1.0 \\ \exp\left(2b_0^2\left[\dfrac{1}{\sqrt{\pi}b_0}\left(1-\dfrac{1}{16b_0^2}\right)\right]\right) & \text{for } b_0 > 1.0 \end{cases} \quad [3.40]$$

$$b_0 = 0.0001\left(\frac{2\pi b_e}{T_n}\right) \quad [3.41]$$

The effective foundation size is calculated in feet (ft) units per Eq. [3.42]

$$b_e = \sqrt{A_{base}} \le 260 \text{ ft} \quad [3.42]$$

Where A_{base} is the area of the foundation footprint measured in ft^2.

3.4.3. Ground Motion Acceleration Histories

For the NDP (NLTHA), a suite of not less than eleven ground motion pairs (one for each orthogonal horizontal direction) must be defined to determine the seismic demands according to ASCE-41 based on the guidelines in Chapter 16 of ASCE-7. For this study, the eleven pairs selected are shown in **Table 3.9**. Information regarding the event name, the year, the magnitude, M_w, the record serial number (RSN) given in the database from which they were downloaded, the distance to the fault from where they were recorded, the 5-95 Duration or significant duration of the record -corresponding to the time span of the record in which between the 5% and 95% percent of the energy measured with the Arias Intensity (I_a) is concentrated-, the soil shear wave velocity characteristic of the station location, the orthogonal components to which the peak-ground accelerations (PGA) and velocities (PGV) refer in the last two columns of data. Note from the distance column that all time-histories were recorded beyond the $10km$ limit to establish that all records are *Far-Field*. In addition, events correspond to ground-motion shaking generating $M_w 6.3$ or greater. Both characteristics were specified earlier in Section 2.3.

It is worth mentioning that ground motion records were downloaded from the PEER Ground Motion, NGA-West2 Database (Bozorgnia et al., 2014). They were selected in such a way that their response spectra resemble as much as possible to the code-prescribed counterpart to facilitate the scaling process explained further in this section.

Table 3.9. Unscaled ground motion suite data for time-history analyses.

Earthquake	Year	M_w	RSN	Dist [km]	5-95% Duration [s]	v_{so} [m/s]	Comp.	PGA [cm/s²]	PGV [cm/s]
Imperial Valley	1979	6.53	169	22.03	51.41	242.1	1	234.35	26.88
							2	326.98	35.08
Imperial Valley	1979	6.53	178	12.58	14.17	162.9	1	289.91	39.75
							2	212.56	37.56
Loma Prieta	1989	6.93	759	43.94	23.14	116.4	1	262.75	26.72
							2	285.47	44.66
Loma Prieta	1989	6.93	806	24.23	25.48	267.7	1	196.78	29.83
							2	215.02	39.32
Landers	1992	7.28	848	19.74	10.58	352.9	1	274.76	23.33
							2	402.97	46.50
Cioalinga-01	1983	6.36	338	29.48	13.54	246.1	1	272.05	35.63
							2	267.41	30.90
Kocaeli Turkey	1999	7.51	1158	15.37	11.58	281.9	1	319.13	55.11
							2	353.37	47.77
Superstition Hills	1987	6.54	721	18.20	36.66	192.1	1	369.23	34.42
							2	287.16	37.02
Superstition Hills	1987	6.54	729	23.85	36.47	179.0	1	160.33	40.75
							2	219.54	37.19
Chi-Chi Taiwan	1999	7.62	1201	14.82	29.85	278.8	1	311.91	39.38
							2	238.22	40.16
Hector Mine	1999	7.13	1787	11.62	11.62	726.0	1	258.46	20.50
							2	353.25	35.53

As explained in Section 3.4.2, even though the LTHA and NLTHA require the ground motions record histories to perform the analysis, these records must be adequately modified to accommodate a selected SHL described through a GRS. This GRS may or may not consider SSI effects obeying what was exposed in the same earlier section. In addition, GMs treated as signals should be processed and corrected if needed.

The following steps are followed in this study to process and modify the GMs before being applied to the structural model:

a. Signal processing to each of the orthogonal components of the GMs, including the steps detailed below, in that specified order.
    - First, records are trimmed, taking into account the signal's Significative Duration (5-95SD). This means that only a portion of the signal generating between 5% and 95% of the I_a is considered. Since each orthogonal component can show different 5-95SD values, the larger is taken and applied in both orthogonal signals. It shall be recalled

that during NLTHA, both orthogonal components are applied simultaneously; hence both signals should have the same length.

- A baseline correction is executed -to the acceleration histories- to avoid unwanted linear or quadratic trends in the velocity and displacement responses resulting from the integration process.
- Then, the signal is filtered with a bidirectional band-pass filter model using a second-order Butterworth filter. A forward-backward filtering procedure is performed to eliminate the phase difference.
- Finally, the signal processing ends by applying a Tukey window to smoothen the signal's beginning and end of data values. In addition, the record is zero-padded at the end of the signal to add the equivalent of $3.0s$ -or twice the fundamental period- to let the response of the building in free vibration be recorded during the analysis.

b. Ground motion records are scaled to accommodate the corresponding GRS introduced in Section 3.4.2, taking into account the following guidelines:
   - A Maximum Direction Spectrum (MDS) is constructed from the two horizontal ground motion components for each event in the GMs suite. The MDS is calculated according to guidelines by (David M. Boore, 2010).
   - Both orthogonal ground motion components are scaled with the identical correction factor, such that the average MDS of all GMS matches or exceeds the target GRS within a specific period range.
   - The period range has an upper-bound period beyond $1.5T_{max}$ and its lower-bound counterpart of $0.2T_{min}$. T_{max} and T_{min} correspond, respectively, to the first vibration mode's largest and minor periods for the two orthogonal analysis directions.
   - The average MDS of all GMs in the suite shall not fall below 90% along any of the target GRS ordinates within the period range described before.

Notice that the scaling process must be performed for each building independently every time a performance assessment is initiated because of its vibration period value T_n (or $\tilde{T}_n$ for *flexBase*-BSC). Also, since target GRS are defined for each selected SHL (i.e., for BSE-1N and BSE-2N), the correction factors applied to ground motion records differ depending on the SHL. Thus, due to the enormous amount of models to be assessed for different BSCs and SHLs, it is hard to graphically show the signal-processing and the scaling procedure for each evaluated structure. Thus, an example building is selected to demonstrate these modifications using the pair of orthogonal components from one event in the GMs suite. **Figure 3.13** and **Figure 3.14** shows the procedures described in previous paragraphs for the GM1-Imperial Valley, 1979 (RSN 169) for seismic hazard levels BSE-1N and BSE-2N, respectively.

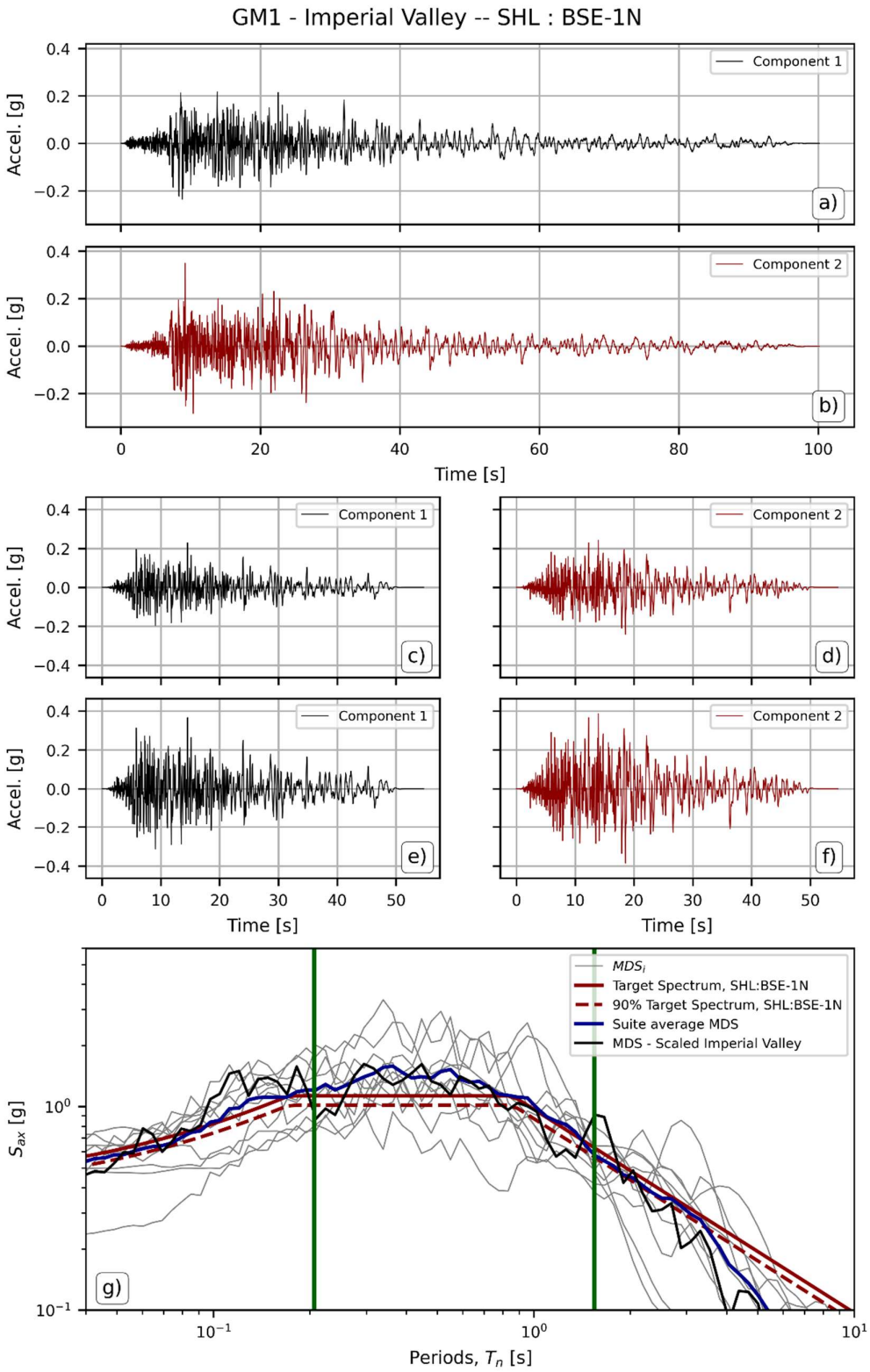

Figure 3.13. GM1-Imperial Valley processing and scaling for BSE-1N seismic hazard level. Shown are a) the original signal for component 1; b) the original signal for component 2; c) the trimmed, filtered, and zero-padded signal for component 1; d) the trimmed, filtered, and zero-padded signal for component 2; e) the scaled signal for component 1; f) the scaled signal for component 1; and g) plot depicting the target 3%-damped GRS for SHL=BSE-1N (solid red) along with its 90% representation (dashed red), the MDS obtained from both scaled components of the event (solid black), MDS for all other events in the suite (MDSi – solid gray), and the average MDS for all scaled events in the GMs suite.

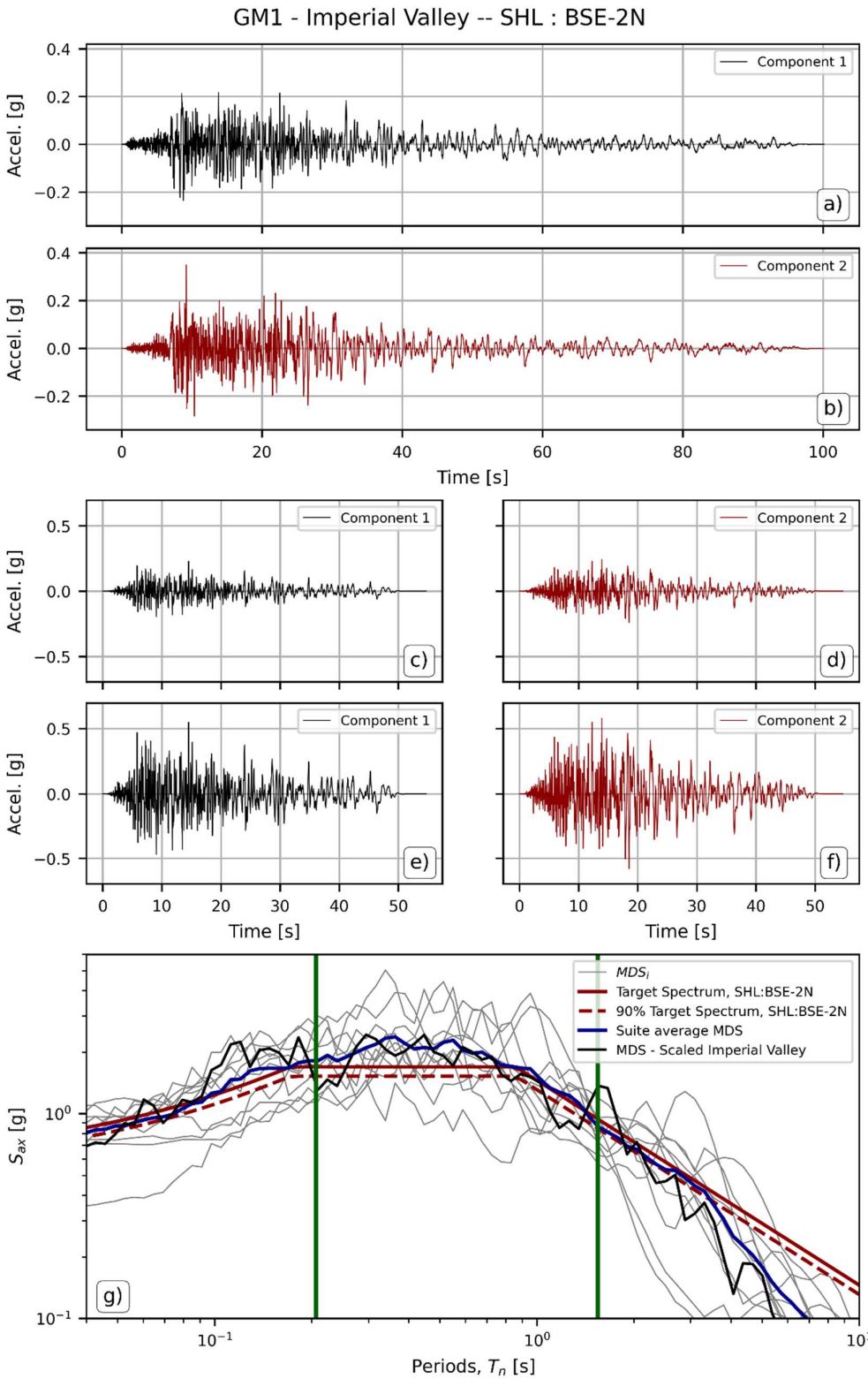

Figure 3.14. GM1-Imperial Valley processing and scaling for BSE-2N seismic hazard level. Shown are a) the original signal for component 1; b) the original signal for component 2; c) the trimmed, filtered, and zero-padded signal for component 1; d) the trimmed, filtered, and zero-padded signal for component 2; e) the scaled signal for component 1; f) the scaled signal for component 1; and g) plot depicting the target 3%-damped GRS for SHL=BSE-2N (solid red) along with its 90% representation (dashed red), the MDS obtained from both scaled components of the event (solid black), MDS for all other events in the suite (MDSi – solid gray), and the average MDS for all scaled events in the GMs suite (solid blue).

Let us consider **Figure 3.13** and **Figure 3.14**. The explanation in the following lines applies to both figures since the only difference lies in the SHL selected for the scaling process. Graphics **a)** and **b)** depict the original unscaled, unprocessed records for components 1 and 2, respectively. Graphics **c)** and **d)**, on the other hand, correspond to the same components once they are signal-processed (trimmed, filtered, and zero-padded at the end of the record). Notice how the length of the records has shortened relative to the signals in graphics **a)** and **b)** as a result of the 5-95SD trimming consideration. The scaling process is executed as described earlier, and each component is plotted in graphics **e)** and **f),** respectively. Notice how the amplitude of the signal is increased for these records. According to ASCE-41 and ASCE-7, the same correction factor should apply to both components; thus, the scaling process requires an amplification factor of 1.60 to accomplish scaling conditions. Finally, in graphic **g),** the target 3%-damped GRS for SHL=BSE-XN (solid red) along with its 90% representation (dashed red), the MDS obtained from both scaled components of the event (solid black), MDS for all other events in the suite (MDSi – solid gray), and the average MDS for all scaled events in the GMs suite (solid blue) are presented. Also, the two lower- and upper-bound period range limits are shown in solid green lines; $T_{min} = 0.21s$ and $T_{max} = 1.56s$ for the example building. It is worth noting how the mean MDS of the suite lies above the 90% representation of the target spectrum within the period range limits even though the ordinates of the independent MDS_i show indistinctive ordinates.

The demands presented so far are used to execute the performance assessment of buildings in the database, as described in **Figure 3.1**, and following the code-prescriptions detailed in earlier sections of the current chapter. The following last sections present, in a summarized fashion, the results obtained from the assessment, a discussion about the essential findings, and a brief introduction of how to take advantage of the outcomes.

3.5. Review and discussion of overall results

Even though the number of buildings in the database -1,458 for both *convDs* and *SSIDs* DTs- would not seem too large, the amount of analyses performed reaches 23,328, as explained in Section 3.1 (refer to **Figure 3.1**). Since it is not easy to evaluate each structure independently to get a better insight into the performance assessment outcomes, the results are summarized, taking into account a generalized perspective of what is expected in terms of performance. In this regard, three aspects are considered as indicators of the overall performance of buildings in the database.

First, the percentage of buildings in the database that resulted in an unfavorable performance is examined. It is important to recall that the $DCR_{(ac)}$ detailed in Eq. [3.12] represents the ratio of the demand to the capacity of a determined element action in the structure; this ratio defines whether a structure achieves the selected SPL (if $DCR_{(ac)} < 1.0$) or doesn't (if $DCR_{(ac)} > 1.0$).

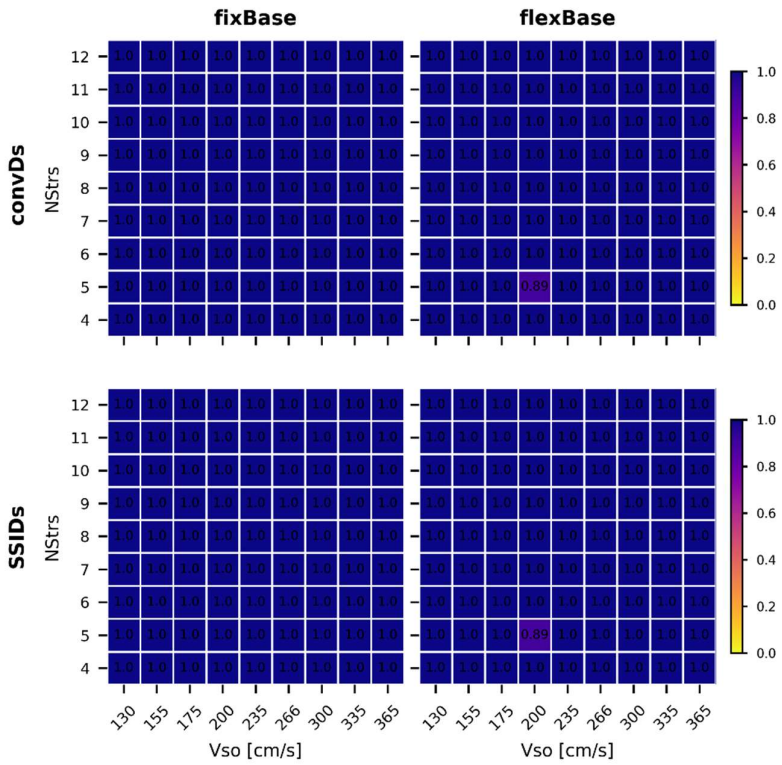

Figure 3.15. Percentages of buildings in the database resulting in an unfavorable performance objective achievement through the MRSA procedure. SHL: BSE-1N / SPL: LS.

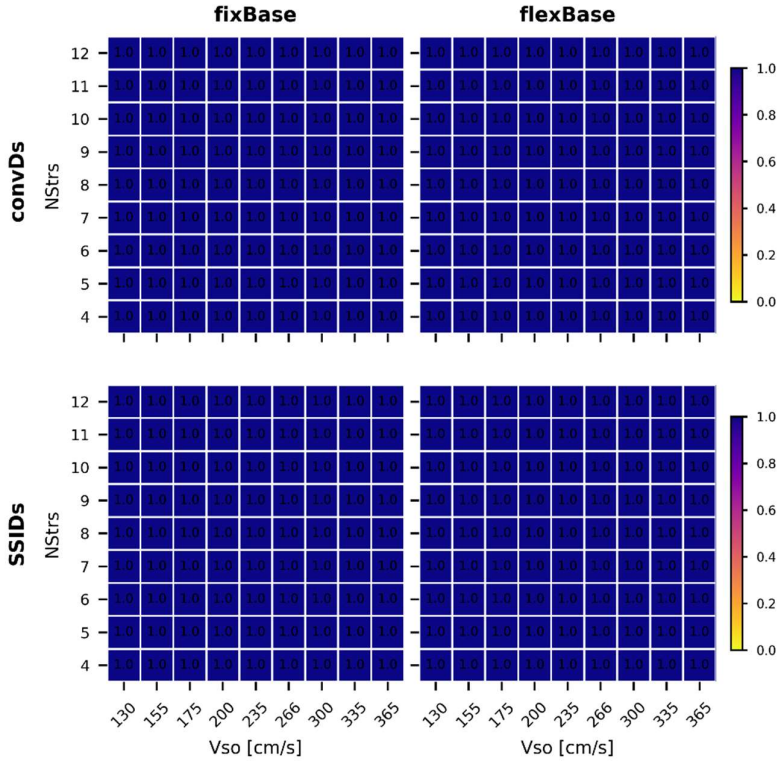

Figure 3.16. Percentages of buildings in the database resulting in an unfavorable performance objective achievement through the LTHA procedure. SHL: BSE-1N / SPL: LS.

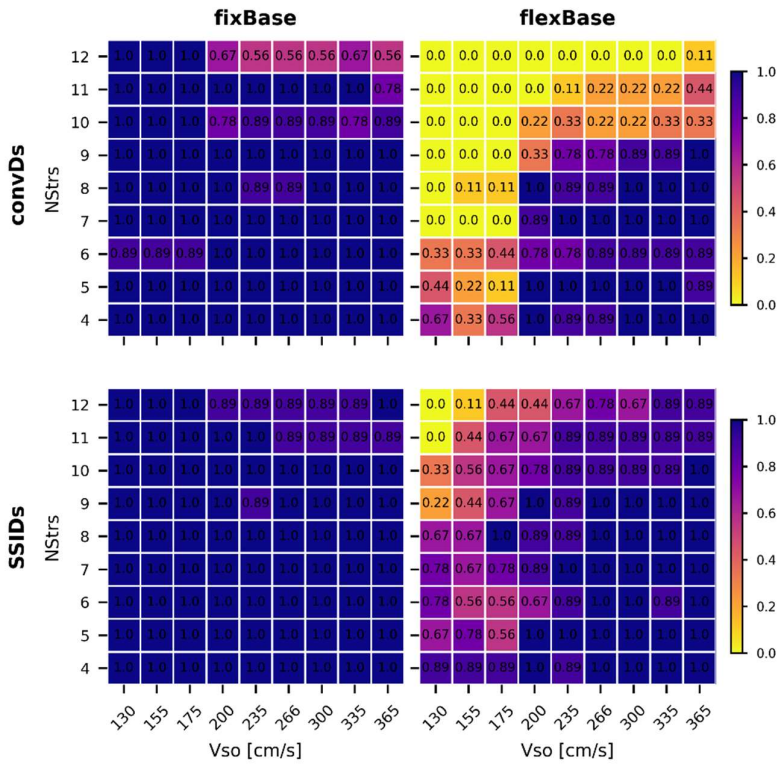

Figure 3.17. Percentages of buildings in the database resulting in an unfavorable performance objective achievement through the NSP procedure. SHL: BSE-1N / SPL: LS.

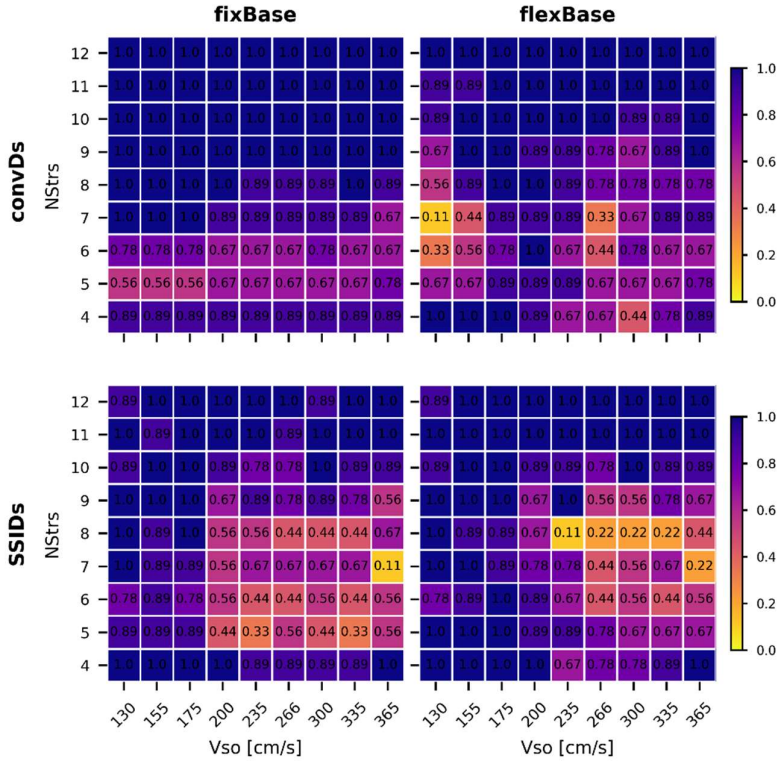

Figure 3.18. Percentages of buildings in the database resulting in an unfavorable performance objective achievement through the NLTHA procedure. SHL: BSE-1N / SPL: LS.

For this first evaluation, please refer to **Figure 3.15** through **Figure 3.18**, where annotated heatmaps show the percentage of buildings not achieving the Life Safety SPL, i.e., structures subjected to the BSE-1N seismic hazard level. Each figure depicts a heatmap for every DT-BSC combination considered during the performance assessment. The first row in the figures describes the outcomes from analyses executed on *convDs*-designed buildings with both *fixBase*- (left column) and *flexBase*-BSC (right column) assessment models. Notice that the heatmaps reflect the performance results in the same $h_n - v_{so}$ space introduced in Section 2.2 used to define geometric and mechanical characteristics of the SSS before the design process.

Responses of the LDPs are shown in **Figure 3.15** and **Figure 3.16**, corresponding to the MRSA and LDTHA procedures. Employing these APs, it results clear that no DT-BSC combination of buildings in the $h_n - v_{so}$ space show an acceptable performance according to ASCE-41 prescriptions. In fact, it can be noticed that 100% of the evaluated buildings with this AP fail to get a $DCR_{(ac)}$ values below 1.0. It is well-known that linear procedures used during design or analysis tend to give conservative estimates of buildings' performance, explaining the performance outcomes shown in these figures.

On the other hand, the performance assessment responses using the nonlinear analysis procedures are shown in **Figure 3.17** and **Figure 3.18**. Let's first consider the responses corresponding to the *convDs-fixBase* combination in the upper-left graphic in both figures, which would be viewed as a traditional design and analysis condition. It can be noted that for the NSP, there are some buildings with more than 10-story height and located on SC-D with acceptable performance since a reduced percentage (between 56% and 67%) is deemed non-acceptable. Some 6-story buildings also receive a good performance for SC-E soils but are relatively few (11%). However, the performance results are quite different for the same *convDs-fixBase* combination in the NLTHA procedure. There is a notorious range of building heights between 4-story and 6-story buildings for which the SPL is achieved in all soil site class conditions, contradicting the trend shown by the NSP. The same behavior in the responses obtained from NSP and NLTHA procedures can be appreciated in other DT-BSC combinations. These other combinations, though, include either in the design or in the assessment process, SSI effects. For *flexBase*-BSC, regardless of the design type, NSP procedures show even a 100% success in achieving the LS-SPL for 7-story buildings and higher for SC-E soil types and all SCs when buildings are as tall as 12-story. The opposite trend is evidenced in the same DT-BSC in NLTHA procedure results, where mid-height buildings ranging from 5 to 9 stories are more likely to achieve the LS-SPL for any SC condition than taller buildings. It would seem odd to obtain these different trends in the outcomes from two nonlinear analysis procedures; however, it will be explained later in Chapter 5 that this becomes evident once it is realized that the NSP is based on an SDOF behavior rather than in the actual MDOF one in which higher modes of vibration can be considered. Such is the case of the NLTHA.

Maybe the most relevant DT-BSC combination to be evaluated are the ones related to the *SSIDs*-DT for the NLTHA procedure. Notice how the *fixBase*-BSC buildings clearly show a range between 5 and 9 stories, and for v_{so} values beyond $200 m/s$, where it is more likely to achieve the desired SPL. On the contrary, according to NSP results, there is almost no chance of obtaining buildings with acceptable performance. For the *SSIDs-flexBase* combination, on the other hand, a similar trend to the *SSIDs-fixBase* is seen. This time, the building height range tightens to 6 to 8 stories and v_{so} beyond $235 m/s$ to find buildings likely to achieve the expected SPL using the NLTHA procedure.

It is worth recalling that the responses shown in previous figures are specific to buildings subjected to the BSE-1N seismic hazard level; hence the achievement of the LS-SPL was evaluated. Similar figures for the evaluation at CP-SPL are introduced in **Appendix D.** From those figures, the same trends are noticeable regarding the differences in the performance indicators obtained from each AP. Employing linear analysis procedures, the results still show that no building would be capable of achieving the CP-SPL. However, for the cases where the performance determined through the NSP and NLTHA is even more likely to reach the CP-SPL successfully.

The difference in the performance results obtained based on the APs shown in previous figures could be better understood based on the second aspect that treats this section and relates to what **Figure 3.19** and **Figure 3.20** demonstrate.

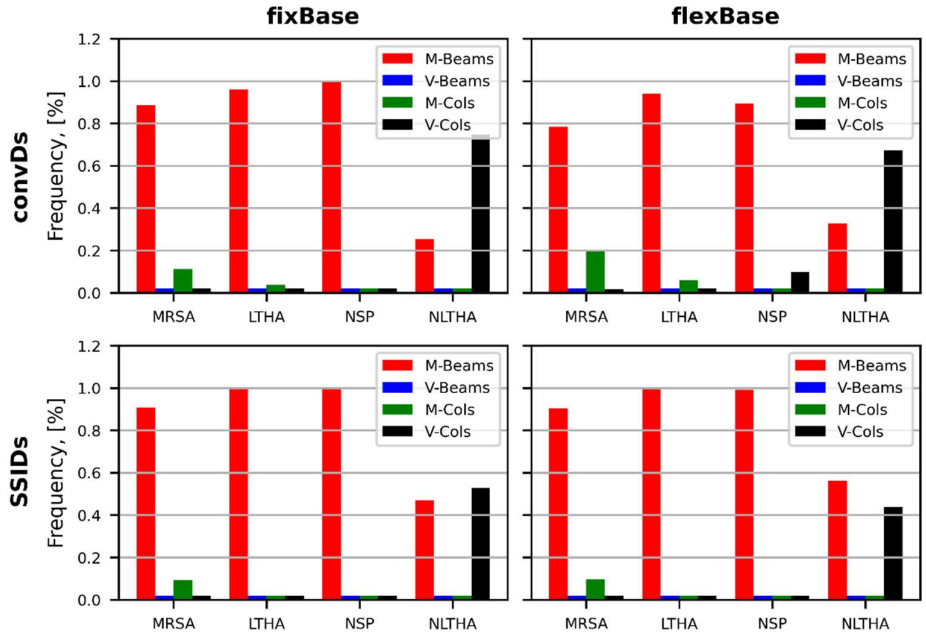

Figure 3.19. Barplots showing the action that most frequently triggers the unfavorable $DCR_{(ac)}$ at each APs for SHL: BSE-1N. All graphics in the first row corresponds to *convDs*-DT; the second row to its *SSIDs* counterpart. Al graphics in the first column relates to *fixBase*-BSC; the second column to its *flexBase* counterpart.

The specific $DCR_{(ac)}$ defining whether a structure has surpassed the 1.0-value limit is the maximum DCR among all the calculated for every action (V, M, or plastic rotations) at each element within the

system. In this regard, the DCR triggering the $DCR_{(ac)}$ could be related to any action in any element indistinctively. To clarify this statement, **Figure 3.19** shows frequency bar plots again for DT-BSC combinations and each AP used in the assessment process for buildings subjected to the BSE-1N SPL. Notice how regardless of the DT-BSC, the most frequent action triggering $DCR_{(ac)}$ are related to either moment forces in linear procedures (MRSA and LTHA) or plastic rotations (NSP) beams and beams only. On the other hand, looking at the frequency bars of the NLTHA procedure, it can be noted that the most frequent action is related to the shear in columns for any of the *convDs-BSC* combinations but in the *SSIDs-flexBase* combination. In the latter, even though plastic rotation in beams is the more frequent trigger, the shear actions in columns are not negligible. From the outcomes expressed in terms of actions as presented in these figures, it is clear that depending on the AP, the behavior of the building during analysis reflects a different nature. While linear procedures or those based on an SDOF system (MRSA, LTHA, and NSP) demonstrate a flexural behavior of the buildings, the NLTHA demonstrates a more accurate actual behavior in the same structures, given the importance of shear demands in the $DCR_{(ac)}$ evaluation under BSE-1N SHL, which is equivalent to the design earthquake level. As emphasized before, this helps understand the difference in performance responses depicted in **Figure 3.15** through **Figure 3.18**. Also, later in Chapter 5, it will be demonstrated how these facts have been influencing the design of buildings with SSI effects considerations.

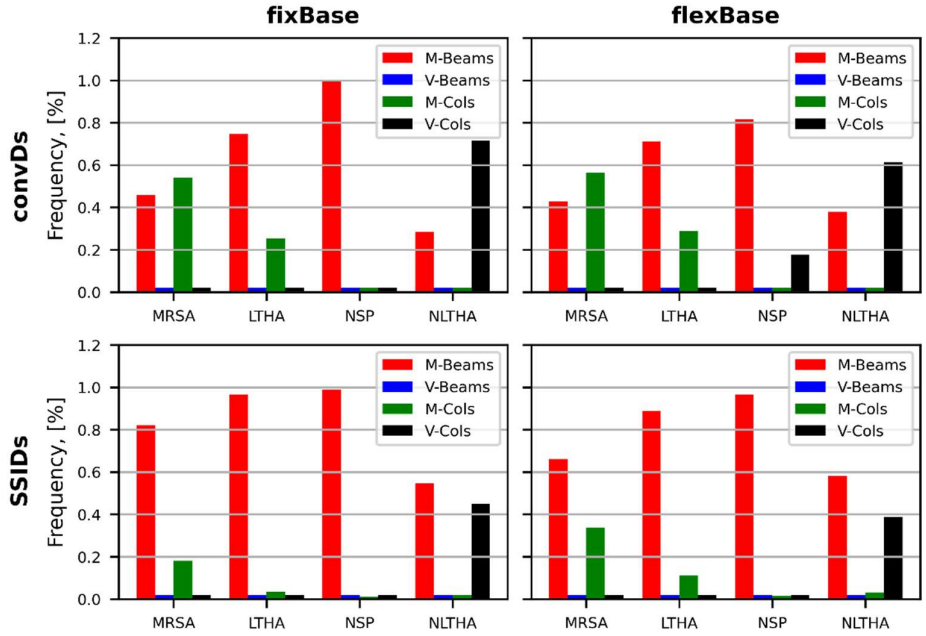

Figure 3.20. Barplots showing the action that most frequently triggers the unfavorable $DCR_{(ac)}$ at each APs for SHL: BSE-2N. All graphics in the first row corresponds to *convDs*-DT; the second row to its *SSIDs* counterpart. Al graphics in the first column relates to *fixBase*-BSC; the second column to its *flexBase* counterpart.

The same analysis can be made in **Figure 3.20** for the evaluation of CP-SPL under the action of BSE-2N SPL. The same trend regarding flexure actions in MRSA, LTHA, and NSP procedures is noticed,

except for the flexure of columns that notoriously increases for the linear procedures in the *convDs-BSC* combinations. Still, this behavior contradicts what the NLTHA for the same combination demonstrates.

The third and last aspect worthy of evaluation from the performance assessment outcomes is related to the interstory drifts. **Figure 3.21** and **Figure 3.22** present, through frequency bars, the percentage of buildings showing their maximum drift ratio in either the low-, mid-, or high-third of the relative buildings' height for each AP and for BSE-1N and BSE-2N SHL, respectively.

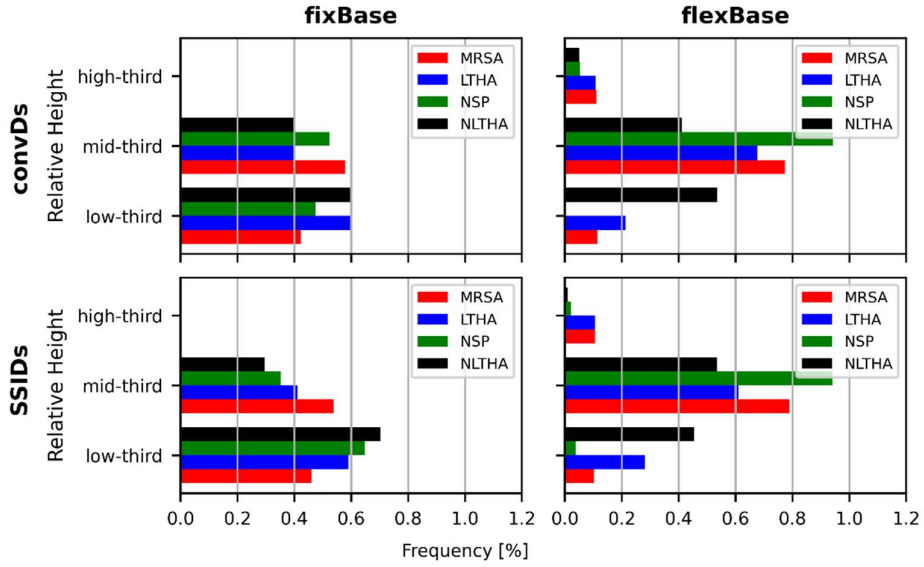

Figure 3.21. Barplots showing the frequency [%] in which the maximum interstory drift affects a specific portion of the buildings' relative height depending on the used AP, with SHL: BSE-1N. All graphics in the first row corresponds to *convDs*-DT; the second row to its *SSIDs* counterpart. Al graphics in the first column relates to *fixBase*-BSC; the second column to its *flexBase* counterpart.

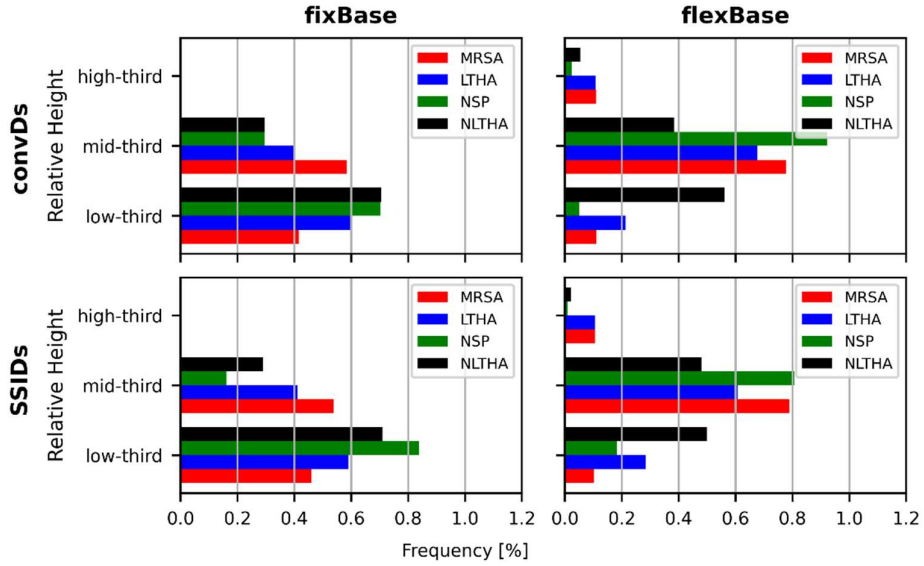

Figure 3.22. Barplots showing the frequency [%] in which the maximum interstory drift affects a specific portion of the buildings' relative height depending on the used AP, with SHL: BSE-2N. All graphics in the first row corresponds to *convDs*-DT; the second row to its *SSIDs* counterpart. Al graphics in the first column relates to *fixBase*-BSC; the second column to its *flexBase* counterpart.

After noticing that the NLTHA shows a more accurate response relative to the actual behavior of buildings compared to the other APs, these results are taken as reference points. It is shown in both figures (both SHLs) and for every DT-BSC combination that the low-third height of the building is the zone where the maximum interstory drift is found more frequently. The responses obtained using MRSA at both SHLs show that the mid-third height is the most commonly affected relative height for any DT-BSC combination, unlike any result in NLTHA. NSP and LTHA, on the other hand, are more likely to reflect similar results as those in NLTHA, but only in some specific cases. Let us recall that, specifically for the NSP, a modification factor related to the MDOF's actual behavior of the system was introduced through C_o-factor in Eq. [3.9]. Nevertheless, this factor is calculated employing only the first vibration mode ordinate and participation factors which are incapable of including the participation of higher modes in the response as the NLTHA is.

After evaluating these three aspects of the performance assessment results, a few remarks can be clearly stated. In general terms, the NLTHA procedure seems to be the only AP that can reflect the most accurate response relative to the actual behavior of structures. Thus, executing the assessment using any other AP could deliver responses that lead to unnecessary retrofit actions in an evaluated structure or improve the design of a new one. Finally, even though SSI effects are considered during the design process, neither the *fixBase* nor the *flexBase* models used during the assessment show achievement of the LS- or the CP-SPL for all buildings in the database.

To tackle these issues, Chapter 4 presents estimation models to translate the performance indicators obtained with MRSA, LTHA, and NSP procedures to those obtained through the NLTHA, which are considered to be the closest to the actual behavior of buildings. Then, Chapter 5 presents some recommendations derived from this study and the estimation of the actual response expected at the design SHL to modify design base shear demands and expected nonlinear displacement ratios used traditionally in the design process.

3.6. An introduction to Ψ-ratios

Since the actual response of buildings to earthquakes is typically nonlinear, it may be evident that nonlinear analysis procedures (applied to nonlinear models) should result in better estimates of the seismic performance of buildings in comparison to the use of linear procedures. It has become evident from previous sections that acceptance criteria established for the performance assessment employing linear APs consider conservative estimates of the building response, hence the performance results for an evaluated SHL. In this regard, it may be reasonable to think of performing nonlinear procedures only, when evaluating a performance assessment if, say, a reduction in retrofit measures is desired at the end of the day. Nevertheless, linear procedures are more attractive to most professionals due to the ease of their application -especially regarding the modeling process- and because they are less time-consuming than nonlinear procedures. Aiming to facilitate this task and

being aware of the differences encountered between the responses of the NLTHA and the rest of the APs, a novel parameter is proposed and evaluated in the form of Eq. [3.43].

$$\Psi = \frac{DCR_{(ac)}{}^{DT:flexBase}_{NDP:SHL}}{DCR_{(ac)}{}^{DT:BSC}_{AP:SHL}} \qquad [3.43]$$

The numerator in the equation above is the performance indicator for a specific seismic hazard level (SHL) obtained from the NDP analysis procedure of a building designed with any of the *convDs* or *SSIDs* design types (DT), modeled with flexible-base support conditions. The denominator, on the other hand, is the performance indicator for the same SHL obtained using any other analysis procedure (AP) and base support condition (BSC) but the same design type (DT). Thus, this Ψ-factor is in charge of translating the performance indicator determined using any AP different from the NLTHA to that of this later AP. To do this, the following considerations are followed:

a) It is assumed that the actual performance of buildings is obtained through the NLTHA procedure since it can take into account more complex modal and mechanical natures in nonlinear models than the other APs.
b) The assumed actual performance for any building is that of the *flexBase*-BSC model. It has been recognized that SSI effects are always present; hence, this BSC is considered here as the reference point of an actual response condition.
c) DTs are treated as fixed parameters within the Ψ-factor, i.e., if *convDs*-designed buildings' performance evaluated with any AP is to be translated to the performance obtained with the NLTHA, it will be translated into *convDs*-DT performance only. The same considerations are used if *SSIDs*-DT is employed. *SSIDs*-DT performance translates into *SSIDs*-DT performance.
d) As for the DTs, SHLs are also considered fixed parameters within the Ψ-factor.
e) BSCs are considered variable parameters within the Ψ-factor. It means that the $DCR_{(ac)}$ obtained with any AP and considering any BSC (*fixBase* or *flexBase*) can be translated into a $DCR_{(ac)}$ obtained with the NLTHA, with *flexBase*-BSC.

A more in-depth insight into the Ψ-factor is presented in Chapter 4, along with a complete study of its dependencies on the dynamical parameters of the SSS. Also, prediction models using different methods are presented with a final discussion of the uses for this novel factor.

4. Estimation of Structural Performance

4.1. Overview

By the end of Chapter 3, a brief introduction to Ψ-factors was presented. It was established that the purpose of these factors is to translate the performance indicators $DCR_{(ac)}$, obtained from the assessment using any of the Modal Response Spectrum Analysis (MRSA), Linear Time-History Analysis (LTHA), or Nonlinear Static Procedure (NSP) analysis procedures (APs), to that of the "actual" performance determined by employing the NLTHA as an NDP. Some considerations apply, though, regarding the design type (DT) and Structural Performance Level (SHL) fixity within the starting-DCR_{ac} – Ψ-factor – target-$DCR_{(ac)}$ triplet, while APs are related to the starting-$DCR_{(ac)}$ and gives the name to the corresponding Ψ-factor. **Figure 4.1** shows the relationship between the parameters in the triplet mentioned earlier and helps clarify the Ψ-factor conceptual purpose.

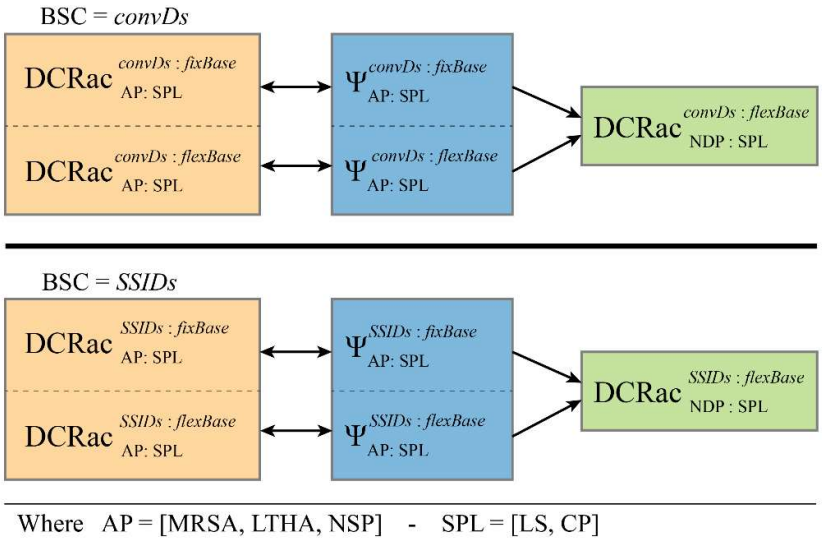

Figure 4.1. Relationship between the $DCR_{(ac)}{}^{DT:BSC}_{AP:SPL}$ values and the target-$DCR_{(ac)}{}^{DT:flex}_{NLTHA:SPL}$ through Ψ-factors.

Notice in **Figure 4.1** that the term SHL related to the Seismic Hazard Level shown in the expressions in Eq. [3.43] has been replaced by the Structural Performance Level, SPL. Both terms are related to the performance objective that has to be evaluated so that these terms can be treated indistinctively. Actually, throughout this chapter, the term SPL is preferred instead of SHL since it is related to the level of structural performance wanted to be achieved. Also, one can observe there are a total of 24 Ψ-factors leading to the translation of any AP-DT-BSC-SPL combination $DCR_{(ac)}$ into their corresponding target demand-capacity ratio for the specific NLTHA-DT-*flexBase*-SPL. As the result of this translation process, 6 target-$DCR_{(ac)}$ are obtained for the combination of 2 DTs and 2 SPLs. As explained in the previous chapter, the purpose is to get "actual" performance measures when buildings have been designed with either *convDs* or *SSIDs* considerations for one of the two structural

performance levels established in the performance objective, namely, the Life Safety (LS) and the Collapse Prevention (CP) SPLs.

To get an initial insight into the Ψ-factors' behavior with respect to their corresponding starting- and target-$DCR_{(a)}$ indicators, **Figure 4.2** through **Figure 4.7**, are presented below. These figures show scatter plots of starting-$DCR_{(ac)}$ (x-axis) against their corresponding Ψ-factors (y-axis), color-scaled according to the appropriate target-$DCR_{(ac)}$ expressed through the color-bar scale at the top-right corner of each plot. Scatter plots are identified at every figure for different DT-BSC combinations, i.e., graphics a) and b) correspond to *convDs-fixBase* and *convDs-flexBase* combinations. Graphics c) and d), on the other hand, are focused on *SSIDs-fixBase* and *SSIDs-flexBase* combinations. In addition, the figures present the behavior mentioned above for the MRSA, LTHA, and NSP APs regarding the LS and CP SPLs.

Let us first observe **Figure 4.2** and **Figure 4.3** related to the MRSA AP for the LS and CP SPLs, respectively. It is worth noting that all $\Psi_{MRSA:LS}$-factors presented in these figures have values lesser than 1.0, indicating that the performance measured employing this AP tends to be underestimated compared to the one measured with the NLTHA. This fact was previously evidentiated from the performance responses obtained from the assessment carried out in Chapter 3 and agrees with what was shown in **Figure 3.15** and **Figure 3.18**.

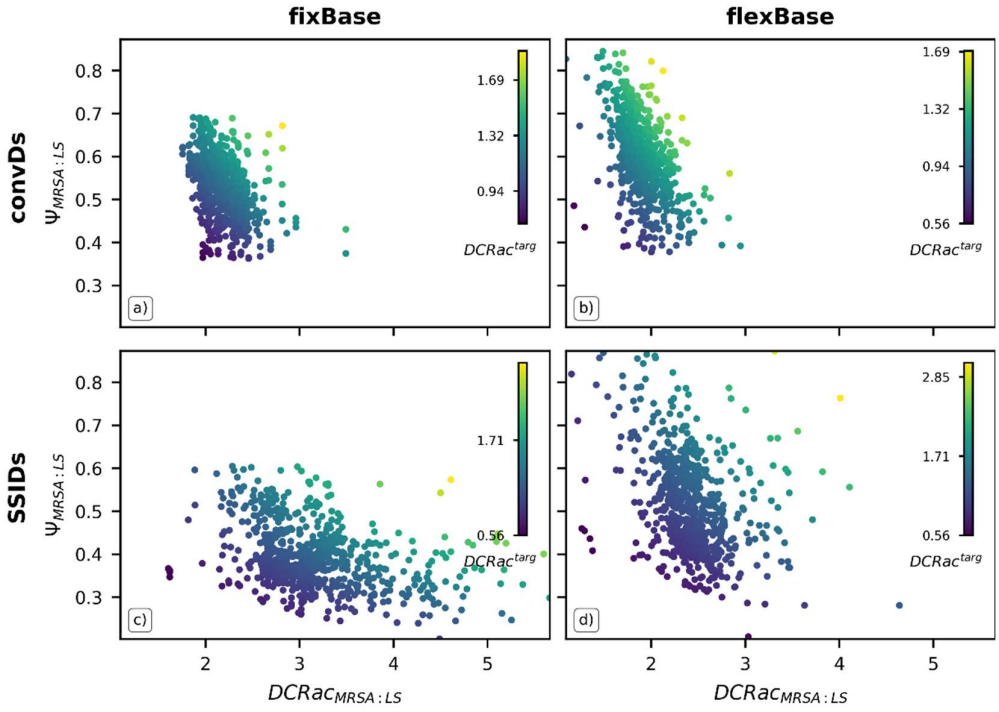

Figure 4.2. Noticeable trends between $DCR_{(ac)}{}^{DT:BSC}_{AP:SPL}$ and Ψ-factors for the LS-SPL when the MRSA is used as AP. a) and b) relationships for *convDs*-DT with *fixBase* and *flexBase* BSCs, respectively. c) and d) relationships for *SSIDs*-DT with *fixBase* and *flexBase* BSCs, respectively.

Comparing the graphics related to the *convDs* -a) and b)- to those of its *SSIDs* counterpart -c) and d)- in the same **Figure 4.2**, it is notorious how the starting-$DCR_{(ac)}$ values are higher for the later DT. However, a greater dispersion in the data can be observed in the scatter plots, and some apparent outliers may be identified, especially in the case of the *SSIDs-flexBase* combination of **Figure 4.2d**. Later in this Chapter, it will be explained how data is processed to avoid misinterpretations of their trends and to be suitable for estimation model generation. In the *convDs* for both *fixBase* and *flexBase* BSCs, it is evident how the Ψ-factors reveal a more significant gap between the starting- and target-$DCR_{(ac)}$ indicator values; as the former increases the farther it gets to the actual measure of the performance. This may imply that the evaluation of the performance using the MRSA AP is less accurate when a higher $DCR_{(ac)}$ is obtaiend. For the *SSIDs-fixBase* combination of **Figure 4.2d** does not show this trend in such a clear way compared to the other DT-BSC combinations but is still slightly present. Such behavior can also be noticed for the rest of the APs (LTHA and NSP) in upcoming figures reflecting a generalized issue within the responses.

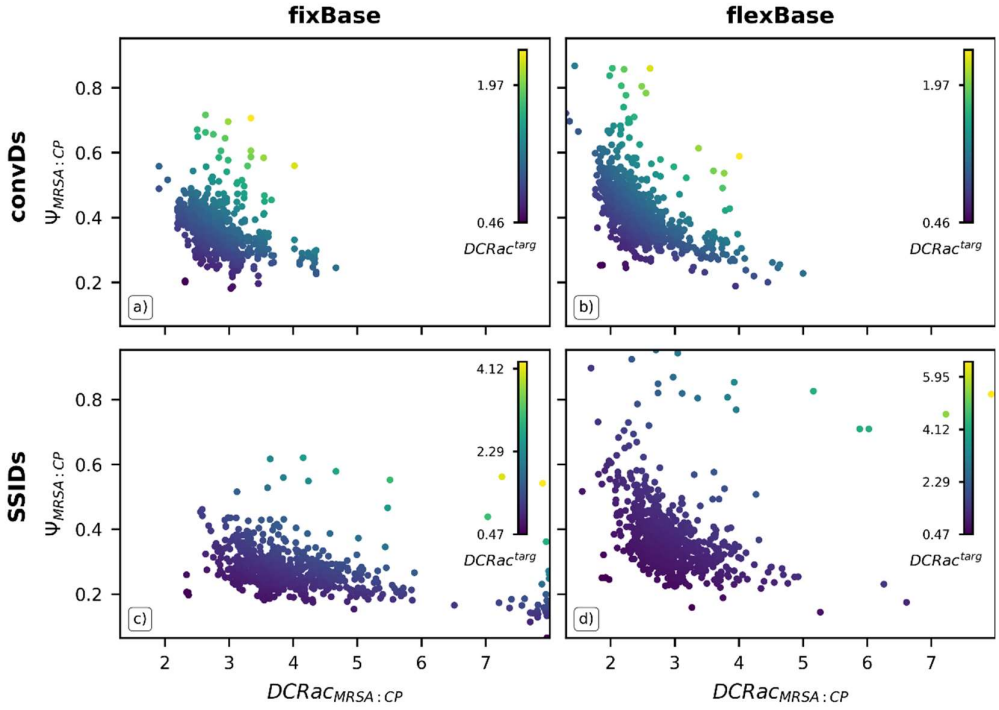

Figure 4.3. Noticeable trends between $DCR_{(ac)}{}^{DT:BSC}_{AP:SPL}$ and Ψ-factors for the CP-SPL when the MRSA is used as AP. a) and b) relationships for *convDs*-DT with *fixBase* and *flexBase* BSCs, respectively. c) and d) relationships for *SSIDs*-DT with *fixBase* and *flexBase* BSCs, respectively.

The same conclusions can be driven by observing the graphics in Figure 4.3 for the CP-SPL. However, in this latter case, the dispersion is less pronounced even though a few data can also be considered outliers, especially for the *SSIDs-flexBase* combination.

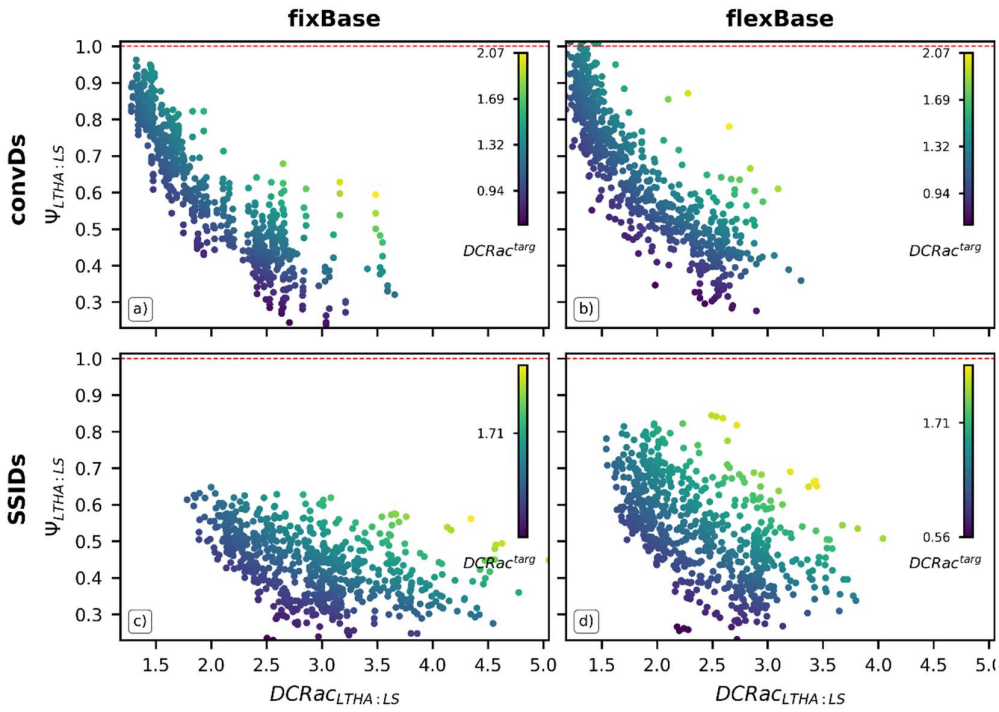

Figure 4.4. Noticeable trends between $DCR_{(ac)}{}^{DT:BSC}_{AP:SPL}$ and Ψ-factors for the LS-SPL when the LTHA is used as AP. a) and b) relationships for *convDs*-DT with *fixBase* and *flexBase* BSCs, respectively. c) and d) relationships for *SSIDs*-DT with *fixBase* and *flexBase* BSCs, respectively.

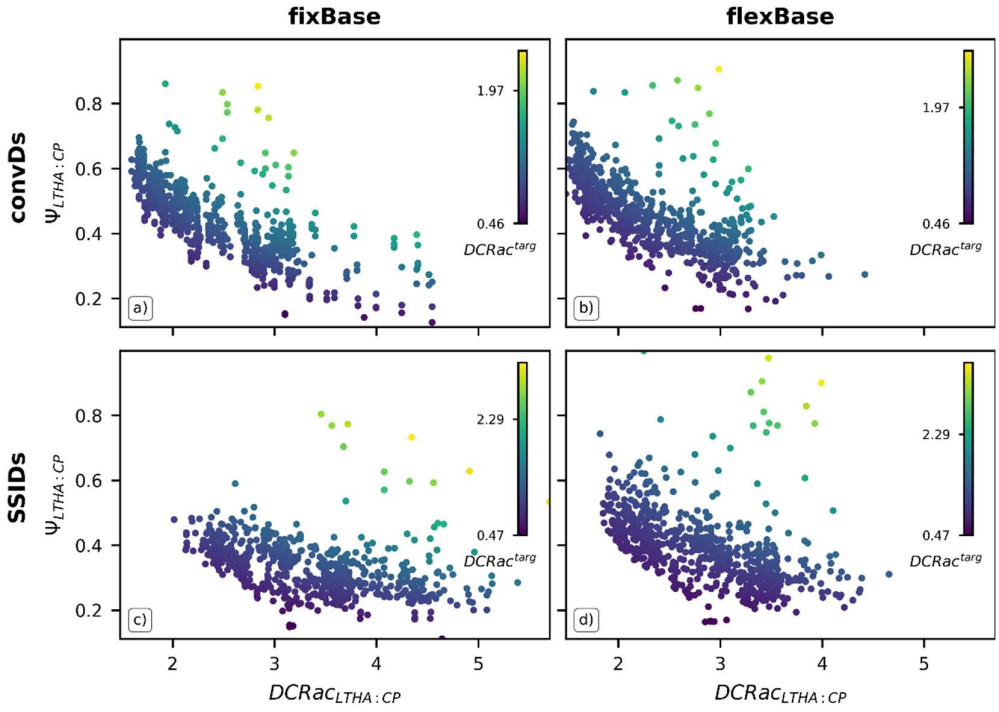

Figure 4.5. Noticeable trends between $DCR_{(ac)}{}^{DT:BSC}_{AP:SPL}$ and Ψ-factors for the CP-SPL when the LTHA is used as AP. a) and b) relationships for *convDs*-DT with *fixBase* and *flexBase* BSCs, respectively. c) and d) relationships for *SSIDs*-DT with *fixBase* and *flexBase* BSCs, respectively.

Regarding the LTHA procedure, **Figure 4.4** and **Figure 4.5** show that, in general, the underestimation of the performance measured with this AP is again present. The target-$DCR_{(ac)}$ tends to be smaller

than that of the starting-$DCR_{(ac)}$ obtained with this AP indicating that the evaluated structures actually perform better in the more realistic modeling scenario. This time, however, it is worth mentioning that there is a more noticeable trend explaining the relationship between the starting- and target-$DCR_{(ac)}$ values that could be represented by a linear oa higher-order function if one would want to express the Ψ-factor values in terms of starting-$DCR_{(ac)}$ indicators.

Figure 4.6 and **Figure 4.7** show the same LS and CP-SPL relationships but for the NSP AP. Notice that for this nonlinear analysis procedure, the performance measures lead to Ψ-factor values that are both above and below 1.0. It indicates that there are some evaluated structures whose starting-$DCR_{(ac)}$ are also overestimated, contrasting what was found through the figures related to linear analysis procedures. There is also noticeable a more evident trend in the behavior of the Ψ-factors due to the starting-$DCR_{(ac)}$ variation in contrast to the previous APs. Particualry for the *flexBase* BSC models used during the performance assessment of any DT-designed structure, it is clear that when small starting-$DCR_{(ac)}$ values are obtained, they reflect an overestimation of the performance in comparison to the target-$DCR_{(ac)}$. Nevertheless, the performance indicators tend to adopt values closer to the actual performance as the former increases up to a point where both starting- and target- $DCR_{(ac)}$ equals. Notice that for any DT-BSC-SPL combination, the range of starting-$DCR_{(ac)}$ values for which it eaquls to the target one, lays between 1.0 and 1.5.

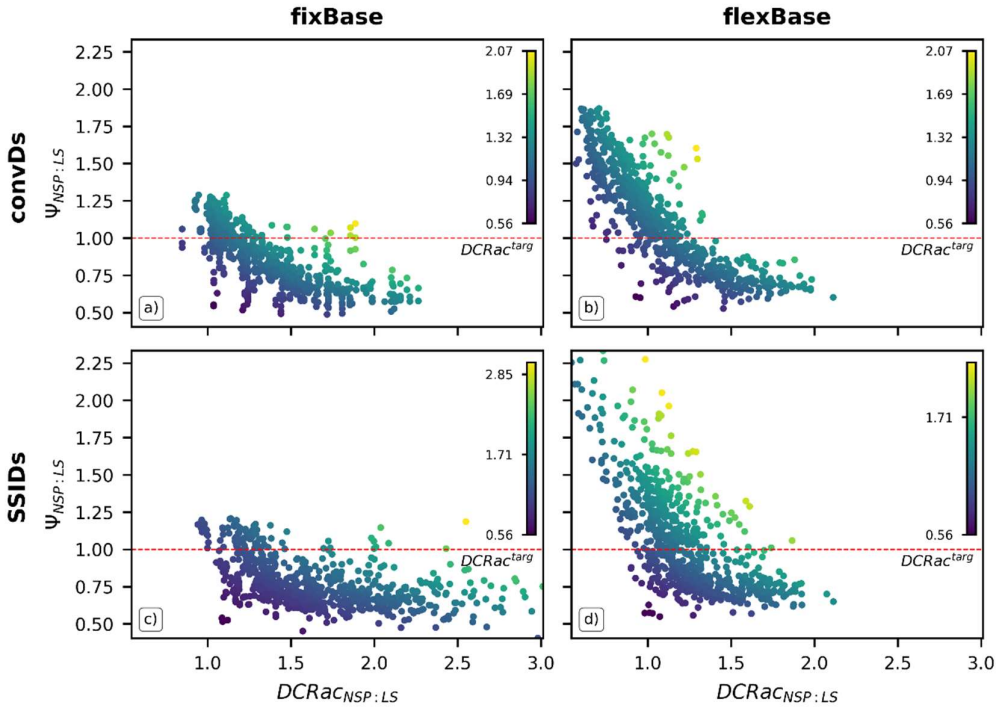

Figure 4.6. Noticeable trends between $DCR_{(ac)}{}^{DT:BSC}_{AP:SPL}$ and Ψ-factors for the LS-SPL when the NSP is used as AP. a) and b) relationships for *convDs*-DT with *fixBase* and *flexBase* BSCs, respectively. c) and d) relationships for *SSIDs*-DT with *fixBase* and *flexBase* BSCs, respectively.

By examining **Figure 4.6** and **Figure 4.7**, it is also worth noting that regardless of the SPL being evaluated and neglecting some data that can be further treated as outliers, the values of Ψ-factor consistently indicate an overestimation of the performance of up to a 75% above the actual performance measure and an underestimation of no more than 50%.

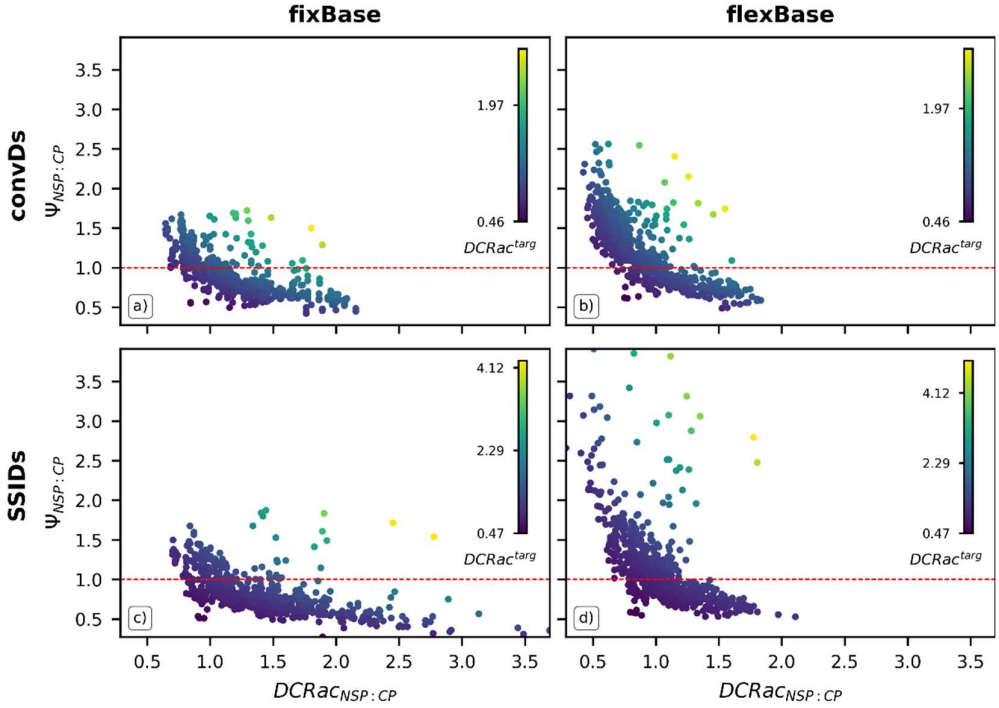

Figure 4.7. Noticeable trends between $DCR_{(ac)}{}^{DT:BSC}_{AP:SPL}$ and Ψ-factors for the CP-SPL when the NSP is used as AP. a) and b) relationships for *convDs*-DT with *fixBase* and *flexBase* BSCs, respectively. c) and d) relationships for *SSIDs*-DT with *fixBase* and *flexBase* BSCs, respectively.

The figures analyzed above demonstrate that Ψ-factors depend on the variability of the starting-$DCR_{(ac)}$ values and, especially for the NSP, they showed that there is an evident trend in the $DCR_{(ac)}$-Ψ relationship. Seeking to fulfill the purpose of determining Ψ-factor values that let us translate any starting- $DCR_{(ac)}$ to the actual target- $DCR_{(ac)}$, it would be possible to generate straightforward mathematical expressions derived from a regression analysis employing the responses obtained from the NSP AP. Even though these expressions, or estimation models, would explain the relationship mentioned above, they would depend on the starting-$DCR_{(ac)}$ values only. Essential characteristics of the relationship that additional parameters could better explain may be mistakenly neglected, thus avoiding obtaining an accurate regression model.

In this regard, the following section (Section 4.2) introduces selected additional parameters that are believed to generate an improved estimation model for determining Ψ-factors. Later in Section 4.3, a Classical Linear Regression analysis is executed, employing the selected parameters to generate estimation models in the form of equations that help calculate Ψ-factors. Section 4.4 other cutting-edge regression techniques for big data are introduced in this study and used in generating

regression models that estimate the same factors. Finally, Section 4.5 summarizes the outcomes of the encountered regression models, and some suggestions are made based on the efficiency of each one of them.

4.2. Definition of Response- and Predictor-Variables (labels and features)

The observable behavior of the relationship between the performance indicators and translators Ψ-factors was presented in the previous section. Nevertheless, it was stated that additional or different parameters were to be evaluated to find better explaining parameters to the Ψ-factors behavior in an estimation model. In generating such a model through regression analysis, it is worth recalling that the aim is to employ independent variables denominated as *predictor variables* in adjusting an estimated response that fits accurately enough to an observed dependent variable or *response variable*. How these predictors and responses are processed within the regression process differs depending on the methodology adopted and is further explained in the following sections.

In this concern, a set of predictors was selected and presented in **Table 4.1**.

Table 4.1. Description of X_i-predictor variables used in regression analysis

Predictors X_i	Parameter	[units] Description
X_1	T_n	[s] fundamental period of the *fixBase* structure.
X_2	$\tilde{T}_n$	[s] fundamental period of the *flexBase* structure.
X_3	$\tilde{T}_n/T_n$	[-] ratio of the *flexBase* to the *fixBase* fundamental periods.
X_4	v_{so}	[m/s] shear-wave velocity at small-strain range.
X_5	σ_{SSI}	[-] wave parameter as described in Eq. [2.1].
X_6	λ_{str}	[-] structure's slenderness ratio as described in Eq. [2.2].
X_7	B/L	[-] footprint aspect ratio.
X_8	a_o	[-] dimensionless frequency factor as described in Eq. [2.3].
X_9	S_{ax}	[g] spectral acceleration for the *fixBase* structure as per Section 3.4.2.
X_{10}	$\tilde{S}_{ax}$	[g] spectral acceleration for the *flexBase* structure as per Section 3.4.2.
X_{11}	V_y^*	[-] ratio of the *flexBase* to the *fixBase* structure yield strength.
X_{12}	S_{ax}^*	[-] ratio of the *flexBase* to the *fixBase* structure assessment spectral acceleration.
X_{13}	V_d^*	[-] ratio of the *flexBase* to the *fixBase* structure design base shear.
X_{14}	μ^*	[-] ratio of the *flexBase* to the *fixBase* structure displacement ductility.
X_{15}	R_d^*	[-] ratio of the *flexBase* to the *fixBase* structure ductility strength reduction factors.

These parameters were selected such that they represent four different groups of properties. The first group is related to parameters that somehow reflect the mechanical or dynamic characteristics of the SSS. It is the case of T_n, $\tilde{T}_n$, and v_{so}, which have been introduced in earlier chapters of this document. The second group is focused on some parameters that, according to the state-of-the-art,

are decisive to the behavior of structures considering the SSI effects. Such parameters are σ_{SSI}, λ_{str}, B/L, and a_o; also introduced in advance. The third group takes into account the spectral demand used during the assessment process, represented by the assessment spectral accelerations S_{ax} and $\tilde{S}_{ax}$. Finally, the third group of parameters is related to the response of structures obtained from the NSP due to its apparent importance in giving accuracy to the $DCR_{(ac)}$-Ψ-factors relationship as demonstrated in Section 4.1. This last group includes parameters V_y^*, S_{ax}^*, V_d^*, μ^*, and R_d^* whose descriptions are included in **Table 4.1**. Eqs. [4.1] through [4.5] also describes these predictors mathematically.

$$V_y^* = \frac{V_y^{flexBase}}{V_y^{fixBase}} \quad [4.1]$$

$$S_{ax}^* = \frac{\tilde{S}_{ax_{NSP}}}{S_{ax_{NSP}}} \quad [4.2]$$

$$V_d^* = \frac{\tilde{V}}{V} = \left(1 - \tilde{C}_m\right) + \left(\frac{\tilde{C}_s}{C_s}\right)\left(\frac{\tilde{C}_m}{B_{SSI}}\right) \quad [4.3]$$

$$\mu^* = \frac{\tilde{\mu}}{\mu} = \frac{\tilde{\delta}_t / \tilde{\Delta}_y}{\delta_t / \Delta_y} \quad [4.4]$$

$$R_d^* = \frac{\tilde{R}_d}{R_d} = \frac{\tilde{V}_E}{V_E}\frac{V_y}{\tilde{V}_y} \quad [4.5]$$

As usual, in all the previous equations, the symbol ~ indicates that the parameter has been calculated considering *flexBase*-BSC for accounting for SSI effects. For obtaining Eq. [4.3], the expressions shown in Eqs. [2.31] and [2.32] are operated assuming that the effective seismic weight $\overline{W}$ can be calcualted as $\overline{W} = \tilde{C}_m W$. The rest of parameters within Eqs. [4.1] through [4.5] have been already introduced elsewhere in this document.

Scatter plots for the 15 X_i predictors in **Table 4.1** are generated to get an idea of the possible relationship between these and the response variable to be estimated, Ψ-factors. **Figure 4.8** shows an example of scatter plots for every X_i against Ψ-factor and **Figure 4.9** a Perason correlation coefficient matrix depicted in a heatmap. As for the latter heatmap, it is intended to show any existing linear relationship between the evaluated variables. It is important to note that since 24 Ψ-factors as translation mechanisms are expected, as explained in Section 4.1, only a reference example case is presented for a *convDs-fixBase*-LTHA-LS combination; all 24 combinations are included in **Appendix E** of this study by the end of the document.

By observing the scatter plots in **Figure 4.8**, it is noticeable that a somewhat evident relationship exists between predictors X_1, X_6, and X_9 and the response Ψ-factor. The predictors correspond to the

fixBase fundamental period of vibration, the slenderness ratio λ_{str} and the assessment spectral acceleration $\tilde{S}_{ax}$, respectively. Considering that the reference example case is a conventionally designed structure evaluated using fixed base support conditions, the correlation results, to say the least, intuitive. The heatmap in **Figure 4.9** corroborates what is observed in the scatter plots by showing values of 0.77, 0.75, and 0.80 for the X_1, X_6, and X_9 predictors, respectively. Other predictors that appear to have heavy correlations but are not as strong as the previous ones are the *flexBase* fundamental period, $\tilde{T}_n$, assigned to predictor X_2 and *flexBase* assessment spectral acceleration assigned to the predictor X_{10}. However, notice that these predictors are also strongly correlated to their respective *fixBase* counterparts; thus, they can eventually be interchanged with each other but risking the accuracy of the desired estimation model. Besides, as mentioned before, the reference example case accounts for a *fixBase*-BSC condition; hence predictors shall be selected accordingly.

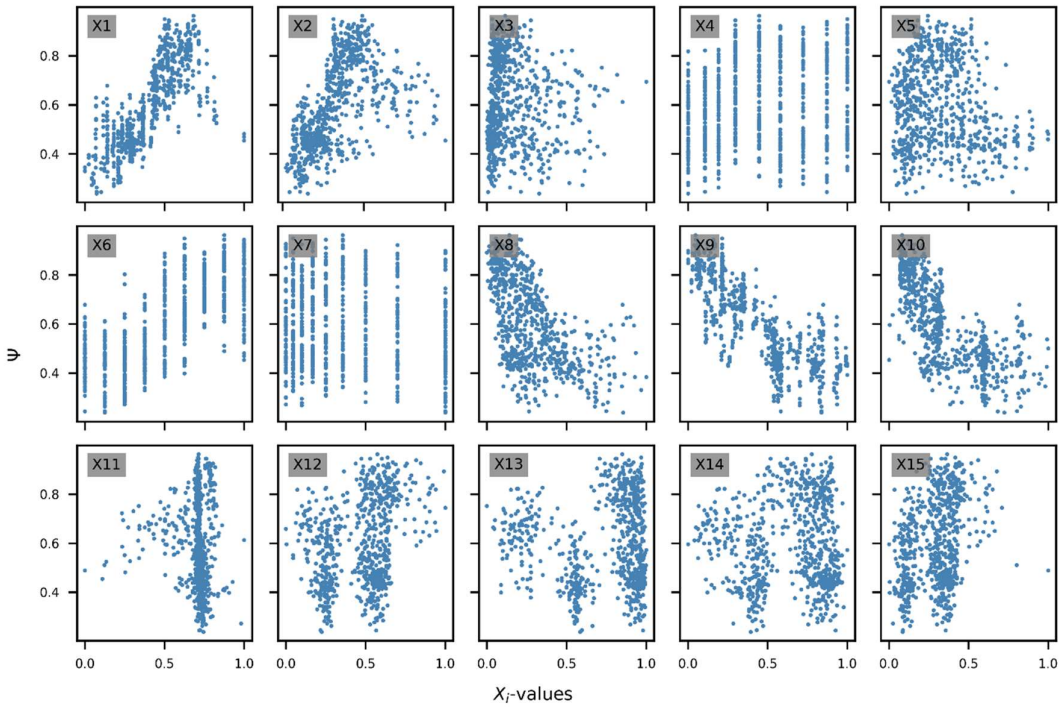

Figure 4.8. Scatter plots showing trends between scaled and standardized Xi-predictors and the Ψ-factor. Reference example case, AP:LTHA / DT:*convDs* / BSC:*fixBase* / SPL:LS.

The analysis of the results plotted in **Figure 4.8** and **Figure 4.9**, described in previous lines, is also made for the rest of the similar figures in **Appendix E** for a visual understanding of the behavior of Ψ-factors against X_i predictors. However, it should be recalled that by this visual inspection to scatter plots and heatmaps, only linear correlations can be identified; any other higher-order correlation cannot be perceived. Despite the drawback described above, linear regression analysis is still a good starting point for generating an estimation model that gives an initial insight into explaining the behavior of the response variable in terms of the predictors. The following section concisely describes the procedures involved in generating an estimation model based on the classical linear regression analysis and the strategies selected to overcome the drawbacks mentioned earlier.

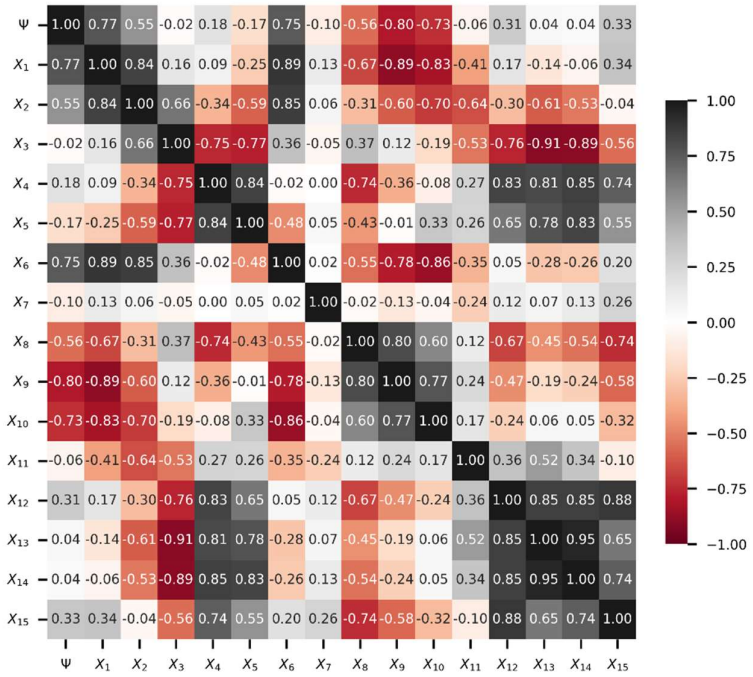

Figure 4.9. Heatmap of Pearson correlation coefficients revealing a possible linear correlation between predictors and the Ψ-factor. Reference example case, AP:LTHA / DT:*convDs* / BSC:*fixBase* / SPL:LS.

4.3. Classical Regression Analysis

A Regression Analysis can be understood as a simple method for investigating functional relationships among variables, expressed in the form of an equation or a model that connects predictor- and response-variables (Chatterjee & Hadi, 2012). Regarding the classical linear regression analysis or multiple linear regression analysis for the case in which more than one predictor is involved, the relationship between the response and predictors can be formulated as a linear equation, as shown in Eq. [4.6].

$$\Psi = \mathrm{B}_0 + \mathrm{B}_1 X_1 + \mathrm{B}_2 X_2 + \ldots + \mathrm{B}_p X_p + \varepsilon \qquad [4.6]$$

Where the response and predictor variables have been introduced before (Ψ and X_i), B_i are the so-called regression coefficients with subindex $i = 0{:}p$; being p the number of selected predictors. On the other hand, ε is a term representing the random error that must not contain any intrinsic information that helps to determine the response that is not already captured by the predictors. Based on the available data of responses and predictors from the database, regression analysis aims to estimate the B_i regression coefficients in such a way that the sum of the squares of the error ε is minimized. This methodology is the so-called Least Squares method. Once the estimated regression coefficients β_i are calculated, the *fitted* regression model can be written in the form of Eq. [4.7]

$$\Psi_{fitted} = \beta_0 + \beta_1 X_1 + \beta_2 X_2 + \ldots + \beta_p X_p \qquad [4.7]$$

In the equation shown above, it is worth noting that the regression coefficient β_0 is a constant value part of the regression model.

For measuring the quality of the fitted response obtained through Eq. [4.7], the determination coefficient, R^2, the adjusted determination coefficient R^2_{adj}, the standard error or Root Mean Squared Error, RMSE, and the Mean Absolute Percentage Error, MAPE, metrics can be used. These metrics are presented in Eqs. [4.8] through [4.11].

$$R^2 = 1 - \frac{\sum_{j=1}^{n}\left(\psi_j - \psi_{(fitted)j}\right)^2}{\sum_{j=1}^{n}\left(\psi_j - \bar{\psi}_j\right)^2} \quad [4.8]$$

$$R^2_{adj} = 1 - \frac{n-1}{n-1-p}\left(1-R^2\right) \quad [4.9]$$

$$RMSE = \sqrt{\frac{\sum_{j=1}^{n}\left(\psi_j - \psi_{(fitted)j}\right)^2}{n-p-1}} \quad [4.10]$$

$$MAPE = \frac{1}{n}\sum_{j=1}^{n}\left|\frac{\psi_j - \psi_{(fitted)j}}{\psi_j}\right| \quad [4.11]$$

In the equations above, n represents the number of observations or data in the dataset used for the regression analysis, ψ_j are the (actual) values of the response at each observation j, and $\bar{\psi}$ is the mean of the observed response values. R^2 can be interpreted as the proportion of the total variation in actual response variable Ψ that the predictor variables can explain. R^2_{adj} on the other hand, can not be interpreted in the same way but is an adjustment to the former metric based on the unconstrained degrees of freedom ($n-1-p$). RMSE is a measure of the error between the estimated and observed values. The advantage of this parameter is that it is measured in the same units as the response variable Ψ. Conversely, MAPE is the mean of absolute percentage errors between the estimated and observed values of the whole database. As such, sometimes, it is easier to use this metric to evaluate the fit quality because of its intuitive nature. MAPE values closer to zero indicates a smaller error or a better fit.

4.3.1. Pre-processing of Variables

Regarding additional aspects of the regression analysis procedure, it is important to acknowledge that data is not always presented initially in a directly suitable form for analysis. Both predictors and response variables often need to be transformed in advance to ensure the fit quality; thus, the regression is performed on the transformed variables instead of the original ones. However, not all the variables may require transformation and not in the same way. For this study, for instance, only

predictor variables (not all of them and not always) are transformed while Ψ responses are kept unaltered. **Table 4.2** show a list of applicable transformation options selected for this purpose.

Table 4.2. Transformation options applicable to predictor variables.

Transformation	Transformation type
X_i^{-1}	Power transformation.
X_i^2	Power transformation.
$\sqrt{X_i}$	Power transformation.
$\ln X_i$	Logarithmic transformation.
$\log X_i$	Logarithmic transformation.

Logarithmic and power transformations are the most widely used strategies for modifying the variables in a regression analysis. Logarithmic transformations are beneficial when the analyzed variables have a significant standard deviation compared to their mean. On the other hand, power transformations are selected based on empirical or theoretical evidence to ensure linearity in the model, achieve normality, or stabilize the error measure's variance between the fitted and observed values. All these characteristics are essential for obtaining an appropriate estimation model.

As explained in previous paragraphs, the resulting product of the Classical Regression (CR) is to obtain a model or estimation equation with the form of Eq. [4.7]. Defining this model implies the estimation of the regression coefficients, β_i, whose units depend on the unit of measurement of the treated variables. Consider the predictor variable X_1 related to the fundamental period T_n, for instance. The regression coefficient β_1 will be measured in units involving $[s]$ (seconds) that conjugated with X_1 gives as a result the unitless values of the response Ψ. Following this train of thought, it is evident that every regression coefficient is expected to be expressed in different units depending on its accompanying predictor, leading in some cases to very large or small β_i quantities with strange units. To overcome this cumbersome situation, the variables (predictors only for this study) can be further modified by either scaling or centering their original values. For modifying the values of predictor variables in the regression analysis carried out in this study, two types of scaling are executed in advance, even before their transformations by the options in **Table 4.2**. The scaling strategies used are *standardization* and *min-max scaling*.

As for *standardization*, it consists of normalizing the predictors by removing the mean value of all observations and scaling to unit variance. Eq. [4.12] shows the expression employed for this scaling.

$$\hat{z}_{i,j} = \frac{\left(x_{i,j} - \overline{x}_i\right)}{\sigma_i} \qquad [4.12]$$

Where $\hat{z}_{i,j}$ is the standardized value of the i^{th}-predictor $x_{i,j}$ at the observation j. $\bar{x}_i$ is the mean value of the n observations in the dataset corresponding to i^{th}-predictor, and σ_i is the standard deviation of the data corresponding to the same i^{th} predictor. The result of this normalization is a unitless value for the predictors that ultimately will deliver unitless regression coefficients, β_i, after the regression analysis is performed.

On the other hand, *min-max* scaling aims to enclose predictor values within a range of values $[z_{min}, z_{max}]$ that results in easier processing through the regression analysis execution. Eq. [4.13] demonstrate how the scaling is performed.

$$z_{i,j} = \frac{\left(x_{i,j} - \min\left(x_i\right)\right)}{\left(\max\left(x_i\right) - \min\left(x_i\right)\right)}\left(z_{\max} - z_{\min}\right) + z_{\min} \qquad [4.13]$$

Where $z_{i,j}$ is the *min-max* scaled value of the i^{th}-predictor $x_{i,j}$ at the observation j, z_{max} and z_{min} are the lower- and upper-bounds for the range of values that predictor values should adopt after scaling.

The *min-max* scaling is often performed within a [0,1] range of values. In such a case, the expression in Eq. [4.13] reduces to Eq. [4.14].

$$z_{i,j} = \frac{\left(x_{i,j} - \min\left(x_i\right)\right)}{\left(\max\left(x_i\right) - \min\left(x_i\right)\right)} \qquad [4.14]$$

By thus scaling the predictor variables, their values are limited to a range between zero and one. Refer back to **Figure 4.8**. Notice how the values of all the predictor variables X_i in the graphic's horizontal axis varies in the range [0,1]. This figure, as the rest in **Appendix E**, is plotted once predictor values have been standardized and scaled; in that order.

Since it is advisable always to pre-process the predictor variables applying the considerations described so far, the regression analysis is finally performed using the standardized-scaled-transformed predictors such that the modified values obey the process described in Eq. [4.15]

$$x_{i,j}^{\text{mod}} = \text{Transf}(\text{MinMaxScale}(\text{Standardize}(x_{i,j}))) \qquad [4.15]$$

Operating Eqs. [4.12] and [4.14], Eq. [4.15] can be expressed in the form of Eq. [4.16] for any $x_{i,j}^{mod}$ in predictor X_i^{mod}.

$$X_i^{\text{mod}} = \text{Transf}\left(\hat{a}_i X_i - \hat{b}_i\right) \qquad [4.16]$$

Where $\hat{a}_i$ and $\hat{b}_i$ are scaling parameters derived from Eqs. [4.12] and [4.14], expressed as:

$$\begin{cases} \hat{a}_i = \left[\sigma_i \left(\max\left(x_i\right) - \min\left(x_i\right) \right) \right]^{-1} \\ \hat{b}_i = \dfrac{\overline{x}_i + \sigma_i \ \min\left(x_i\right)}{\sigma_i \left(\max\left(x_i\right) - \min\left(x_i\right) \right)} \end{cases} \quad [4.17]$$

Hence, the estimation model would use regression coefficients β_i estimated based on modified predictors, as shown in Eq. [4.18].

$$\Psi_{fitted} = \beta_0 + \beta_1 X_1^{\text{mod}} + \beta_2 X_2^{\text{mod}} + \ldots + \beta_p X_p^{\text{mod}} \quad [4.18]$$

4.3.2. Selection of Predictors

In Section 4.2, it was demonstrated that not all the predictors show an evident relationship against the response variable Ψ just by observing the scatter plots or the Pearson correlation coefficients in **Figure 4.8**. For cases where a large number of potential predictors can be included in the estimation model, a series of procedures to select the more significant ones can be performed to generate an appropriate model. Among these procedures, a *Forward Selection* (FS) strategy is chosen in this study for predictor selection purposes. This strategy consists of the following steps:

a) Starting the definition of the estimation model with the form of a simple constant explaining the "variation" of Ψ response variable (i.e., $\Psi = \beta_0$).
b) One X_i^{mod}-predictor at a time is added to the estimation model if it is significant enough to be kept. The significance of a specific X_i^{mod}-predictor is established by:
   - Evaluating the increment in R_{adj}^2 that this X_i^{mod} induces in the model by its inclusion.
   - Checking if the corresponding *p*-value that is associated to the X_i^{mod}-predictor is less than a limit value of 0.05. The *p*-value is defined as the probability of obtaining the β_i coefficient assuming that the null-hypothesis is true. In other words, it represents the probability of obtaining such a regression coefficient, given that it does not belong to the model. The lower the probability, the more likely the coefficient exists in the estimation model.
   - The X_i^{mod} predictor inducing the higher R_{adj}^2 increment and showing the lesser *p*-value is included in the estimation model.
c) Not all X_i^{mod}-predictors are added to the model based on step b). The FS strategy stops when no predictors of significance (i.e., not complying with step b)) are left to be added to the model.

It is worth mentioning that when performing step b), each transformation of **Table 4.2** is applied to the standardized and scaled X_i-predictor before evaluating the significance of the X_i^{mod} in the

estimation model. The transformation that leads to the maximum R^2_{adj} is kept before cheking its p-value. Besides, it is reasonable to think that the order in which X_i^{mod}-predictors are added to the model reflects the degree of importance of such a predictor within the estimation model.

4.3.3. Results from Classical Regression Analysis

Based on the considerations and procedures described in previous sections, a regression analysis has been performed to obtain all the 24 Ψ response variables for translating the starting-$DCR_{(ac)}$ to the target one. Due to the large number of responses that were obtained, **Table 4.3** and **Table 4.4** show only the regression analysis results only for the estimation models with higher R^2_{adj} among all models for the LS and CP strucutral performance levels, respectively. The information presented in these tables includes the fit quality metrics R^2, R^2_{adj}, RMSE, and MAPE, along with the X_i-predictors of significance to the estimation model, the transformation required to get an optimal R^2_{adj} value for each predictor, the regression coefficients, their corresponding p-values, and the scaling parameters $\hat{a}_i$ and $\hat{b}_i$.

Table 4.3. Statistical efficiency metrics and Classical Regression results.
Example case for best R^2 values for the LS-SPL / (*convDs – flexBase – NSP*)

$\boldsymbol{R^2}$ = 0.807	$\boldsymbol{R^2_{adj}}$ = 0.805	**RMSE** = 0.248		**MAPE** = 0.148	
Predictor $\boldsymbol{X_i^{mod}}$	**Transf.**	$\boldsymbol{\beta_i}$**-coef.**	**p-values**	$\boldsymbol{\hat{a}_i}$	$\boldsymbol{\hat{b}_i}$
constant	none	2.810	0.0000	1.000	1.000
X_6	X_6	0.992	0.0000	0.417	0.450
X_{10}	X_{10}^2	-0.774	0.0000	1.339	0.465
X_2	$\log X_2$	-5.462	0.0000	0.753	0.429
X_4	$1/X_4$	-1.157	0.0000	0.004	0.553

Observe **Table 4.3**, it corresponds to the *convDs-flexBase*-NSP combination for which an $R^2_{adj} = 0.805$ is calculated. For this estimation model, the constant coefficient β_0 along with 4 X_i^{mod} predictors are needed to generate a suitable model; modified predictors are $X_6 = \lambda_{str}$, $X_{10} = \tilde{S}_{ax}$, $X_2 = \tilde{T}_n$, and $X_4 = v_{so}$. The estimation model that allows calculating a fitted Ψ-response depending on the predictors mentioned above takes the form of Eq. [4.19].

$$\Psi_{fitted} = 2.810 + 0.992X_6^{\text{mod}} - 0.774X_{10}^{\text{mod}} - 5.462X_2^{\text{mod}} - 1.157X_4^{\text{mod}} \quad [4.19]$$

The advantage of presenting the estimation model as an equation is that some critical information can be deduced by observing its terms' behavior based on the sign and the accompanying β_i-coefficient. Notice, for example, how sensitive the model is to the change in X_2^{mod} and less sensitive to other predictors, indicating that the change in the logarithm of $\tilde{T}_n$ produces considerable

alterations in Ψ_{fitted}. The *flexBase* period can increase or decrease the value of the fitted response depending on whether its standardized-scaled value is less or more than 1.0. As for the slenderness ratio λ_{str}, one can tell that as its value increases, the starting-$DCR_{(ac)}$ obtained through the *convDs-flexBase*-NSP combination tends to overestimate the performance of the structure compared to the actual performance. Thus the need to increase Ψ_{fitted} through X_6 so that starting-$DCR_{(ac)}$ can reach higher values of target-$DCR_{(ac)}$. The opposite effect has the other predictors involved in the model, $\tilde{S}_{ax}$ and v_{so} following the same train of thought.

It could be useful to express the modified predictors with their corresponding transformations and scaling parameters to present the estimation model with terms that allow entering the predictor values with their original units presented in **Table 4.1**. Eq. [4.20] shows such a representation of the estimation model.

$$\Psi_{fitted} = 3.089 + 0.414X_6 - \left(1.388X_{10} + 0.964\right)X_{10} - 5.462\log\left(0.753X_2 + 0.429\right) - \frac{1.157}{0.004X_4 + 0.553} \quad [4.20]$$

Notice, however, how impractical this representation is to evaluate the behavior of the response parameter in terms of the predictors as done before by observing Eq. [4.19]. Nevertheless, it is a straightforward equation to compute an estimated Ψ without further scaling operations.

The same analysis made for the LS-SPL results presented in **Table 4.3** can be performed on the results in **Table 4.4** for the CP-SPL. In this case, the *SSIDs-fixBase*-LTHA is the combination leading to the best-fitting-quality estimation model. However, the R^2_{adj} reaches only a value of 0.69; approximately 10% lower than the model for the LS-SPL.

Table 4.4. Statistical efficiency metrics and Classical Regression results. Example case for best R^2 values for the CP-SPL / (*SSIDs – fixBase – LTHA*)

$\boldsymbol{R^2}$ = 0.693	$\boldsymbol{R^2_{adj}}$ = 0.690	**RMSE** = 0.286		**MAPE** = 0.170	
Predictor X_i	**Transf.**	**β_i-coef.**	**p-values**	$\hat{a}$	$\hat{b}$
constant	none	-0.129	0.0202	1.000	1.0
X_9	$1/X_9$	1.061	0.0000	0.486	0.783
X_6	X_6^2	0.424	0.0000	0.417	0.500

The equation representing the estimation model with modified predictors is described in Eq. [4.21].

$$\Psi_{fitted} = -0.129 + 1.061X_9^{\text{mod}} + 0.424X_6^{\text{mod}} \quad [4.21]$$

Where the predictors correspond to S_{ax} and λ_{str} for the X_9 and X_6 respectively. These predictors were also present in the estimation model of Eqs. [4.19] and [4.20], but for the current model, the

assessment spectral acceleration parameter is that of the *fixBase* BSC instead of the *flexBase* counterpart. It may result obviously since the combination that gives the best R^2_{adj} corresponds to the *fixBase* BSC structure used during the performance assessment.

The expression considering the proper units for the involved predictors is shown in the following equation.

$$\Psi_{fitted} = -0.129 + \frac{1.061}{(0.486X_9 + 0.783)} + 0.424\left(0.417X_6 + 0.500\right)^2 \quad [4.22]$$

The results of the CR analysis for all 24 Ψ_{fitted} response variables are presented graphically and summarized in **Figure 4.10**. R^2 metrics are presented in stem plots for any DT-BSC-AP-SHL combination. Note that the models generated using Ψ-factor based on the MRSA deliver the least accurate estimation models through linear regression analysis. On the other hand, the NSP-based Ψ-factors allow developing the most accurate estimation models for all DT-BSC-AP-SHL combinations but those of the SSIDs-fixBase. For the latter, the LTHA is preferable in estimating Ψ_{fitted} factors.

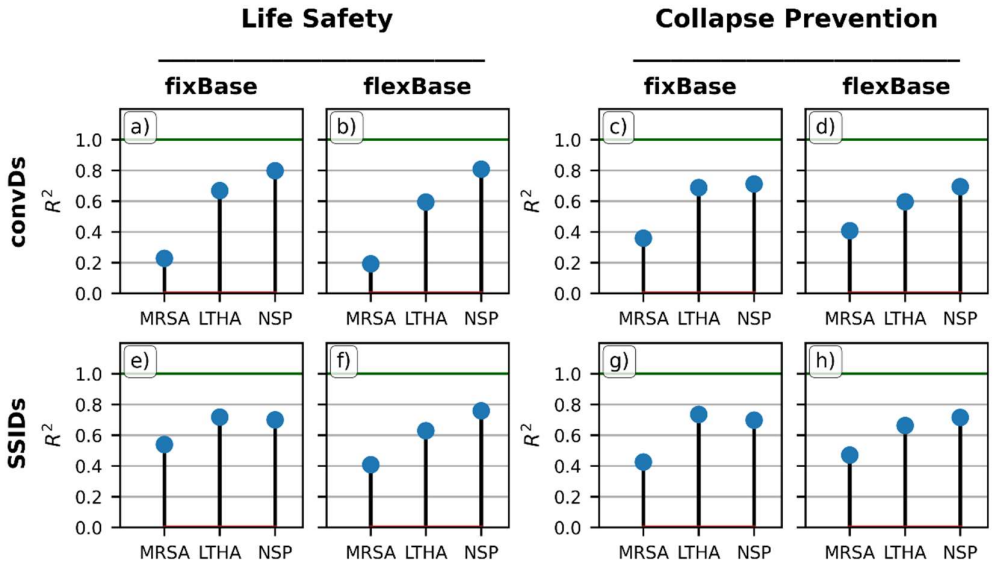

Figure 4.10. R^2 values obtained from the Classical Regression analysis for all combinations of DT / BSC / AP / SPL.

Based on what is shown in **Figure 4.10**, the 24 translation option can be reduced to only four if the models with the best R^2 are selected for each DT-SPL combination aiming to obtain the actual or target-$DCR_{(ac)}$. This is explained as follows:

- For conventionally designed structures (DT=*convDs*), assessed to check the achievement of Life Safety structural performance level (SPL=LS), it is advisable to use the $DCR_{(ac)}$

performance indicators obtained through the NSP AP applied on *flexBase*-BSC models. This estimation model shows a value of $R^2 = 0.807$.

The translation would be applied through the following equation:

$$DCR_{(ac)NDP:LS}^{conv:flex} = \Psi_{(fitted)NSP:LS}^{conv:flex} \times DCR_{(ac)NSP:LS}^{conv:flex} \quad [4.23]$$

Where the estimation model is represented by the equation of Ψ_{fitted} as a function of X_i^{mod} predictors, and for this particular combination is presented in Eq. [4.19] (or [4.20] for the real units expression).

- For structures considering SSI effects (DT=*SSIDs*), assessed to check the achievement of Life Safety structural performance level (SPL=LS), it is advisable to use the $DCR_{(ac)}$ performance indicators obtained through the NSP AP applied on *flexBase*-BSC models. This estimation model shows a value of $R^2 = 0.76$.

  The translation would be applied through the following equation:

$$DCR_{(ac)NDP:LS}^{SSI:flex} = \Psi_{(fitted)NSP:LS}^{SSI:flex} \times DCR_{(ac)NSP:LS}^{SSI:flex} \quad [4.24]$$

  Where the estimation model expression with modified predictors is, Ψ_{fitted} for the recommended DT-BSC-AP-SPL combination is:

$$\Psi_{fitted} = 0.528 + 1.258X_6^{\text{mod}} + 1.713X_3^{\text{mod}} - 1.220X_2^{\text{mod}} + 0.447X_4^{\text{mod}} - 0.410X_{14}^{\text{mod}} \quad [4.25]$$

  By considering the predictors with their actual units, the expression is somewhat extensive with the form of Eq. [4.26].

$$\begin{aligned}\Psi_{fitted} = {} & 0.528 + 1.258\left(0.420X_6 + 0.500\right)^2 + 1.713\sqrt{\left(1.260X_3 + 1.280\right)} \\ & - 1.220\log\left(0.720X_2 + 0.400\right) + 0.447\sqrt{0.004X_4 + 0.550} \\ & - 0.410\left(1.300X_{14} + 0.260\right)^2\end{aligned} \quad [4.26]$$

- For conventionally designed structures (DT=*convDs*) assessed to check the achievement of Collapse Prevention structural performance level (SPL=CP), it is advisable to use the $DCR_{(ac)}$ performance indicators obtained through the NSP AP applied on *fixBase*-BSC models. This estimation model shows a value of $R^2 = 0.71$.

  The translation operation, the modified-predictors estimation model, and the corresponding real-units equation for combination are shown in Eqs. [4.27] through [4.29].

$$DCR_{(ac)NDP:CP}^{conv:flex} = \Psi_{(fitted)NSP:CP}^{conv:fix} \times DCR_{(ac)NSP:CP}^{conv:fix} \quad [4.27]$$

$$\Psi_{fitted} = 3.842 - 2.390X_6^{\text{mod}} - 0.507X_{10}^{\text{mod}} + 0.174X_7^{\text{mod}} - 1.920X_{11}^{\text{mod}} \quad [4.28]$$

$$\Psi_{fitted} = 3.842 - 2.390\frac{1}{\left(0.420X_6 + 0.500\right)} - 0.507\left(0.890X_{10} + 0.460\right) + 0.174\left(1.500X_7 + 0.500\right)^2 - 1.920\log\left(1.080X_{11} + 0.380\right) \quad [4.29]$$

- For structures considering SSI effects (DT=*SSIDs*), assessed to check the achievement of Collapse Prevention structural performance level (SPL=CP), it is advisable to use the $DCR_{(ac)}$ performance indicators obtained through the LTHA AP applied on *fixBase*-BSC models. This estimation model shows a value of $R^2 = 0.693$.

  The translation would be applied through the following equation:

  $$DCR_{(ac)NDP:CP}^{SSI:flex} = \Psi_{(fitted)LTHA:CP}^{SSI:fix} \times DCR_{(ac)LTHA:CP}^{SSI:fix} \quad [4.30]$$

  Where the estimation model is represented by the equation of Ψ_{fitted} as a function of X_i^{mod} predictors, and for this particular combination is presented in Eq. [4.21] (or [4.22] for the actual units expression).

Despite the convenience of having regression models presented in the form of an equation, there is still a lack in the reached quality of the fit through linear regression analysis. For instance, the highest R^2 that corresponds to the Ψ_{fitted} obtained from the *convDs-flexBase*-NSP-LS reaches a value of 0.807. It is considered to be a good R^2 value, but, as will become evident in later sections, it can be improved with other regression techniques. The lowest R^2 obtained is that for the Ψ_{fitted} obtained from the *SSIDs-fixBase*-LTHA-CP combination with a value of 0.693. This R^2 is even smaller than the LS-SPL value, so there is more room for improvement in the estimation model devoted to this combination.

In the following section, additional techniques based on machine learning are presented and used to generate estimation models that improve the fit's quality.

4.4. Machine-Learning Techniques

In the last decades, analyzing big data sets from the information of activities in daily life has become a common need. Assessing enormous amounts of data and inferring valuable information from it is no longer a matter of manual or visual evaluation of the trends and relationships of the stored data against parameters of interest, as was done in Section 4.3. With the Classical Regression Analysis technique, predictor and response variables were evaluated through scatter plots and heatmaps before generating an estimation model. However, not all the data was presented in the mentioned

section due to the massive amount of information, even though they were internally evaluated for the sake of this research.

On the other hand, machine learning (ML) introduces itself as a subfield of Artificial Intelligence (AI) from computer sciences that involves self-learning algorithms that derive "knowledge" from data to make estimations and predictions (ML regression) or classify data (ML classification). Human skills to manually create awareness of relationships or rules to generate models from potential predictors with massive data are replaced by a potentially more efficient alternative supported by self-learning algorithms that gradually improve the performance of an estimation model in a so-called *training* process. Practical daily-life applications of ML techniques include email spam filters, voice and text recognition software, and web search engines. However, in the field of applied sciences, such as structural and earthquake engineering, ML has also gained ground through several applications.

For instance, pattern recognition using Deep Neural Networks (DNN) and data mining techniques were employed in (Javadi & Rezania, 2009) for modeling soil behavior. In the study carried out by (Zhou & Chang, 2021), buildings in China were classified using Gradient Boosted Classification Trees (GBCT) for sustainable urban studies. Automatized structural design, as well as the mechanical and structural behavior such as crack pattern detection, characterization, and diagnosis of specific concrete elements, are also estimated or predicted in studies developed by (Alagundi & Palanisamy, 2022; Du et al., 2021; Huang et al., 2022; Park et al., 2021; Pizarro & Massone, 2021; Sánchez Calderón & Bairán, 2020; Sanchez, 2017; Tarfan & Tajammolian, 2021; Torky & Ohno, 2021), to name a few. Other general applications focused on structural engineering are referred to in state-of-the-art review publications such as (Thai, 2022). In the field of seismic engineering, vulnerability, and risk assessment, a variety of ML techniques have been used to estimate or predict responses associated with each discipline, as described in the references (Alimoradi & Beck, 2015; Arslan, 2010; David M. Boore & Bommer, 2005; Derbal et al., 2020; Esfandiari & Urgessa, 2020; Gulgec et al., 2019; Kiani et al., 2019; Mangalathu et al., 2019; Moller et al., 2010; Siam et al., 2019; Zhang & Foschi, 2004). Finally, regarding the study of SSI effects on buildings' and foundations' response, ML also meets its quota in research studies carried out by (Gajan, 2021; Ilhan et al., 2019; Shahin, 2015).

As for the varieties of ML techniques, there are three broad groups depending on the data type and expected outcomes: supervised, unsupervised, and reinforced learning. For this study, in particular, supervised learning is employed due to the nature and characteristics of the available data by using TensorFlow (Abadi et al., 2015) and Scikit-learn (Pedregosa et al., 2011) ML packages within the Python environment. This ML variety makes use of labeled data (identified predictors or *features*) to estimate and/or predict an outcome based on direct feedback (labeled response to be fit or simply *labels*), i.e., by performing an ML-regression analysis.

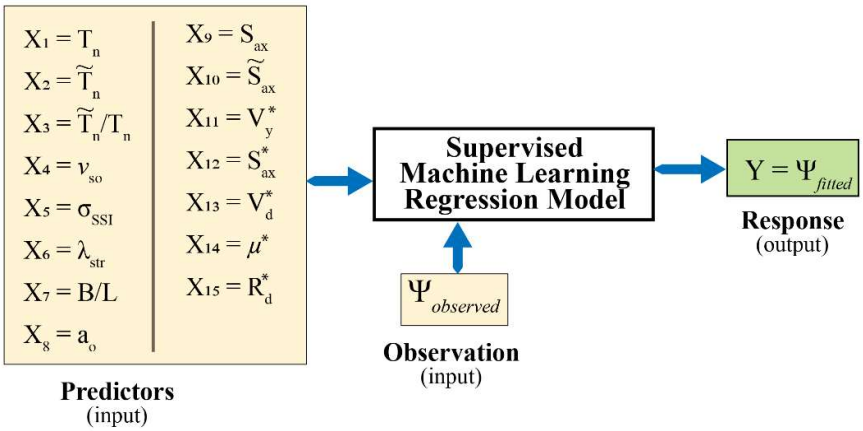

Figure 4.11. General schematization of selected predictors and responses for the ML-based regression models.

Figure 4.11 shows a schematic description of the labeled input and output data used to generate a supervised ML regression model to estimate the studied response Ψ_{fitted}. Note that the same predictors as in **Table 4.1** are selected for the ML regression analysis in this section. As was done in Section 4.3 for the CR analysis, the predictors must be pre-processed before being used in the ML regression model generation.

The following steps describe the roadmap for generating such a regression model:

a) ***Pre-processing data***: as mentioned before, the initial data (predictors and responses) rarely comes in a shape suitable for direct use within a regression model generation. The same treatment described in Section 4.3.1 regarding the standardization, scaling, and transforming modifications applies when preparing data for ML regression techniques. In addition, the dataset must be separated into portions used for the *training* and *testing* process involved in generating and evaluating the ML estimation model. It is a common practice to select a bigger portion to train the model than to test it (between 60% and 90% of the entire dataset), and the split of these portions is generally done by random or statistical sampling. This topic will be addressed later in the specific section.

b) ***Learning or training***: during this step, a model type is selected and optimized in a recursive process to make it efficient, accurate, and precise to the extent the data allows it to be and how well-tunned the *hyperparameters* of the selected model type are. Model types chosen for this study are Deep Neural Networks (DNN) and Gradient Boosting Regression Trees (GBRT). Each type mentioned before has its own set of hyperparameters that allows tuning the model, depending on the data characteristics, to find an optimal final model. The hyperparameter tuning is also addressed in its corresponding section later in this chapter.

c) ***Evaluation or testing:*** as the last step, the portion of the entire dataset reserved for testing the model is used to evaluate its quality by analyzing a so-called *loss function*. Efficiency

metrics as the R^2, MAPE, and RMSE here are also valuable for determining the model's suitability in estimating a desired response.

It is worth mentioning that steps b) and c) in the above-described roadmap make up a recursive process that stops when the loss function is minimized to a point where the ML regression model can no longer be optimized. A critical issue to take care of during the model training process is overfitting, which in a few words, consists of making the model efficient for estimating responses with values of the training data but useless for other data. Training early-stopping strategies are used to overcome the overfitting issue and are briefly described in the corresponding sections.

After this short introduction to ML regression techniques, the following sections present more information regarding the selected ML regression model types in this study and the results obtained from applying these techniques to the estimation of Ψ-factor. Sections 4.4.1 and 4.4.2 are devoted to DNN and GBRT regression models, respectively. However, since these sections do not aim to provide a deep and strict insight into what a DNN or a GBRT is, nor how they work, the information presented intends to be sufficient to understand the process involved.

4.4.1. Deep Neural Networks Regression

The most common way of representing a neural network is by using layers made up of nodes or neurons. Each neuron executes a simple operation and is connected to the neurons of the previous and next layer through weights (w_i) that regulate the information propagated to the next layer of neurons. **Figure 4.12** shows the simplified architecture of a DNN, specifying its layers and neurons. Note that there are three types of layers; an input layer contains the data of the predictors, one or more *hidden* layers in charge of weighing and propagating the information received from the previous layer, and finally, the output or response layer, which combines the values of all previous layers to generate the response (refer to **Figure 4.12a**).

Two simple inner operations are performed within the neuron: the ponderate sum of the input data and weights delivered by the previous layers, along with a bias ($\Sigma w_i X_i + b$) and the application of an activation function ($g(\Sigma w_i X_i + b)$), as shown in **Figure 4.12b**.

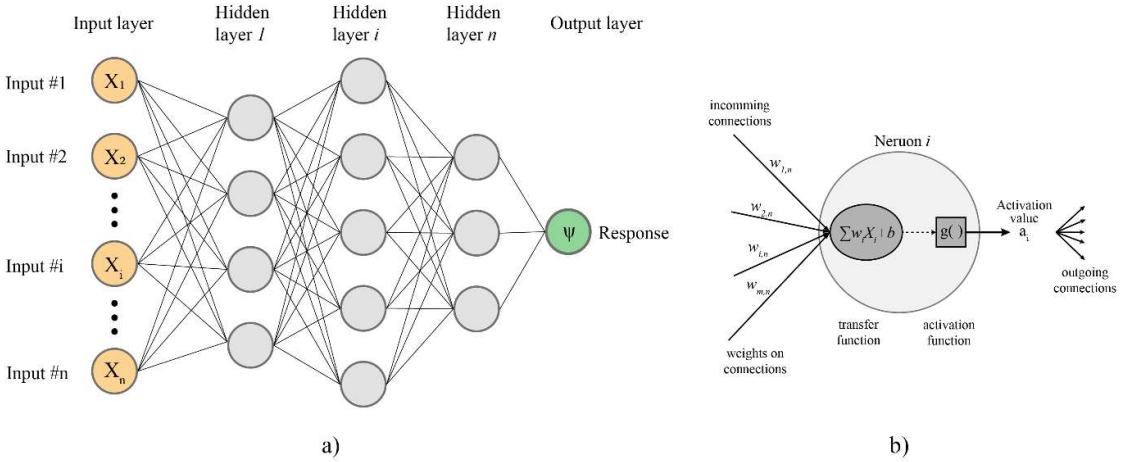

Figure 4.12. Architecture schematization of a Deep-Neural-Network (DNN) regression model. Adapted from (Patterson & Gibson, 2019)

The activation functions control the information propagated to the next layer since they transform the neuron net input values in combination with the weights and the bias, to a new value that ranges between 0 and 1 (or between -1 and 1). These new values are the ones that activate (if 1) or deactivate (if 0) the information output from a specific neuron in a layer, thus the name. Thanks to the activation functions in combination with several hidden layers, the DNN can learn and reflect nonlinear relationships between the predictors and the response. The most common activation functions are the ReLU, Sigmoid, and the hyperbolic Tangent, Tanh. This study uses the Tanh as the activation function while generating the DNN regression model. This activation function was preferred over the other available because it gave better results in initial training exercises with the data gathered for this study. Compared to the ReLU and the Sigmoid activation functions, whose output values range between 0 and 1, the Tanh is a zero-centered function with extreme values of -1 and 1. Hence, the output values passed to the next layer can be easily mapped as strongly negative, neutral, or strongly positive. Such behavior is valuable when the data used in the training and testing processes are also zero-centered. It should be recalled that in pre-processing the predictor variables (Section 4.3.1), standardization and min-max scaling criteria were employed for transforming raw data to zero-centered values between -1 and 1. This compatibility between the activation function and the data shape improves the neural network's performance (Patterson & Gibson, 2019).

As for the loss function in charge of quantifying the error between the observed and fitted response variable values, the mean squared error is the most common for regression analysis problems; hence this is the loss function used in this work.

Another important aspect of accounting for during the DNN training process is to avoid overfitting. Adequately defining the hyperparameters of the DNN's architecture is a critical step in generating models that don't "memorize" the expected responses but estimate an approximate value based on

the input information. Such hyperparameters include the number of layers and the number of neurons contained in each layer, the optimization algorithm, and the regularization strategies used.

The number of layers and neurons has been defined through an iterative try-and-error optimization process in this study. On the other hand, the Adam optimizer algorithm, the L2 regularization to control excessively high weight values, and the 50% random Dropout strategy were adopted to complete the DNN ensemble. It is worth mentioning that no more than two hidden layers with less than ten nodes per layer were obtained from the optimization process for getting acceptable DNN regression models.

It was explained earlier that, implied in the pre-processing of data, the database is split into two portions: one for training, and the other for testing the ML regression model. Since the recommendations on splitting databases are sparse and depend on the nature of the data used during the training, again, an iterative evaluation of the efficiency of generated DNN regression models has been performed with varying percentages of training portions used in each iteration. The results obtained from this efficiency evaluation are presented in **Figure 4.13** and **Figure 4.14**. The R^2 metric has been selected as efficency indictator to be evaluated at each train portion for DT-BSC combinations for LS and CP SPLs in **Figure 4.13** and **Figure 4.14**, respectively.

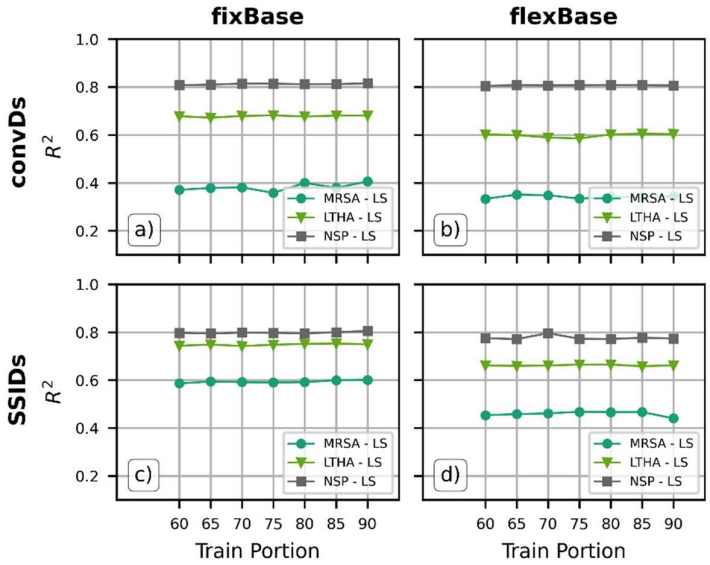

Figure 4.13. Maximum R^2 values obtained with DNN model depending on different train portions selected from the whole database evaluating the LS-SPL. a) and b) for *convDs*-DT with *fixBase* and *flexBase* BSCs, respectively. c) and d) for *SSIDs*-DT with *fixBase* and *flexBase* BSCs, respectively.

Note in the figures that in each graphic (a,b,c, and d) the R^2 metric measure is included for the estimation of Ψ_{fitted} when calculated based on MRSA, LTHA, and NSP analysis procedures. Thus, the presented figures include the response of every DT-BSC-AP-SPL combination.

From these two figures, there is one important thing to note: there is no significant change in the obtained value of R^2 metric within a specific AP but for some isolated training portions applied in the MRSA-based estimation of Ψ. Nevertheless, it can be recognized that there is a range of training portions that give the overall best-fit metric between 75% and 85% of the database values. Thus, the selected split ratio for generating the definitive DNN regression model is 80% for the training and 20% for the test portions.

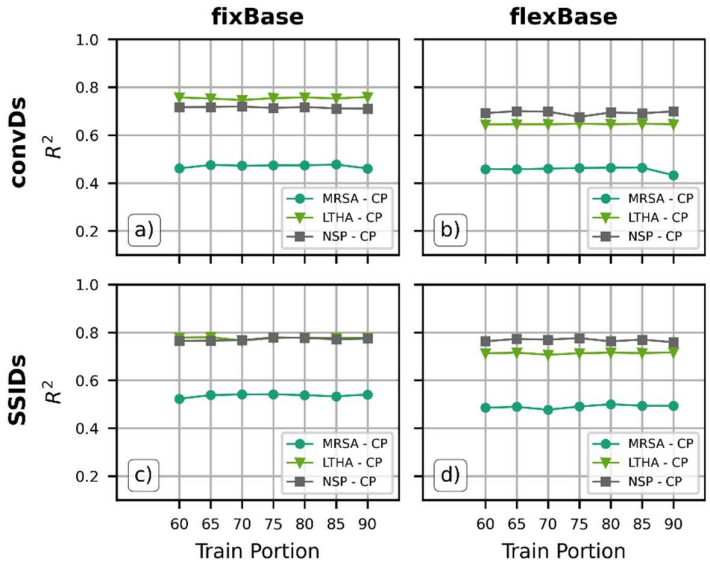

Figure 4.14. Maximum R^2 values obtained with DNN model depending on different train portions selected from the whole database evaluating the CP-SPL. a) and b) for *convDs*-DT with *fixBase* and *flexBase* BSCs, respectively. c) and d) for *SSIDs*-DT with *fixBase* and *flexBase* BSCs, respectively.

It can also be anticipated from observing **Figure 4.13** that in every DT-BSC combination for the LS SPL regression model for Ψ_{fitted}, the AP resulting in the highest R^2 is the NSP, followed by the NLTHA, and the MRSA-AP is the least efficient of the evaluated APs. From **Figure 4.14** for the CP-SPL evaluation, on the contrary, even though the LTHA gives the highest R^2 values for the *convDs-fixBase* combination, the NSP turns out to be the one with the highest R^2 for the rest. These appreciations are valid for any train-test ratios, as can be noticed from these figures.

Figure 4.15 is introduced to present the efficiency metric R^2 obtained from the DNN regression models using the 80-20 train-test split ratio in a summarized fashion (similar to **Figure 4.10**). R^2 for every DT-BSC-AP-SPL combination are shown in this figure, from which an optimal BSC-AP combination can be defined for each DT-SPL couple for estimation of the translator Ψ_{fitted}.

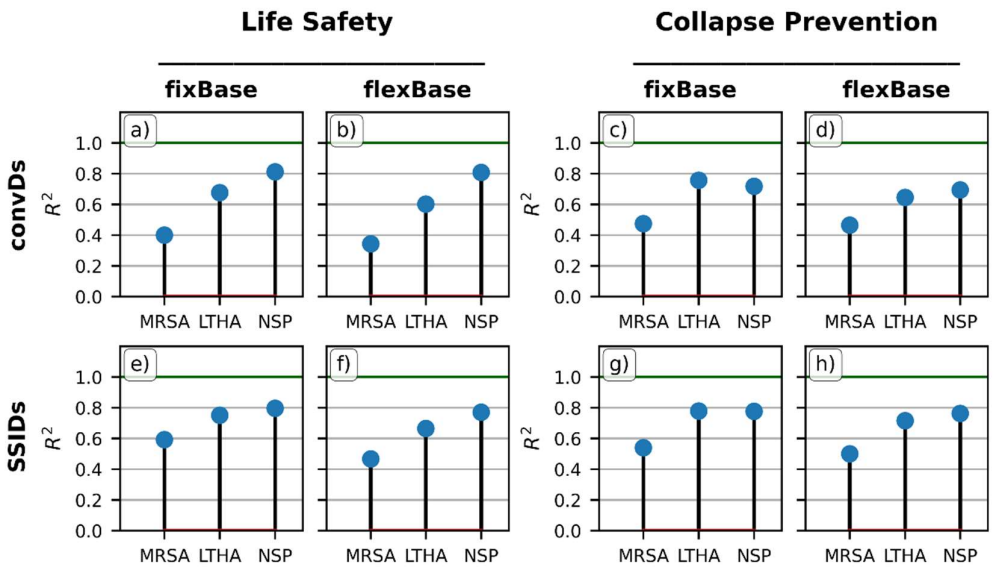

Figure 4.15. R^2 values obtained from the DNN Regression analysis for all combinations of DT / BSC / AP / SPL.

In this regard, notice that:

- For the *convDs*-LS combination in **Figure 4.15a,b**, a $\Psi_{fitted}{}^{conv:fix}_{NSP:LS}$ would be advised to translate from the starting-$DCR_{(ac)}$ to the target $DCR_{(ac)}{}^{conv:flex}_{NDP:LS}$.
- In aiming for the same translation purpose but for the *convDs*-CP combination (**Figure 4.15c,d**), a $\Psi_{fitted}{}^{conv:fix}_{LTHA:LS}$ is recommended instead.
- Concerning the *SSIDs*-LS combination of **Figure 4.15e,f**, the suggested translator factor is $\Psi_{fitted}{}^{SSI:fix}_{NSP:LS}$.
- Lastly, when it is desired to translate into the actual $DCR_{(ac)}$ for the *SSIDs*-CP combination, the optimal DNN-regression model would be the one estimating $\Psi_{fitted}{}^{SSI:fix}_{LTHA:CP}$.

The drawback of this ML regression technique lies in the fact that the influence predictors can not be evaluated in the same way they were for the CR. The weight and the activation functions are in charge of propagating the information from one layer of the DNN to the next and are adjusted every time a cycle of train-test is performed. Hence, the output layer containing the fitted response results from the combination of several train-test cycles in which the neurons could be partially activated or deactivated, leading to models where, to some extent, all the predictors participate in the outcome. Even though there are a few modules in TensorFlow and Scikit-learn that can be used to decipher the most significant or influential predictors within the ML regression models, this analysis is left to the GBRT regression models in Section 4.4.2. As it would be evident from the R^2 obtained in the before-mentioned section, GBRT generates more efficient models from where valuable information will be derived.

Despite what has been stated in the previous paragraph, important information can be observed from the regression results using DNN techniques. **Table 4.5** and **Table 4.6** show the efficiency metrics and the X_i transformations needed to the develop the best DNN regression model within all the DT-BSC-AP combinations for LS- and CP-SPL, respectively.

Table 4.5. Statistical efficiency metrics and DNN Regression results. Example case for best R^2 values for the LS-SPL / (*convDs – fixBase – NSP*)

R^2 = 0.811			R^2_{adj} = 0.807				RMSE = 0.275				MAPE = 0.171				
Predictor	X_1	X_2	X_3	X_4	X_5	X_6	X_7	X_8	X_9	X_{10}	X_{11}	X_{12}	X_{13}	X_{14}	X_{15}
Transf.	X_1	$1/X_2$	$\sqrt{X_3}$	$1/X_4$	X_5	X_6	X_7^2	$\sqrt{X_8}$	$1/X_9$	X_{10}^2	$\log X_{11}$	$1/X_{12}$	$1/X_{13}$	X_{14}	X_{15}^2

Notice that for the LS-SPL, the R^2 (0.811) for the DNN regression model barely surpasses the R^2 (0.807) for the same SPL in the CR model of **Table 4.3**. However, observing the MAPE value for these two regression models, one can tell that for the CR, MAPE= 0.148 against a MAPE=0.171 for the DNN counterpart. It indicates that even when the R^2 gives an idea of how suitable a model is for estimation purposes, the big picture is completed by evaluating and comparing the rest of the efficiency metrics. In this case, for instance, the efficiency metrics suggest that even though the predictors are (roughly) better explaining the variation of Ψ_{fitted} in the DNN regression model, they give a slightly higher error -in absolute percentage- than the CR.

Table 4.6. Statistical efficiency metrics and DNN Regression results. Example case for best R^2 values for the CP-SPL / (*SSIDs – fixBase – LTHA*)

R^2 = 0.717			R^2_{adj} = 0.710				RMSE = 0.293				MAPE = 0.215				
Predictor	X_1	X_2	X_3	X_4	X_5	X_6	X_7	X_8	X_9	X_{10}	X_{11}	X_{12}	X_{13}	X_{14}	X_{15}
Transf.	X_1	$1/X_2$	X_3^2	$\sqrt{X_4}$	X_5^2	X_6^2	$\sqrt{X_7}$	$\sqrt{X_8}$	$1/X_9$	$1/X_{10}$	X_{11}^2	X_{12}^2	X_{13}	$1/X_{14}$	X_{15}^2

The same comparison can be made with the efficiency metrics for the regression model focused on the CP-SPL for the DNN regression in **Table 4.6** and the CR of **Table 4.4**, leading us to the same qualitative conclusions. Values of $R^2 = 0.717$ and MAPE= 0.215 for the DNN model and of $R^2 = 0.693$ and MAPE= 0.17 for the CR suggest again that predictors explain better the variability of Ψ_{fitted} but the error in absolute percentage is more significant for the DNN regression model.

It becomes clear that when evaluating and comparing the efficiency of any model, at least the two measures employed for the analysis carried out lines above should be used before a more reliable conclusion can be driven.

4.4.2. Gradient Boosting Decision Tree Regression

In general terms, decision trees are predictive (or estimation) models governed by binary rules (yes/no) that let the observations of the predictor variables, X_i, split the response variable values into segments depending on the X_i's attributes. Then, the prediction of the response variable is obtained as the mean of all response variable values contained in the segments generated at the last split. In a single decision tree configuration, the built segments are known as terminal nodes or *leaves*, the points where the binary decisions are made are the internal nodes or splits, and the segments connecting two splits are the *branches*.

The idea of a single decision tree model, described in the previous paragraph, brings a few drawbacks. For instance, unlimited ramifications of the decision tree can generate a very complex and *deep* structure such that terminal nodes would be developed in the same number as independent observed response values exist in the database, causing overfitting. On the other hand, insufficient or unprecise splits could lead to *weak* tree structures resulting in poor response estimations. A set of strategies and hyperparameters are available to overcome general issues regarding the generation, training, and testing of the decision tree models. One of the solutions to tackle the problems mentioned above is the *ensemble* methods. The ensemble methods combine multiple small tree structures called *weak learners* in a single system, thus obtaining a better prediction from the whole instead of a single unit (Hastie et al., 2009). The ensemble method used in this study is the so-called *Gradient Boosting* ensemble, in which weak learners are sequentially trained and improved based on the error information coming from the previous one. This method employs a differentiable loss function that measures the error and its variability in order to adjust them as more weak learners are added to the model.

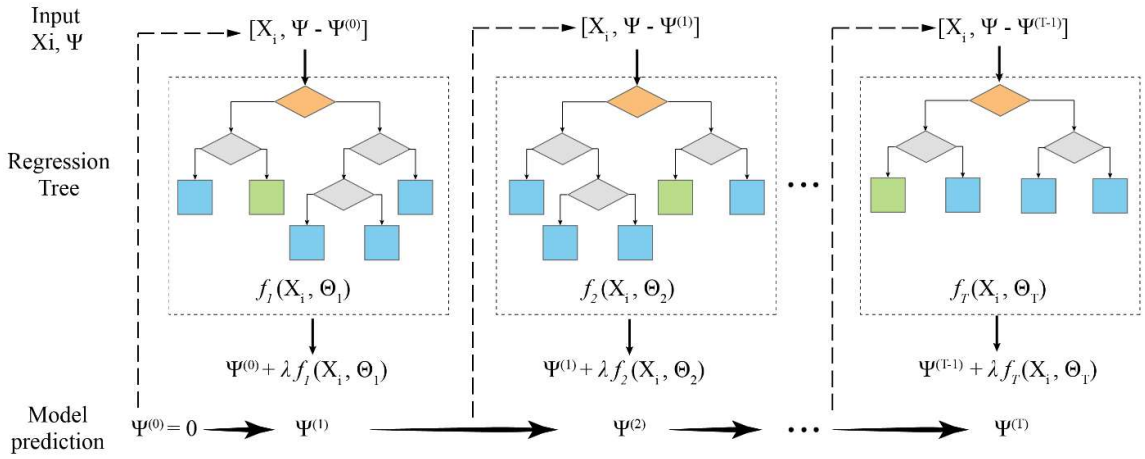

Figure 4.16. Architecture schematization of a Gradient-Boosting-Regression Tree (GBRT) regression model. Adapted from (Wang et al., 2020)

A schematization of the architecture of a Gradient Boosting Regression Tree (GBRT) is shown in **Figure 4.16**. T weak learners are consecutively trained having the X_i and a measure of the error from the predictions made a step before as input data. The outcome of each weak learner is the function $f_j(X_i, \Theta_j)$ that has the information relative to the structure of the independent j^{th} weak learner and the residuals of its estimation, i.e., $\Psi - \Psi^{j-1}$. This function is affected by a penalty parameter λ or learning rate used to control the importance of the weak learner estimations relative to that of the whole system. Finally, this outcome is added to the estimations of previously defined trees to prepare the input for the next, and the process goes on until certain criteria are met.

In addition to the ensemble method, some hyperparameters must be defined and optimized to generate an adequate GBRT regression model. Among the most important are: the learning rate parameter, λ, to ponderate the contribution of each weak learner within the whole system, the number of estimators or weak learners that are consecutively added, the subsample parameter representing the fraction of observations to be used for fitting the independent weak learners, the minimum number of observations required to split an internal node, the minimum number of observations required to be at the terminal nodes or leaves, the maximum depth of the individual weak learners related to the number of branches that a learner can be made of, and the random_state or random seed given to the weak learners to control the random permutation of predictors X_i and the random split of the training data.

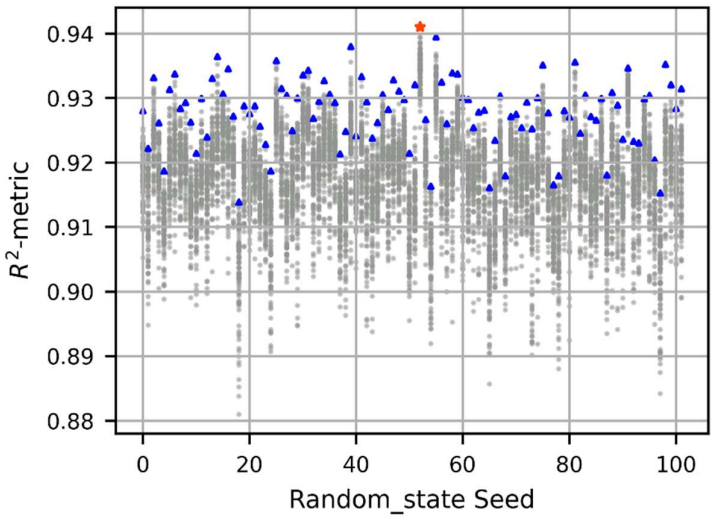

Figure 4.17. Visualization of the GBRT hyper-parameters optimization process for obtaining the best R^2 value. Reference example case, AP:LTHA / DT:*SSIDs* / BSC:*fixBase* / SPL:LS

To generate the most accurate GBRT regression model to be used in estimating Ψ-response, a recursive optimization process was performed on each desired model to get the appropriate hyperparameter for each specific estimation of Ψ_{fitted}. A typical result of the hyperparameter optimization is shown in **Figure 4.17**.

In the figure, each grey point represents a change in the hyperparameters described in the previous paragraph, as the random seed varies from 0 to 101. It can be observed that the determination of these hyperparameters can alter the efficiency of the estimation based on the R^2 metric. For the particular example of the figure in which the *SSIDs-flexBase*-NSP-CP combination is examined, R^2 value varies within a range between approximately 0.88 and 0.94; that is, 6% spanning the minimum and the maximum reachable R^2. Hence, the importance of tuning the hyperparameters becomes evident.

As for the DNN regression model generation and any other ML technique, the dataset must also be divided into train and test portions while building the estimator model. **Figure 4.18** and **Figure 4.19** depict the evolution of R^2 in the GBRT models as the train portion is increased from 60% to 90% for the LS and the CP structural performance level, respectively. All four DT-BSC combinations are evaluated for each AP in each figure. Once again, it can be observed that the less efficient model is generated when the MRSA Ap is employed in the performance assessment and Ψ_{fitted} estimation in both figures. Like for the DNN regression model, for the GBRT counterpart, the NSP AP is the procedure inducing the best R^2 values for every DT-BSC-SPL combinations but for the *convDs-fixBase*-CP, where the LTHA performs better.

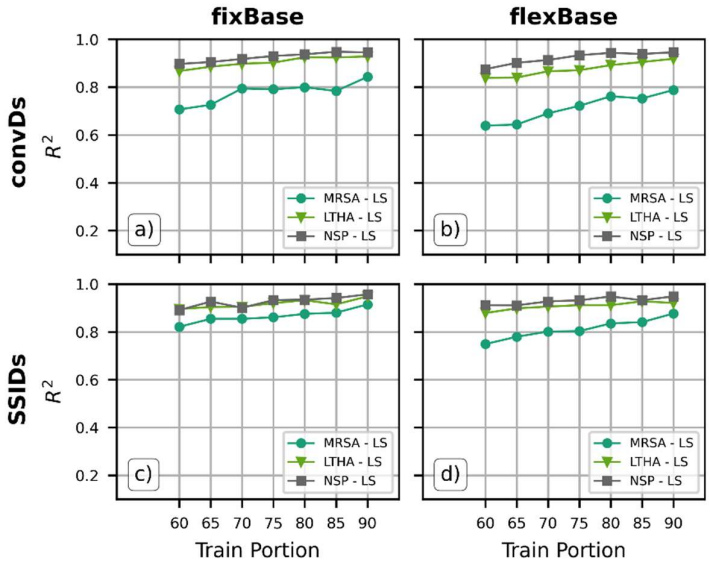

Figure 4.18. Maximum R^2 values obtained with GBRT model depending on different train portions selected from the whole database evaluating the LS-SPL. a) and b) for *convDs*-DT with *fixBase* and *flexBase* BSCs, respectively. c) and d) for *SSIDs*-DT with *fixBase* and *flexBase* BSCs, respectively.

It is also important to note that as the train portion increases, the R^2 value also increases. It was explained earlier that decision trees are more susceptible to developing overfitting of the estimator leading to potentially unrealistic responses. Thus, by observing the graphics in **Figure 4.18** and **Figure 4.19**, selecting an 80-20 train-test ratio could be a reliable dataset split ratio.

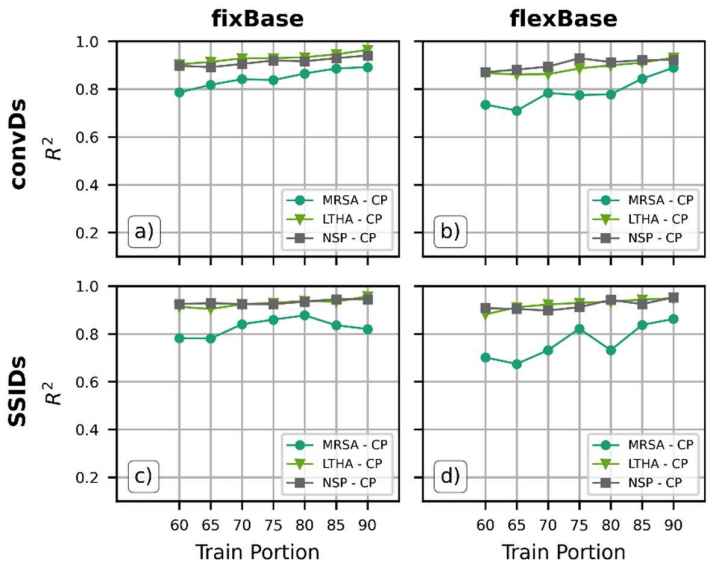

Figure 4.19. Maximum R^2 values obtained with GBRT model depending on different train portions selected from the whole database evaluating the CP-SPL. a) and b) for *convDs*-DT with *fixBase* and *flexBase* BSCs, respectively. c) and d) for *SSIDs*-DT with *fixBase* and *flexBase* BSCs, respectively.

For the selected 80-20 test-train split ratio, the achieved R^2 for every DT-BSC-AP-SPL combination is presented in **Figure 4.20** in a summarized fashion. It can be noticed that, as could be anticipated from **Figure 4.18** and **Figure 4.19**, the best AP option for deriving Ψ_{fitted} translators is the NSP overall. It is true that again for the *convDs-fixBase* combination, the LTHA gives slightly better efficiency metric values, but in general terms, NSP still prevails. Nevertheless, it is worth acknowledging that employing the GBRT regression technique helps increase the efficiency of the responses obtained from the MRSA AP, reaching R^2 values over 0.80 for most of the combinations but those of the *flexBase* BSC in the *convDs*-LS and -CP combinations and for the *SSIDs*-CP. Despite what would be thought regarding this observation, it indicates a convenient fact. It suggests that regardless of the DT-SPL combination, it would be enough to calculate the $DCR_{(ac)}$ performance indicator of a *fixBase* BSC structural model analyzed using the MRSA AP to approximate the actual $DCR_{(ac)}$ (DT-*flexBase*-NDP-SPL) using its corresponding $\Psi_{fitted}{}^{DT:fix}_{MRSA:SPL}$ translator. It is obviously advantageous due to the simplicity of assessing a structure using the MRSA AP under fixed-base conditions; it is most common to professionals and less time-consuming compared to the LTHA and the NSP procedures. Besides, the R^2 values thus obtained (0.80 or greater), are above what was obtained for the best-case scenario using the DNN regression models, leading to potentially good predictions.

As for the other analysis procedures employed in determining Ψ_{fitted} translators, it is evident that NSP is the one showing the best overall R^2. However, the LTHA also provides nearly the same good estimation results with R^2 over 0.90. In this regard, the $DCR_{(ac)}$ obtained from the performance assessment using either the NSP or LTHA would be successfully translated to the target-$DCR_{(ac)}$.

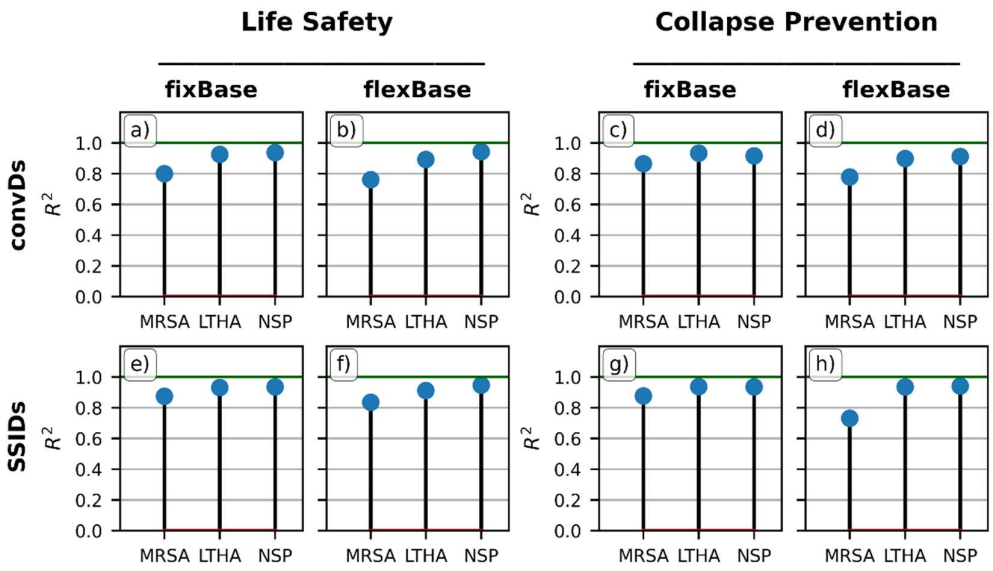

Figure 4.20. R^2 values obtained from the GBRT Regression analysis for all combinations of DT / BSC / AP / SPL.

Unlike the DNN, the GBRT regression technique allows us to determine the importance ratios of every predictor involved in generating the regression model. This model outcome is critical for a rational qualitative evaluation of the Ψ_{fitted}'s behavior. For instance, **Table 4.7** shows the most significant predictors to define the variability of Ψ_{fitted} for the SSIDs-flexBase-NSP combination, which leads to the highest R^2 among the combinations for the LS-SPL. Efficiency statistics for this model are also presented in the table.

Table 4.7. Statistical efficiency metrics and GBRT Regression results. Example case for best R^2 values for the LS-SPL / (*SSIDs – flexBase – NSP*)

$\boldsymbol{R^2}$ = 0.948	$\boldsymbol{R^2_{adj}}$ = 0.947	**RMSE** = 0.129	**MAPE** = 0.043
Predictor $\boldsymbol{X_i}$		**Transf.**	**Importance Ratio**
X_6		X_6^2	0.600
X_3		$\sqrt{X_3}$	0.118
X_2		$\log X_2$	0.039
X_{10}		X_{10}^2	0.038
X_8		$\sqrt{X_8}$	0.036
			$\Sigma =$ 0.831

Predictors X_6, X_3, X_2, X_{10}, and X_8 corresponding respectively to λ_{str}, $\tilde{T}_n/T_n$, $\tilde{T}_n$, $\tilde{S}_{ax}$, and a_o are five of the most significant predictors summing up to 83% of the total influence assigned to the whole set of predictors. The other 17% is explained by the other ten predictors not presented in the table but still part of the GBRT regression model. Note that the most significant characteristic of the structure for defining the model is the slenderness ratio λ_{str}. It should be recalled that this parameter is one of the

key characteristics in anticipating potential SSI effects in the building's response, along with a_o, also present in **Table 4.7**. The strong λ_{str} significance can be explained by connecting three ground ideas: (1) the slenderness ratio is defined by the expression $2h^*/B$, (2) the building height is directly proportional to the period of vibration T_n, so the expression defining λ_{str}, to some extent, relates the buildings' flexibility with the stiffness against its rotation about the weak axis that B provides, and (3) one of the most meaningful effects of the SSI phenomenon is the period elongation which is expressed through Eq. [4.31] for an SDOF system. It is reasonable to assume, based on these considerations, that λ_{str} is closely related to the period elongation effect and hence to the change in the spectral acceleration demand that modifications in the vibration period of the flexible-base structure induce.

$$T_n = T_n\sqrt{1+\frac{k}{k_x}+\frac{kh^2}{k_{yy}}} \qquad [4.31]$$

With a smaller importance ratio, are also included the period elongation ratio, the flexible-base structure fundamental period related to SSS characteristics, and the spectral assessment acceleration parameter showing that the estimation of Ψ_{fitted} also depends on the seismic demand of the flexible-base system.

On the other hand, the efficiency metrics indicate that R^2 is as high as 0.948 and a percentual absolute error, MAPE, as low as 4.3%; showing good estimation model capabilities.

Table 4.8. Statistical efficiency metrics and GBRT Regression results. Example case for best R^2 values for the CP-SPL / (*SSIDs – flexBase – NSP*)

$\boldsymbol{R^2}$ = 0.942	$\boldsymbol{R^2_{adj}}$ = 0.940	**RMSE** = 0.155	**MAPE** = 0.048
Predictor X_i		**Transf.**	**Importance Ratio**
X_6		X_6	0.543
X_3		X_3	0.087
X_8		X_8	0.038
X_{10}		X_{10}	0.038
X_1		X_1	0.038
			$\Sigma =$ 0.744

Regarding the combination leading to the best estimation model for the CP-SPL, see from **Table 4.8** that the SSIDs-flexBase-NSP prevails again. The R^2 and MAPE metrics for this model also reach scores indicating its high efficiency, and as for the significant predictors, there is a consistency compared to the ones listed in **Table 4.7**. The slenderness ratio (X_6) appears as the most influencing predictor in the response, followed by the period elongation ratio (X_3), the dimensionless frequency (X_8), the

assessment spectral acceleration parameter for the flexible-base structure (X_{10}) and at least the fixed-base fundamental period. The latter differs with respect to the model generated for the LS-SPL but still is the least important of the five shown in the table. Finally, it is worth noting that, as shown in **Table 4.8**, there was no need for variable transformation to reach a good estimation model. However, it shall be recalled that the standardization and scaling processes are always performed before any model is built.

4.5. Review and Discussion on Performance Estimation Models

From the performance assessment carried out in Chapter 3 to the *convDs*- and *SSIDs*-designed buildings, performance indicators $DCR_{(ac)}$ have been obtained employing different analysis procedures, namely, the MRSA, the LTHA, the NSP, and NDP. These $DCR_{(ac)}$ were used to introduce a novel parameter Ψ-factor described in Eq. [3.43], which aims to expose the relationship between the performance indicators. The ultimate purpose of the Ψ-factor was displayed in the current chapter, set to be used as a translator. It aims to obtain a so-considered *actual* measure of a building's seismic performance described by the $DCR_{(ac)}$ of either a *convDs* or *SSIDs* designed structure assessed with *flexBase* base support conditions through the NDP when any of both SPL from the selected performance objective is evaluated, i.e., the $DCR_{(ac)}{}^{DT:flex}_{NDP:SPL}$. Such a translation involves the generalized operation shown in Eq. [4.32] following the considerations exposed by the end of Section 3.6.

$$DCR_{(ac)}{}^{DT:flex}_{NDP:SPL} = \Psi^{DT:BSC}_{AP:SPL} \times DCR_{(ac)}{}^{DT:BSC}_{AP:SPL} \quad [4.32]$$

In addressing this goal, the urge to define an appropriate $\Psi^{DT:BSC}_{AP:SPL}$ translator was tackled by generating estimation models that lead to approximations of such a translator fitted to the observed values calculated per Eq. [3.43], whose behavior can be explained by the X_i-predictors listed in **Table 4.1**. In this regard, three methods for regression analysis were presented in this chapter: Classical Linear Regression Analysis, Deep Neural Networks, and the Gradient Boosting Regression Trees. The last couple are based on Machine Learning techniques.

The efficiency achieved in the estimation models built through these three regression methods was measured and evaluated in their corresponding sections separately. Also, the adequacy of generating such models starting from APs different from the NDP was studied, yet separately too. Hence, this section consolidates the information gathered throughout this chapter to reach broader conclusions regarding the generated models and their most advisable uses.

With this in mind, **Figure 4.21** and **Figure 4.22** first depict, using bar plots, the R^2 metrics achieved in each regression method, for every DT-BSC-AP combination when the LS and CP SPLs are evaluated, respectively. As anticipated from previous sections, the regression method exhibiting the most

efficient prediction model in all studied combinations is the GBRT method. Another recognizable pattern in these figures is the fact that, in order to reach such high-efficiency levels, besides using the GBRT technique, Ψ observations calculated through the NSP or the LTHA must be used to build the estimation model that approximates the translator $\Psi_{AP:SPL}^{DT:BSC}$ (or Ψ_{fitted} as denominated throughout this chapter). In this manner, R^2 is likely to reach values of 0.90 or higher most of the time.

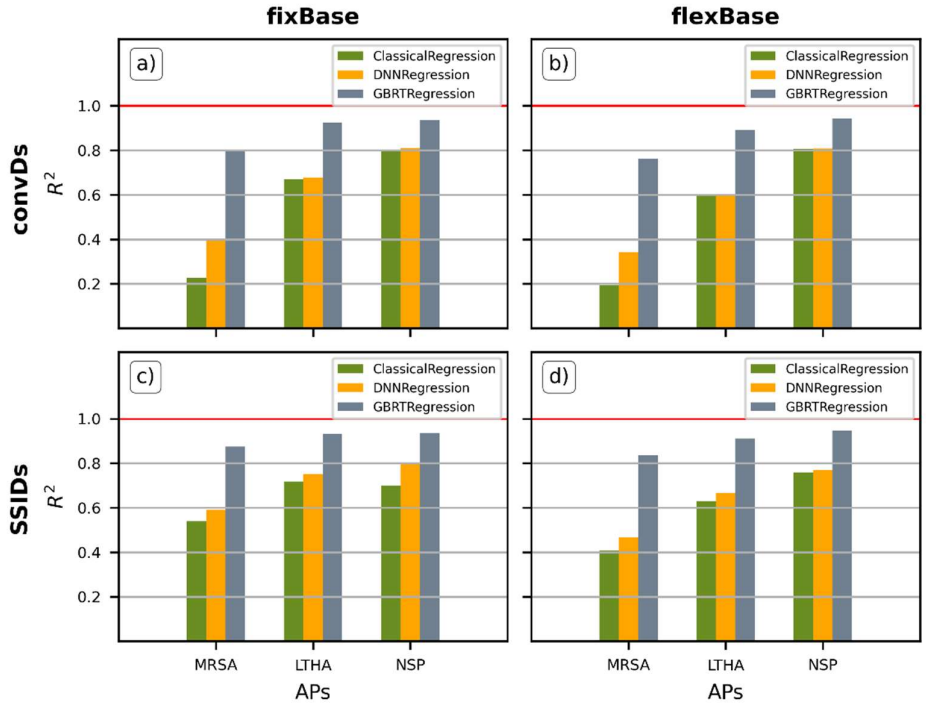

Figure 4.21. Comparison of regression techniques efficiency depending on the AP employed in the assessment for the LS-SPL. a) and b) for *convDs*-DT with *fixBase* and *flexBase* BSCs, respectively. c) and d) for *SSIDs*-DT with *fixBase* and *flexBase* BSCs, respectively.

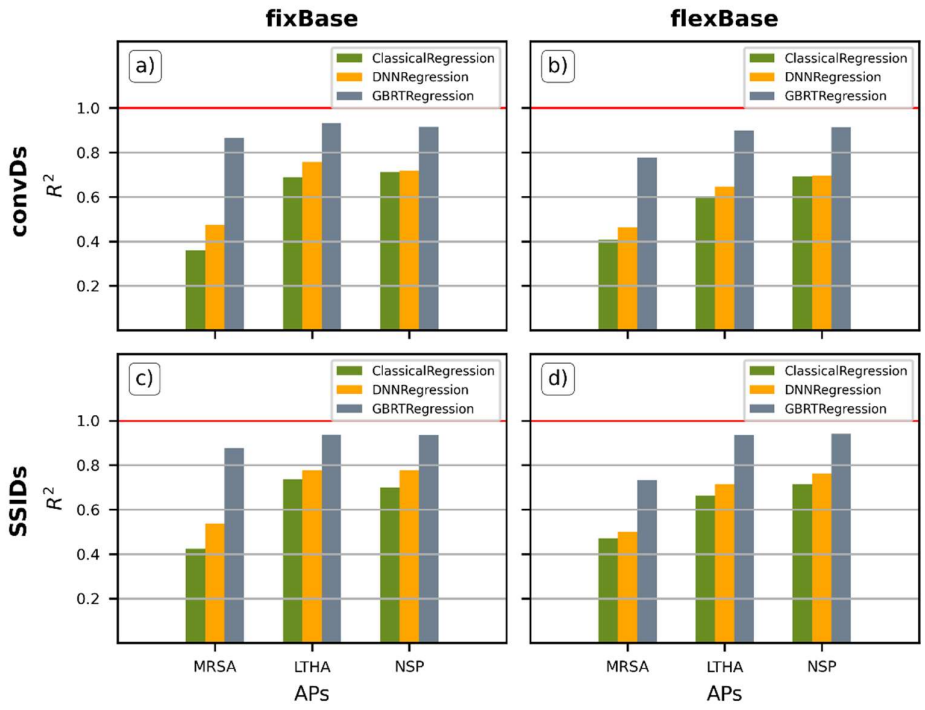

Figure 4.22. Comparison of regression techniques efficiency depending on the AP employed in the assessment for the CP-SPL. a) and b) for *convDs*-DT with *fixBase* and *flexBase* BSCs, respectively. c) and d) for *SSIDs*-DT with *fixBase* and *flexBase* BSCs, respectively.

Nevertheless, it is worth noting that regression models built based on Ψ_{fitted} calculated based on an MRSA procedure may not be overestimated or neglected for the GBRT technique. R^2 metrics indicate, in general, the presence of good estimation models (0.80 or greater) for all DT-BSC-SPL combinations but for those in **Figure 4.22b** and **Figure 4.24b** and **d**. As mentioned in Section 4.4.2, this is considered rather advantageous.

On the other hand, **Figure 4.23** through **Figure 4.25** are presented to get a deeper insight into the behavior of Ψ_{fitted} translators relative to its predictors of influence and visually inspect the agreement between the observed and fitted values of this factor.

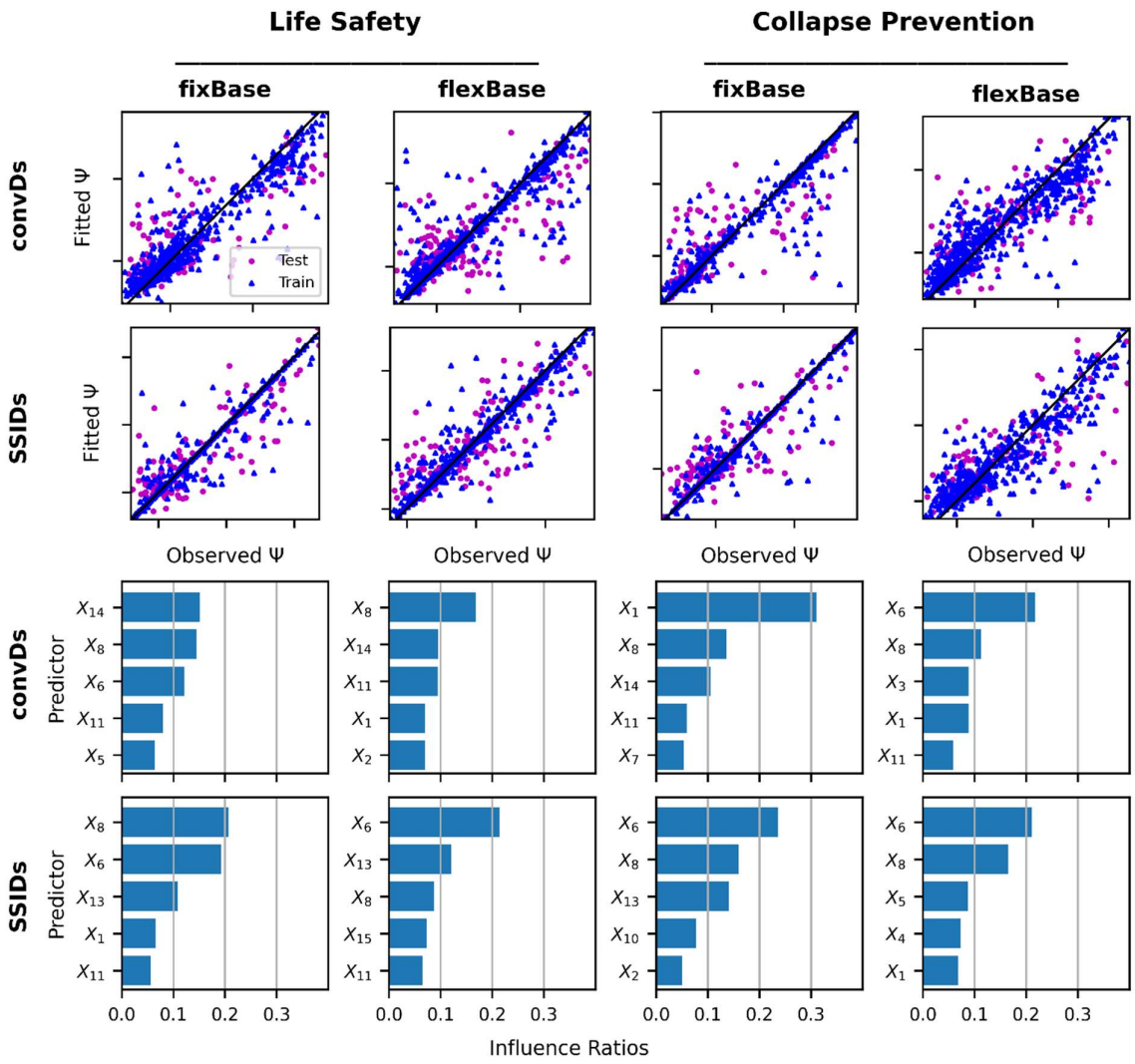

Figure 4.23. Observed vs. fitted values agreement for train- and test-portions of Ψ-factors database, using the GBRT technique at the MRSA-AP responses (top couple of rows). Most influencing X_i-predictors and corresponding influence ratios (bottom couple of rows). Different combinations of DT-BSC for both LS and CP SPLs are shown.

Observed versus fitted values from the train (triangled-blue dots) and test (rounded blue dots) splits of Ψ-factor are shown using scatter plots in the figures. Bar plots indicating the importance ratio value in the horizontal scale for five of the most significant predictors are also depicted to measure the level of their influence in Ψ_{fitted} estimation model. This information is introduced for every DT-BSC-SPL combination for the MRSA (**Figure 4.23**), the LTHA (**Figure 4.24**), and the NSP (**Figure 4.25**) analysis procedures.

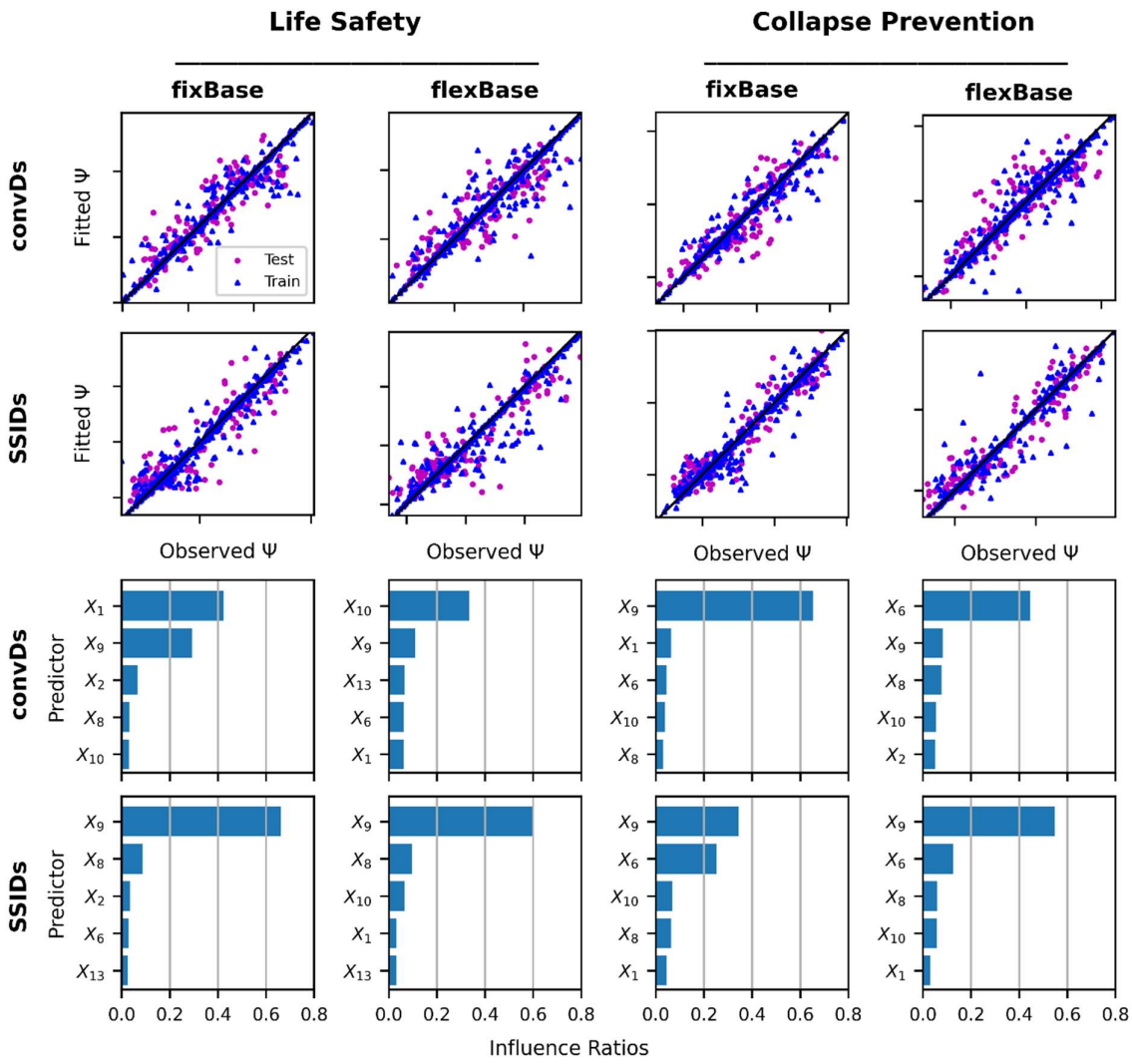

Figure 4.24. Observed vs. fitted values agreement for train- and test-portions of Ψ-factors database, using the GBRT technique at the LTHA-AP responses (top couple of rows). Most influencing X_i-predictors and corresponding influence ratios (bottom couple of rows). Different combinations of DT-BSC for both LS and CP SPLs are shown.

Overall, it shall be noted that a good agreement between the observed and fitted Ψ values is achieved regardless of the analysis procedure used. As would be expected from analyzing **Figure 4.21** and **Figure 4.22**, sparsity in the scatter plots from the MRSA is wider than the other analysis procedures due to the lower R^2 and higher MAPE values shown in the corresponding section. However, they still offer acceptable performance.

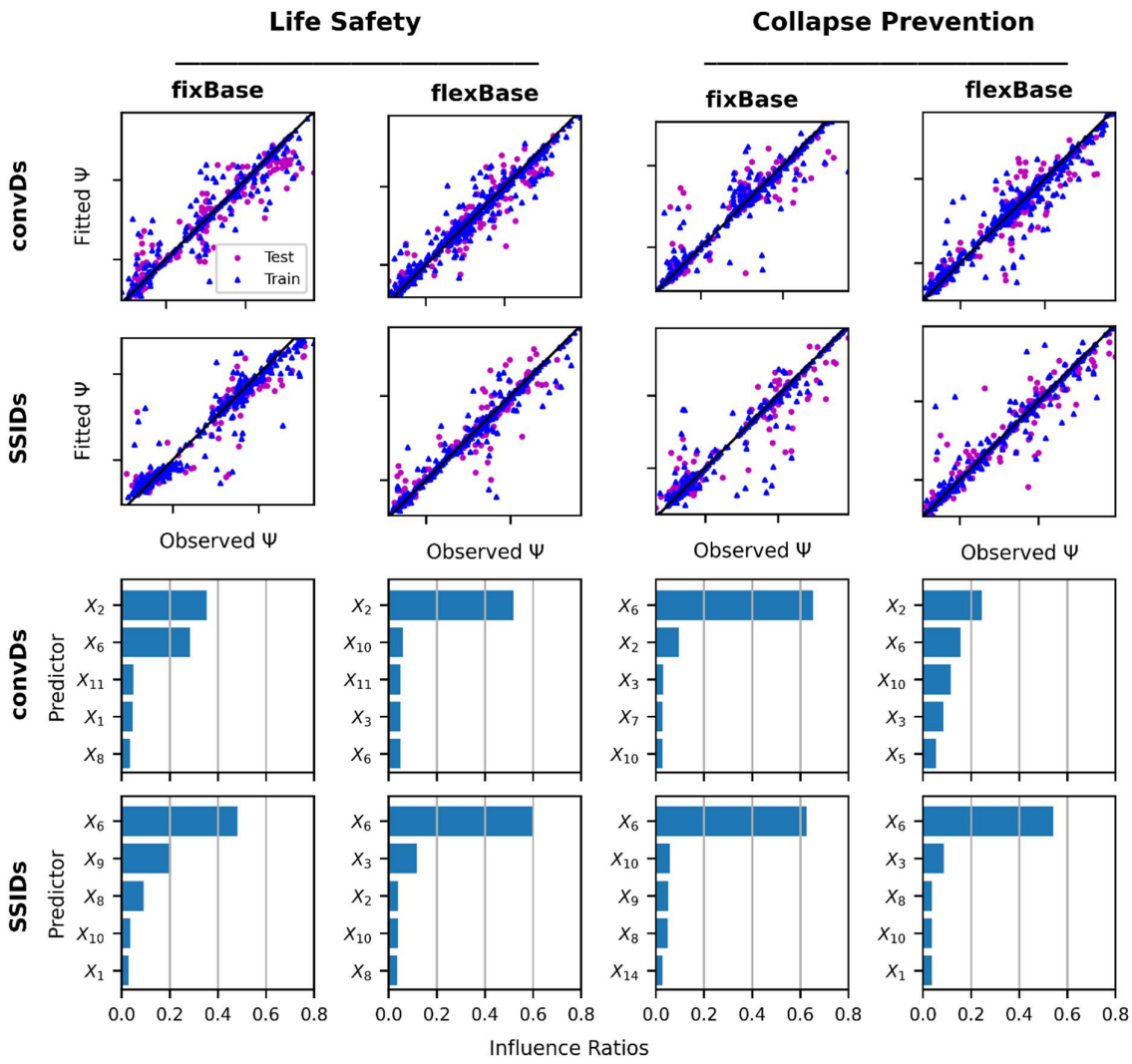

Figure 4.25. Observed vs. fitted values agreement for train- and test-portions of Ψ-factors database, using the GBRT technique at the NSP-AP responses (top couple of rows). Most influencing X_i-predictors and corresponding influence ratios (bottom couple of rows). Different combinations of DT-BSC for both LS and CP SPLs are shown.

One of the most relevant results in this section is related to the influence ratios or predictor significance, shown as bar plots in the last figures. Observe, for instance, the predictor's influence ratio in the estimation model for Ψ-factors calculated based on MRSA AP in **Figure 4.23**. Even though the most influencing predictor among the chosen 15 can be appreciated, the magnitude of its influence ratio does not differ much from the rest in the top five. This behavior is repeated for all DT-BSC-SPL combinations but for the *convDs-fixBase*-CP, where the most influencing predictor, $X_1 = T_n$, doubles the influence ratio value of the following one, $X_8 = a_o$. Notice thus, that the influence ratios' magnitudes are at or below a value of 0.20 for most cases, and the influence quota is sort of evenly distributed among the predictors.

It is not the case when analyzing the influence ratios from the LTHA and the NSP analysis procedures in **Figure 4.24** and **Figure 4.25**, respectively. The influence quota is typically concentrated in a sole

predictor. The most likely influence ratio magnitude for such a predictor ranges between 0.40 and 0.60, leaving the rest of the predictors with a lower influence quota to fulfill. Thus, it would be reasonable to think that for estimating the target-Ψ implicit nonlinear nature the most accurately through the linear MRSA AP results, it would be necessary to consider the influence of more than one predictor variable that wraps the explanation of Ψ's variation. The opposite is true for more sophisticated APs such as the LTHA and the NSP. For generating a GBRT estimation model based on the results of these APs, just one or two predictors suffice to collaborate with a considerable influence in the explanation of Ψ variability.

Still, a question arises: what predictors are the most influencing when estimating the translator factor, Ψ? The color-coded information presented in **Table 4.9** helps answer that question. Data in the table is separated into two blocks, each for the evaluated LS and CP SPLs. The numerical value displayed in each table's cell (accompanied by the grey quadrant-split boxes) is calculated as the average influence ratio of all DT-BSC combinations for the specific AP-X_i coordinate, ponderated to the maximum value thus calculated in the whole SPL block. This way, the influence ratios presented in **Figure 4.23** through **Figure 4.25** are condensed in this sole table. It means that, in the LS SPL block, values in the 45 cells will range from 0 to 1, and the gray boxes quadrants will turn blue as their value approach 1. This helps us identify the most influential X_i predictor (the more box quadrants are turned into blue or the higher its value) for the LS-SPL regardless of the DT-BSC-AP combination.

The color scheme, on the other hand, addresses the most influencing predictors associated with a specific AP only; the darker the color, the more influence the predictor exerts while generating the model. For example, it can be noticed from the LTHA row in the CP-SPL block that S_{ax} and λ_{str} (X_9 and X_6 respectively) are the most influencing predictors regardless of the DT-BSC combination.

Table 4.9. Influencing predictors in the overall behavior of Ψ_{fitte} response variable.

	Predictors															
AP	X_1 T_n	X_2 $\tilde{T}_n$	X_3 $\tilde{T}_n/T_n$	X_4 v_{so}	X_5 σ_{SSI}	X_6 λ_{str}	X_7 B/L	X_8 a_o	X_9 S_{ax}	X_{10} $\tilde{S}_{ax}$	X_{11} V_y^*	X_{12} S_{ax}^*	X_{13} V_d^*	X_{14} μ^*	X_{15} R_d^*	
MRSA	0.15	0.13	0.13	0.05	0.12	0.35	0.12	0.37	0.07	0.10	0.18	0.10	0.21	0.20	0.12	LS
LTHA	0.33	0.11	0.05	0.03	0.03	0.07	0.06	0.15	1.00	0.27	0.07	0.06	0.08	0.05	0.04	LS
NSP	0.08	0.56	0.13	0.01	0.07	0.85	0.05	0.12	0.15	0.10	0.09	0.05	0.06	0.06	0.05	LS
MRSA	0.26	0.08	0.11	0.07	0.10	0.35	0.09	0.29	0.06	0.10	0.11	0.08	0.14	0.11	0.08	CP
LTHA	0.09	0.06	0.04	0.01	0.03	0.44	0.06	0.12	0.82	0.11	0.06	0.05	0.04	0.04	0.04	CP
NSP	0.07	0.20	0.12	0.03	0.05	1.00	0.05	0.08	0.05	0.12	0.06	0.04	0.05	0.07	0.04	CP

Notice that what was stated for the MRSA-AP regarding the need to consider additional predictors that explain the nonlinear nature of the Ψ-factor is evidentiated in the table. In the LS-SPL block of data is more notorious that MRSA requires the V_y^*, and the μ^* predictors' contribution of information regarding the nonlinear condition of the building. Nevertheless, the most influencing predictors for the case mentioned are the dimensionless frequency a_o and the slenderness ratio λ_{str}, in that order. In addition, it is not negligible the influence of the fundamental period of the *fixBase* building, T_n. And

the same pattern repeats with different proportions in the CP-SPL block for the MRSA, showing consistency in the results for both SPLs.

Examining LTHA for both SPLs blocks, it can be noticed that the *fixBase* BSC assessment spectral acceleration parameter, S_{ax} is the most influencing predictor. It is followed by either T_n in the LS block or the λ_{str} in the CP block. These two predictors are correlated, though, since the slenderness ratio depends on the buildings' height as the *fixBase* fundamental period does. Hence it would also show consistency, at least in a rational physical way.

Lastly, it should be noted that the NSP AP is the one showing more consistency between the LS and CP blocks. The most influencing predictors for both cases are λ_{str} and $\tilde{T}_n$, followed by $\tilde{S}_{ax}$ and a_o in a lesser but not negligible degree.

In an overall manner, it can be appreciated that the most influential predictors when generating an estimator for the translator Ψ, regardless of the DT-BSC-AP-SPL combination, are dynamical properties of the structure such as either T_n or $\tilde{T}_n$, some measures of their nonlinear characteristics wrapped into V_y^*, V_d^*, and μ^* (only if MRSA is used), by far, some indicators of the SSI effects presence such as λ_{str} and a_o, and a measure of the seismic demand preferable through S_{ax}. There are some predictors that, in perspective, can be neglected, such as the soil shear-wave velocity, v_{so}, the footprint aspect ratio B/L, also S_{ax}^*, and R_d^*. Most of them will be neglected in the evaluations coming in the following chapter.

As closure remarks, it can be stated that the most appropriate regression method for estimating the translator factors Ψ_{fitted} is the GBRT regression method based on ML techniques. Traditionally, professionals have been used to operating with equations when explaining a physical phenomenon mathematically. However, it was demonstrated throughout this chapter that the classical regression alternative would not be adequate for fulfilling the purpose of this study. Eqs. [4.19] through [4.29] would lead to inaccurate estimations even though they may result practical to use them.

ML-generated models, on the other hand, while throwing more accurate estimations, are no longer straightforwardly applicable; the models are not equations anymore but computational objects that require to be evaluated through a computer. This fact could be a drawback when a professional application is desired. However, every time is more common to have and make use of digital resources to enlarge the professional's toolkit and capabilities. In this regard, digital resource libraries are now available from where apps or collections of programming scripts can be stored and retrieved. Aware of the necessity of making the GBRT estimation models here generated available to readers, one of these libraries is used to share them. Hence, data is open to download and use at the following web address:

https://mybinder.org/v2/gh/jsbaquero86/SSI_PBSD/HEAD?labpath=SSI_ModFactors.ipynb

5. Recommended Modifications on the Prescriptive Seismic Design with considerations of SSI Effects

5.1. Overview

In terms of prescriptive building design considering soil-structure interaction (SSI) effects, e.g., ASCE-7 allows determining a modified -reduced- design shear demand, $\tilde{V}$, which represents the interacting soil-structure system behavior. To define $\tilde{V}$, the conventionally calculated design shear demand, V, is reduced by a shear variation, ΔV, limiting the entire reduction through factor α as detailed in the following equation.

$$\tilde{V} = V - \Delta V \geq \alpha V \qquad [5.1]$$

In Eq. [5.1], α depends on the response modification factor (R), resulting in a more significant reduction for structures designed for limited inelastic response ($R = 3$) than for those designed for higher ductility ($R \geq 6$). This limitation reflects the little understanding of the interaction effects against R -especially for ductile structures- and the fact that these reductions are based on theoretical linear elastic models of the structure and the soil beneath.

Some research has focused explicitly on the design demand under SSI using different modeling and assessment approaches, comparing the seismic demand obtained from a flexible-base structure against its fixed-base counterpart. Results from 2D and 3D equivalent linear representations of the superstructure and the soil in (Torabi & Rayhani, 2014) and (Fu et al., 2018), or nonlinear single-degree-of-freedom (SDOF) models from (Lu et al., 2016), demonstrate an increase in the base shear demand of the soil-structure system (SSS). In (Emami & Halabian, 2020), 3D nonlinear models were studied, and their results suggest a 10% increase in the flexible-base structure demand over the design shear. From a probabilistic point of view, nonlinear SDOF-SSSs are evaluated in (Khosravikia et al., 2017) and (Mirzaie et al., 2017), where authors concluded that an unsafe design is likely to be obtained due to the excessive underestimation of the design shear demand. Another probabilistic analysis conducted in (Abtahi et al., 2020) suggests that the probability of the increase in demand can be even more significant when using a nonlinear MDOF instead of an SDOF used in previous references. Similarly, in the experimental evaluation of (Trombetta et al., 2015), it was found that up to a 63% increase in demand can be reached when considering SSI effects, compared to the analysis neglecting such effects.

In general, the conclusions driven by the above references differ from prescriptions related to the reduced design shear demand by code recommendations, as ASCE-7 does, showing that a lesser reduction is advisable in most cases. Moreover, depending on the SSS characteristics, the use of 2D

or 3D models, and the analysis procedure employed, the shear demand might be even higher than the one calculated for conventional design. Still, there is no overall consensus about under what circumstances SSI effects lead to a safer calculation of the design demand.

In light of this background, this chapter studies the behavior of α in ductile RC buildings while exposing the need to reflect the beneficial effects of SSI and the detrimental ones by increasing the magnitude of design shear demand. To this end, the same database of buildings designed and assessed in previous chapters is used. Also, linear and nonlinear APs are used considering *fixBase* and *flexBase* base support conditions (BSCs) following the same ASCE-41 recommendations employed in Chapter 3. In addition, α is estimated from the outcome of these analyses. Then, a predictive model is generated to estimate α using the already introduced Gradient-Boosting Regression Tree Machine Learning technique (GBRT-ML) (see Section 4.4.2). By the end of this chapter, it will be evident that, as expected, this factor can adopt values both lesser or greater than 1.0, exhibiting the ambivalent consequences of SSI effects in the design.

5.2. Basis of the prescriptive seismic design of buildings

Regular seismic design of buildings has traditionally been treated through code prescriptions to resist site-specific earthquake ground motions. These ground motion demands are generally described by a design response spectra (DRS), which represents the smoothened spectrum of maximum pseudo-acceleration responses of an SDOF system characterized by its vibration period. Underlying the concept of the DRS is the assumption that the system behaves mainly in its first mode of vibration; thus, the actual MDOF system can be replaced by an equivalent SDOF. Acknowledging that buildings can reach some level of nonlinear behavior during an earthquake, the ordinates of the DRS are affected by a response reduction factor, R, to get the magnitude of the base shear demand, V, used ultimately for the design. This process is depicted in **Figure 5.1**.

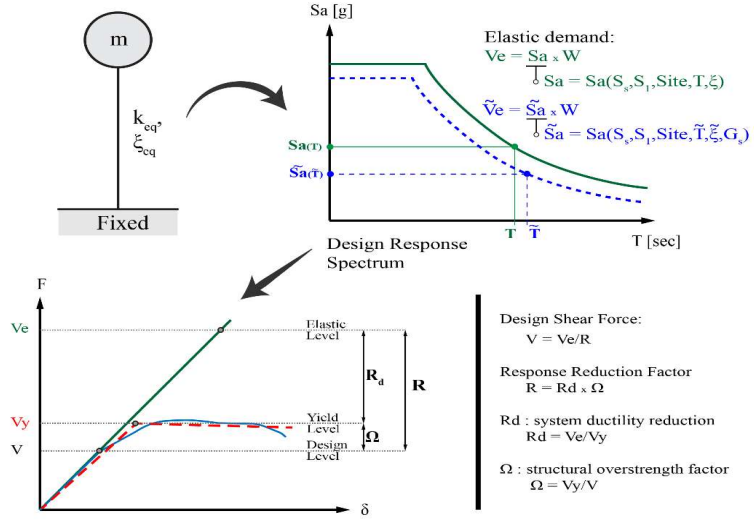

Figure 5.1. Conventional and SSI building design framework.

Regarding the seismic design considering SSI effects, the assumption of SDOF behavior still prevails along with the consideration of the beneficial-only effects of SSI, which, decades ago, has been demonstrated to be an oversimplification that might lead to unsafe designs (Mylonakis & Gazetas, 2000). As portrayed in **Figure 5.2**, the interacting effects are considered through the reduction of V in ASCE-7 standard. This reduction is calculated in terms of the flexible-base vibration period, $\tilde{T}_n$, and the increased damping ratio of the SSS. In **Figure 5.2**, ΔV represents the base shear demand decrement and $\tilde{V}$, the design shear demand for SSI considerations.

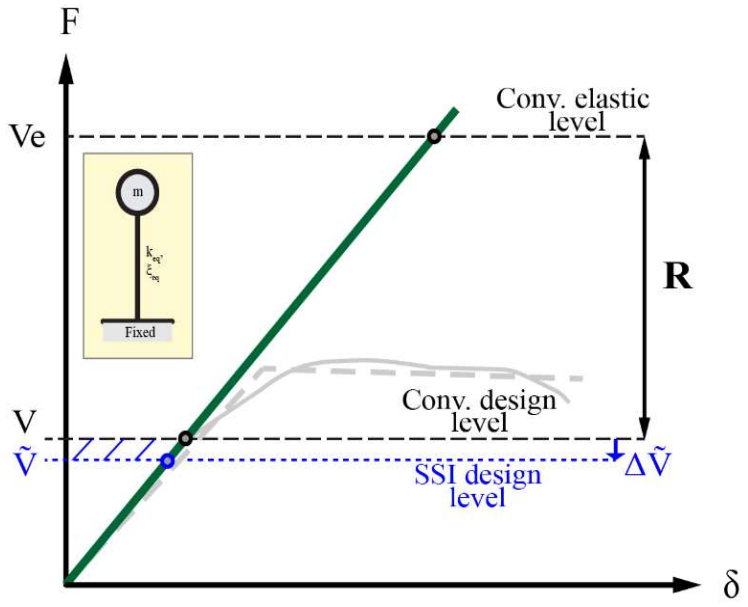

Figure 5.2. Base shear demand for accounting SSI effects.

As explained in Section 5.1, the magnitude of $\tilde{V}$ is limited by a factor α depending on the building's expected nonlinear capacity. The reduction of the demand allowed at buildings with lower expected nonlinear behavior ($R \leq 3$) is more significant than for those with a higher one ($R \geq 6$). The differentiation in the values that α can adopt reflects the knowledge over which these recommendations are founded. While theoretical linear elastic models were used to support the interaction effects embodied in ASCE-7, the actual responses should be better estimated from a nonlinear representation of both the superstructure and the soil beneath.

The building database described in Chapter 2.2 is again assessed in this chapter, this time focusing on providing a better insight into a more realistic modification of the design shear demand.

5.3. Procedure for assessing the effects of SSI on base shear

5.3.1. Analysis procedure-based scenarios for the definition of demands

Following Eq. [5.1], the α factor can be defined as the ratio of the *flexBase* system to the *fixBase* system design shear demand, as shown in Eq. [5.2].

$$\alpha = \tilde{V}/V \qquad [5.2]$$

In this regard, four different scenarios are proposed to determine α values that reflect a more realistic relationship between the demand expected in a flexible- compared to a fixed-base system. Each scenario corresponds to a hypothetical base shear response of a *convDs*-designed building when subjected to a Life Safety-Seismic Hazard Level (LS-SHL). Both *fixBase* and *flexBase* BSCs are considered using different APs during the analysis. Thus, α values were obtained by means of base shear responses from linear and nonlinear analysis procedures applied to each structure of the database, giving a chance to corroborate prescriptive reduction limitations and, at the same time, highlight the actual reduction/amplification from the SSI effects.

Scenario I in **Figure 5.3** considers the case in which alpha is calculated straightforwardly by simply taking the ASCE-7 prescribed design base shear demands. The α values thus obtained represent a control-value definition. Eq. [5.3] mathematically reflects α for this scenario.

$$\alpha_1 = \frac{V_{dsgn}^{flex:el}}{V_{dsgn}^{fix:el}} \qquad [5.3]$$

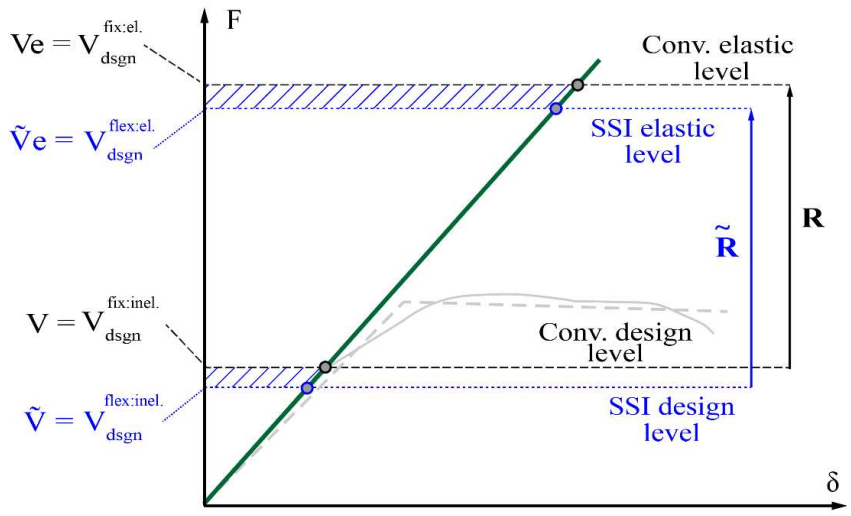

Figure 5.3. Analysis Procedure cases for which α can be obtained. Scenario I: as prescribed in ASCE-7

Secondly, Scenario II of **Figure 5.4** involves the base shear response from a *flexBase* building using the Modal Response Spectrum Analysis (MRSA) and compared again to the prescribed *fixBase* base shear demand. For this case, α is determined according to Eq. [5.4].

$$\alpha_2 = \frac{V_{MRSA}^{flex:el}}{V_{dsgn}^{fix:el}} \qquad [5.4]$$

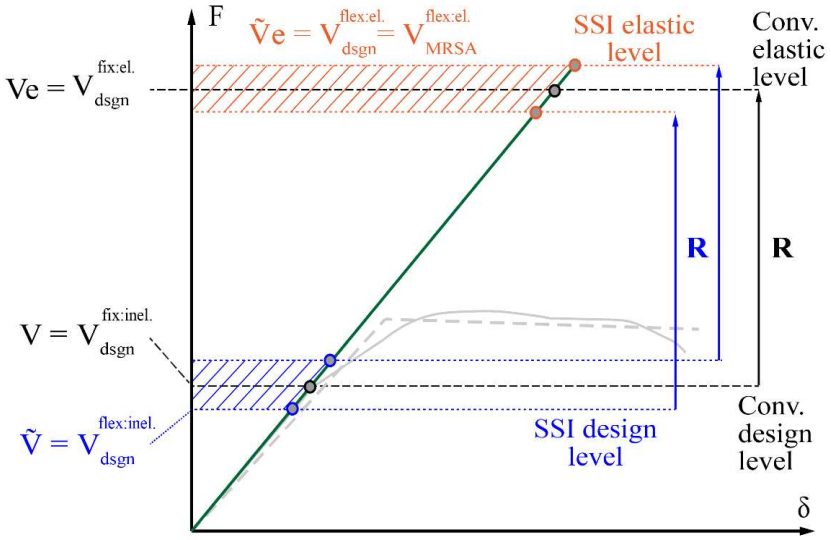

Figure 5.4. Analysis Procedure cases for which α can be obtained. Scenario II: Considering MRSA flexible-base shear demand as SSI elastic level.

On the other hand, Scenario III, shown in **Figure 5.5**, considers the NSP for determining the nonlinear base shear response of a *flexBase* building. Here, it is assumed that this response equals the yielding strength, $\tilde{V}_y$, due to the mentioned BSC. Since this scenario relates to a nonlinear procedure, the *fixBase* building base shear demand used in determining α is the actual design value, $V_{dsgn}^{fix:el}$, but taking into account the flexible-base overstrength parameter, $\tilde{\Omega}_{(T_n)}$, and the response reduction factor, R, as detailed in Eq. [5.5].

$$\alpha_3 = \frac{V_{NSP}^{flex:inel}}{\tilde{\Omega}_{(T_n)} \dfrac{V_{dsgn}^{fix:el}}{R}} \qquad [5.5]$$

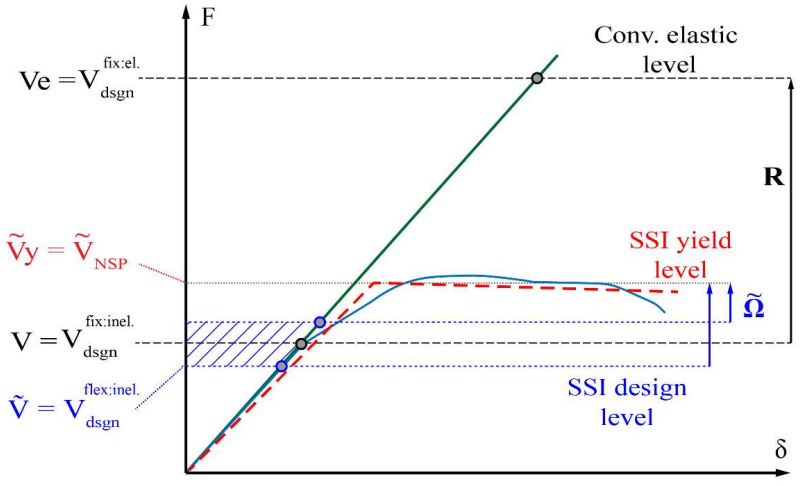

Figure 5.5. Analysis Procedure cases for which α can be obtained. Scenario III: Using NSP flexible-base shear demand along with $\tilde{\Omega}_{(T_n)}$ to get $\tilde{V}$.

Where $R = 8$ was used here, as suggested by ASCE-7 for special RC moment frame buildings. The parameter can be calculated from the Pushover analysis as the ratio of the maximum base-shear capacity of the *flexBase*-BSC building to the design base-shear from the *ConvDs*. Alternatively, Eq. [5.6] provides a reasonable estimation of $\tilde{\Omega}_{(T_n)}$ in terms of the fixed-base period of vibration derived from a regression analysis on the 729 design cases of the database. The study of this parameter and how Eq. [5.6] is derived is addressed more in-depth in **Appendix F**.

$$\tilde{\Omega}_{(T_n)} = \frac{1.969T_n - 0.841}{T_n - 0.456} \qquad [5.6]$$

Lastly, following the same train of thought, Scenario IV of **Figure 5.6** relates the *flexBase* building nonlinear base shear response from an NDP. It is assumed that, for the LS-SHL, the nonlinear base demands obtained from the nonlinear dynamic procedure (NDP) approximate the value of $\tilde{V}_y$. Refer to Eq. [5.7] for the calculation of α in this scenario.

$$\alpha_4 = \frac{V_{NDP}^{flex:inel}}{\tilde{\Omega}_{(T_n)} \dfrac{V_{dsgn}^{fix:el}}{R}} \qquad [5.7]$$

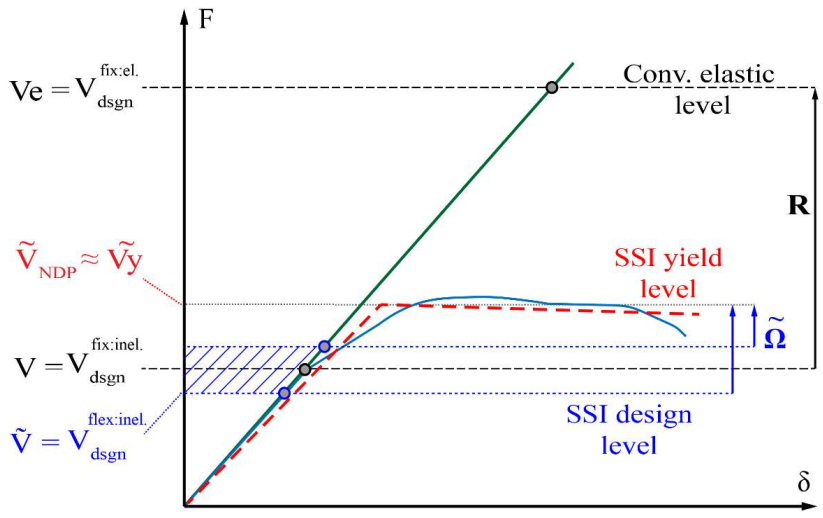

Figure 5.6. Analysis Procedure cases for which α can be obtained. Scenario IV: Using NDP flexible-base shear demand along with $\tilde{\Omega}_{(T_n)}$ to get $\tilde{V}$.

5.3.2. Seismic demand for the analysis

As mentioned in the previous section, the seismic demand for the structural assessment corresponds to the LS-SHL. For this study, let's recall that $S_s = 1.50g$ and $S_1 = 0.817g$ were selected in Section 2.3 as short period ($T_n = 0.2s$) and $1.0s$ period spectral acceleration parameters, respectively. Again, a response spectrum was constructed based on these parameters when using either MRSA linear

analysis or NSP for the nonlinear analysis procedures for evaluating Scenarios II and III. When dealing with *flexBase* BSCs, such spectrum is modified following the recommendations of ASCE-41, applying Section 2.4 for the General Horizontal Response Spectrum and Section 8.5 for the Soil-Structure Interaction Effects prescriptions, already introduced in this document.

For the NDP, the same suite of eleven ground motion pairs (two orthogonal horizontal directions) is employed for determining the nonlinear base shear demand ($V_{NDP}^{flex:inel}$) detailed in Eq. [5.7]. The procedure for adjusting and scaling the ground motions before applying them to the structural models follows the steps enumerated in Section 3.4.3.

With these demand considerations, along with the descriptions of the Scenarios based on available APs, calculated values of α are presented in the next section.

5.3.3. Obtained α values

From the structural assessment and calculation of α with Eqs. [5.3] to [5.7], at the frequency histograms of **Figure 5.7**, one can tell the range of values this factor can adopt depending on the evaluated scenario.

Interesting findings can be derived from analyzing plots in **Figure 5.7** by couples. Consider, for instance, scenarios I and III (**Figure 5.7a, c**). Both are related to APs that lean on the assumption of an SDOF behavior; hence, a tight range of α values can be appreciated in the two scenarios. In the case of scenario I, it was expected to be this way because α values are calculated using prescriptive base shear demands, as the reader may recall. On the other hand, a wider range of α values are found by observing scenarios II and IV (**Figure 5.7b, d**). MRSA and NDP analysis procedures employed in these scenarios consider the participation of higher modes during the analysis, which clearly influences the response of the *flexBase* building.

Now, consider scenarios I and II together (**Figure 5.7a, b**). APs used for these scenarios are both linear procedures, and as can be appreciated from these two plots, α values are more frequent to lay below unity for both cases. Scenarios III and IV (**Figure 5.7c, d**) use nonlinear procedures, and for both cases, values of α are found beyond unity more frequently.

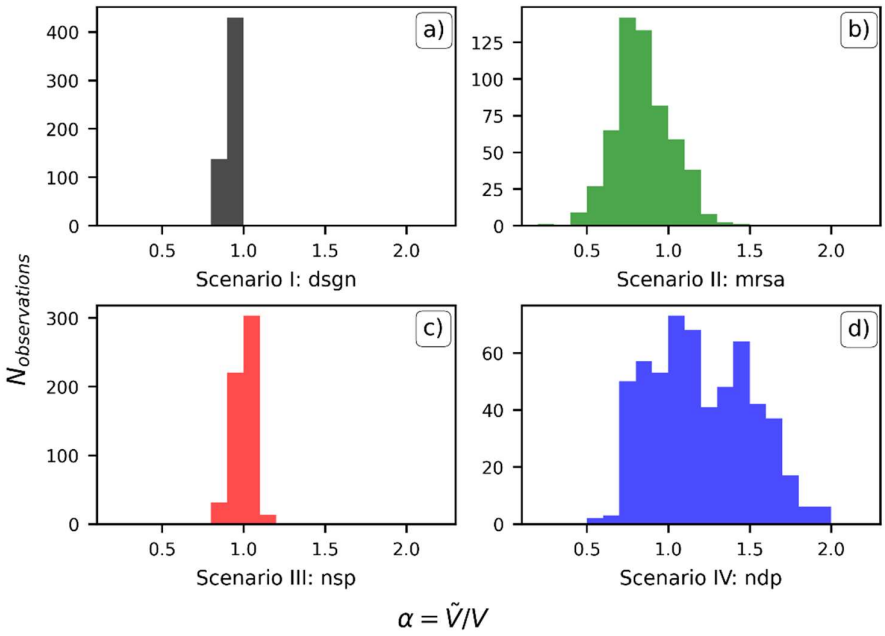

Figure 5.7. Frequency histograms for obtained values of α. a) Scenario I, b) Scenario II, c) Scenario III, and d) Scenario IV.

The previous analysis suggests that depending on the AP used and the sections' mechanics considered during analysis, SSI effects outcomes can vary considerably. Only beneficial SSI effects are obtained for linear analysis through an SDOF behavior assumption; hence the always-below-one recommendations found at ASCE-7. A broader range of SSI effects can be appreciated through nonlinear dynamic procedures considering the actual MDOF behavior. Moreover, the beneficial or detrimental consequences of the interaction are evident, as α_4 (α of scenario IV) adopts values of $1.20 \pm 2\sigma_{a,}$ where 1.20 is the mean value of α_4 and σ_a the standard deviation ($\sigma_a = 0.30$). This scenario is considered to be the more realistic. Hence, it is used in the next section to develop predicting models.

5.4. Regression models for the estimation of α

Regression techniques have already been introduced in Chapter 4, two of those techniques are used in this section to find helpful models that estimate the value of α: the Classical Linear Regression and the Gradient-Boosting Regression Tree ML (GBRT-ML) technique. **Figure 5.8** sketches the process of generating a prediction model for the current evaluation of α values and the predictor used. Based on a preliminary analysis and acknowledging from Chapter 4 that not all the selected predictors in **Table 4.1** are significant for explaining performance-related parameters, the number of predictors for the study in the current section has been reduced to eight. Hence, the predictor variables considered here are referred to as X_1 to X_8, being the fixed-base vibration period, T_n, the flexible-base vibration period, $\tilde{T}_n$, the period elongation ratio, $\tilde{T}_n/T_n$, the shear wave velocity at small strain level, v_{so}, the wave parameter, σ_{SSI}, the slenderness ratio, λ_{str}, the footprint aspect ratio, B/L, and

the dimensionless frequency, a_o, respectively. All parameters making up the predictors shown in **Figure 5.8** have been introduced and described earlier in Section 4.2.

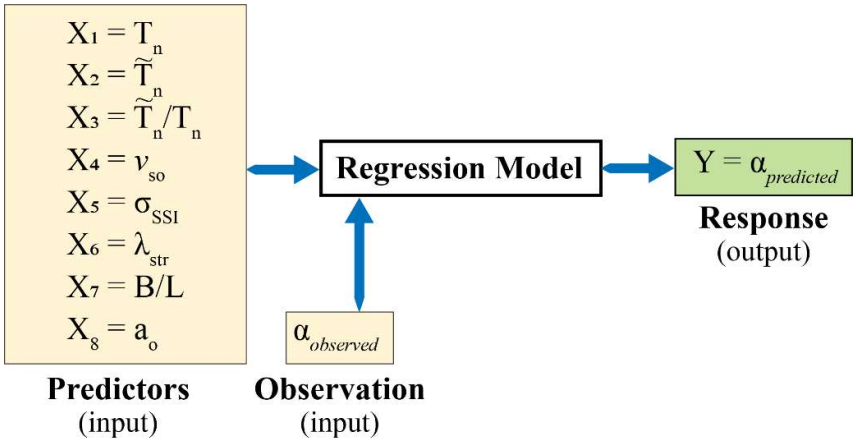

Figure 5.8. Schematization of selected predictors and responses for the regression model.

Additional input for generating the model is the calculated or observed value of the response (α_{obs}). The predictor variables and the observed response conform to the input parameters needed to create a predictive model.

5.4.1. Classical regression method outputs

Before dealing with classical linear regression analysis, a Pearson-correlation coefficients matrix is developed and shown in **Figure 24**. These coefficients uncover how two variables are linearly correlated by evaluating their magnitude. For instance, the correlation between variables is strong for values of the Pearson correlation coefficient close to unity. Conversely, if coefficients are close to zero, there is no appreciable correlation.

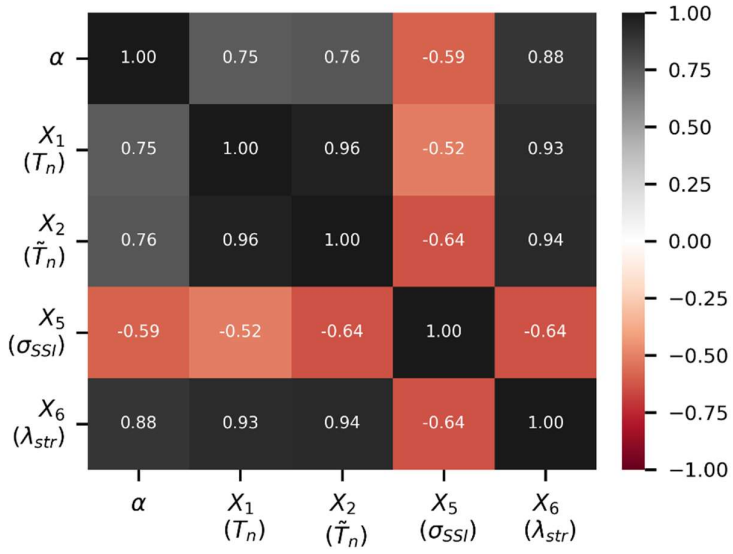

Figure 5.9. Pearson-correlation coefficients matrix for representative predictors against α.

Among the eight considered predictors, only four resulted in values for the Pearson coefficient against α greater than $abs(0.50)$, showing a considerable degree of correlation and therefore included in the matrix. In that sense, in **Figure 5.9**, it is evidenced that the strongest correlation of α occurs against X_6 predictor (slenderness ratio, λ_{str}), followed by X_1 predictor (T_n). However, these two predictors are also strongly correlated, which may seem obvious from the fact that the vibration period of buildings is frequently well approximated with a function of the structure's height. Therefore, for the classical linear regression, X_6 is used to find a predictive equation that describes the response in the form of:

$$\alpha\left(X_6\right)_{PP^{th}} = \beta_1 X_6 + \beta_2 \qquad [5.8]$$

Where PP^{th} stands for the PP percentile of α values considered in the specific regression equation, and β_1 and β_2 are the regression coefficients. Three percentiles were adopted to consider a lower-bound, an upper-bound, and a median value of the predicted value of α, α_{pred}.

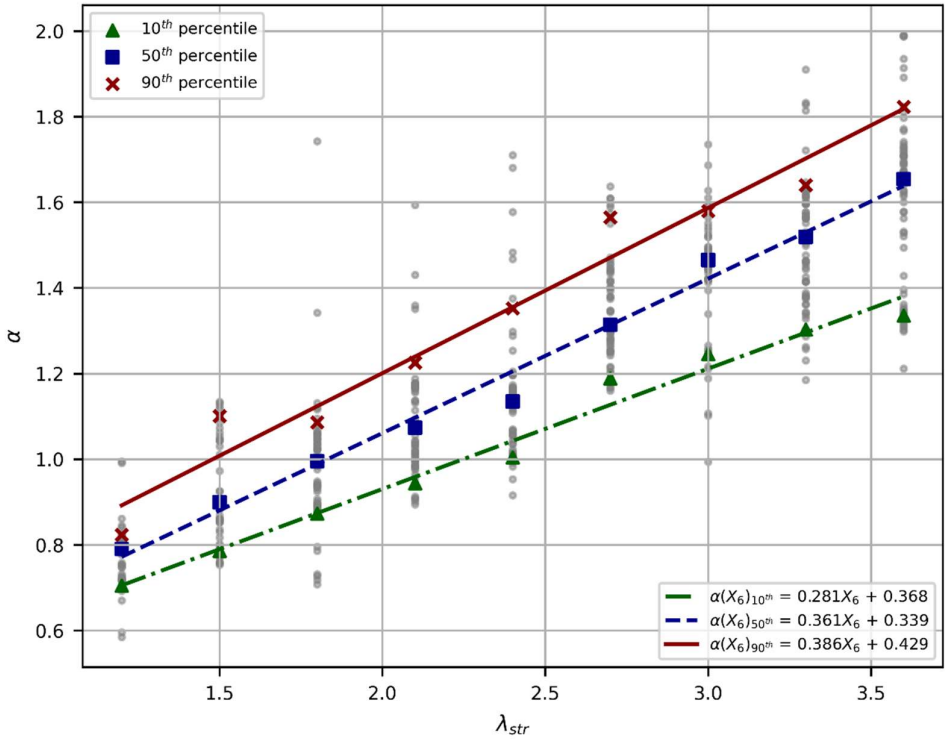

Figure 5.10. Linear estimation functions for α. The solid (red) line for the 90^{th} percentile, the dashed (blue) line for the 50^{th} percentile, and the dashed-dotted (green) line for the 10^{th} percentile

Figure 5.10 depicts a scatter plot of observed values of α relative to λ_{str} where, as can be noticed, the scale in which is presented the slenderness ratio corresponds to the unstandardized and unscaled values. The three bounds for which the regression equations are generated are also shown in the figure, demonstrating a strong correlation between these two parameters. Regression equations

having the form of Eq. [5.8] are also explicit in **Figure 5.10** as an outcome (regression model) of the CR process; nevertheless, they are also presented below in Eqs. [5.9] through [5.11].

$$\alpha_{(X_6)10^{th}} = 0.281\, X_6 + 0.368 \quad [5.9]$$

$$\alpha_{(X_6)50^{th}} = 0.361\, X_6 + 0.339 \quad [5.10]$$

$$\alpha_{(X_6)90^{th}} = 0.386\, X_6 + 0.429 \quad [5.11]$$

These equations have R^2 regression coefficients of 0.980, 0.988, and 0.967 for the lower-bound, median, and upper-bound regression equations, respectively. It should be emphasized that since the regression analysis has been performed considering the unstandardized and unscaled values of the predictor, these equations can be used straightforwardly with a direct calculation of λ_{str} before using the proposed equations. It is worth noting that the values of α_{pred} reflect both the beneficial and detrimental effects of SSI. In the case of the median-value regression equation representation (blue dashed line), for example, values of this factor span from 0.80 to approximately 1.60. These results imply that a reduction in the demand could be permitted at buildings with λ_{str} between 1.00 to 1.70 (relatively squat structures). In contrast, for slender buildings with λ_{str} greater than 2.00, an amplification of the demand should be considered.

5.4.2. Gradient-Boosting Regression-Tree. Machine-learning regression outputs.

Although this technique has already been introduced in Section 4.4, a brief explanation of the procedure for generating the regression model using such an ML technique is presented in the next paragraph.

First, the entire predictors and response values database is split into two sub-sets oriented to train (80% of the set) and test (20% of the set) the model. In addition, an algorithm written from scratch for this research was in charge of optimizing other hyperparameters of the model to obtain the best R^2. The graphical results of this optimization algorithm are shown in the top plot of **Figure 5.11**. A red star indicates the best determination coefficient obtained from the optimization process, giving $R^2 = 0.9$.

The bottom-left plot in **Figure 5.11** depicts the train and test data versus the observed values. It is clear that the predicted values suitably fit the observed ones when considering at least the four predictors detailed in the right-bottom plot of the same figure. Notice how the predictor X_6, is confirmed to be the most important predictor among the eight initially selected, confirming the findings of the CR method. This method (GBRT-ML technique), in contrast to the classical linear regression, uses more than one predictor to explain the variation of α. This explains, in part, why R^2 for the GBRT method is lower than the ones obtained from CR. Nevertheless, both techniques deliver R^2 greater than 0.90, giving a good fit.

As can be noticed up to this point, the results obtained from the analysis carried out in this chapter show that the demand used traditionally for the seismic design of RC ductile buildings, according to ASCE-7, may be underestimated. It is evident from the scenario-based comparison of the seismic demands that structures are indeed subjected to higher forces than those prepared to withstand following recommendations of ASCE-7 with SSI effects considerations.

Through the regression analysis performed, it was demonstrated that the slenderness ratio parameter, λ_{str}, is the most important in correlating a structure characteristic to the increment or decrement of the design forces translated in the α parameter. Predictor models were thus generated to estimate this parameter and expressed as α_{pred}.

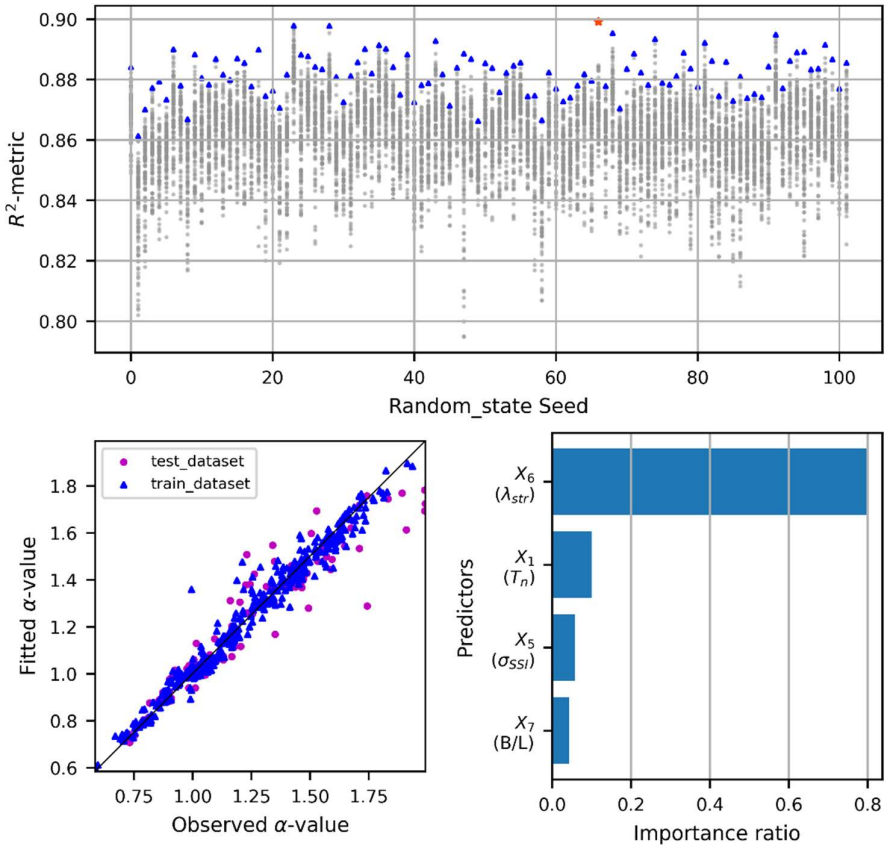

Figure 5.11. Results from GBRT-ML technique. (top) optimization process outcome for the highest R^2, (bottom-left) observed versus fitted α, and (bottom-right) sorted importance ratio for key predictors.

This predicted value can be employed to modify the traditionally calculated base-shear demand, V, to get $\tilde{V}$. However, there is still a need not only to address the design forces but also to control the inelastic deformations that could be generated during ground motion events, and should be taken care of during the design process. In sections to follow, this specific evaluation is further studied.

5.5. Assessing Inelastic Deformations from NDP

The previous section presented recommendations for modifying the seismic design shear forces. Still, the seismic design of buildings, according to ASCE-7, also involves the control of inelastic deformations (IDs) by limiting it to an allowable inelastic story drift ratio (ISDR), Δ_a, tabulated depending on the structural type. In the case of the structures that were designed to make up the buildings database, this Δ_a shall be determined according to Eq. [5.12] for Risk Categories I and II.

$$\frac{\Delta_a}{\rho} = \frac{0.025}{\rho} \qquad [5.12]$$

Where ρ is the Redundancy Factor applicable to structures assigned to the SDCs D, E, and F with a value of 1.30. Evaluating the previous equation for $\rho = 1.30$, the allowable ISDR becomes $\Delta_a/\rho = 0.019$.

It is worth recalling that when assessing the seismic performance of buildings for the LS SPL, according to FEMA 356 (FEMA, 2000), a 2% transient ISDR (0.02) is expected to develop a controlled damage state in the members of the concrete frame system. Given that the LS level of structural performance in this study is directly related to the expected design level performance, the 0.02 drift ratio mentioned above corresponds to that evaluated from Eq. [5.12]. With this fact in mind, it would be reasonable to assume that drift ratios obtained during the performance assessment carried out in Chapter 3 with any of the available APs (for the LS-SPL) should not result in values above $\Delta_a/\rho = 0.019$. Let us consider the ISDRs obtained from the *SSIDs* designed buildings' assessment of the *flexBase*-NDP BSC-AP combination for evaluating the LS-SPL. This study previously established that such a combination is assumed to show closer responses to the actual structural behavior; hence, it is considered again in this section as the reference point for drift quantities.

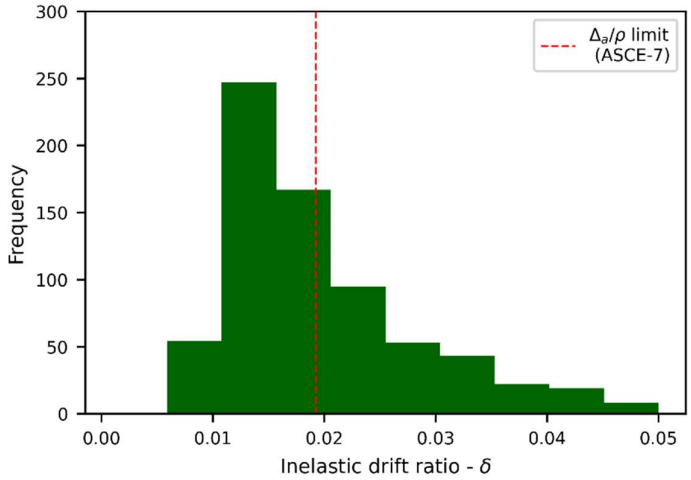

Figure 5.12. Frequency histogram for the inelastic story drift ratio, δ, for buildings in the database assessed for the *SSIDs-flexBase*-NDP-LS combination.

Figure 5.12 shows a frequency histogram of the measured maximum ISDR, δ, in each building of the database for the *SSIDs-flexBase*-NDP-LS combination. The limit value recommended by the ASCE-7 standard is also plotted in the graphic. Notice that even though the more frequent ISDR values lie below Δ_a/ρ, there are some assessed structures that show δ values beyond this limit. In some cases, the measured maximum ISDR values reach up to twice the prescriptive limit or higher values.

Focusing our attention on this observation, it is evident that the standard prescriptions regarding the seismic design considering SSI effects are again insufficient to fulfill minimum performance requirements. Similar to the case of the deficiencies in defining design forces, failing to limit the inelastic deformations in 3D nonlinear models can be explained by the fact that standard recommendations are based on theoretical linear elastic models of the structure and the soil instead of more realistic models. Moreover, it is important to mention that standard prescriptions address only the modification of the seismic design forces when considering SSI effects (refer to Section 5.2), and no further measures are taken for estimating and controlling the inelastic deformations during design.

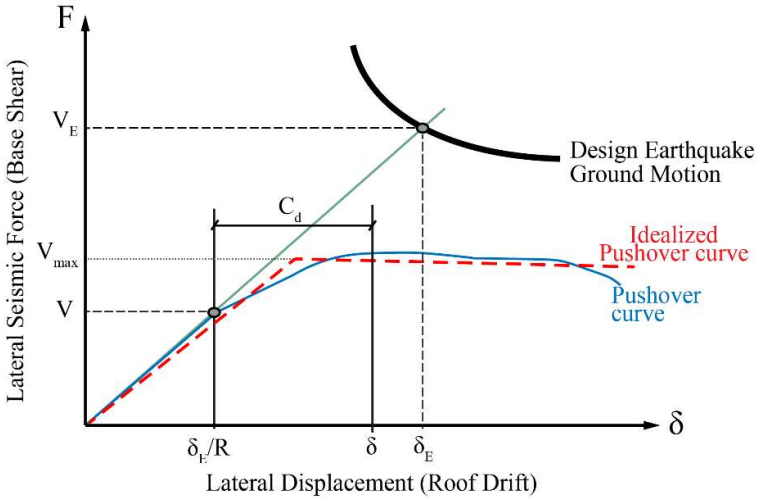

Figure 5.13. Graphical description of the meaning of C_d.

In practice, when designing structures using any LDP as the MRSA employed in Chapter 2, the ASCE-7 standard estimates the inelastic deformations using the so-called Deflection Amplification Factor, C_d. For this purpose, linear elastic story drift ratios quantities developed at the design level, δ_E/R, are multiplied by C_d to estimate the inelastic counterparts, δ, which is ultimately limited to Δ_a/ρ. Hence, the C_d factor can be described by Eq. [5.13].

$$C_d = \frac{\delta}{\delta_E/R} \qquad [5.13]$$

Where δ_E is the story drift ratio measured at the roof level, assuming the system remains elastic for the design earthquake level. All other parameters have been introduced earlier throughout the

document. **Figure 5.13** shows a graphical representation of the C_d factor depicted as a difference in lateral deformations measured in the horizontal direction. However, it should be emphasized that C_d obeys to the ratio shown in [5.13], and the way it is shown in the figure aims to ease the understanding of such a factor.

Theoretically, the deflection amplification factor recommended by ASCE-7 for every structural system could be expressed as in Eq. [5.14], assuming that δ equals Δ_a/ρ limit.

$$C_d^{theo} = \frac{\Delta_a/\rho}{\frac{\delta_{LDP}}{R}} \qquad [5.14]$$

Where δ_E have been replaced by elastic drift ratios calculated using any LDP, δ_{LDP}, at the LS-SPL. A more realistic C_d factor value could be obtained involving the responses calculated through the NDP, though, knowing that δ can be replaced by δ_{NDP} in Eq. [5.13]. The *real* C_d factor thus, would be expressed as follows:

$$C_d^{real} = \frac{\delta_{NDP}}{\frac{\delta_{LDP}}{R}} \qquad [5.15]$$

Even though it would seem evident, a ratio showing how above or below to the Δ_a/ρ limit the δ_{NDP} values are, results from dividing Eq. [5.15] by [5.14], leading to $\delta_{NDP}/(\Delta_a/\rho)$. The rational development of the ideas written in previous lines is deemed necessary since the ratio described earlier can also be interpreted as a correction factor of the C_d^{real} relative to the C_d^{theo} as expressed in Eq. [5.16].

$$\alpha_{C_d} = \frac{C_d^{real}}{C_d^{theo}} = \frac{\delta_{NDP}}{\Delta_a/\rho} \qquad [5.16]$$

Hence, a C_d factor adjusted to the actual structural behavior considering SSI effects can be determined for design purposes by operating the $\alpha_{C_d} \times C_d^{theo}$ product, where C_d^{theo} shall adopt the value recommended by the ASCE-7 standard. For the structural system evaluated in this research, $C_d^{theo} = 5.5$.

The correction factor α_{C_d} has been calculated employing the δ_{NDP} responses for the LS-SPL obtained from the buildings in the database to get an insight into its behavior. **Figure 5.14** shows a frequency histogram of α_{C_d} factor values along with the limit unitary value reflecting the condition when $C_d^{real} = C_d^{theo}$. Values above 1.0 relfect the need for an increase in the C_d^{theo} during the design process to limit the ISDR values and decrease otherwise. Notice the obvious resemblance with the frequency histogram in **Figure 5.12**. Even though it can be observed that α_{C_d} values below unity are more

frequent, there are still some structures resulting in actual values exceeding the C_d for which they where design.

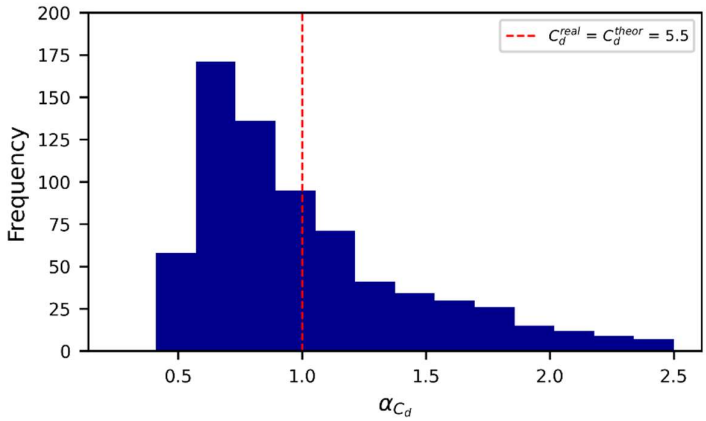

Figure 5.14. Frequency histogram of the correction factor α_{C_d} values calculated as per Eq. [5.16].

To tackle the inconsistencies presented so far and aiming to complement the analysis and recommendations exposed in previous sections of this chapter, estimation models of the correction factor α_{C_d} are developed. The procedure followed for this purpose is carried out in the same fashion as it was done for the force correction factor, α of Eq. [5.2]. First, a strong correlation is sought between the α_{C_d} factor, adopted as the response variable, and the same predictor variables detailed in **Table 4.1** to generate an estimation model in the form of an equation obtained through the linear classical regression method. Then, an ML estimation model alternative is evaluated and presented based on the GBRT technique for the same estimation purposes. It is important to mention that since these methods were already introduced and used in two chapters so far (refer to Sections 4.4 and 5.4.2), they are not addressed in depth throughout this section, but overall results and conclusions are driven and supported by graphical information presented in the following paragraphs.

5.5.1. Estimation Models for Correction Factor, α_{C_d}

Let us begin with the individual evaluation of possible relationships existing between the response and the predictor variables, α_{C_d} and X_i, respectively. As mentioned before, this study is done by observing if any strong correlation exists between both variable types. The heatmap presenting the Pearson correlation coefficient matrix is used again to identify any strong linear correlation as has been made before in this research. In this regard, refer to the heatmap displayed in **Figure 5.15**, where at least four predictor variables show a strong linear correlation, namely, the X_5, X_{10}, X_{13}, and X_{14} predictors corresponding to the wave parameter, σ_{SSI}, the *flexBase* assessment spectral acceleration parameter, $\tilde{S}_{ax}$, the *flexBase* to *fixBase* design force ratio, V_d^*, and the *flexBase* to *fixBase* deformation ductility ratio, respectively. All four predictors show correlation values above $abs(0.75)$.

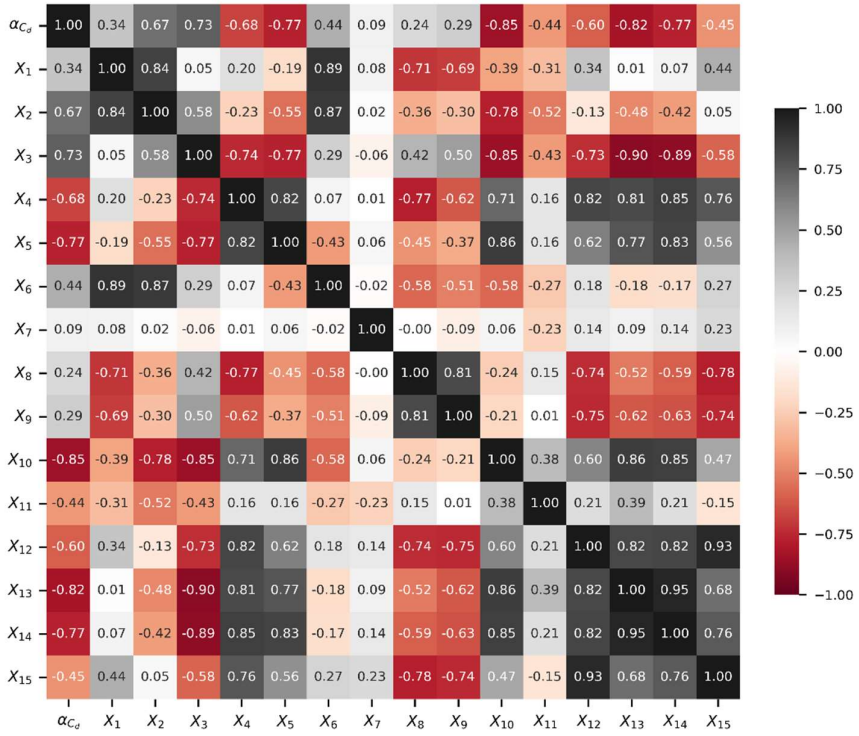

Figure 5.15. Heatmap showing the Pearson correlation coefficient between the response variable α_{C_d} and all selected predictors.

However, observing this heatmap more cautiously, one can tell that these variables are also strongly correlated with each other. Let us consider, for instance, the X_5 predictor. Relative to X_{10}, X_{13}, and X_{14} predictors, their Pearson coefficients are all above $abs(0.75)$. The same trend can be noticed by analyzing the rest of the predictors, indicating that theoretically, when using the classical linear regression method to generate an estimation model, any of these predictors could be used indistinctively.

Since the general purpose of this study is to give tools that facilitate the design process, the predictor selected (among the four identified earlier) for generating the estimation model based on the CR method is chosen in a way that is the most practical to calculate. Besides, such a predictor was selected, ensuring that it represents a parameter the most familiar to professionals with ground knowledge regarding the SSI effects and seismic design.

In that sense, two alternatives are presented for the estimation of α_{C_d} employing a couple of predictors from the previous analysis made on the heatmap of **Figure 5.15**. The first is the X_5 predictor (σ_{SSI}) of Eq. [2.1]. A curve-fitting function of the *scipy* of the Python package is used to adjust the curves for the 10^{th}, 50^{th}, and 90^{th} percentiles of the scatter data shown in **Figure 5.16**. This function employs the least squares method for adjusting a selected algebraic function shape, which in this case, a reciprocal function shape has been selected.

In regard to the σ_{SSI} predictor, it shall be recalled that it was mentioned in Section 2.2 that this parameter is one of the decisive parameters to establish the influence of the SSI effects. According to the literature (already referenced in the same section mentioned before), when σ_{SSI} values are below 10, it results imperative to consider the interacting effects, while higher values up to a limit of 20 indicate that the possibility of evidentiating SSI effects is still of consideration but not as important. Notice in **Figure 4.17** that this statement is confirmed by the behavior of the predictor relative to α_{C_d} correction factor. Focusing our attention on the median (50_{th}) and the (90^{th}) of the α_{C_d} values, it results evident that SSI effects induce an increase in the ISDR for σ_{SSI} values below 12.5 and 15, respectively; hence in the need of also increasing the C_d value for which the structures should be designed if SSI effects are to be controlled appropriately. For higher values, on the contrary, it can be observed that the SSI effects are still present but in this range for reducing the ISDR instead. It also corroborates that the interacting effects are always present in the structural response; a statement has also been established in advance.

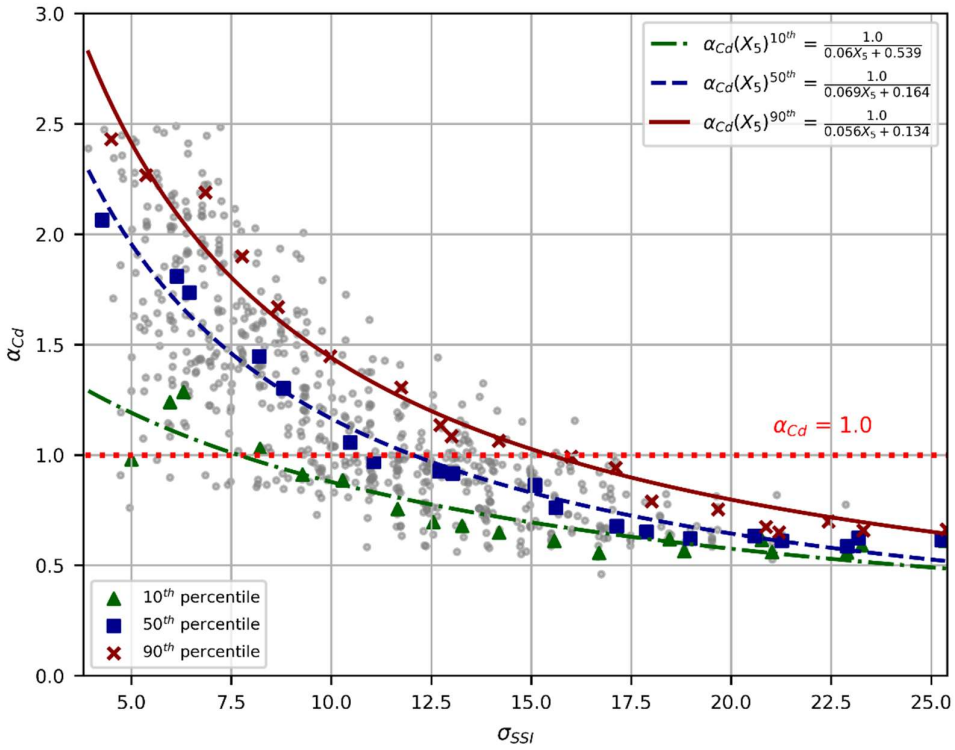

Figure 5.16. Scatter plot showing the relationship between the significant unscaled and unstandardized X_5 predictor, σ_{SSI}, and the response variable α_{C_d}. Regression model equations shown for the 10^{th}, 50^{th}, and 90^{th} data percentiles.

It is worth noting that neither the α_{C_d} response nor the σ_{SSI} predictor are scaled or standardized. Thus, the estimation models use the predictor values straightforwardly to approximate the response. Also, note that the median values of α_{C_d}, reach up to 2.3 when the wave parameter is as low as approximately 4.8. it means that to control the SSI effects, it would be necessary to duplicate the C_d amplification factor to soundly estimate inelastic deformations calculated based on an LDP

procedure. On the opposite side of the relationship, where SSI induces favorable effects, the same factor (i.e., C_d) may be reduced to half its recommended value.

As for the estimation equations, they are shown in the textbox included in **Figure 5.16**. Nevertheless, they are transcribed to Eqs. [5.17] through [5.19] to ease their reading.

$$\alpha_{C_d(X_5)^{10th}} = \frac{1}{0.06\,X_5 + 0.539} \quad [5.17]$$

$$\alpha_{C_d(X_5)^{50th}} = \frac{1}{0.069\,X_5 + 0.164} \quad [5.18]$$

$$\alpha_{C_d(X_5)^{90th}} = \frac{1}{0.056\,X_5 + 0.134} \quad [5.19]$$

The R^2 metrics obtained from the fitted model equations show its acceptable performance with values of 0.832, 0.978, and 0.975 for models corresponding to the 10^{th}, 50^{th}, and 90^{th}, respectively. Note that the model for the α_{C_d} lower-bound limit is the one showing the lesser of the R^2 values, but the median and upper bound values models show excellent results.

The second alternative chosen to explain the variability of α_{C_d} is the X_{10} predictor, i.e., the *flexBase* assessment spectral acceleration parameter $\tilde{S}_{ax}$. The scatter plot portrayed in **Figure 5.17** shows the relationship between the response variable α_{C_d} and X_{10} predictor. Again, for curve fitting purposes, the scatter data has been discretized into percentiles, and representative values of the same percentiles used before are employed for generating three estimation models. From the scatter plot and the fitted curves shown in the figure, it can be observed that α_{C_d} values decrease as $\tilde{S}_{ax}$ increases, which would be explained by thinking of the corresponding acceleration and displacement spectra. In the former spectrum, it is well known that when the fundamental period ($\tilde{T}_n$) is low, representing stiff squat structures, acceleration values (say $\tilde{S}_{ax}$) are the highest found in the spectrum, and they decrease as $\tilde{T}_n$ increases for large or flexible structures. In the displacement spectrum, on the contrary, the relationship between $\tilde{T}_n$ and the spectral displacements $\tilde{S}_{dx}$ is iverted; displacements start with null values and increase with period values. Hence, it is no wonder that α_{C_d}, representing the excess in inelastic deformation relative to what is expected, is higher when $\tilde{S}_{ax}$ is low because there is where spectral displacements are higher.

Another relevant observation from this $\tilde{S}_{ax} - \alpha_{C_d}$ relationship lies in that there is quite a wide range of spectral acceleration values for which α_{C_d} would adopt unitary values. This can be noted from the span between the lower and the upper bound percentiles lines showing the regression models. In a range between approximately $0.78g$ and $1.02g$ there can exist different structural configurations for which the prescribed C_d amplification factor agrees with the actual inelastic deformation demand.

Since the estimation model uses only a single independent variable, the effects of other predictors are not captured; thus, the need to present a third estimation model alternative based on the ML techniques (shown later in this section) to uncover additional relationships between predictors and response.

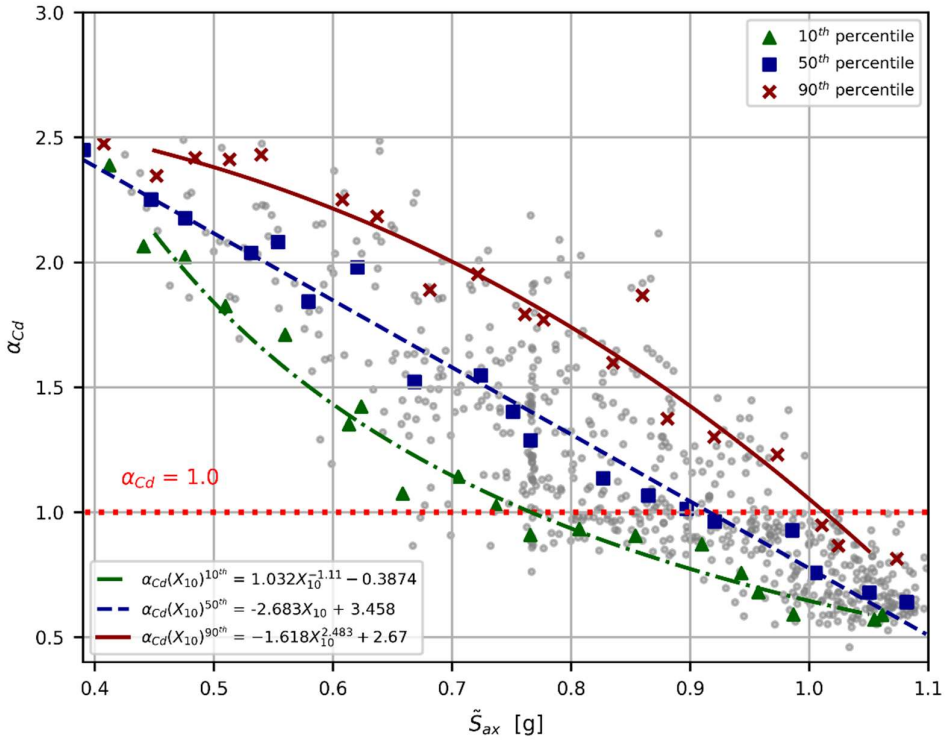

Figure 5.17. Scatter plot showing the relationship between the significant unscaled and unstandardized X_{10} predictor, $\tilde{S}_{ax}$, and the response variable α_{C_d}. Regession model equations shown for the 10^{th}, 50^{th}, and 90^{th} data percentiles.

Lastly, see in **Figure 5.17** that estimation model equations are presented for each analyzed percentile data. Still, they are also expressed in Eqs. [5.20] through [5.22] showing a polynomial shape. This function shape demonstrated to give the best efficiency metrics in the curve-fitting process.

$$\alpha_{C_d(X_{10})^{10th}} = 1.032\ X_{10}{}^{-1.11} - 0.3874 \qquad [5.20]$$

$$\alpha_{C_d(X_{10})^{50th}} = -2.683\ X_{10} + 3.458 \qquad [5.21]$$

$$\alpha_{C_d(X_{10})^{90th}} = -1.618\ X_{10}{}^{2.483} + 2.67 \qquad [5.22]$$

Regarding the R^2 metrics for these equation models, values of 0.981, 0.979, and 0.966 are obtained for Eqs. [5.20], [5.21], and [5.22], respectively. It suggests that this predictor is capable of explaining quite effectively the variation in the values of α_{C_d}.

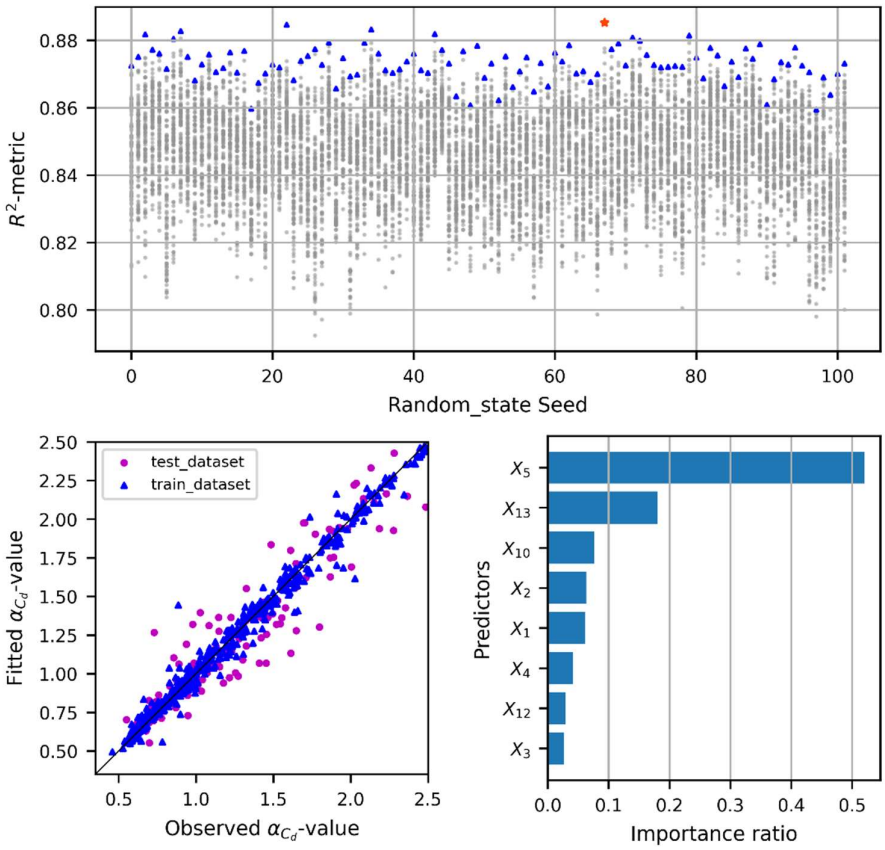

Figure 5.18. Results from GBRT-ML technique. (top) optimization process outcome for the highest R^2, (bottom-left) observed versus fitted α_{C_d}, and (bottom-right) sorted importance ratio for key predictors

Finally, to get a better perspective of the predictors' influence on the variability of α_{C_d} factor, the GBRT regression method based on ML techniques was also used to generate an estimation model. A parallel aim of utilizing this ML technique was to find a more efficient model for the estimation of α_{C_d}, however, it is evident that the R^2 values obtained for the previous classical regression models are way superior to the $R^2 = 0.885$ value measured at the test portion of the GBRT model, whose results are summarized in **Figure 5.18**. See in the figure that the observed versus fitted values show an acceptable agreement in both test and train data splits, and the hyperparameters optimization process allows to reach such R^2 value instead of a possible one below 0.80 for a random seed of 25 (approximately).

Nonetheless, the predictors deemed more significant to generate the estimation model may be more important to look at. Notice that, by far, the most important predictor is X_5 (σ_{SSI}) with an importance ratio of over 50%; in agreement with what was observed in the heatmap of **Figure 5.15** and the previous classical regression results. Even though the GBRT model shows lesser R^2 compared to those of the CR, it was developed to involve additional parameters that help explain α_{C_d} uncovering hidden relationships that the CR is unable to detect. Thus, despite its relatively low R^2 it should not be neglected when attempting to estimate α_{C_d}.

5.6. Closing Remarks on Chapter 5

Throughout this chapter, important shortcomings regarding current code prescriptions for the seismic design of building structures considering SSI effects have been identified. To put it short, such prescriptions cannot entirely ensure adequate seismic structural performance at different seismic hazard levels, neither in elements' strength nor in global inelastic deformations. Based on the performance assessment outcomes in Chapter 3, two modification recommendations concerning strength- and displacement-related design considerations were presented to improve the design products.

First, addressing the strength design, it was recognized that SSI effects are always present in the structural response and are readily appreciated through the NDP analysis procedure on the *flexBase* structure, unlike what is stated in the ASCE-7 standard supported on equivalent linear elastic systems. In such a standard, seismic design force is always reduced to account for SSI effects during design; however, Section 5.3.3 stressed the deen of considering the detrimental consequences of interacting effects as well. To do this, an α factor was defined to modify the conventionally calculated seismic design forces for SSI considerations.

Estimation models in the form of equations and computational objects were generated through classical regression analysis and ML techniques, respectively. In the case of the former, the variation of α factor value was found to depend primarily on the structure's slenderness ratio, λ_{str}, and approximations of α factor using Eqs. [5.9] through [5.11] demonstrate to give a good fit relative to observed data. In the same way, ML-based estimation models corroborate the dependency of α on the slenderness ratio and also shows a remarkable efficiency in estimating its values.

Regarding the displacement-related design recommendations to modify the design procedures considering SSI effects, it was found in Section 5.5 that the Deflection Amplification Factor, C_d, in charge of projecting the ISDR in terms of the elastic ones during design using LDPs, fails to accomplish its purpose in not a few studied cases. Hence, also based on the NDP displacement responses from the performance assessment, the behavior of a correction factor, α_{C_d}, that permits to modify the theoretical C_d^{theo} value prescribed in ASCE-7 to calculate the actual C_d^{real} was studied. It was found that the increment or decrement of values in C_d^{real} through α_{C_d} strongly depend on the assessment spectral acceleration parameter for the *flexBase* structure, $\tilde{S}_{ax}$. Moreover, the dependency on the wave parameter, σ_{SSI}, is also considerable, thus its use for estimating α_{C_d} could also be allowed. Two sets of estimation models in the form of equations are presented to approximate α_{C_d}. Eqs. [5.17] to [5.19] correspond to the first set of equations explaining the variation of the correction factor in terms of σ_{SSi}. Eqs. [5.20] to [5.22], on the other hand, uses $\tilde{S}_{ax}$ for estimating the same response. Both sets of equations can be used indistinctively.

Finally, an ML estimation model was also generated to approximate the value of α_{C_d}. The GBRT method was again found to show the best results in terms of fitting the response by evaluating the influence of more than a single predictor on the variability of α_{C_d}. Even though the ML-based estimation models are good alternatives to traditional equation models, the necessity of being used through computational tools may be inconvenient for some professionals. To ease the use of the ML-based estimation models for both α (for strength design) and α_{C_d} (for inelastic deformation control), the computational models are available and ready to be used in the following link:

https://mybinder.org/v2/gh/jsbaquero86/SSI_PBSD/HEAD?labpath=SSI_ModFactors.ipynb

In the next chapter, the factors introduced in the current one will be used in a design and performance assessment example case to evaluate their appropriateness in designing structures with SSI effects considerations.

6. Verification: RC Building Design Based on Estimations

In the previous chapter, new recommendations for the design of RC buildings with SSI effects considerations were presented. First, estimations of the design base shear force amplification or reduction were proposed by means of the α-afctor based on the responses obtained from the performance assessment carried out in Chapter 3 and making assumptions regarding the expected performance level in buildings in scenarios depending on the nonlinear dynamic procedure (NDP) analysis procedure (deemed as the most accurate for showing the actual structural response). Then, considering the actual inelastic story drift ratios obtained from the same analysis procedure and relating them to the allowable prescribed deformation Δ_a/ρ, estimations for the increase or decrease in the deflection amplification factor, C_d, were also introduced as a novel mechanism in the deformation control during design through the correction factor α_{C_d}.

In easing the estimation of such factors (i.e., α-factor and α_{C_d}), estimation models in the form of equations and computational objects were generated through the classical regression analysis using the least squares method and Machine Learning (ML) techniques, respectively. However, as noted in the corresponding sections, a significant number of equations can be utilized for estimation purposes concerning each of the factors mentioned above; 3 equation models and 1 ML model addressing α-factor, and 6 equation models and 1 ML model in the case of α_{C_d}. Moreover, since the estimation of each factor was performed independently, i.e., not considering the interaction of these two factors acting simultaneously, a concern arises regarding the application of both factors at once during the design process. It is thought that the simultaneous use of these factors could induce either over-conservative or unconservative design outcomes.

This chapter is in charge of analyzing the use of α- and α_{C_d} factors aiming to fulfill a twofold objective. First, to evaluate the effectiveness of these factors in improving the building's seismic performance, and second, to find the most efficient $\alpha - \alpha_{C_d}$ combination to get a sound design.

With this in mind, a soil-structure system (SSS) configuration among the ones used in creating the buildings database is selected to be designed using 28 $\alpha - \alpha_{C_d}$ combinations resulting from the 4 models for estimating α and 7 models for α_{C_d}. A performance assessment using the NDP procedure through the NLTHA is carried out on each of the 28 designed buildings to measure $DCR_{(ac)}$ and inelastic story drift ratios (ISDR). These performance indicators are compared to those obtained from the same building designed per Chapter 2 without the modification recommendations, and finally, conclusions are drawn based on this analysis.

6.1. Building description

To evaluate the effectiveness of α-factor and the α_{C_d} correction factor, a building is selected from the database to be designed for SSI effects consideration using both modification factors simultaneously. The geometrical characteristics of this structure are detailed as follows: ten-story height ($NStr = 10$) with 3.0m of inter-story height, seven bays in global X-direction ($NbaysX = 7$), four bays in global Z-direction ($NbaysZ = 4$) as shown in **Figure 6.1**. Regarding the supporting soil characteristics, they are selected from **Table 2.2**, corresponding to an SC-E soil with a $v_{so} = 175m/s$ of shear-wave velocity. All other parameters defining the soil properties are indicated in the table above.

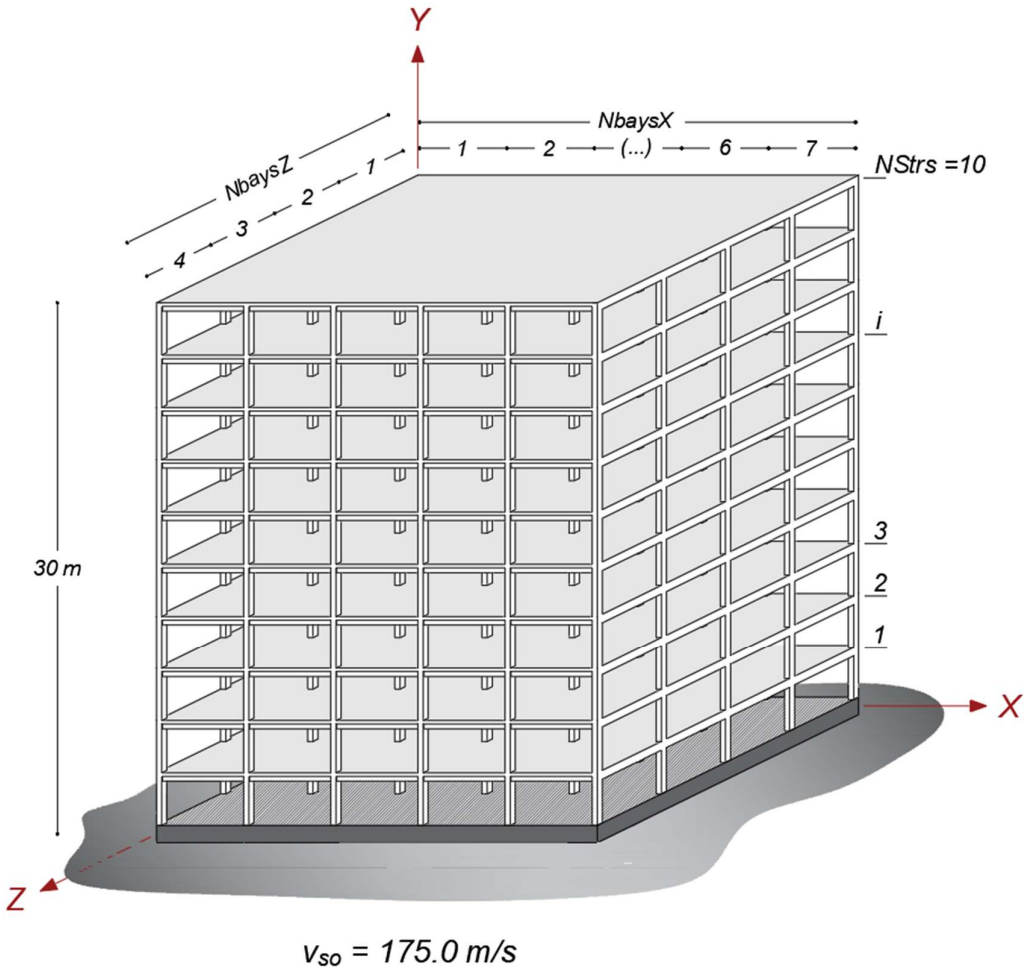

Figure 6.1. Graphical description of the example building.

It is important to recall that the equation models, along with the ML models for estimating the modification parameters (i.e., α and α_{C_d}), make use of not all the X_i predictors listed in **Table 4.1** but just those significant for achieving a proper response fit. In that sense, **Table 6.1** shows the model equations used in this section retrieved from Chapter 5, the calculated factor value from these models, and the predictors acting in such models.

Table 6.1. Estimation models for α and α_{C_d} factors, their values, and predictors taking part in the estimation.

	Model	α and α_{C_d} factors value	X_i predictors[a]	Description
α-factor	$\alpha_{(X_6)10^{th}} = 0.281X_6 + 0.368$	1.211	$X_1 = 0.99s$	T_n fundamental period of the fixed-base structure.
	$\alpha_{(X_6)50^{th}} = 0.361X_6 + 0.339$	1.422		
	$\alpha_{(X_6)90^{th}} = 0.386X_6 + 0.429$	1.587	$X_2 = 1.16s$	$\tilde{T}_n$ fundamental period of the flexible-base structure.
	$\alpha^{GBRT}_{(X_1,X_5,X_6,X_7)}$	1.455		
α_{C_d} correction factor	$\alpha_{C_d(X_5)10^{th}} = 1/(0.06X_5 + 0.539)$	1.030	$X_5 = 7.20$	σ_{SSI} wave parameter.
	$\alpha_{C_d(X_5)50^{th}} = 1/(0.069X_5 + 0.164)$	1.514	$X_6 = 3.00$	λ_{str} structure's slenderness ratio.
	$\alpha_{C_d(X_5)90^{th}} = 1/(0.056X_5 + 0.134)$	1.862	$X_7 = 0.57$	B/L footprint aspect ratio.
	$\alpha_{C_d(X_{10})10^{th}} = 1.032X_{10}^{-1.11} - 0.387$	1.314	$X_{10} = 0.64$	$\tilde{S}_{ax}$ flexible-base assessment spectral acceleration parameter.
	$\alpha_{C_d(X_{10})50^{th}} = -2.683X_{10} - 3.458$	1.748		
	$\alpha_{C_d(X_{10})90^{th}} = -1.62X_{10}^{2.48} + 2.67$	2.141	$X_{13} = 0.65$	V_d^* ratio of the flexible- to fixed-base structure design base shear.
	$\alpha^{GBRT}_{C_d(X_1,X_2,X_5,X_{10},X_{13})}$	1.789		

[a] Indistinctive of the model.

From the table, it can be observed first that most of the predictors involved in estimating the modification factors are also involved in approximating the performance translators Ψ studied in Chapter 4. Refer back to **Table 4.9** and compare the significant predictors there against the ones in **Table 6.1**. both fixed- and flexible-base structure fundamental periods seem important in estimating the responses in both tables. Moreover, correlated predictors such as the slenderness ratio λ_{str} are essential for the same purpose in the cases of Ψ and α-factor values. Regarding the models estimating α_{C_d}, the wave parameter σ_{SSI} and the flexible-base assessment spectral acceleration parameter $\tilde{S}_{ax}$ are crutial predictors. In contrast with what is observed in **Table 4.9**, similar parameters are also considered necessary for the estimation of Ψ, namely, the fixed-base acceleration parameter S_{ax} and the dimensionless parameter a_o. The latter, along with σ_{SSI} are deemed decisive in the determination of SSI effects according to (Bielak, 1971; Jennings & Bielak, 1973; Veletsos & Meek, 1974), as stated earlier in Section 2.2. In addition, the V_d^* parameter is also of interest in approximating α_{C_d} using the ML estimation model. More about this particular parameter is addressed later in this same chapter.

On the other hand, the values adopted by both α and α_{C_d} factors are greater than 1.0, indicating an increase in design considerations regarding forces and deformation amplifications should be considered. An upper bound for the α_{C_d} factor reaches even as high values as 2.141, increasing the theoretical C_d value to twice the recommended by the ASCE-7 standard of $C_d = 5.5$. However, this value may seem exaggerated; thus, the study in this section appears imperative.

6.2. Building Design considering SSI

As described in the introductory section of the current chapter, the design is performed for a selected example structure with the characteristics described earlier, ensuring that SSI effects are present. It is evident by evaluating the σ_{SSI} value obtained for such example shown in **Table 6.1** ($\sigma_{SSI} = 7.20$). Referring back to **Figure 2.1** where the $h_n - v_{so}$ space is shown relative to the limits values that σ_{SSI} should adopt to consider the SSI effects, it can be noticed that this example building is located within the range where interaction effects are *essential* for the structural response. **Figure 6.2** replicates in this section the figure mentioned above for convenience, including the location of the example building with a golden star symbol, according to its characteristics; $h_n = 30m$ and founded on soils with $v_{so} = 175.0m/s$.

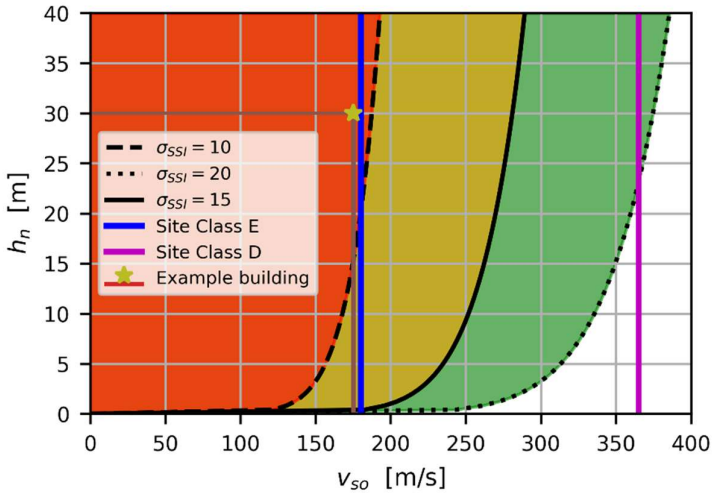

Figure 6.2. $h_n - v_{so}$ space for fixed σ_{SSI} values showing the example building.

It is worth noticing in this example that even though the ASCE-7 standard agrees with the presence of the SSI effects and, thus, allows design base shear modification in accounting for such interaction effects, such modification implies a reduction in design forces, as explained in Section 5.2. This fact can be evidentiated by observing X_{13} predictor in **Table 6.1**, which stands for the ratio of the flexible- to the fixed-base structure design base shear, V_d^*. It was shown in Section 4.2 that V_d^* can be calculated using Eq. [6.1] assuming that the effective seismic weight of the building with SSI effects considerations is defined as $\overline{W} = \tilde{C}_m W$. However, notice also that the same ratio definition in Eq. [5.2] (i.e., $\alpha = \tilde{V}/V$), corresponds to that in the equation shown below, indicating that V_d^* approximates the thoeritecial value of α (α^{theo}) prescribed in ASCE-7.

$$V_d^* = \frac{\tilde{V}}{V} = \left(1 - \tilde{C}_m\right) + \left(\frac{\tilde{C}_s}{C_s}\right)\left(\frac{\tilde{C}_m}{B_{SSI}}\right) \qquad [6.1]$$

It is important to recall that α^{theo} is used to reduce the design shear force, assuming that the SSI effects induce only beneficial responses, yet it cannot adopt values below 0.70. Now, observe that V_d^*

for this example gets a value of 0.64, suggesting that the design force is to be reduced by a limited value of 0.70, opposing to what α and α_{C_d} values are showing in **Table 6.1**. As stated in Chapter 5, SSI effects could be beneficial or detrimental regarding structural response, which is evident by the analysis made so far.

Being aware of the actual influence of SSI effects in the example structure, it was designed to consider such effects but accounting for the increase in both design forces and the deflection amplification factor. The denomination of design type for this building is $DT = SSIDs$; its seismic structural performance is assessed through the NDP (NLTHA) for the LS and CP structural performance levels and two base support conditions: *fixBase* and *flexBase*. **Figure 6.3** shows a schematization of the design and assessment process; notice that 28 designs were carried out, and four analyses were executed at each design outcome, summing 112 NLTHA calculations.

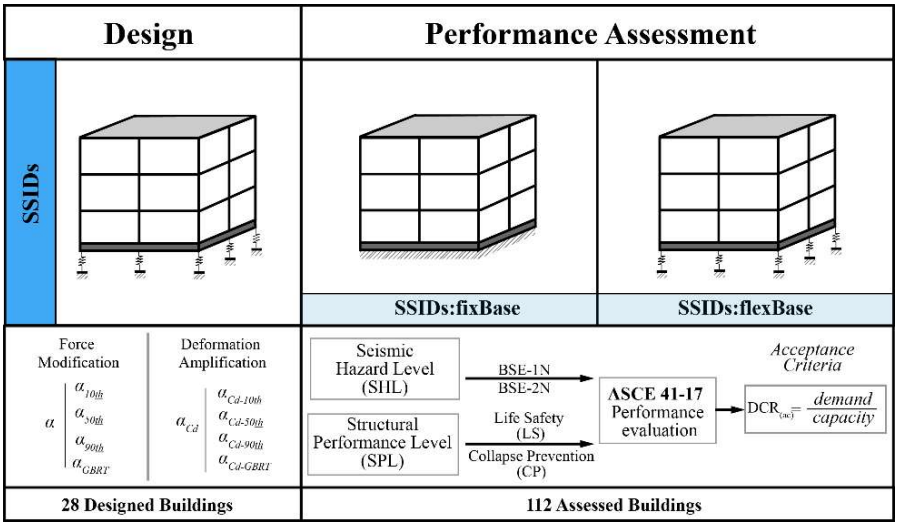

Figure 6.3. Design and assessment process schematization for validation of α and α_{C_d}.

Design results are presented similarly to Section 2.6 through a parameter introduced in this study called the relative mass or mass ratio, M^*. In this section, though, the relative mass is calculated as the ratio of the building's mass calculated employing modified α and α_{C_d} to the mass of the building designed using SSI prescriptions as per ASCE-7. Notice that in this case, both masses correspond to that of an *SSIDs*-designed structure in contrast to how it was established in the section mentioned earlier. Thus, the relative mass is determined by the expression $M^* = M_{SSIDs}^{mod}/M_{SSIDs}^{original}$. **Figure 6.4** portrays the variation in M^* depending on the $\alpha - \alpha_{C_d}$ combination used during the design process.

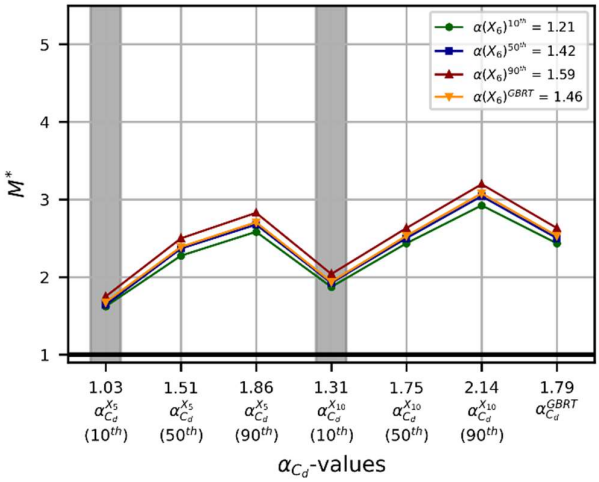

Figure 6.4. Design outputs in terms of the mass ratio M^* for different $\alpha - \alpha_{C_d}$ combinations.

Notice in the figure above that values corresponding to α_{C_d} correction factors are located on the horizontal axis but not ordered numerically. Their order obeys the same order in which they were presented in **Table 6.1** instead. The first three values correspond to the estimation models involving X_5 predictor for the lower- median and upper-bound limits of the approximated values of α_{C_d}. The following three values show the same bound limits but for the models depending on the X_{10} predictor. Finally, the last α_{C_d} value corresponds to that obtained using the ML estimation model through the GBRT technique. On the other hand, four lines are plotted for the three bounds described earlier, plus the GBRT calculated α values depending on the X_6 predictor. In this sense, the green, blue, red, and orange solid lines describe the variation of M^* relative to α_{C_d} values when combined with $\alpha(X_6)^{10^{th}}$, $\alpha(X_6)^{50^{th}}$, $\alpha(X_6)^{90^{th}}$, and $\alpha(X_6)^{GBRT}$, respectively.

As would seem obvious, the value of M^* increases as the either α or α_{C_d} increase. For the building to adequately withstand the augmented forces and be able to control the amplified deflections, the elements' cross-sections would need to be also augmented to improve their strength and stiffness, accordingly. This is ultimately reflected in the volume and, thus, in the mass of the structure designed using the modified $\alpha - \alpha_{C_d}$ combinations. In all cases, M_{SSIDs}^{mod} are larger than their $M_{SSIDs}^{original}$ counterparts, leading to M^* values consistently above 1.0.

It is worth noting that M^* is more sensitive to the variation of α_{C_d} values than that of α, partly because it is well-known that lateral displacements tend to control the building design when high seismicity levels are present instead of providing adequate strength to elements' sections. Another reason relies upon the fact that the lower- and upper-bounds of α_{C_d} span on a broader range than those of the α factor.

Anyways, key observations in **Figure 6.4** are directed to point out the $\alpha - \alpha_{C_d}$ combination that delivers the lowest increment in mass for the modified design. As shown in the figure, this condition

is accomplished by the combinations involving the 10^{th} percentile lower-bound values of $\alpha_{C_d}^{X_5}$ and $\alpha_{C_d}^{X_{10}}$, both highlighted with a gray band. The latter implies an amplification of C_d^{theo} of 31% while the former needs barely a 3% amplification of the same parameter and an increase in the structure's mass of approximately 70% and 100%, respectively. As for the α value that should be chosen, additional information may be required before making any sound recommendation since it has already been acknowledged that the variation in M^* is not that sensitive to α variations.

In the following section, the results from the performance assessment are introduced to help understand how the design modifications through $\alpha - \alpha_{C_d}$ combinations improve structural behavior, allowing one to make decisions regarding the most effective combination to be used in such a design process.

6.3. Performance Assessment Results

Following the assessment scheme presented in **Figure 6.3**, the 28 structures designed with the modifications introduced in the previous section were assessed for both LS and CP SPLs and considering *fixBase* and *flexBase* BSCs for a total of 112 analysis outcomes. Similar to the design responses evaluation and to be consistent with how α and α_{C_d} were conceived in the first place, the performance assessment results from the example building are compared to those performance indicators of the original *SSIDs* designed structures analyzed through the NDP analysis procedure with *fixBase* and *flexBase* base support conditions for the LS and CP structural performance levels.

Addressing the main focus of the modification factors, strength $DCR_{(ac)}$ indicators and ISDR (δ) are evaluated from the assessment results. In this regard, **Figure 6.5** and **Figure 6.6** show, respectively, the strength and deformation responses for the BSC-SPL pairs. It should be considered that horizontal axes are presented in the same fashion as they were in **Figure 6.4**, i.e., α_{C_d} are represented in these axes but not ordered numerically. Again, plotted lines stand for the variation of the strength and deformation indicators as α_{C_d} varies with respect to each α value employed in the design process. In addition, horizontal dashed red lines indicate the values obtained from the performance assessment in the originally designed and analyzed building (i.e., without the recommended modifications), with the $DCR_{(ac)}$ and δ values also shown in **Figure 6.5** and **Figure 6.6**, respectively. Moreover, in the figures, the limiting values of an adequate performance are shown in bold black horizontal solid lines. For $DCR_{(ac)}$ indicators, they are plotted at the 1.0 ordinate regardless of the SPL. In the case of δ indicators, these limit lines are plotted at an ordinate of 0.02 for the LS, and at 0.04 for the CP structural performance level (FEMA, 2000).

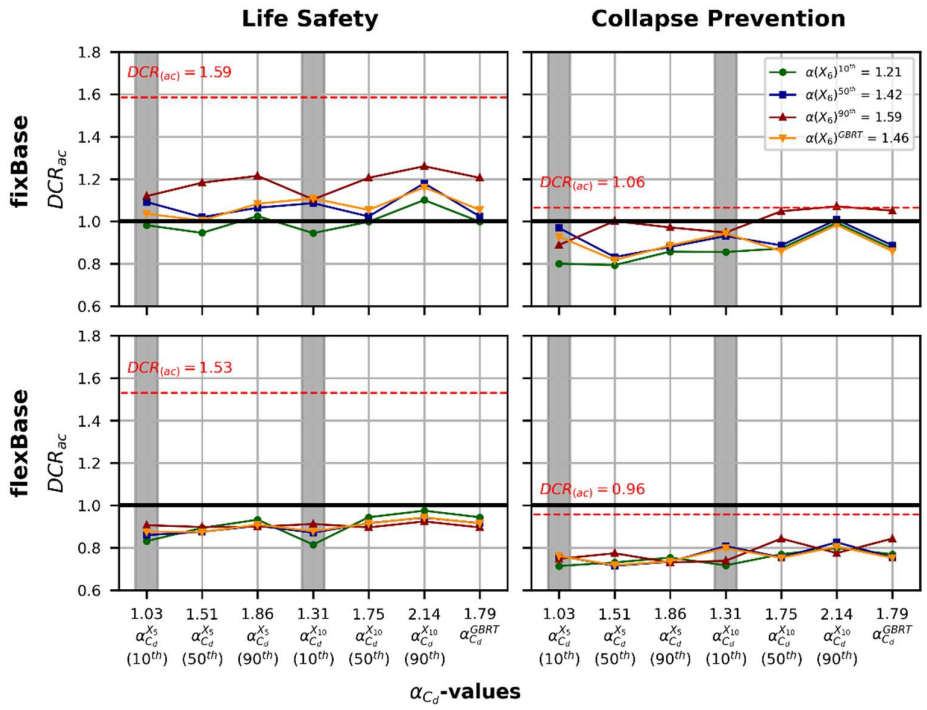

Figure 6.5. Performance assessment results for the example building designed using α and α_{C_d} factors in terms of $DCR_{(ac)}$. *fixBase* and *flexBase* DTs in combination with the LS and CP SPLs are depicted as shown in the figure.

Let's look first at **Figure 6.5** for the evaluation of $DCR_{(ac)}$ performance indicators. From the demand-capacity values obtained at the originally assessed building, at first glance, it can be noticed that indicator values obtained at the models with *flexBase* BSC are lower than values for the *fixBase* structures. This trend was first advised from the global overview of results presented in Chapter 4 and corroborated by observing this figure. In addition, a considerable difference of $DCR_{(ac)}$ values between the LS and the CP SPL can be observed, suggesting that regardless of the BSC selected during the assessment, it is more likely to accomplish the latter SPL than the former. This fact is also evident by examining figures in Section 3.5 compared to their complements in Appendix D. Such a difference may be due to the incapacity of the response reduction factor R to adequately address the structural behavior while considering the SSI effects in demand ranges close to the design demand $\tilde{V}$ and that of the LS level. On the other hand, it appears that at more advanced levels of demand where the correct definition of the strength ductility reduction factor, $R_d = V_E/V_y$, is more relevant, the building's strength is sufficient to withstand CP demand levels. Hence, it may be concluded that R_d would not be sensitive to the SSI effects (refer to **Figure 5.1** for refreshing nomenclature if needed).

Regarding $DCR_{(ac)}$ values of the structure designed based on the modification factors α and α_{C_d}, it can be noticed that for the *flexBase* BSC structures, all performance indicators lay below the 1.0 limit value for the LS SPL, and even a more considerable margin is observed for the CP SPL. Even though the difference between the outcomes of both SPLs remains, it has been dramatically shortened. In contrast to what was drawn in the previous paragraph concerning R and R_d reduction factors and

their dependency on SSI effects here can be appreciated that it is no longer an issue. It is worth recalling that in defining α (through Eq. [5.7]), an approximation of the actual behavior of the overstrength factor $\widetilde{\Omega}_{(T_n)}$ is involved. The manner in which this latter factor is conceived allows us to consider the SSI effects implicitly in *R* factor (refer to Appendix F for further information). Thus, the shortening in the difference mentioned above is explained.

On the other hand, $DCR_{(ac)}$ values obtained from the *fixBase* BSC display cases for which the building achieves the SPL and fails to do it. Observing with more attention the graphic devoted to the *fixBase*-LS combination, notice that the highest $DCR_{(ac)}$ values correspond to the building design based on the $\alpha(X_6)^{90^{th}}$ factor, i.e., the upper bound value displayed by the red line. On the contrary, the lowest $DCR_{(ac)}$ values obey to the lower bound $\alpha(X_6)^{10^{th}}$ in green. It can be rationally explained considering that, as a structure stiffens and increases its mass by employing a higher α value (upper bound value), the spectral acceleration affecting the mass to induce the seismic demand also increases due to the reduction in the vibration period, T_n. Hence, even though the structure would seem more robust, the demand augments accordingly, failing to accomplish the expected performance level. On the contrary, applying the lower bound α estimate, the increase in mass and stiffness is such to keep the seismic demands low enough while improving the global building strength to accomplish the expected performance level. Moreover, since *fixBase* BSC is being evaluated, there is no period elongation due to the SSI effects that help reduce the spectral acceleration demand. The same analysis is also valid for the *fixBase*-CP combination; however, the performance indicator values are again lower for this SPL than those for the LS for the reasons already explained.

Nevertheless, it shall be recalled that both α and α_{C_d} modification factors were defined considering the influence of SSI effects on *flexBase* models, and the response aimed to be improved corresponds to that of the *flexBase* structure deemed the actual response, which indeed was achieved.

From the analysis carried out so far concerning the results shown in **Figure 6.5**, highlighted by a gray band are the $\alpha - \alpha_{C_d}$ combinations leading to the most effective and efficient structural performance overall. In terms of α_{C_d}, the same lower bound values obtained from estimation models involving both X_5 and X_{10} are chosen because of the low M^* obtained as shown in **Figure 6.4**. As for α, also the lower bound value gives $DCR_{(ac)}$ indicators that remains below the 1.0 limit in every BSC-SPL combination while keeping M^* low. In that sense, considering so far, the strength performance indicators, the suggested $\alpha - \alpha_{C_d}$ combination for design would be $\alpha(X_6)^{10^{th}} - \alpha_{C_d}(X_5 \; or \; X_{10})^{10^{th}}$. However, by evaluating the ISDR performance indicators the recommendations can be further narrowed down.

Now, refer to **Figure 6.6** for δ performance indicators. Observe that the same differences between the LS and the CP SPLs responses identified in the $DCR_{(ac)}$ are also visualized for both the original

and the modified designs. In this case, though, all δ values lie below the corresponding limit to achieve the expected LS and CP performance.

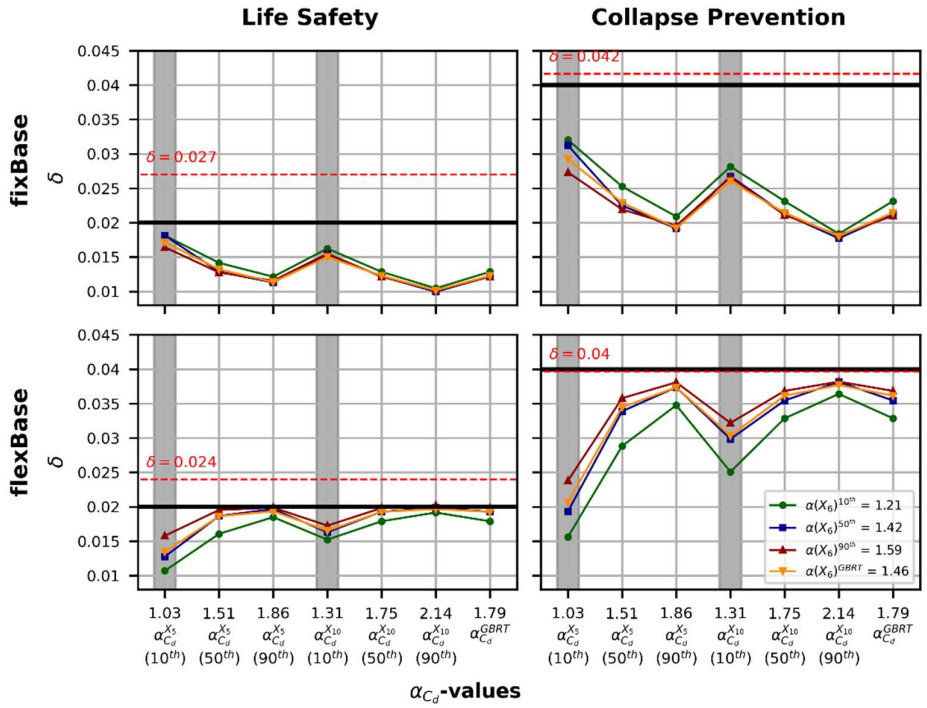

Figure 6.6. Performance assessment results for the example building designed using α and α_{C_d} factors in terms of inelastic drift ratios, ISDR (δ). *fixBase* and *flexBase* DTs in combination with the LS and CP SPLs are depicted as shown in the figure.

The variation of obtained δ values seems to be more sensitive in terms of α_{C_d} than to α. However, by observing the performance indicator values for the *flexBase* BSC of interest, it is again clear that the lower bound value $\alpha(X_6)^{10^{th}}$ is the most effective in reducing the inelastic story drift ratios. In addition, also from the *flexBase* graphics in **Figure 6.6**, the $\alpha(X_6)^{10^{th}} - \alpha_{C_{d(X_{10})^{10^{th}}}}$ combination seems to show a less over-conservative mechanism to control excessive inelastic deformations.

6.4. Final Comments on New Design Recommendations

Throughout this chapter, it was demonstrated that the modification factors developed in Chapter 5 give adequate results in designing an example building from the database with SSI effects considerations. As a quick reminder, the current prescribed approach to performing a building´s design with such considerations requires considering two main aspects when LDPs are used as analysis methods. The first relates to the necessity of including the soil-foundation system flexibility (so-called *flexBase* base support conditions in this study). The second focuses on calculating a modified design base shear force that accommodates the inertial interaction effects of the SSI phenomenon. The latter, however, was proven insufficient in fulfilling the goal of providing enough strength and stiffness to the building to withstand seismic actions and deformations. Such a

prescribed design base shear force modification implicitly suggests that interacting phenomenon induces only beneficial effects on the structural behavior, which is not true. Both beneficial and detrimental effects have been demonstrated to be of consideration for an SSS depending on the characteristics of the supporting soil, the structure's geometrical and mechanical properties, and those of the seismic actions.

Aiming to overcome this particularity, a couple of factors, namely, α and α_{C_d}, were proposed to give the building elements adequate strength and control excessive inelastic deformations to a limited design value already established in the reference design code, respectively. These correction factors were derived based on the responses obtained from the performance assessment of the buildings in the database created in Chapter 2 through the NLTHA nonlinear dynamic procedure with *flexBase* BSC, deemed closest to the actual structural response. In this regard, α and α_{C_d} factor are ment to be used straightforwardly in calculating the design forces (Eq. [6.2]) and the deflection amplification factor (Eq. [6.3]) employed in the seismic design considering SSI effects.

$$\tilde{V} = \alpha \times V \quad [6.2]$$

$$C_d^{real} = \alpha_{C_d} \times C_d^{theo} \quad [6.3]$$

As mentioned earlier, the definition of each factor was developed separately. Thus, it was necessary to evaluate the appropriateness of using them together to avoid any over- or under-estimation of their values that could generate either unsound or over-conservative design outcomes. It should be recalled that α and α_{C_d} factors were defined based on estimation model equations (through the classical regression method) and estimation model computational objects (through the GBRT technique). Because of this, four models are available for the former factor and seven for the latter. Hence the need to select an adequate pair of $\alpha - \alpha_{C_d}$ models that deliver reasonable values for design purposes.

By analyzing the products of the design in Section 6.2 by means of the relative mass M^* shown in **Figure 6.4**, and the $DCR_{(ac)}$ and δ ISDR performance indicators of **Figure 6.5** and **Figure 6.6**, an effective and efficient $\alpha - \alpha_{C_d}$ combination was defined. Such a combination involves the lower bound estimation equation for α and the same for α_{C_d} but the one depending on the *flexBase* spectral acceleration parameter, $\tilde{S}_{ax}$ (X_{10} predictor), i.e., $\alpha(X_6)^{10^{th}} - \alpha_{C_d}(X_{10})^{10^{th}}$ combination. The estimation equations are shown in the following equations, neglecting sub- and super-indices used so far to identify them from the others.

$$\alpha = 0.281\ \lambda_{str} + 0.368 \quad [6.4]$$

$$\alpha_{C_d} = 1.032\ \tilde{S}_{ax}^{\ -1.11} - 0.387 \quad [6.5]$$

The equations shown above are recommended for use in the seismic design of buildings accounting for SSI effects. However, the authors still consider the pending task of evaluating the appropriateness of all models in **Table 6.1** for all buildings in the database. An enormous amount of work would imply knowing that the actual database comprises 729 buildings, and such verification represents the expansion of twenty-eight times the current number of buildings, i.e., 20,412 in total. Anyhow, designing such amount of buildings with the automatized Python algorithm developed by the authors for this research work is not as time-consuming as it would be performing the 81,648 NLTHA required for this purpose. Nevertheless, it is still hoped that the efforts reflected in Eqs. [6.4] and [6.5] become the starting point of a more elaborated yet rational and sound methodology for the seismic design of buildings considering SSI effects, which are always present.

7. Conclusions and Recommendations for Future Work

7.1. Overall Conclusions

The seismic design of reinforced-concrete moment-frame buildings, their seismic performance assessment, and a set of estimation and correction factors have been presented throughout the development of this thesis. Considerations of the soil-structure interaction (SSI) effects were accounted for in each of these processes to evaluate its influence on the structural response. It was demonstrated that the SSI phenomenon couldn't be neglected neither in the design process nor in the performance evaluation. It was acknowledged that current code prescriptions fail to produce safe designs. Thus, novel design correction factors are introduced, aiming to provide tools that prove to improve the design outcomes easily. More detailed conclusions derivated from each chapter are emphasized in this section in the same order as the thesis was structured.

Regarding the design of buildings carried out in Chapter 2 to construct the database, a set of SSS parameters was used to define the geometrical and mechanical characteristics of the buildings and the soil, so the SSI effects are appreciable. These parameters included but were not limited to σ_{SSI}, and λ_{str}, whose calculated values depending on the SSS have been demonstrated to indicate the presence of the SSI effects in the dynamic response of structures. Based on an $h_n - v_{so}$ space identified by operating on these parameters, along with the approximate calculation of the period of vibration of the fixed-base system, T_a, the buildings geometry and the main soil mechanic characteristics were defined. Hence, varying the building height (through the number of stories), the footprint aspect ratio, B/L, (through keeping constant the number of bays in one direction and varying the number of bays in its orthogonal counterpart) 729 different structural and mechanical configurations combinations were defined for the design process. The total number was doubled (i.e., the total number of cases was 1,458) because the same configurations were used to design buildings with fixed- and flexible-base support conditions, *convDs* and *SSIDs* design types (DT), respectively. The design outcomes from both design types' considerations were concisely examined by calculating the relative mass, M^*, and stiffnesses, K^*, of the *SSIDs*-designed structure to that of the *convDs* counterpart. These ratios indicate whether an *SSIDs*-designed building is heavier or stiffer than a *convDs*-designed one if ratios are greater than 1.0, or lighter and more flexible otherwise. It was demonstrated that the magnitude of M^* and K^* ratios increases as the fixed-base period of vibration T_n increases getting values first below and then above unity. It suggests that, although *SSIDs* buildings are initially lighter and more flexible than their *ConvDs* counterpart, they gradually become heavier and stiffer as the *fixBase* structure fundamental period rises. This means that more rigid buildings tend to be more sensitive to the beneficial effects of the SSI phenomenon, while more flexible counterparts are to the detrimental ones regarding the design needs in terms of the required cross-sectional area needed to control the strength and deformation demands. In addition, the relationship

between the design outcomes and the SSS parameter mentioned above was studied. It was demonstrated that the most influencing parameter in the design results is the slenderness ratio, for which linear trends were appreciable regarding its relationship with M^* and K^* ratios. A similar behavior was observed relative to these ratios, T_n and λ_{str}: i.e., as the period of vibration increases, the slenderness ratio increases too, also showing de dependence between these two parameters (which could seem obvious). Moreover, it was noticed that regardless of λ_{str}, the pace of increment in M^* and K^* factors relative to the increment of T_n is constant up to a limit where $T_n > 1.0s$. From this point on, the slope of the linear $\lambda_{str} - T_n$ trends to decrease. This indicates that, as the period of vibration goes beyond this limit, beneficial effects change slower into detrimental counterparts for flexible structures. Finally, it was also observed that the linear trends representing λ_{str} passes through the unitary axis at approximately the same T_n value when examining both M^* and K^* ratios. This points out that the buildings designed using either of the two design types for specific periods of vibration result in the same design outcome, and the observed period is higher for higher slenderness ratios. It suggests that the SSI effects could be neglected for specific structures' configurations even though the SSS parameters indicate otherwise.

In Chapter 3, the performance assessment of buildings designed to make up the database was executed following the guidelines prescribed in ASCE-41. Four analysis procedures, APs, were used: LDP through the MRSA, LDP through the LTHA, NSP through the Pushover analysis, and NDP through the NLTHA. Besides, as established by the standard, a performance objective was defined to study the achievement of two structural performance levels, SPL (LS and CP), when accordingly subjecting the structures to specific seismic hazard levels, SHL (BSE-1N and BSE-2N). In generating the building mathematical models, linear and nonlinear force-deformation relationships were considered according to the AP used. Two base support conditions were modeled, accounting for the fixed- and the flexible-base support conditions, BSC. Thus, 23,328 analyses were performed (1,458 buildings in database × 4 APs × 2 SPLs × 2 BSCs) to evaluate the performance reached by the buildings designed following either conventional or SSI-related prescriptions. It is worth mentioning that the purpose of developing the mathematical models considering both BSCs was oriented to answering the questions: Could a conventionally designed building lead to adequate performance when assessed considering a flexible-base BSC? And, would it be enough to assess an SSI-designed building considering fixed-base BSC models? In short, none of these questions get definitive affirmative answers. A more elaborate explanation for the last statement is presented in the following points:

- The NLTHA is assumed to give the closest to the actual structural performance among the four analysis procedures used in the assessment process.
- For conventionally designed buildings evaluated with the fixed-base BSC, there is a notorious range of building heights between 4-story and 6-story buildings for which the SPL is achieved

in all soil site class conditions. It shows a narrow range of building characteristics for adequate performance.

- Regardless of the design type being assessed through a flexible-base BSC model, mid-height buildings ranging from 5 to 9 stories are more likely to achieve the LS-SPL for any value of v_{so}. This trend is repeated for the CP-SPL as well.
- Being more specific concerning the SSI-designed buildings, fixed-base BSC buildings clearly show a range between 5 and 9 stories, and for v_{so} values beyond $200 m/s$, where it is more likely to achieve the desired SPL. For the same design type but for flexible-base BSC models, the building height range tightens to 6 to 8 stories and v_{so} beyond $235 m/s$ to find buildings likely to achieve the expected SPL. In this way, it is demonstrated that even though SSI effects are considered in the design and the performance assessment processes, buildings so designed could result in unsafe structures for a broad range of SSS configurations.
- On the other hand, none of the buildings achieved the evaluated SPL when evaluating their performance using LDPs (either MRSA or LTHA). It is well-known that linear procedures used during analysis tend to give conservative estimates of buildings' performance, explaining the obtained performance outcomes.
- On the contrary, the performance outcomes from the NSP show better results than the NLTHA procedure. Nevertheless, these results are questionable since, in defining the shape of applied lateral forces to reach the target displacement in the NSP, a modification factor related to the MDOF's actual behavior of the system is used (C_o factor). This factor is calculated employing only the first vibration mode ordinate and participation factors which are incapable of including the participation of higher modes in the response as the NLTHA is.
- Another observed source of variation in the obtained performance outcomes lies in the analysis procedures themselves. It was observed that regardless of the DT-BSC combination, the most frequent action triggering the performance indicators (i.e., $DCR_{(ac)}$) are related to either moment forces in linear procedures (MRSA and LTHA), or plastic rotations (NSP) on beams and beams only. On the other hand, from the NLTHA procedure, it was noticed that the most frequent action is related to the shear in columns. It is clear that, depending on the AP, the behavior of the building during analysis reflects a different nature. While linear procedures or those based on an SDOF system (MRSA, LTHA, and NSP) demonstrate a flexural behavior of the buildings, the NLTHA shows a more accurate actual behavior in the same structures, demonstrating the importance of shear demands in the $DCR_{(ac)}$.

Based on the observations above, two facts came to our attention. First, it was evident that there is a considerable difference between the performance indicator values obtained using the NDP and the rest of the analysis procedures due to their simplified, over-conservative nature. And second, even when employing the NDP for evaluating the achievement of a desired performance level, neither

conventionally designed buildings nor those supposed to be prepared to withstand SSI effects show acceptable behavior but for some isolated cases. Focused on addressing these issues, Chapter 4 and Chapter 5 present a set of modification factors that are the core novel outcomes of this research.

The first, denominated Ψ, is proposed as a translation factor. It aims to transform the performance indicator values obtained from buildings designed using any DT, assessed considering any BSC through either the LDPs or the NSP, to the performance indicator values of a DT-designed building evaluated with flexible-base BSC through the NDP. The DT-*flexBase*-NDP combination was taken as the one showing the closest to the actual structural performance. Thus, the main objective of Ψ is to give professionals the possibility to approximate the actual performance of RC moment-resisting frame buildings that would be obtained from the DT-*flexBase*-NDP combination, using other DT-BSC-APs counterparts that require less computational effort and are less time-consuming.

As for the rest of the proposed modification factors, α and α_{C_d}, address the flaws identified in the prescriptive design guidelines in the currently available standard, ASCE-7, regarding the SSI effects consideration. In the case of α, it is proposed as a correction factor for the design base shear demand that implicitly considers the interacting effects. It is worth mentioning that the terminology and use for this factor are adopted from the standard mentioned above, α factor deduced in this study, though, considers the detrimental effects of the soil-structure interaction phenomenon, unlike the prescribed α factor recommended in ASCE-7. This limitation in the design standard reflects the little understanding of the interaction effects against the response modification factor, R, -especially for ductile structures- and the fact that the prescribed modifications using α are based on theoretical linear elastic models of the SSS. On the other hand, α_{C_d} focuses on modifying the Deflection Amplification Factor, C_d, in charge of estimating expected inelastic deformations from those calculated using design-oriented analysis procedures to consider SSI effects. The outcomes obtained from the performance evaluation at the LS structural performance level were used to define these three factors that are oriented to complement the design process.

Using classical regression (CR) and machine learning (ML) regression techniques, estimation models were generated using SSS parameters selected to explain the SSI effects in the variation of Ψ, α, and α_{C_d}. Depending on the regression analysis method, these three factors were introduced as equations or computational objects leading to the conclusions detailed in the following points.

Regarding factor Ψ:

- In translating performance indicators obtained with linear methods, i.e., MRSA and LTHA, the Ψ factor always gets values less than unity. This confirms the previously identified conservativism issue behind linear procedures for evaluating structural performance.

Moreover, the actual performance indicator values (those obtained from NDP) could represent between 30% and 80% of those obtained using linear analysis procedures.

- On the other hand, comparing the actual $DCR_{(ac)}$ indicators with those obtained with the NSP, the need to either amplify or reduce the latter's values to be approximated to the actual performance indicators was observed. In this case, $DCR_{(ac)}$ values calculated from the NSP, range between half and twice the actual $DCR_{(ac)}$ values from the NDP. This makes evident some of the conclusions drawn from Chapter 3, relative to the differences in the response obtained from different nonlinear analysis procedures and the change in the structural response, due to the lack in the NSP of reflecting the effects of higher vibration modes in the dynamic response.
- Regarding the estimation models generated for explaining the variation in the Ψ factor, it was demonstrated, by examining the determination coefficient (R^2), that the regression method leading to models with high values of this statistic is the Gradient Boosting Regression Tree (GBRT) method.
- As for the analysis procedures from which the estimation is carried out, it was observed that models based on performance indicators calculated with both the LTHA and the NSP could be appropriate for approximating Ψ. The R^2 value of models thus generated reach up to 0.90 or more, showing their proficiency. In this case, it would be a matter of the practitioner's expertise in selecting, processing, and modifying (scaling or matching) the ground motion records needed to execute the LTHA instead of choosing the less intricate NSP procedures. The latter, though, requires that the mathematical model include adequate force-deformation relationship representations, which may be somewhat challenging for less experienced practitioners.
- As expected, the mathematical model used in the assessment of buildings through the LTHA and NSP requires the consideration of flexible-base support conditions to generate more efficient estimation models for approximating Ψ.
- Regarding the predictors that better explain the variation of Ψ, it could be appreciated that when generating an estimator for the translator Ψ, regardless of the DT-BSC-AP-SPL combination, are dynamical properties of the structure such as either T_n or $\tilde{T}_n$, some measures of their nonlinear behavior characteristics wrapped into V_y^*, V_d^*, and μ^* (only if MRSA is used), by far, some indicators of the SSI effects presence such as λ_{str} and a_o, and a measure of the seismic demand preferable through S_{ax}.
- There are some predictors that, in perspective, can be neglected, such as the soil shear-wave velocity, v_{so}, the footprint aspect ratio B/L, also S_{ax}^*, and R_d^*.

Regarding factors α and α_{C_d}:

- For generating the estimation models, again, the performance assessment outcomes ($DCR_{(ac)}$ or performance estimators) obtained from the assessment through the NDP analysis procedures applied to flexible-base models were used. This AP demonstrated to reflect the ambivalent effects of the SSI phenomenon. In the case of the proposed α, for instance, it was observed that depending on the SSS configuration, this factor gets values between 0.5 and 2.0. This indicates that the magnitude of the design base shear force used in the design with SSI considerations, contrasting with the current practice, where α only reduces such demand according to ASCE-7.
- A similar trend was observed by evaluating the calculated α_{C_d} values. Actual inelastic deformations measured from the flexible-base structures assessed through the NDP range between 0.50 and 2.5 times the expected inelastic deformations estimated from linear elastic analyses by using C_d alone. ASCE-7 prescriptions don't address the variation of C_d relative to the SSI effects; thus, α_{C_d} comes to resolve this issue.
- The estimation models generated to estimate α and α_{C_d} factors showed adequate fit capabilities with R^2 values ranging from 0.90 and 0.885, respectively, for the GBRT models and as high as 0.98 approximately for models in the form of equations for both factors.
- As for the most influencing predictors explaining the variation of α, the slenderness ratio λ_{str} proved to be the most important as it was in the estimation of Ψ. Considering that both α and Ψ are focused on estimating force-related actions, it becomes evident that this parameter (i.e., λ_{str}) undoubtedly exerts a key influence on the strength required by the building while being designed and its capacity when being assessed considering SSI effects. Such significance can be explained by connecting three ground ideas: (1) the slenderness ratio is defined by the expression $2h^*/B$, (2) the building height is directly proportional to the period of vibration T_n, so the expression defining λ_{str}, to some extent, relates the buildings' flexibility with the stiffness against its rotation about the weak axis that B provides, and (3) one of the most meaningful effects of the SSI phenomenon is the period elongation which is expressed as $\tilde{T}_n = T_n\sqrt{1 + k/k_x + kh^2/k_{yy}}$ for an SDOF system. It is reasonable to assume, based on these considerations, that λ_{str} is closely related to the period elongation effect and hence to the change in the spectral acceleration demand that modifications in the vibration period of the flexible-base structure induce.
- Regarding the influence predictor for the α_{C_d} factor, it was observed that the essential parameters in explaining its variation are either the flexible-base spectral assessment acceleration $\tilde{S}_{ax}$ or the wave parameter σ_{SSI} which is a measure of the relative stiffness of the soil to that of the structure. When using the GBRT method to generate the α_{C_d} estimation

model, the latter parameter was identified as the most relevant, showing the importance of considering the soil mechanical properties in the variation of α_{C_d}. When using classical regression techniques to put estimation models in the form of equations, either of the two parameters can be used.

- From the previous two points, it was noticed that the strength-related factors (Ψ and α) to be predicted are mainly sensitive to the superstructure characteristics. On the other hand, deformation-related factor (α_{C_d}) is more sensitive to the characteristics of the SSS system as a whole through σ_{SSI} or to a directly related parameter as the flexible-base spectral acceleration $\tilde{S}_{ax}$.

Finally, in Chapter 6, the appropriateness of α and α_{C_d} as design force demand and expected inelastic deformation modification factors for designing an example building was verified. A ten-story height ($NStr = 10$) with $3.0m$ of inter-story height, seven bays in global X-direction ($NbaysX = 7$), four bays in global Z-direction ($NbaysZ = 4$) was selected. Regarding the supporting soil characteristic, it corresponds to SC-E soil with a $v_{so} = 175m/s$ of shear-wave velocity. With these SSS configurations, the presence of SSI effects is noticed since $\sigma_{SSI} = 7.20$, less than the limit value of 10, to deem the consideration of interaction effects as essential for evaluating the building response. In summary, it was observed that $\alpha - \alpha_{C_d}$ combination to produce a sound building design (i.e., a building that achieves the LS and the CP structural performance levels when analyzing its flexible-base mathematical model) while keeping the increment in cross-section dimensions in an efficient range is given by the equations shown below.

$$\alpha = 0.281\,\lambda_{str} + 0.368 \qquad [7.1]$$

$$\alpha_{C_d} = 1.032\,\tilde{S}_{ax}^{\,-1.11} - 0.387 \qquad [7.2]$$

Nevertheless, since the SSI effects for this particular example are detrimental to the structural response, reaching an adequate performance level involved the increment of the elements' dimensions, thus an increment in mass and stiffness. The increment in mass resulted in about a 70% increase, indicating that properly designed buildings prepared to withstand desired levels of seismic demand would imply an increment in the construction cost. Despite this fact, it is emphasized that these novel modification factors can be considered valuable complements for the seismic design of buildings considering soil-structure interaction effects.

7.2. Future Work

Once the tasks and outcomes of a research work that has been carried out over several years are summarized in a *few* pages, it is inevitable to feel that there is more left to do than what has already been done. Being involved in the research field allows us to open our eyes to a firm understanding of

the enormous amount of work still pending to be addressed. However, the time available to close gaps or expand the boundaries of knowledge is sadly limited when it becomes a one-person job. Thus, just a few recommendations for further work, taking as starting point the information delivered throughout this thesis, are introduced in the following paragraphs.

To consider SSI effects in the design process, the proposed modification factors α and α_{C_d} gathered all the interaction information within the estimation models based on their relationships with the significant predictor variables (SSS parameters). It should be recalled that these estimation models were generated based on the performance assessment outcomes of nonlinear flexible-base building models analyzed through the NDP. This particular AP was recognized as the more accurate procedure in reflecting the SSS response since the major source of affectation regarding the SSI phenomenon is related to the radiation and the hysteretic damping induced by the nonlinear soil behavior. Both actions were independently considered in the nonlinear modeling strategy used in Chapter 3; however, the still simplified nature of the sub-structuring modeling approach (in comparison to the direct modeling approach) prevented us from considering a broader list of predictors able to explain the interaction effects in terms of the nonlinear soil behavior. It was stated in earlier chapters of this thesis that the decision concerning the SSS modeling approach was focused on time limitations, being the sub-structuring approach the most convenient due to the enormous amount of analyses performed. Nevertheless, the author encourages researchers and practitioners to make use of the evergrowing computing force in designing and assessing more complex and complete mathematical models to tackle the potential flaws of simplified counterparts. It is highly probable that the more precisely significant predictors are identified, the more accurate the estimation factors proposed in this thesis become. Setting aside the time limitations involved in a thesis research scope like this, the improvement in design and assessment methodologies or processes that would imply using the direct modeling approach is worth the wait.

A more detailed evaluation regarding the R, Ω, and μ behaviors when considering SSI effects deserves special attention. It was shown in Chapter 5 that, to some extent, expressing Ω in terms of the flexible-base period of vibration, along with the appropriately selected predictors, helped explain the behavior of α. In this regard, it would be reasonable to think that examining the dependence of R and μ to the SSS parameters influencing the SSI effects could improve the accuracy of estimating α, producing, in turn, more efficient design when using linear dynamic or static procedures in the design process. The implicit modification of these factors (i.e., R, Ω, and μ) would imply the consequent evaluation of the fragility evaluation of so-designed structures. Adequate probability of collapse according to demand levels would need to be examined. In addition, it should be acknowledged that this study focused on buildings supported on shallow foundations only. The study can also be extended so the structural system also considers deep foundations. Finally, once more generalized α

and α_{C_d} factors are generated, a new performance evaluation of a comprehensive building database should be carried out.

References

Abadi, M., Agarwal, A., Barham, P., Brevdo, E., Chen, Z., Citro, C., Corrado, G. S., Davis, A., Dean, J., Devin, M., Ghemawat, S., Goodfellow, I., Harp, A., Irving, G., Isard, M., Jozefowicz, R., Jia, Y., Kaiser, L., Kudlur, M., … Zheng, X. (2015). *TensorFlow: Large-scale machine learning on heterogeneous systems*. https://www.tensorflow.org

Abdel Raheem, S. E., Ahmed, M. M., & Alazrak, T. M. A. (2015). Evaluation of soil–foundation–structure interaction effects on seismic response demands of multi-story MRF buildings on raft foundations. *International Journal of Advanced Structural Engineering*, *7*(1), 11–30. https://doi.org/10.1007/s40091-014-0078-x

Abtahi, S., Mahsuli, M., Asce, A. M., & Ghannad, M. A. (2020). Probabilistic Evaluation of Soil – Structure Interaction Effects on Strength Demands of Shear Buildings. *Journal of Structural Engineering*, *146*(1), 1–12. https://doi.org/10.1061/(ASCE)ST.1943-541X.0002458

ACI Committee 318. (2019). ACI CODE 318-19(22): Building Code Requirements for Structural Concrete and Commentary. In *ACI 318-19(22)*. www.concrete.org

Alagundi, S., & Palanisamy, T. (2022). Neural network prediction of joint shear strength of exterior beam-column joint. *Structures*, *37*(December 2021), 1002–1018. https://doi.org/10.1016/j.istruc.2022.01.013

Alimoradi, A., & Beck, J. L. (2015). Machine-Learning Methods for Earthquake Ground Motion Analysis and Simulation. *Journal of Engineering Mechanics*, *1*, 1–13. https://doi.org/10.1061/(ASCE)EM.1943-7889.0000869.

American Society of Civil Engineers. (2017a). Minimum Design Loads and Associated Criteria for Buildings and Other Structures. In *ASCE/SEI 7-16*. ASCE/SEI 7. https://doi.org/10.1061/9780784414248

American Society of Civil Engineers. (2017b). Seismic Evaluation and Retrofit of Existing Buildings. In *ASCE/SEI 41-17* (ASCE/SEI41). ASCE/SEI. https://doi.org/10.1061/9780784414859

Anand, V., & Satish Kumar, S. R. (2018). Seismic Soil-structure Interaction: A State-of-the-Art Review. *Structures*, *16*, 317–326. https://doi.org/10.1016/j.istruc.2018.10.009

Applied Technology Council. (1996). Seismic evaluation and retrofit of concrete buildings (Volume 1). In *ATC-40* (Vol. 1). https://doi.org/10.1193/1.1586093

Applied Technology Council. (2017a). Guidelines for Nonlinear Structural Analysis for Design of Buildings; Part I – General. In *NIST GCR 17-917-46v1*. https://doi.org/10.6028/NIST.GCR.17-

917-46v1

Applied Technology Council. (2017b). Recommended Modeling Parameters and Acceptance Criteria for Nonlinear Analysis in Support of Seismic Evaluation, Retrofit, and Design. In *NIST GCR 17-917-45*. https://doi.org/10.6028/NIST.GCR.17-917-45

Applied Technology Council. (2020). *A Practical Guide to Soil-Structure Interaction* (Issue December).

Arslan, M. H. (2010). An evaluation of effective design parameters on earthquake performance of RC buildings using neural networks. *Engineering Structures*, *32*(7), 1888–1898. https://doi.org/10.1016/j.engstruct.2010.03.010

ATC. (2005). Improvement of Nonlinear Static Seismic Analysis Procedures. In *FEMA 440* (Issue 2005). http://scholar.google.com/scholar?hl=en&btnG=Search&q=intitle:Improvement+of+Nonlinear+Static+Seismic+Analysis+Procedures#2%5Cnhttp://scholar.google.com/scholar?hl=en&btnG=Search&q=intitle:440,+Improvement+of+nonlinear+static+seismic+analysis+procedures%232

ATC. (2009). Quantification of building seismic performance factors. In *FEMA P695* (Issue June).

ATC. (2012). Soil-Structure Interaction for Building Structures. In *NIST GCR 12-917-21*. https://doi.org/12-917-21

Awchat, G., Monde, A., Sirsikar, R., Dhanjode, G., & Tayade, S. (2022). Soil-Structure Interaction: Comparative Review of International Codes and Other Literature With Indian Seismic Code. *Civil and Environmental Engineering*, *18*(1), 87–95. https://doi.org/10.2478/cee-2022-0009

Aydemir, Müberra Eser, & Aydemir, C. (2016). Overstrength factors for SDOF and MDOF systems with soil structure interaction. *Earthquake and Structures*, *10*(6), 1273–1289. https://doi.org/10.12989/eas.2016.10.6.1273

Aydemir, Muberra Eser, & Ekiz, I. (2013). Soil-structure interaction effects on seismic behaviour of multistorey structures. *European Journal of Environmental and Civil Engineering*, *17*(8), 635–653. https://doi.org/10.1080/19648189.2013.810177

Bapir, B., Abrahamczyk, L., Wichtmann, T., & Prada-Sarmiento, L. F. (2023). Soil-structure interaction: A state-of-the-art review of modeling techniques and studies on seismic response of building structures. *Frontiers in Built Environment*, *9*(February), 1–17. https://doi.org/10.3389/fbuil.2023.1120351

Bhattacharya, K., & Dutta, S. C. (2004). Assessing lateral period of building frames incorporating soil-flexibility. *Journal of Sound and Vibration*, *269*(3–5), 795–821. https://doi.org/10.1016/S0022-

460X(03)00136-6

Bielak, J. (1971). *Earthquake Response of Building Foundation System* (p. 153).

Bolton, M. D. (1986). The strength and dilatancy of sands. *Geotechnique*, *36*(1), 65–78. https://doi.org/10.1680/geot.1986.36.1.65

Boore, D. M., Stewart, J. P., Seyhan, E., & Atkinson, G. M. (2014). NGA-West2 Equations for Predicting Response Spectral Accelerations for Shallow Crustal Earthquakes. In *Peer Report 2013-05*. Pacific Earthquake Engineering Research Center, University of California. https://peer.berkeley.edu/sites/default/files/webpeer-2013-05-david_m._boore_jonathan_p._stewart_emel_seyhan_and_gail_m._atkinson.pdf

Boore, David M. (2010). Orientation-independent, nongeometric-mean measures of seismic intensity from two horizontal components of motion. *Bulletin of the Seismological Society of America*, *100*(4), 1830–1835. https://doi.org/10.1785/0120090400

Boore, David M., & Bommer, J. J. (2005). Processing of strong-motion accelerograms: Needs, options and consequences. *Soil Dynamics and Earthquake Engineering*, *25*(2), 93–115. https://doi.org/10.1016/j.soildyn.2004.10.007

Borcherdt, R. D. (1994). Estimates of Site-Dependent Response Spectra for Design (Methodology and Justification). In *Earthquake Spectra* (Vol. 10, Issue 4, pp. 617–653). https://doi.org/10.1193/1.1585791

Borcherdt, R. D., & Glassmoyer, G. (1992). On the characteristics of local geology and their influence on ground motions generated by the Loma Prieta Earthquake in the San Francisco Bay region, California. *Bulletin of the Seismological Society of America*, *82*(2), 603–641.

Boulanger, R. W., Curras, C. J., Kutter, B. L., Wilson, D. W., & Abghari, A. (1999). Seismic Soil-Pile-Structure Interaction Experiments and Analyses. *Journal of Geotechnical and Geoenvironmental Engineering*, *125*(9), 750–759. https://doi.org/10.1061/(ASCE)1090-0241(1999)125:9(750)

Bozorgnia, Y., Abrahamson, N. A., Al Atik, L., Ancheta, T. D., Atkinson, G. M., Baker, J. W., Baltay, A., Boore, D. M., Campbell, K. W., Chiou, B. S. J., Darragh, R., Day, S., Donahue, J., Graves, R. W., Gregor, N., Hanks, T., Idriss, I. M., Kamai, R., Kishida, T., … Youngs, R. (2014). NGA-West2 Research Project. *Earthquake Spectra*, *30*(3), 973–987. https://doi.org/10.1193/072113EQS209M

Brunelli, A., de Silva, F., Piro, A., Parisi, F., Sica, S., Silvestri, F., & Cattari, S. (2021). Numerical simulation of the seismic response and soil–structure interaction for a monitored masonry school building damaged by the 2016 Central Italy earthquake. In *Bulletin of Earthquake Engineering* (Vol. 19, Issue 2). Springer Netherlands. https://doi.org/10.1007/s10518-020-00980-3

Cao, V. Van. (2021). External GFRP confinement to decrease near-fault earthquake damage of reinforced concrete structures considering soil-structure interaction. *Structures*, *34*(February), 2318–2339. https://doi.org/10.1016/j.istruc.2021.08.027

Chatterjee, S., & Hadi, A. S. (2012). *Regression Analysis by Example* (Fifth Edit). John Wiley & Sons, Inc.

Chopra, A. K., & Goel, R. K. (2000). Building Period Formulas for Estimating Seismic Displacements. *Earthquake Spectra*, *16*(2), 533–536. https://doi.org/10.1193/1.1586125

Chouw, N., & Hao, H. (2008a). Significance of SSI and non-uniform near-fault ground motions in bridge response II: Effect on response with modular expansion joint. *Engineering Structures*, *30*(1), 154–162. https://doi.org/10.1016/j.engstruct.2007.02.020

Chouw, N., & Hao, H. (2008b). Significance of SSI and nonuniform near-fault ground motions in bridge response I: Effect on response with conventional expansion joint. *Engineering Structures*, *30*(1), 141–153. https://doi.org/10.1016/j.engstruct.2007.02.020

Coduto, D. P. (1998). *Geotechnical Engineering - Principles and Practices*. Prentice-Hall.

Crouse, C. B., & McGuire, J. W. (1996). Site response Studies for Purpose of Revising NEHRP Seismic Provisions. *Earthquake Spectra*, *12*(3), 407–439.

Dabaghi, M., & Der Kiureghian, A. (2018). Simulation of orthogonal horizontal components of near-fault ground motion for specified earthquake source and site characteristics. *Earthquake Engineering and Structural Dynamics*, *47*(6), 1369–1393. https://doi.org/10.1002/eqe.3021

Darbandsari, S. K., & Kashani, A. H. (2018). A critical review on structure-soil-structure interaction. *Journal of Structtural Engineering and Geotechnics*, *8*(2), 57–68.

Day, R. W. (2010). *Foundation Engineering Handbook. Design and Construction with the 2009 International Building Code* (Second Edi).

Derbal, I., Bourahla, N., Mebarki, A., & Bahar, R. (2020). Neural network-based prediction of ground time history responses. *European Journal of Environmental and Civil Engineering*, *24*(1), 123–140. https://doi.org/10.1080/19648189.2017.1367727

Dhadse, G. D., Ramtekkar, G. D., & Bhatt, G. (2021). Finite Element Modeling of Soil Structure Interaction System with Interface: A Review. *Archives of Computational Methods in Engineering*, *28*(5), 3415–3432. https://doi.org/10.1007/s11831-020-09505-2

Du, X., Xu, H., & Zhu, F. (2021). A data mining method for structure design with uncertainty in design variables. *Computers and Structures*, *244*, 106457. https://doi.org/10.1016/j.compstruc.2020.106457

Dutta, S. C., & Roy, R. (2002). A critical review on idealization and modeling for interaction among soil-foundation-structure system. *Computers and Structures*, *80*(20–21), 1579–1594. https://doi.org/10.1016/S0045-7949(02)00115-3

Elnashai, A. S., & Mwafy, A. M. (2002). Overstrength and force reduction factors of multistorey reinforced-concrete buildings. *Structural Design of Tall Buildings*, *11*(5), 329–351. https://doi.org/10.1002/tal.204

Emami, A., & Halabian, A. M. (2020). Seismic response assessment of reinforced concrete structures based on displacement, force and energy criteria, considering soil-structure interaction. *Australian Journal of Structural Engineering*, *21*(1), 64–93. https://doi.org/10.1080/13287982.2019.1706700

EN 1998-5. (2004). *Design of structures for earthquake resistance - Part 5: Foundations, retaining structures and geotechnical aspects*.

Esfandiari, M. J., & Urgessa, G. S. (2020). Progressive collapse design of reinforced concrete frames using structural optimization and machine learning. *Structures*, *28*, 1252–1264. https://doi.org/10.1016/j.istruc.2020.09.039

Far, H. (2019). Advanced computation methods for soil-structure interaction analysis of structures resting on soft soils. *International Journal of Geotechnical Engineering*, *13*(4), 352–359. https://doi.org/10.1080/19386362.2017.1354510

Fatahi, B., Tabatabaiefar, S. H. R., & Samali, B. (2014). Soil-structure interaction vs Site effect for seismic design of tall buildings on soft soil. *Geomechanics and Engineering*, *6*(3), 293–320. https://doi.org/10.12989/gae.2014.6.3.293

Fatahi, B., Van Nguyen, Q., Xu, R., & Sun, W. (2018). Three-Dimensional Response of Neighboring Buildings Sitting on Pile Foundations to Seismic Pounding. *International Journal of Geomechanics*, *18*(4). https://doi.org/10.1061/(asce)gm.1943-5622.0001093

FEMA. (2000). Prestandard and Commentary for the Seismic Rehabilitation of Buildings. In *FEMA 356* (Issue 1).

FEMA. (2003). NEHRP Recommended Provisions for Seismic Regulations for New Buildings and Other Structures. In *FEMA 450-2* (Issue Part 2). https://www.fema.gov/media-library/assets/documents/5543

FEMA. (2020). *Future Issues and Research Needs Identified During Development of the 2020 Nehrp Recommended Seismic Provisions*. 43.

Fernandez-Sola, L. R., Davalos-Chavez, D., & Tapia-Hernandez, E. (2014). Influence of the dynamic

soil structure interaction on the inelastic response of steel frames. *NCEE 2014 - 10th U.S. National Conference on Earthquake Engineering: Frontiers of Earthquake Engineering*, *July*. https://doi.org/10.4231/D35H7BV0V

Filippou, F. C., Popov, E. P., & Bertero, V. V. (1983). Effects of bond deterioration on hysteretic behavior of reinforced concrete joints. In *Technical report EERC-83/19*. Earthquake Engineering Research Center, University of California.

Fu, J., Todorovska, M. I., & Liang, J. (2018). Correction factors for SSI effects predicted by simplified models: 2D versus 3D rectangular embedded foundations. *Earthquake Engineering and Structural Dynamics*, *47*(9), 1963–1983. https://doi.org/10.1002/eqe.3051

Gaja, S., Hutchinson, T. C., Kutter, B. L., Raychowdhury, P., Ugalde, J. A., & Stewart, J. P. (2008). Numerical Models for Analysis and Performance-Based Design of Shallow Foundations Subjected to Seismic Loading. In *PEER Report 2007/04*.

Gajan, S. (2021). Application of machine learning algorithms to performance prediction of rocking shallow foundations during earthquake loading. *Soil Dynamics and Earthquake Engineering*, *151*(August), 106965. https://doi.org/10.1016/j.soildyn.2021.106965

Gajan, S., Raychowdhury, P., Hutchinson, T. C., Kutter, B. L., & Stewart, J. P. (2010). Application and Validation of Practical Tools for Nonlinear Soil-Foundation Interaction Analysis. *Earthquake Spectra*, *26*(1), 111–129. https://doi.org/10.1193/1.3263242

Galal, K., & Naimi, M. (2008). Effect of Soil Conditions on the Response of Reinforced Concrete Tall Structures To Near- Fault Earthquakes. *Structural Design of Tall and Special Buildings*, *17*(3), 541–562. https://doi.org/10.1002/tal

Ganjavi, B., Gholamrezatabar, A., & Hajirasouliha, I. (2019). Effects of soil-structure interaction and lateral design load pattern on performance-based plastic design of steel moment resisting frames. *Structural Design of Tall and Special Buildings*, *28*(11), 1–15. https://doi.org/10.1002/tal.1624

Gazetas, G. (1991a). Formulas and charts for impedance surface and embedded foundations. *Journal of Geotechnical Engineering*, *117*(9), 1363–1381.

Gazetas, G. (1991b). Foundation Vibrations. In H.-Y. Fang (Ed.), *Foundation Engineering Handbook* (1st Editio, pp. 553–593). Springer US. https://doi.org/10.1007/978-1-4757-5271-7

Ghandil, M., & Behnamfar, F. (2017). Ductility demands of MRF structures on soft soils considering soil-structure interaction. *Soil Dynamics and Earthquake Engineering*, *92*(October 2016), 203–214. https://doi.org/10.1016/j.soildyn.2016.09.051

Girault, D. P. (1987). *Analyses of foundation failures. The Mexico earthquakes - 1985: Factors involved and lessons learned*. American Society of Civil Engineers.

Goel, R. K., & Chopra, A. K. (1997). Period Formulas for Moment-Resisting Frame Buildings. *Journal of Structural Engineering*, *123*(11), 1454–1461. https://doi.org/10.1061/(asce)0733-9445(1997)123:11(1454)

Gulgec, N. S., Takáč, M., & Pakzad, S. N. (2019). Convolutional Neural Network Approach for Robust Structural Damage Detection and Localization. *Journal of Computing in Civil Engineering*, *33*(3), 1–11. https://doi.org/10.1061/(ASCE)CP.1943-5487.0000820

Güllü, H., & Karabekmez, M. (2017). Effect of near-fault and far-fault earthquakes on a historical masonry mosque through 3D dynamic soil-structure interaction. *Engineering Structures*, *152*, 465–492. https://doi.org/10.1016/j.engstruct.2017.09.031

Harden, C., Hutchinson, T. C., & Moore, M. (2006). Investigation into the Effects of Foundation Uplift on Simplified Seismic Design Procedures. *Earthquake Spectra*, *22*(3), 663–692. https://doi.org/10.1193/1.2217757

Harden, C., Hutchinson, T., Martin, G. R., & Kutter, B. L. (2005). Numerical Modeling of the Nonlinear Cyclic Response of Shallow Foundations. In *PEER Report 2005/04*. Pacific Earthquake Engineering Research Center.

Haselton, Curt B., Liel, A. B., Lange, S. T., & Deierlein. (2008). Beam-Column Element Model Calibrated for Predicting Flexural Response Leading to Global Collapse of RC Frame Buildings. In *PEER Report 2007/03* (Vol. 03, Issue May). Pacific Earthquake Engineering Research Center.

Haselton, Curtis B., & Deierlein, G. G. (2007). Assessing Seismic Collapse Safety of Modern RC Moment Frame Buildings. In *The John A. Blume Earthquake Engineering Center* (Issue 156).

Hastie, T., Tibshirani, R., & Friedman, J. (2009). The Elements of Statistical Learning. In *Springer Series in Statistics* (Second Edi, Vol. 27, Issue 2). http://www.springerlink.com/index/D7X7KX6772HQ2135.pdf

Hokmabadi, A. S. (2014). *Effect of Dynamic Soil-Pile-Structure Interaction on Seismic Response of Mid-Rise Moment Resisting Frames of the requirement for the degree of Faculty of Engineering and Information Technology*. University of Technology Sydney (UTS).

Hough, B. K. (1969). *Basic Soils Engineering* (Second Edi). Ronald Press.

Huang, C., Li, Y., Gu, Q., & Liu, J. (2022). Machine Learning–Based Hysteretic Lateral Force-Displacement Models of Reinforced Concrete Columns. *Journal of Structural Engineering*, *148*(3), 1–28. https://doi.org/10.1061/(asce)st.1943-541x.0003257

Ibarra, L. F., & Krawinkler, H. (2005). Global Collapse of Frame Structures under Seismic Excitations. In *Report No. 152* (Issue 152).

Ilhan, O., Harmon, J. A., Numanoglu, O. A., & Hashash, Y. M. A. (2019). Deep learning-based site amplification models for Central and Eastern North America. In F. Silvestri & N. Moraci (Eds.), *7th International Conference on Earthquake Geotechnical Engineering* (pp. 2980–2987). CRC Press.

IS 1893. (2016). *Criteria for Earthquake resistant design of structures. Part I: General Provisions and buildings*.

Javadi, A. A., & Rezania, M. (2009). Applications of artificial intelligence and data mining techniques in soil modeling. *Geomechanics and Engineering*, *1*(1), 53–74. https://doi.org/10.12989/gae.2009.1.1.053

Jennings, P. C., & Bielak, J. (1973). Dynamics of Building-Soil Interaction. *Bulletin of Seismological Society of America*, *63*(1), 9–48.

JSCE. (2007). *Standard Specification s for concrete structures. Design*.

Kami, R., Abrahamson, N. A., & Silva, W. J. (2013). Nonlinear Horizontal Site Response for the NGA-West2 Project. In *PEER Report 2013/12*.

Kausel, E. (2010). Early history of soil-structure interaction. *Soil Dynamics and Earthquake Engineering*, *30*(9), 822–832. https://doi.org/10.1016/j.soildyn.2009.11.001

Khosravikia, F., Mahsuli, M., & Ghannad, M. A. (2017). Probabilistic Evaluation of 2015 NEHRP Soil-Structure Interaction Provisions. *Journal of Engineering Mechanics*, *143*(9), 1–11. https://doi.org/10.1061/(ASCE)EM.1943-7889.0001274

Kiani, J., Camp, C., & Pezeshk, S. (2019). On the application of machine learning techniques to derive seismic fragility curves. *Computers and Structures*, *218*(July), 108–122. https://doi.org/10.1016/j.compstruc.2019.03.004

Kramer, S. L., & Stewart, J. P. (2004). Geotechnical Aspects of Seismic Hazards. In *Earthquake Engineering. From Engineering Seismology to Performance-Based Engineering*. CRC Press.

Kraus, I., & Džakić, D. (2013). Soil-structure interaction effects on seismic behaviour of reinforced concrete frames. *SE-50EEE*.

Lin, C. C., Wang, J. F., & Tsai, C. H. (2008). Dynamic Parameter Identification for Irregular Buildings Considering Soil-Structure Interaction Effects. *Earthquake Spectra*, *24*(3), 641–666. https://doi.org/10.1193/1.2946439

Lou, M., Wang, H., Chen, X., & Zhai, Y. (2011). Structure-soil-structure interaction: Literature review. *Soil Dynamics and Earthquake Engineering*, *31*(12), 1724–1731. https://doi.org/10.1016/j.soildyn.2011.07.008

Louzai, A., & Abed, A. (2015). Evaluation of the seismic behavior factor of reinforced concrete frame structures based on comparative analysis between non-linear static pushover and incremental dynamic analyses. *Bulletin of Earthquake Engineering*, *13*(6), 1773–1793. https://doi.org/10.1007/s10518-014-9689-7

Lu, Y., Hajirasouliha, I., & Marshall, A. M. (2016). Performance-based seismic design of flexible-base multi-storey buildings considering soil-structure interaction. *Engineering Structures*, *108*, 90–103. https://doi.org/10.1016/j.engstruct.2015.11.031

Mander, J. B., Priestley, M. J. N., & Park, R. (1988). Theoretical Stress-Strain Model for Confined Concrete. *Journal of Structural Engineering*, *114*(8), 1804–1826.

Mangalathu, S., Hwang, S., Choi, E., & Jeon, J. (2019). Rapid seismic damage evaluation of bridge portfolios using machine learning techniques. *Engineering Structures*, *201*(July), 109785. https://doi.org/10.1016/j.engstruct.2019.109785

Masaeli, H., Ziaei, R., & Khoshnoudian, F. (2018). Effects of Near-Fault Pulses on Nonlinear Soil-Structure Systems. *Journal of Earthquake Engineering*, *22*(10), 1787–1805. https://doi.org/10.1080/13632469.2017.1297263

McKenna, F., Scott, M. H., & Fenves, G. L. (2010). Nonlinear Finite-Element Analysis Software Architecture Using Object Composition. *Journal of Computing in Civil Engineering*, *24*(1), 95–107. https://doi.org/10.1061/(ASCE)CP.1943-5487.0000002

Minasidis, G., Hatzigeorgiou, G. D., & Beskos, D. E. (2014). SSI in steel frames subjected to near-fault earthquakes. *Soil Dynamics and Earthquake Engineering*, *66*, 56–68. https://doi.org/10.1016/j.soildyn.2014.06.030

Mirzaie, F., Mahsuli, M., & Ghannad, M. A. (2017). Probabilistic analysis of soil-structure interaction effects on the seismic performance of structures. *Earthquake Engineering & Structural Dynamics*, *46*(4), 641–660. https://doi.org/10.1002/eqe.2807

Moghaddasi, M., Chase, J. G., Cubrinovski, M., Pampanin, S., & Carr, A. (2012). Sensitivity analysis for soil-structure interaction phenomenon using stochastic approach. *Journal of Earthquake Engineering*, *16*(7), 1055–1075. https://doi.org/10.1080/13632469.2012.677570

Moller, O., Foschi, R. O., Rubinstein, M., & Quiroz, L. (2010). Estimating structural seismic vulnerability: An approach using response neural networks. *Structure and Infrastructure Engineering*, *6*(1–2), 63–75. https://doi.org/10.1080/15732470802663797

Monti, G., & Petrone, F. (2015). Yield and ultimate moment and curvature closed-form equations for reinforced concrete sections. *ACI Structural Journal*, *112*(4), 463–474. https://doi.org/10.14359/51687747

Mylonakis, G., & Gazetas, G. (2000). Seismic soil-structure interaction: Beneficial or detrimental? *Journal of Earthquake Engineering*, *4*(3), 277–301. https://doi.org/10.1080/13632460009350372

NZS 1170.5. (2004). *Structural design actions - Part 5: Earthquake actions-NewZeland*.

Ohsaki, Y. (1966). Niigata earthquakes, 1964 building damage and soil condition. *Soils and Foundations*, *6*(2), 14–37. https://doi.org/10.3208/sandf1960.6.2_14

Pais, A., & Kausel, E. (1988). Approximate formulas for dynamic stiffnesses of rigid foundations. *Soil Dynamics and Earthquake Engineering*, *7*(4), 213–227. https://doi.org/10.1016/S0267-7261(88)80005-8

Park, S. H., Yoon, D., Kim, S., & Geem, Z. W. (2021). Deep neural network applied to joint shear strength for exterior RC beam-column joints affected by cyclic loadings. *Structures*, *33*(October 2020), 1819–1832. https://doi.org/10.1016/j.istruc.2021.05.031

Patterson, J., & Gibson, A. (2019). Deep Learning A Practioner's Approach. In *Journal of Chemical Information and Modeling* (Issue 9). O'Reilly Media, Inc.

Paulay, T., & Priestley, M. J. N. (1992). *Seismic design of reinforced concrete and masonry buildings* (1st ed.). Wiley & Sons, Inc. https://doi.org/10.5459/bnzsee.25.4.362

Pedregosa, F., Varoquaux, G., Gramfort, A., Michel, V., Thririon, B., Grisel, O., Blonde, M., Prettenhofer, P., Weiss, R., Dubourg, V., Vanderplas, J., Passos, A., Cournapeau, D., Brucher, M., Perro, M., & Duchesnay, E. (2011). Scikit-learn: Machine Learning in Python. *Journal of Machine Learning Research*, *12*, 2825–2830. https://doi.org/10.5555/1953048.2078195

Pizarro, P. N., & Massone, L. M. (2021). Structural design of reinforced concrete buildings based on deep neural networks. *Engineering Structures*, *241*(May), 112377. https://doi.org/10.1016/j.engstruct.2021.112377

Raychowdhury, P. (2008). *Nonlinear Winkler-based Shallow Foundation Model for Performance Assessment of Seismically Loaded Structures*.

Raychowdhury, P., & Hutchinson, T. (2009). Performance evaluation of a nonlinear Winkler-based shallow foundation model using centrifuge test results. *Earthquake Engineering and Structural Dynamics*, *38*, 679–698. https://doi.org/10.1002/eqe

Reza Tabatabaiefar, S. H., Fatahi, B., & Samali, B. (2013). Seismic Behavior of Building Frames

Considering Dynamic Soil-Structure Interaction. *International Journal of Geomechanics*, *13*(4), 409–420. https://doi.org/10.1061/(ASCE)GM.1943-5622.0000231

Roesset, J. M. (2013). Soil structure interaction the early stages. *Journal of Applied Science and Engineering*, *16*(1). https://doi.org/https://doi.org/10.6180/jase.2013.16.1.01

Sánchez Calderón, L., & Bairán, J. (2020). Detección y medición semiautomática de fisuras en elementos de hormigón en fotos digitales usando procesamiento de imágenes. *Hormigón y Acero*, *71*(292), 21–27. https://doi.org/10.33586/hya.2019.2079

Sanchez, L. A. (2017). A system for crack pattern detection, characterization and diagnosis in concrete structures by means of image processing and machine learning techniques. In *Universitat Politècnica de Catalunya* (Issue October).

Scott, M. H., & Fenves, G. L. (2006). Plastic Hinge Integration Methods for Force-Based Beam–Column Elements. *Journal of Structural Engineering*, *132*(2), 244–252. https://doi.org/10.1061/(ASCE)0733-9445(2006)132:2(244)

Shahin, M. A. (2015). A review of artificial intelligence applications in shallow foundations. *International Journal of Geotechnical Engineering*, *9*(1), 49–60. https://doi.org/10.1179/1939787914Y.0000000058

Siam, A., Ezzeldin, M., & El-Dakhakhni, W. (2019). Machine learning algorithms for structural performance classifications and predictions: Application to reinforced masonry shear walls. *Structures*, *22*(December 2018), 252–265. https://doi.org/10.1016/j.istruc.2019.06.017

Stewart, J. P., Comartin, C., & Moehle, J. P. (2004). Implementation of Soil-Structure Interaction Models in Performance Based Design Procedures. *13th World Conference on Earthquake Engineering Vancouver, B.C., Canada*, *1546*.

Stewart, J. P., Fenves, G. L., & Seed, R. B. (1999). Seismic Soil-Structure Interaction in Buildings. I: Analytical Methods. *Journal of Geotechnical and Geoenvironmental Engineering*, *125*(1), 26–37. https://doi.org/10.1061/(ASCE)1090-0241(1999)125:1(26)

Stewart, J. P., Seed, R. B., & Fenves, G. L. (1999). Seismic Soil-Structure Interaction in Buildings. II: Empirical Findings. *Journal of Geotechnical and Geoenvironmental Engineering*, *125*(January), 38–48. https://doi.org/10.1061/(ASCE)1090-0241(1999)125:1(38)

Stewart, J. P., & Seyhan, E. (2013). Semi-Empirical Nonlinear Site Amplification and its Application in NEHRP Site Factors. In *PEER Report 2013-13*. Pacific Earthquake Engineering Research Center, University of California. https://peer.berkeley.edu/sites/default/files/webpeer-2013-13-jonathan_p._stewart_and_emel_seyhan.pdf

Sudret, B., Mai, C., & Konakli, K. (2014). Response of nonlinear soil-MDOF structure systems subjected to distinct frequency-content components of near-fault ground motions. *Earthquake Engineering & Structural Dynamics*, *September 2013*, 701–716. https://doi.org/10.1002/eqe

Tabatabaiefar, H. R., & Massumi, A. (2010). A simplified method to determine seismic responses of reinforced concrete moment resisting building frames under influence of soil-structure interaction. *Soil Dynamics and Earthquake Engineering*, *30*(11), 1259–1267. https://doi.org/10.1016/j.soildyn.2010.05.008

Tabatabaiefar, S. H. R., Fatahi, B., & Samali, B. (2013). Lateral seismic response of building frames considering dynamic soil-structure interaction effects. *Structural Engineering and Mechanics*, *45*(3), 311–321. https://doi.org/10.1061/(ASCE)GM.1943-5622.0000231

Taghizadeh, M., Gholhaki, M., & Rezaifar, O. (2021). A study on effect of soil-structure interaction on performance of strong-back structural system subjected to near and far-field earthquakes. *Structures*, *32*(March), 116–136. https://doi.org/10.1016/j.istruc.2021.02.056

Tahghighi, H., & Mohammadi, A. (2020). Numerical Evaluation of Soil–Structure Interaction Effects on the Seismic Performance and Vulnerability of Reinforced Concrete Buildings. *International Journal of Geomechanics*, *20*(6), 04020072. https://doi.org/10.1061/(asce)gm.1943-5622.0001651

Tarfan, S., & Tajammolian, H. (2021). Developing Nonlinear Behavior of Reinforced Concrete Elements Using an Intelligent Approach. *Journal of Earthquake Engineering*, *25*(13), 2555–2578. https://doi.org/10.1080/13632469.2019.1628126

Thai, H. T. (2022). Machine learning for structural engineering: A state-of-the-art review. *Structures*, *38*(December 2021), 448–491. https://doi.org/10.1016/j.istruc.2022.02.003

Tokimatsu, K., & Seed, H. B. (1987). Evaluation of Settlements in Sands due to Earthquake Shaking. *Journal of Geotechnical and Geoenvironmental Engineering*, *113*(8), 861–878.

Torabi, H., & Rayhani, M. T. (2014). Three dimensional Finite Element modeling of seismic soil-structure interaction in soft soil. *Computers and Geotechnics*, *60*, 9–19. https://doi.org/10.1016/j.compgeo.2014.03.014

Torky, A. A., & Ohno, S. (2021). Deep learning techniques for predicting nonlinear multi-component seismic responses of structural buildings. *Computers and Structures*, *252*, 106570. https://doi.org/10.1016/j.compstruc.2021.106570

Trombetta, N. W., Benjamin Mason, H., Hutchinson, T. C., Zupan, J. D., Bray, J. D., & Kutter, B. L. (2015). Nonlinear Soil–Foundation–Structure and Structure–Soil–Structure Interaction: Engineering Demands. *Journal of Structural Engineering*, *141*(7), 1–12.

https://doi.org/10.1061/(ASCE)ST.1943-541X.0001127

Veletsos, A. S., & Meek, J. W. (1974). Dynamic behaviour of building-foundation systems. *Earthquake Engineering & Structural Dynamics*, *3*(2), 121–138. https://doi.org/10.1002/eqe.4290030203

Vicencio, F., & Alexander, N. A. (2018). Higher mode seismic structure-soil-structure interaction between adjacent building during earthquakes. *Engineering Structures*, *174*(September 2017), 322–337. https://doi.org/10.1016/j.engstruct.2018.07.049

Wang, M.-X., Huang, D., Wang, G., & Li, D.-Q. (2020). SS-XGBoost: A Machine Learning Framework for Predicting Newmark Sliding Displacements of Slopes. *Journal of Geotechnical and Geoenvironmental Engineering*, *146*(9). https://doi.org/10.1061/(asce)gt.1943-5606.0002297

Wolf, J. P. (1985). *Dynamic Soil-Structure Interaction* (W. J. Hall (ed.)). Prentice-Hall International Series in Civil Engineering and Engineering Mechanics.

Wu, W., Wang, J., & Lin, C. (2001). Systematic assessment of irregular building–soil interaction using efficient modal analysis. *Earthquake Engineering and Structural Dynamics*, *30*(4), 573–594.

Yeganeh, N., & Fatahi, B. (2019). Effects of choice of soil constitutive model on seismic performance of moment-resisting frames experiencing foundation rocking subjected to near- field earthquakes. *Soil Dynamics and Earthquake Engineering*, *121*(March), 442–459. https://doi.org/10.1016/j.soildyn.2019.03.027

Zhang, J., & Foschi, R. O. (2004). Performance-based design and seismic reliability analysis using designed experiments and neural networks. *Probabilistic Engineering Mechanics*, *19*(3), 259–267. https://doi.org/10.1016/j.probengmech.2004.02.009

Zhou, P., & Chang, Y. (2021). Automated classification of building structures for urban built environment identification using machine learning. *Journal of Building Engineering*, *43*(July), 103008. https://doi.org/10.1016/j.jobe.2021.103008

Zhu, M., McKenna, F., & Scott, M. H. (2018). OpenSeesPy: Python library for the OpenSees finite element framework. *SoftwareX*, *7*, 6–11. https://doi.org/10.1016/j.softx.2017.10.009

Appendices

Appendix A. Modeling Parameters and Numerical Acceptance Criteria

The tables in this Appendix are used during the performance assessment process followed in this study. The tables presented here are adapted from the ASCE-41 standard (American Society of Civil Engineers, 2017b); symbols and abbreviations referenced within are enlisted in the corresponding chapter at the beginning of this document.

Besides, some terms in tables must be calculated in advance to define specific values in the following tables. These terms are also presented as equations in this same appendix.

The terms ρ, ρ', ρ_l, ρ_t, and ρ_{bal} are steel ratios relative to the concrete net area of the element's cross-section A_g, shown in Eqs. [A.1] through [A.6]. They correspond, respectively, to the regular ratio of traction steel, the ratio of compressed steel reinforcement, the ratio of the area of distributed longitudinal reinforcement to gross concrete area perpendicular to that reinforcement, the ratio of the area of distributed transverse reinforcement to gross concrete area perpendicular to that reinforcement, and the balanced ratio of steel in the cross-section.

$$\rho = \frac{A_s}{A_g} \quad [A.1]$$

$$\rho' = \frac{A_s'}{A_g} \quad [A.2]$$

$$\rho_l = \frac{A_{sl}}{A_g} \quad [A.3]$$

$$\rho_t = \frac{A_v}{bd} \quad [A.4]$$

$$\rho_{bal} = \frac{0.85 f_{c_E}' \beta_1}{f_{y_E}} \left(\frac{0.003}{\varepsilon_y + 0.003} \right) \quad [A.5]$$

In previous equations, b is the cross-section's width, d is the effective depth of the cross-section, A_s is the area of tractioned steel reinforcement, A_S' is the area of compressed steel reinforcement, A_v is the area of shear reinforcement, f_{c_E}' is the expected compressive strength of the concrete, f_{y_E} is the expected yield strength of the reinforcement steel, and β_1 is the factor relating to the depth of the compression equivalent rectangular block of stress to the neutral axis per ACI-318.

In **Table A-1** and **Table A-3**, b_w is the width of the beam's web, and V is the shear force at section concurrent with the flexure action, M. On the other hand, in **Table A-2** and **Table A-4**, N_{UD} is the member design axial load, and V_{ColO_E} is the shear strength of concrete columns at a displacement

ductility demand not exceeding a value of 2.0 evaluated using expected material properties calculated according to Eq. [A.6].

$$V_{ColO_E} = \left[\alpha_{Col} \left(\frac{A_v f_{yt_E} d}{s} \right) + \lambda \left(\frac{0.5\sqrt{f'_{c_E}}}{M_{UD}/V_{UD}\, d} \sqrt{1 + \frac{N_{UG}}{0.5 A_g \sqrt{f'_{c_E}}}} \right) 0.8 A_g \right] \quad [A.6]$$

Where α_{Col} is a factor that depends on the ratio s/d. s is the spacing of shear reinforcement, λ is the ACI-318 that equals 1.0 for normal-weight concrete, M_{UD} and V_{UD} are the design moment and shear forces, respectively, and, N_{UG} is the member design axial force evaluated based on gravity loads only (set to zero for traction).

The information in the tables in this appendix is related to deformation-controlled actions to be evaluated during the performance assessment employing linear or nonlinear analysis procedures.

In **Table A-1** and **Table A-2** for linear procedures, for instance, *m*-factors are presented for different Performance Levels (IO, LS, and CP) and component types. These are elements' demand modification factors to account for expected ductility associated with the action being evaluated at the selected Structural Performance Level.

Table A-3 and **Table A-4** for nonlinear procedures, on the other hand, show both modeling parameters and acceptance criteria for a determined deformation-controlled action being evaluated in the performance assessment. Regarding the latter, maximum allowed rotation angles measured in radians are established as limiting values to the ones obtained as analysis outcomes depending on the evaluated SPL. Additionally, modeling parameters are shown and denominated as ***a***, ***b***, and ***c*,** whose values shape the generalized force-deformation curve shown in **Figure A-1**.

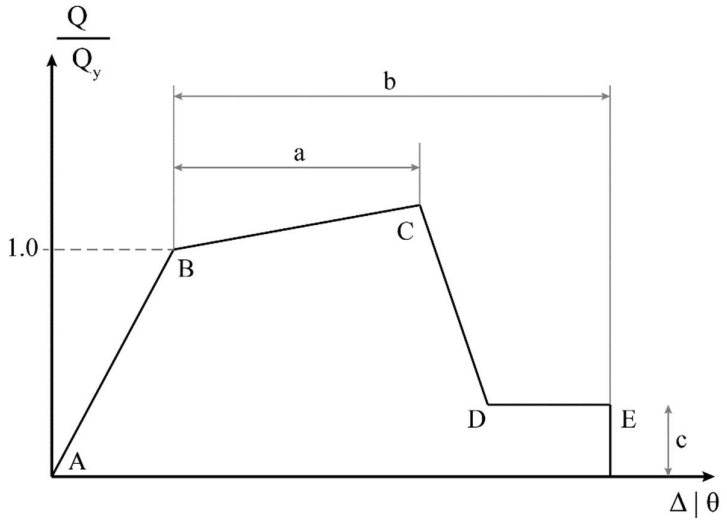

Figure A-1. Generalized force-deformation relationship for concrete elements or components.

Hence, observing the figure above, modeling parameters ***a***, ***b***, and ***c***, are recommended to construct the segments of the force-displacement relationship curve in which the first describes the linear response of the element regarding an action Q. It starts from a state of an unloaded section at A and goes up to a state of effective yielding at point B. Then ***a*** represents the horizontal projection of the post-yield linear behavior with a reduced stiffness (between zero and 10% of the initial stiffness), connecting the state at B to a state C, where a sudden strength reduction occurs until reaching the state in D. Parameter ***b*** is used to define a state of maximum reachable deformation in the element or component while keeping a residual strength capacity given by the ordinate value of the parameter ***c***.

Any other information related to the information of these tables or the description of Performance Levels or Component types was already introduced in Chapter 3.

Table A-1. Numerical Acceptance Criteria for Linear Procedures – Reinforced Concrete Beams

			m-Factors [a]				
			Performance Level				
				Component Type			
				Primary		Secondary	
Conditions			**IO**	**LS**	**CP**	**LS**	**CP**
Condition i. Beams controlled by flexure [b]							
$\frac{\rho - \rho'}{\rho_{bal}}$	Transverse reinforcement [c]	$\frac{V^d}{b_w d\sqrt{f'_{c_E}}}$					
≤ 0.0	C	≤ 3 (0.25)	3	6	7	6	10
≤ 0.0	C	≥ 6 (0.5)	2	3	4	3	5
≥ 0.5	C	≤ 3 (0.25)	2	3	4	3	5
≥ 0.5	C	≥ 6 (0.5)	2	2	3	2	4
≤ 0.0	NC	≤ 3 (0.25)	2	3	4	3	5
≤ 0.0	NC	≥ 6 (0.5)	1.25	2	3	2	4
≥ 0.5	NC	≤ 3 (0.25)	2	3	3	3	4
≥ 0.5	NC	≥ 6 (0.5)	1.25	2	2	2	3
Condition ii. Beams controlled by shear [b]							
Stirrup spacing $\leq d/2$			1.25	1.5	1.75	3	4
Stirrup spacing $> d/2$			1.25	1.5	1.75	2	3
Condition iii. Beams controlled by inadequate development or splicing along the span [b]							
Stirrup spacing $\leq d/2$			1.25	1.5	1.75	3	4
Stirrup spacing $> d/2$			1.25	1.5	1.75	2	3
Condition iv. Beams controlled by inadequate embedment into beam-column joint [b]							
			2	2	3	3	4

Note: f'_{c_E} in lb/in^2 (MPa) units

[a] Values between those listed in the table shall be determined by linear interpolation.

[b] Where more than one of conditions i, ii, iii, and iv occurs for a given component, use the minimum appropriate numerical value from the table.

[c] "C" and "NC" are abbreviations for conforming and nonconforming transverse reinforcement. Transverse reinforcement is conforming if, within the flexural plastic hinge region, hoops are spaced at $\leq d/3$, and if, for components of moderate and high ductility demand, the strength provided by the hoops (V_s) is at least 3/4 of the design shear. Otherwise, the transverse reinforcement is considered nonconforming.

[d] V is the shear force calculated using limit-state analysis procedures in accordance with Section 10.4.2.4.1 of ASCE-41.

Table A-2. Numerical Acceptance Criteria for Linear Procedures – Reinforced Concrete Columns other than Circular with Spiral Reinforcement or Seismic Hoops as defined in ACI-318.

			m-Factors [a]				
			Performance Level				
				Component Type			
				Primary		Secondary	
$\left(\frac{N_{UD}}{A_g f'_{c_E}}\right)$	ρ_t	V_{y_E}/V_{ColO_E}	IO	LS	CP	LS	CP
Columns not controlled by inadequate development or splicing along the clear height [b]							
≤ 0.1	≥ 0.0175	≥ 0.2 < 0.6	1.7	3.4	4.2	6.8	8.9
≥ 0.7	≥ 0.0175	≥ 0.2 < 0.6	1.2	1.4	1.7	1.4	1.7
≤ 0.1	≤ 0.0005	≥ 0.2 < 0.6	1.5	2.6	3.2	2.6	3.2
≥ 0.7	≤ 0.0005	≥ 0.2 < 0.6	1.0	1.0	1.0	1.0	1.0
≤ 0.1	≥ 0.0175	≥ 0.6 < 1.0	1.5	2.7	3.3	6.8	8.9
≥ 0.7	≥ 0.0175	≥ 0.6 < 1.0	1.0	1.0	1.0	1.0	1.0
≤ 0.1	≤ 0.0005	≥ 0.6 < 1.0	1.3	1.9	2.3	1.9	2.3
≥ 0.7	≤ 0.0005	≥ 0.6 < 1.0	1.0	1.0	1.0	1.0	1.0
≤ 0.1	≥ 0.0175	≥ 1.0	1.3	1.8	2.2	6.8	8.9
≥ 0.7	≥ 0.0175	≥ 1.0	1.0	1.0	1.0	1.0	1.0
≤ 0.1	≤ 0.0005	≥ 1.0	1.1	1.0	1.1	1.7	2.1
≥ 0.7	≤ 0.0005	≥ 1.0	1.0	1.0	1.0	1.0	1.0
Columns controlled by inadequate development or splicing along the clear height [b]							
≤ 0.1	≥ 0.0075		1.0	1.7	2.0	5.3	6.8
≥ 0.7	≥ 0.0075		1.0	1.0	1.0	2.8	3.5
≤ 0.1	≤ 0.0005		1.0	1.0	1.0	1.4	1.6
≥ 0.7	≤ 0.0005		1.0	1.0	1.0	1.0	1.0

[a] Values between those listed in the table shall be determined by linear interpolation.
[b] Columns are considered to be controlled by inadequate development or splicing where the calculated steel stress at the splice exceeds the steel stress specified by Eq. (10-1a) or (10-1b) in ASCE-41. Acceptance criteria for columns controlled by inadequate development or splicing shall never exceed those of columns not controlled by inadequate development or splicing.

Table A-3. Modeling Parameters and Numerical Acceptance Criteria for Nonlinear Procedures – Reinforced Concrete Beams

			Modeling Parameters [a]			Acceptance Criteria [a]		
			Plastic Rotation Angle (radians)		Residual Strength Ratio	Plastic Rotation Angle (radians)		
						Performance Level		
Conditions			**a**	**b**	**c**	**IO**	**LS**	**CP**
Condition i. Beams controlled by flexure [b]								
$\frac{\rho - \rho'}{\rho_{bal}}$	Transverse reinforcement [c]	$\frac{V^d}{b_w d\sqrt{f'_{c_E}}}$						
≤ 0.0	C	≤ 3 (0.25)	0.025	0.05	0.2	0.010	0.025	0.05
≤ 0.0	C	≥ 6 (0.50)	0.02	0.04	0.2	0.005	0.02	0.04
≥ 0.5	C	≤ 3 (0.25)	0.02	0.03	0.2	0.005	0.02	0.03
≥ 0.5	C	≥ 6 (0.50)	0.015	0.02	0.2	0.005	0.015	0.02
≤ 0.0	NC	≤ 3 (0.25)	0.02	0.03	0.2	0.005	0.02	0.03
≤ 0.0	NC	≥ 6 (0.50)	0.01	0.015	0.2	0.0015	0.01	0.015
≥ 0.5	NC	≤ 3 (0.25)	0.01	0.015	0.2	0.005	0.01	0.015
≥ 0.5	NC	≥ 6 (0.50)	0.005	0.01	0.2	0.0015	0.005	0.01
Condition ii. Beams controlled by shear [b]								
Stirrup spacing $\leq d/2$			0.003	0.02	0.2	0.0015	0.01	0.02
Stirrup spacing $> d/2$			0.003	0.01	0.2	0.0015	0.005	0.01
Condition iii. Beams controlled by inadequate development or splicing along the span [b]								
Stirrup spacing $\leq d/2$			0.003	0.02	0.0	0.0015	0.01	0.02
Stirrup spacing $> d/2$			0.003	0.01	0.0	0.0015	0.005	0.01
Condition iv. Beams controlled by inadequate embedment into beam-column join [b]								
			0.015	0.03	0.2	0.01	0.02	0.03

Note: f'_{c_E} in lb/in^2 (MPa) units

[a] Values between those listed in the table shall be determined by linear interpolation.

[b] Where more than one of conditions i, ii, iii, and iv occurs for a given component, use the minimum appropriate numerical value from the table.

[c] "C" and "NC" are abbreviations for conforming and nonconforming transverse reinforcement. Transverse reinforcement is conforming if, within the flexural plastic hinge region, hoops are spaced at $\leq d/3$, and if, for components of moderate and high ductility demand, the strength provided by the hoops (V_s) is at least 3/4 of the design shear. Otherwise, the transverse reinforcement is considered nonconforming.

[d] V is the shear force calculated using limit-state analysis procedures in accordance with Section 10.4.2.4.1 of ASCE-41.

Table A-4. Modeling Parameters and Numerical Acceptance Criteria for Nonlinear Procedures – Reinforced Concrete Columns other than Circular with Spiral Reinforcement or Seismic Hoops as Defined in ACI 318.

Modeling Parameters	**Acceptance Criteria**		
	Plastic Rotation Angle (radians)		
	Performance Level		
Plastic Rotation Angles, a and b (radians) **Residual Strength Ratio, c**	**IO**	**LS**	**CP**
Columns not controlled by inadequate development or splicing along the clear height [a]			
$a = \left(0.042 - 0.043\frac{N_{UD}}{A_g f'_{c_E}} + 0.63\rho_t - 0.023\frac{V_{y_E}}{V_{ColO_E}}\right) \geq 0.0$	$0.15a$ ≤ 0.005	$0.5b$ [b]	$0.7b$ [b]
For $\frac{N_{UD}}{A_g f'_{c_E}} \leq 0.5$ $\left\{ b = \frac{0.5}{5+\frac{N_{UD}}{0.8 A_g f'_{c_E}}\frac{1}{\rho t}\frac{f'_{c_E}}{f_{yt_E}}} - 0.01 \geq a \right.$ [a]			
$c = 0.24 - 0.4\frac{N_{UD}}{A_g f'_{c_E}} \geq 0.0$			
Columns controlled by inadequate development or splicing along the clear height [c]			
$a = \left(\frac{1}{8}\frac{\rho_t}{\rho_l}\frac{f_{yt_E}}{f_{yl_E}}\right)$ ≥ 0.0 ≤ 0.025 [d]	0.0	$0.5b$	$0.7b$
$b = \left(0.012 - 0.085\frac{N_{UD}}{A_g f'_{c_E}} + 12\rho_t^e\right)$ ≥ 0.0 $\geq a$ ≤ 0.06			
$c = 0.15 + 36\rho_t \leq 0.4$			

Notes: ρ_t shall not be taken as greater than 0.0175 in any case nor greater than 0.0075 when ties are not adequately anchored in the core. Equations in the table are not valid for columns with ρ_t smaller than 0.0005.
V_{y_E}/V_{ColO_E} shall not be taken as less than 0.2.
N_{UD} shall be the maximum compressive axial load accounting for the effects of lateral forces as described in Eq. (7-34) in ASCE-41. Alternatively it shall be permitted to evaluate N_{UD} based on a limit-state analysis.
[a] b shall be reduced linearly for $N_{UD}/(A_g f'_{c_E}) > 0.5$ from its value at $N_{UD}/(A_g f'_{c_E}) = 0.5$ at zero at $N_{UD}/(A_g f'_{c_E}) = 0.7$ but shall not be smaller than a.
[b] $N_{UD}/(A_g f'_{c_E})$ shall not be taken as smaller than 0.1.
[c] Columns are considered to be controlled by inadequate development or splicing where the calculated steel stress at the splice exceeds the steel stress specified by Eq. (10-1a) or (10-1b) in ASCE-41. Acceptance criteria for columns controlled by inadequate development or splicing shall never exceed those of columns not controlled by inadequate development or splicing.
[d] a for columns controlled by inadequate development or splicing shall be taken as zero if the splice region is not crossed by at least two tie groups over its length.
[e] ρ_t shall not be taken as greater than 0.0075.

Appendix B. Closed-form Equations for Reinforced Concrete Sections

This appendix presents the closed-form equations derived in work carried out by (Monti & Petrone, 2015) to calculate the yield and ultimate moment and curvature parameters for a reinforced concrete section.

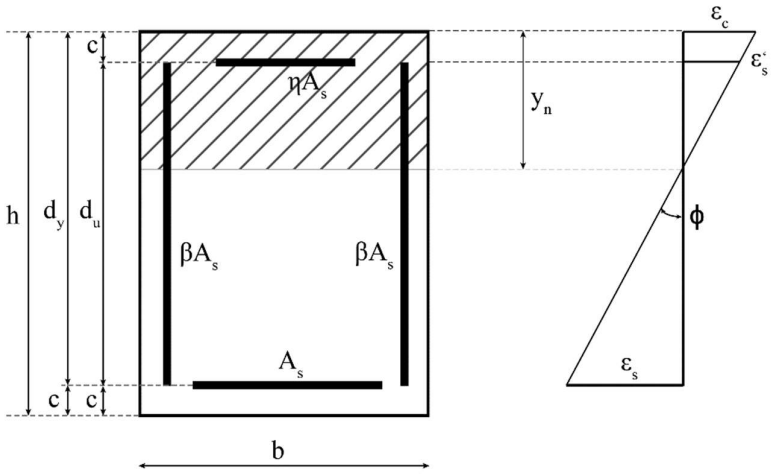

Figure B-1. Reinforced-concrete cross-section notation. Generic strain notation.

Some terms in the derivation of the following equations obey the terminology described in **Figure B-1**. Other symbols are detailed at the end of the appendix.

Determination of parameters at the yielding point

The yielding curvature, ϕ_y:

$$\phi_y = \frac{\varepsilon_{yd}}{d_y}\ \frac{1}{1-\xi_y} \qquad [B.1]$$

With,

$$\varepsilon_{yd} = \frac{f_{yd}}{E_s} \qquad [B.2]$$

$$\xi_y = \frac{n_{sdy} + \hat{\xi}_y^2\left(2\bar{\varepsilon}^2\hat{\xi}_y - n_{sdy} - \rho_{sy,tot}\right) + \rho_{sy}\left[1+\eta\delta_y+\beta\left(1+\delta_y\right)\right]}{2n_{sdy} + 2\hat{\xi}_y\left(3/2\,\hat{\xi}_y - n_{sdy} - \rho_{sy,tot}\right) + \rho_{sy}\left[2+\eta\left(1+\delta_y\right)+\beta\left(3+\delta_y\right)\right]} \qquad [B.3]$$

Where,

$$n_{sdy} = \frac{N_{sd}}{bd_y f_{cd}} \qquad [B.4]$$

$$\hat{\xi}_y = 1/2 \quad [B.5]$$

$$\overline{\varepsilon} = \frac{\varepsilon_{yd}}{\varepsilon_{cu}} \quad [B.6]$$

$$\rho_{sy} = \frac{A_s f_{yd}}{b d_y f_{cd}} \quad [B.7]$$

$$\rho_{sy,tot} = \rho_{sy}\left(1 - \eta + 2\beta\right) \quad [B.8]$$

$$\delta_y = \frac{c}{d_y} \quad [B.9]$$

The yielding moment, M_y:

$$\begin{aligned} M_y = {} & \eta A_s f_{yd} e_s^{'} \frac{1}{2}\left(d_y - c\right) + \overline{\varepsilon}^2 \left(\frac{\xi_y}{1-\xi_y}\right)^2 b\, y_y f_{cd}\left(\frac{1}{2}\left(d_y + c\right) - v_c y_y\right) \\ & + \frac{1}{2}\frac{2\beta A_s}{d_y - c}\left(y_y - c\right) f_{yd} e_s^{'}\left(\frac{1}{2}\left(d_y - c\right) - \frac{1}{3}\left(y_y - c\right)\right) + \\ & + \frac{1}{2}\frac{2\beta A_s}{d_y - c}\left(d_y - y_y\right) f_{yd}\left(\frac{1}{2}\left(d_y - c\right) - \frac{1}{3}\left(d_y - y_y\right)\right) + A_s f_{yd}\frac{1}{2}\left(d_y - c\right) \end{aligned} \quad [B.10]$$

Where,

$$e_s^{'} = \frac{\xi_y - \delta_y}{1 - \xi_y} \quad [B.11]$$

$$y_y = d_y - \frac{\varepsilon_{yd}}{\phi_y} \quad [B.12]$$

Determination of parameters at the ultimate point

The ultimate curvature, ϕ_u:

$$\phi_u = \frac{\varepsilon_{cu}}{d_u}\ \frac{0.80 + 4\beta\rho_{su}}{n_{sdu} + \rho_{su,tot}} \quad [B.13]$$

Where,

$$\rho_{su} = \frac{A_s f_{yd}}{b d_u f_{cd}} \quad [B.14]$$

$$\rho_{su,tot} = \rho_{su}\left(1 - \eta + 2\beta\right) \quad [B.15]$$

$$n_{sdu} = n_{sdy}\frac{d_y}{d_u} \qquad [B.16]$$

The ultimate Moment, M_u:

$$M_u = 0.80b\,\mathrm{y}_u f_{cd}\left(\frac{1}{2}d_u - 0.40y_u\right) + \frac{2\beta A_s}{d_u}y_u f_{yd}\left[\left(d_u - y_u\right) - \frac{1}{3}y_u\left(\frac{\varepsilon_{yd}}{\varepsilon_{cu}}\right)^2\right] + \frac{1}{2}A_s f_{yd} d_u\left(1+\eta\right) \qquad [B.17]$$

Where,

$$y_u = \frac{\varepsilon_{cu}}{\phi_u} \qquad [B.18]$$

Notation:

βA_s	lateral steel reinforcement area on each side.
A_s	bottom steel reinforcement area.
ηA_s	top steel reinforcement area, $\eta \leq 1.0$.
b	section base.
c	concrete cover.
$d_u = h - 2c$	section effective depth at ultimate state.
$d_y = h - c$	section effective depth at yield state.
E_s	steel Young's modulus.
e'_s	normalized strain in compressive bars.
$f_{cd} = 0.85f'_c$	concrete design compressive strength.
f_{yd}	steel design yield strength.
h	section depth.
N_{sd}	design axial force acting in the cross-section.
n_{sdy}, n_{sdu}	normalized design axial force acting in the cross-section at yield and ultimate state.
y_y, y_u	distance of neutral axis from topmost compressive fiber at yield and ultimate state.
ε_c	concrete compressive strength.
ε_{cu}	ultimate concrete compressive strength.
ε_s	steel tensile strain.
ε_{yd}	steel yield design strain.
ρ_{sy}	steel reinforcement ratio with respect to effective cross-section at yield.

Appendix C. Ground Motion Suite: signal processing and scaling

In Section 3.4.3, it was presented the selected earthquake events part of the eleven ground motions suite for the performance assessment of buildings in the database employing LTHA and NLTHA. For convenience, the table with characteristic data of the suite events is replicated in this appendix in **Table C-1**.

Table C-1. Unscaled ground motion suite data for the time-history analyses.

Earthquake	Year	M_w	RSN	Dist [km]	5-95% Duration [s]	v_{so} [m/s]	Comp.	PGA [cm/s²]	PGV [cm/s]
Imperial Valley	1979	6.53	169	22.03	51.41	242.1	1	234.35	26.88
							2	326.98	35.08
Imperial Valley	1979	6.53	178	12.58	14.17	162.9	1	289.91	39.75
							2	212.56	37.56
Loma Prieta	1989	6.93	759	43.94	23.14	116.4	1	262.75	26.72
							2	285.47	44.66
Loma Prieta	1989	6.93	806	24.23	25.48	267.7	1	196.78	29.83
							2	215.02	39.32
Landers	1992	7.28	848	19.74	10.58	352.9	1	274.76	23.33
							2	402.97	46.50
Cioalinga-01	1983	6.36	338	29.48	13.54	246.1	1	272.05	35.63
							2	267.41	30.90
Kocaeli Turkey	1999	7.51	1158	15.37	11.58	281.9	1	319.13	55.11
							2	353.37	47.77
Superstition Hills	1987	6.54	721	18.20	36.66	192.1	1	369.23	34.42
							2	287.16	37.02
Superstition Hills	1987	6.54	729	23.85	36.47	179.0	1	160.33	40.75
							2	219.54	37.19
Chi-Chi Taiwan	1999	7.62	1201	14.82	29.85	278.8	1	311.91	39.38
							2	238.22	40.16
Hector Mine	1999	7.13	1787	11.62	11.62	726.0	1	258.46	20.50
							2	353.25	35.53

To be used in the analysis, these unscaled records should be first processed and scaled following the guidelines described in 3.4.3. Recall that the scaling process must be performed for each building independently every time a performance assessment is initiated because of its vibration period value T_n (or $\tilde{T}_n$ for *flexBase*-BSC) and the DT used for the design (*convDs* or *SSIDs*). Also, since target GRS are defined for each selected SHL (i.e., for BSE-1N and BSE-2N), the correction factors applied to ground motion records differ depending on the SHL. Thus, due to the enormous amount of models to be assessed for different BSCs and SHLs, it is hard to graphically show the signal-processing and the scaling procedure for each evaluated structure. Hence, in this appendix, only signal-processed and scaled ground motions of the suite are demonstrated for both BSE-1N (**Figure C-1** through **Figure C-11**) and BSE-2N (**Figure C-12** through **Figure C-22**) SHLs for a *fixBase*-BSC conventionally designed building with $NbaysX = 6$, $NbaysZ = 4$, $NStrs = 10$ having a period of vibration $T_n = 1.03s$ and assuming a 3%-damped GRS for scalin purposes. A wider description of the plots in these figures is addressed in Section 3.4.3.

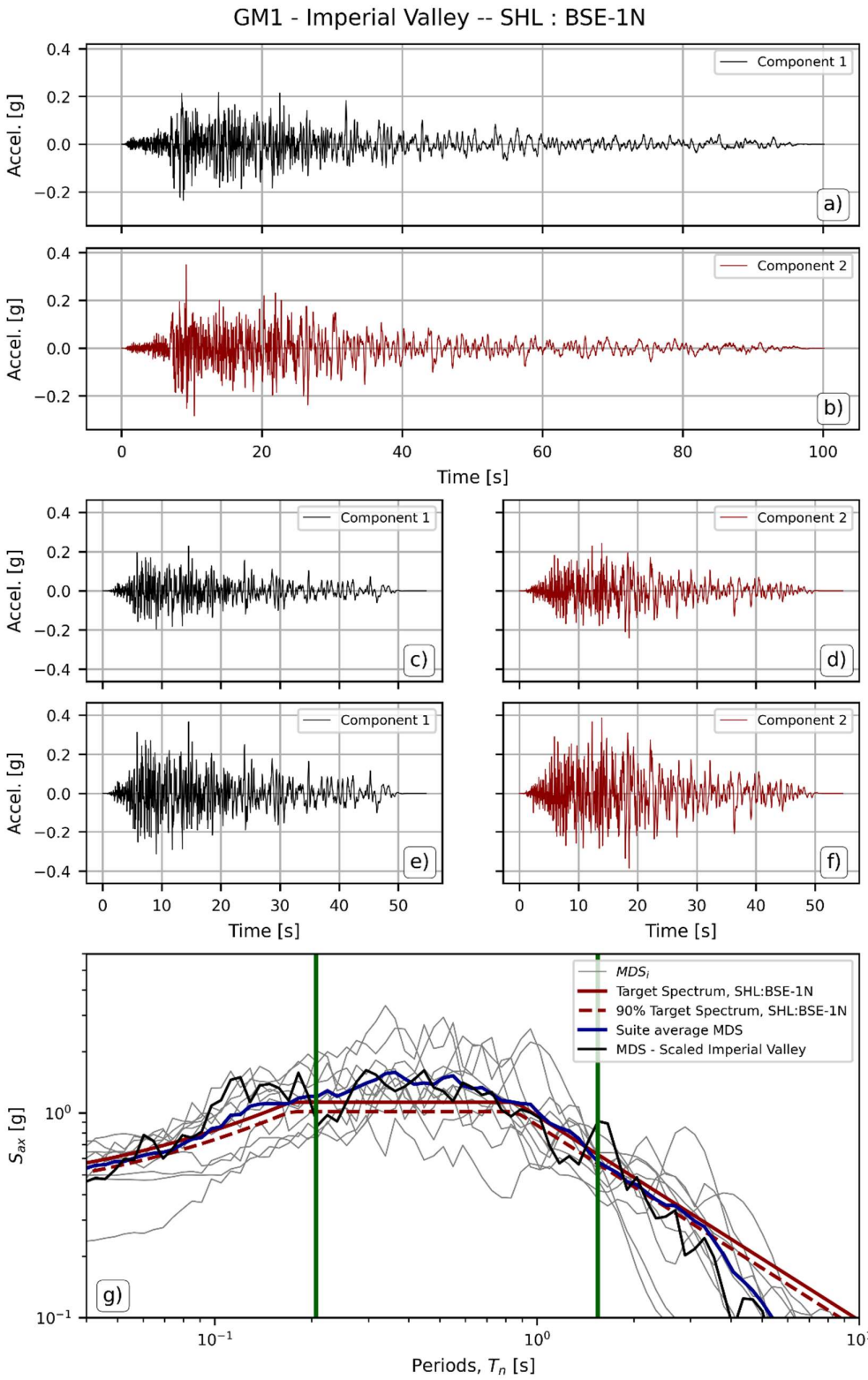

Figure C-1. GM1-Imperial Valley processing and scaling for BSE-1N seismic hazard level. Shown are a) the original signal for component 1; b) the original signal for component 2; c) the trimmed, filtered, and zero-padded signal for component 1; d) the trimmed, filtered, and zero-padded signal for component 2; e) the scaled signal for component 1; f) the scaled signal for component 1; and g) plot depicting the target 3%-damped GRS for SHL=BSE-1N (solid red) along with its 90% representation (dashed red), the MDS obtained from both scaled components of the event (solid black), MDS for all other events in the suite (MDSi – solid gray), and the average MDS for all scaled events in the GMs suite.

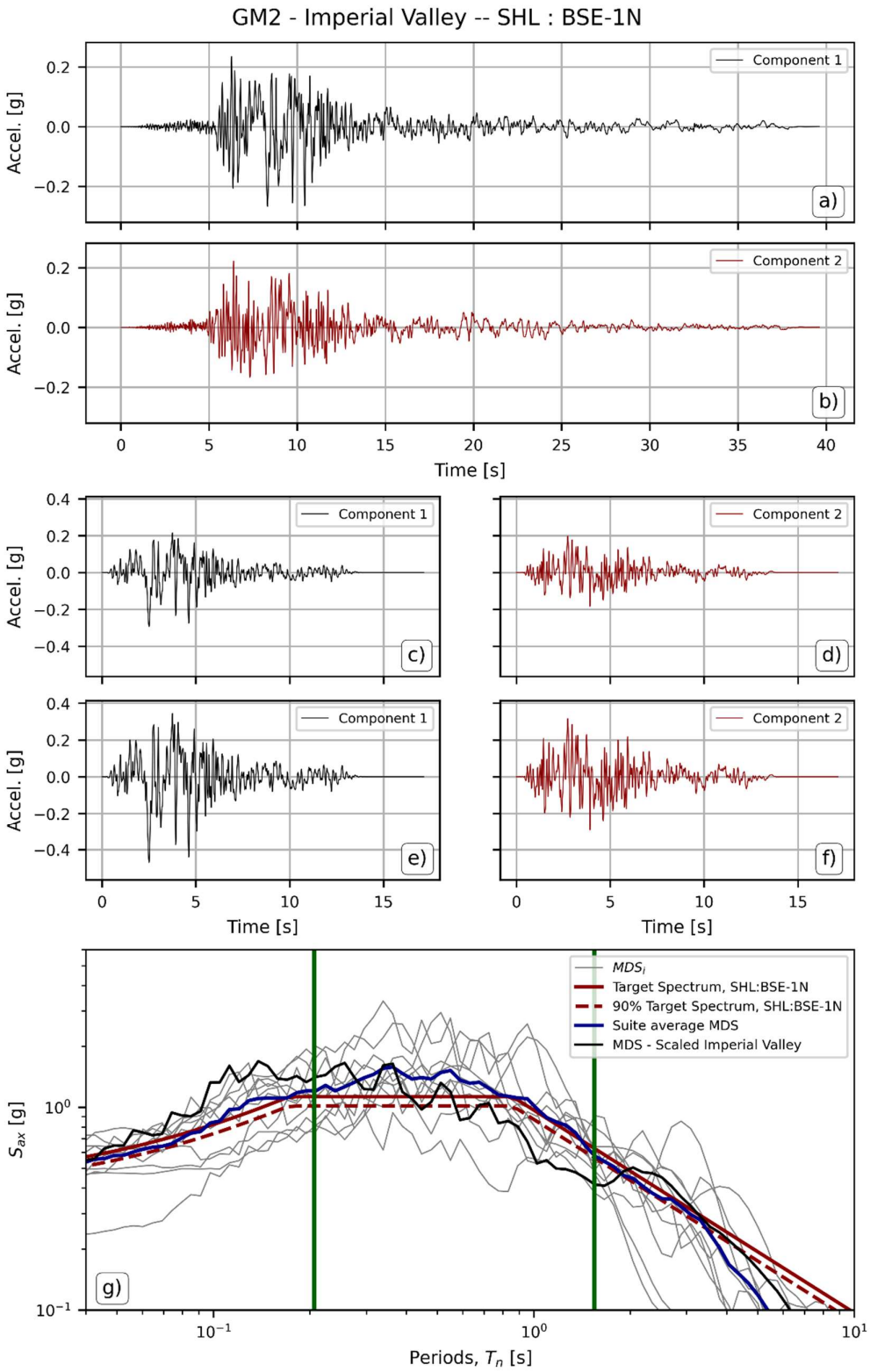

Figure C-2. GM2-Imperial Valley processing and scaling for BSE-1N seismic hazard level. Shown are a) the original signal for component 1; b) the original signal for component 2; c) the trimmed, filtered, and zero-padded signal for component 1; d) the trimmed, filtered, and zero-padded signal for component 2; e) the scaled signal for component 1; f) the scaled signal for component 1; and g) plot depicting the target 3%-damped GRS for SHL=BSE-1N (solid red) along with its 90% representation (dashed red), the MDS obtained from both scaled components of the event (solid black), MDS for all other events in the suite (MDSi – solid gray), and the average MDS for all scaled events in the GMs suite.

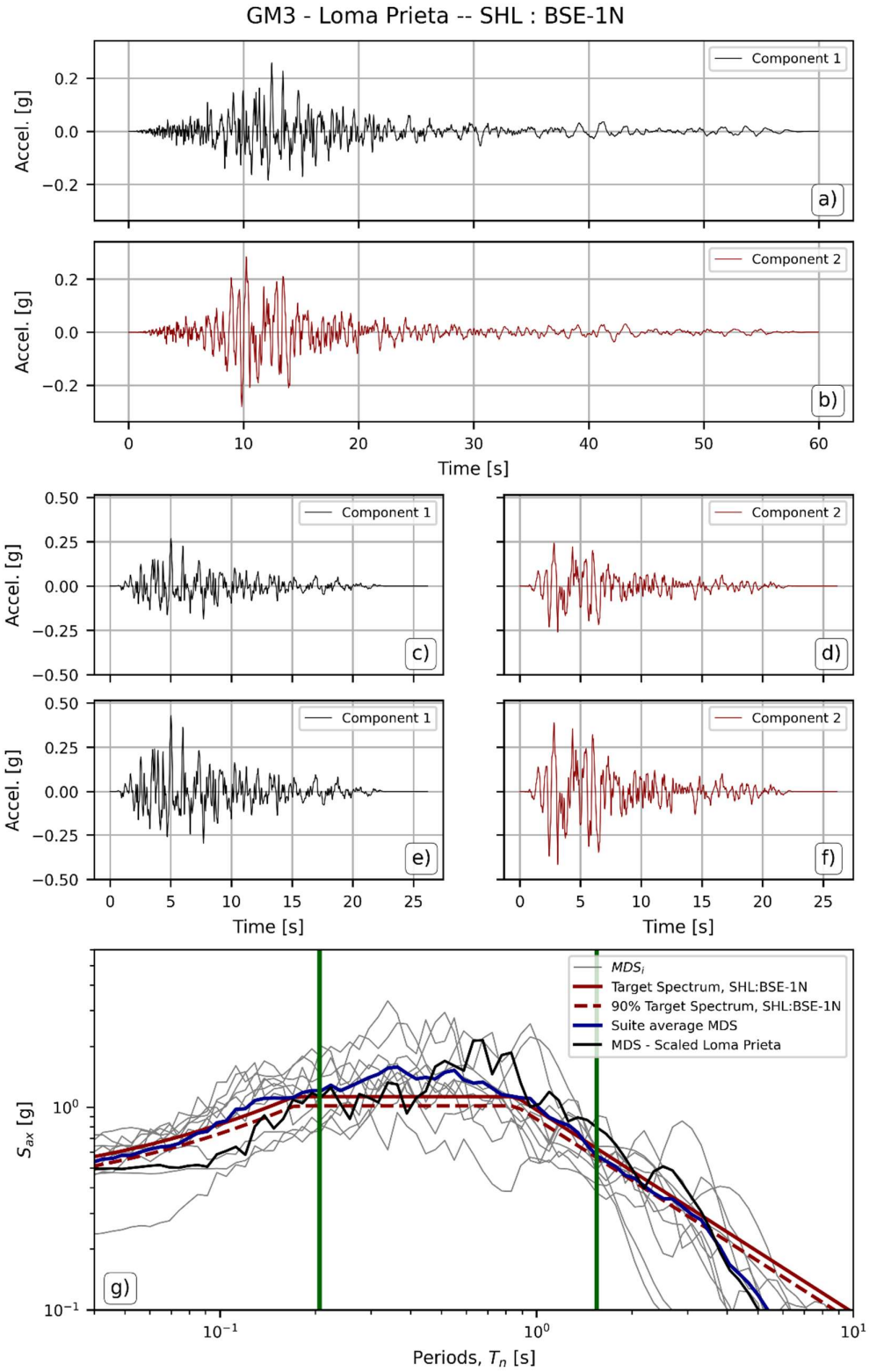

Figure C-3. GM3-Loma Prieta processing and scaling for BSE-1N seismic hazard level. Shown are a) the original signal for component 1; b) the original signal for component 2; c) the trimmed, filtered, and zero-padded signal for component 1; d) the trimmed, filtered, and zero-padded signal for component 2; e) the scaled signal for component 1; f) the scaled signal for component 1; and g) plot depicting the target 3%-damped GRS for SHL=BSE-1N (solid red) along with its 90% representation (dashed red), the MDS obtained from both scaled components of the event (solid black), MDS for all other events in the suite (MDSi – solid gray), and the average MDS for all scaled events in the GMs suite.

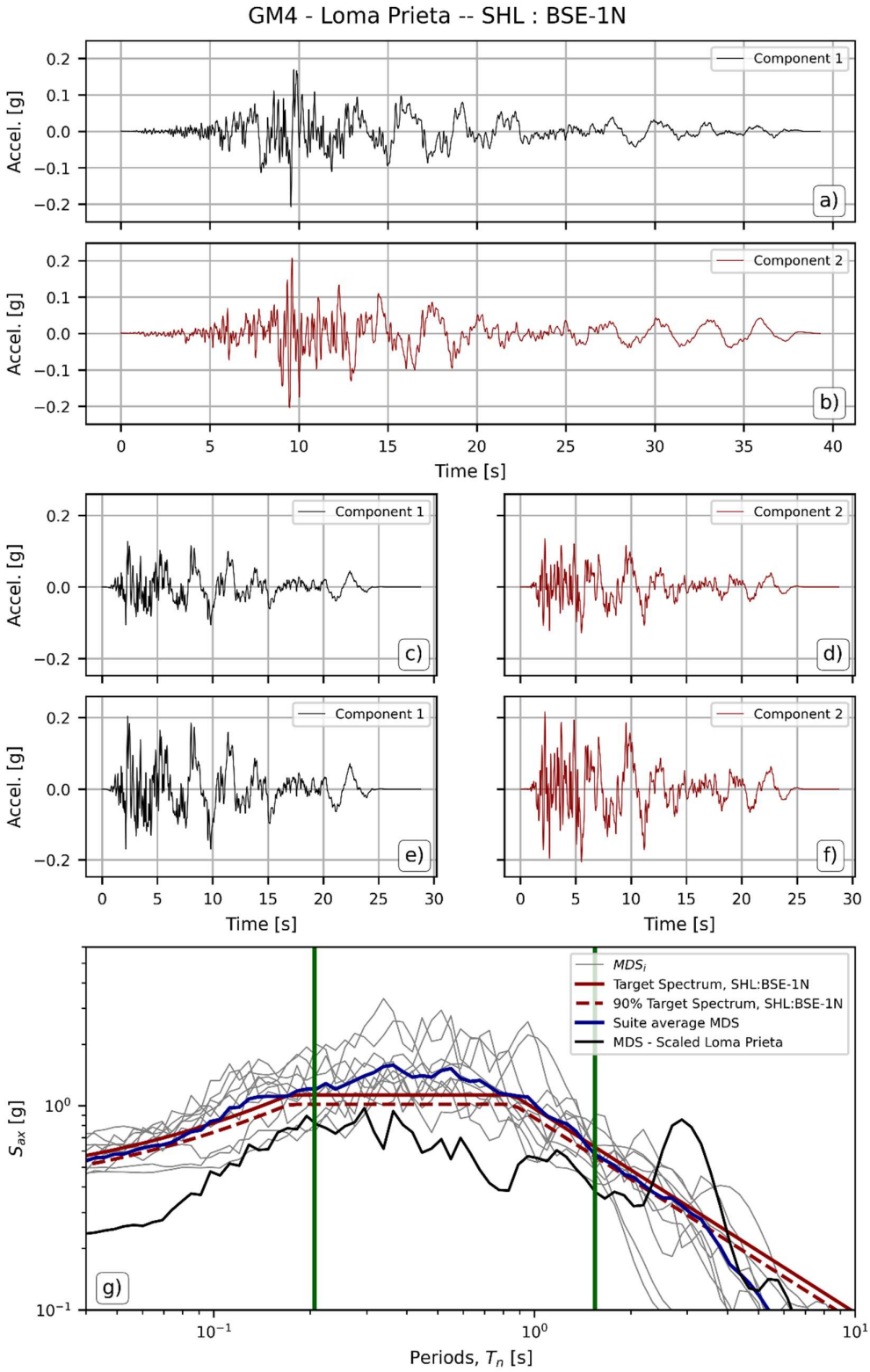

Figure C-4. GM4-Loma Prieta processing and scaling for BSE-1N seismic hazard level. Shown are a) the original signal for component 1; b) the original signal for component 2; c) the trimmed, filtered, and zero-padded signal for component 1; d) the trimmed, filtered, and zero-padded signal for component 2; e) the scaled signal for component 1; f) the scaled signal for component 1; and g) plot depicting the target 3%-damped GRS for SHL=BSE-1N (solid red) along with its 90% representation (dashed red), the MDS obtained from both scaled components of the event (solid black), MDS for all other events in the suite (MDSi – solid gray), and the average MDS for all scaled events in the GMs suite.

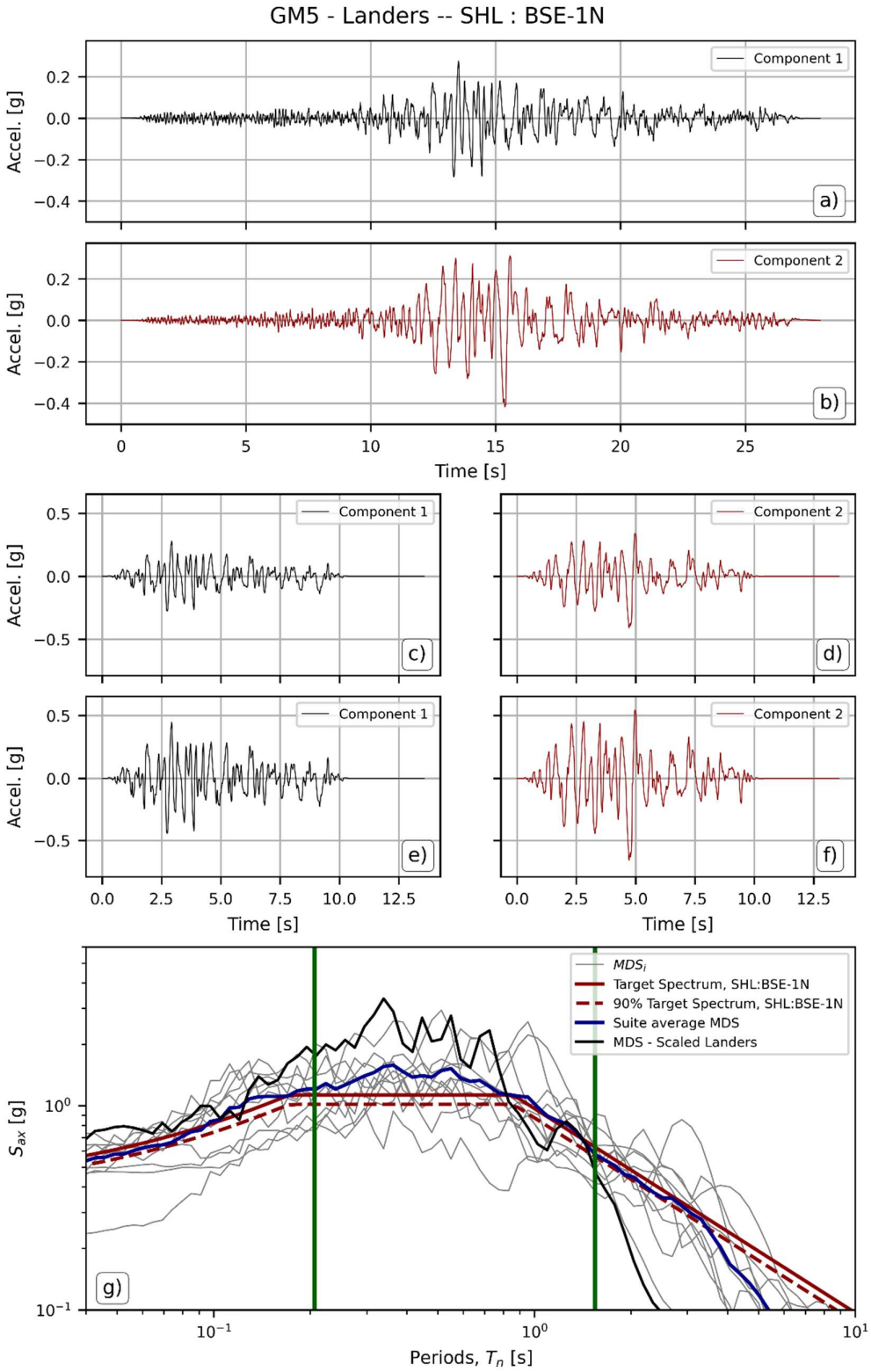

Figure C-5. GM5-Landers processing and scaling for BSE-1N seismic hazard level. Shown are a) the original signal for component 1; b) the original signal for component 2; c) the trimmed, filtered, and zero-padded signal for component 1; d) the trimmed, filtered, and zero-padded signal for component 2; e) the scaled signal for component 1; f) the scaled signal for component 1; and g) plot depicting the target 3%-damped GRS for SHL=BSE-1N (solid red) along with its 90% representation (dashed red), the MDS obtained from both scaled components of the event (solid black), MDS for all other events in the suite (MDSi – solid gray), and the average MDS for all scaled events in the GMs suite.

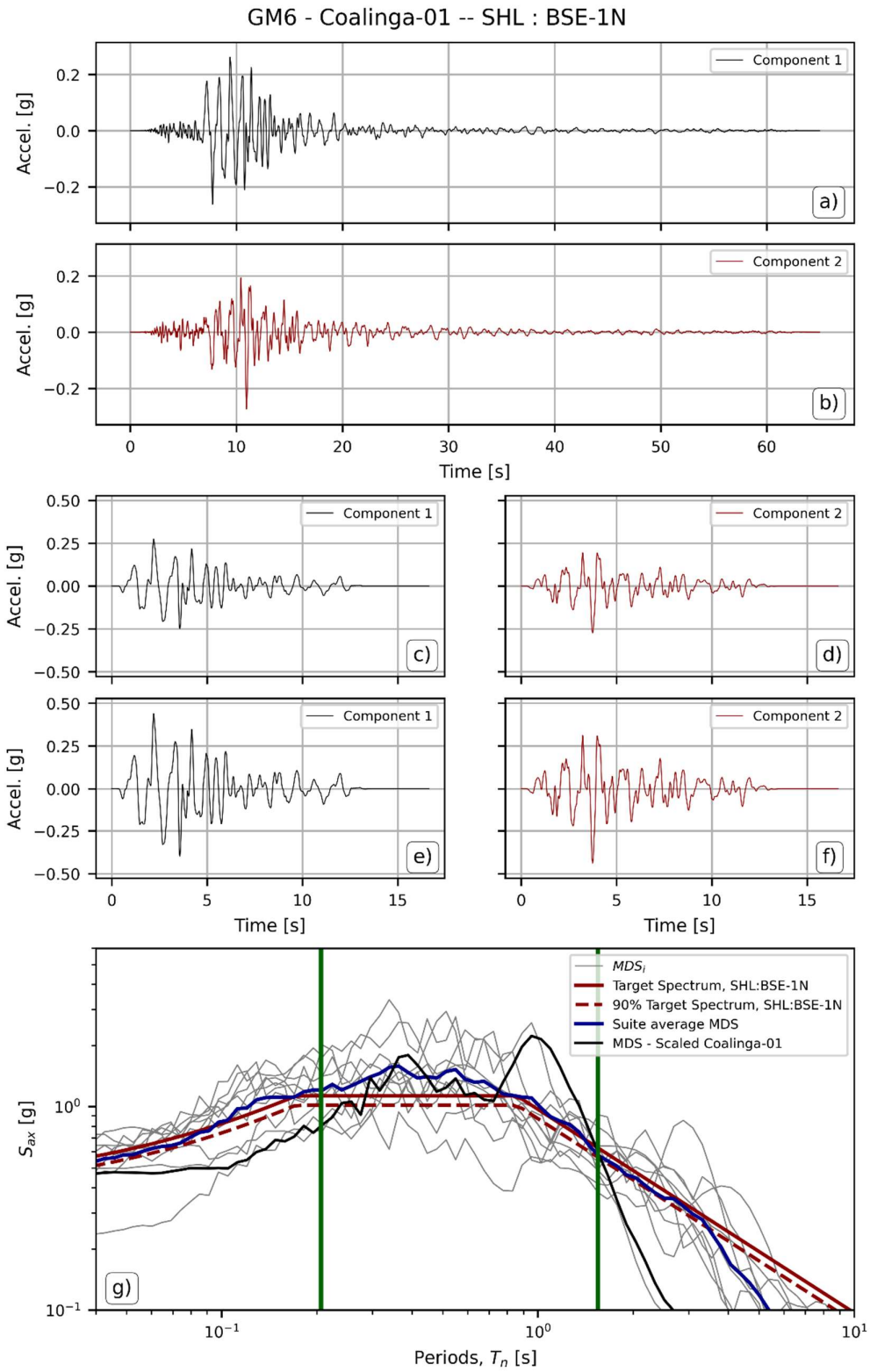

Figure C-6. GM6-Coalinga-01 processing and scaling for BSE-1N seismic hazard level. Shown are a) the original signal for component 1; b) the original signal for component 2; c) the trimmed, filtered, and zero-padded signal for component 1; d) the trimmed, filtered, and zero-padded signal for component 2; e) the scaled signal for component 1; f) the scaled signal for component 1; and g) plot depicting the target 3%-damped GRS for SHL=BSE-1N (solid red) along with its 90% representation (dashed red), the MDS obtained from both scaled components of the event (solid black), MDS for all other events in the suite (MDSi – solid gray), and the average MDS for all scaled events in the GMs suite.

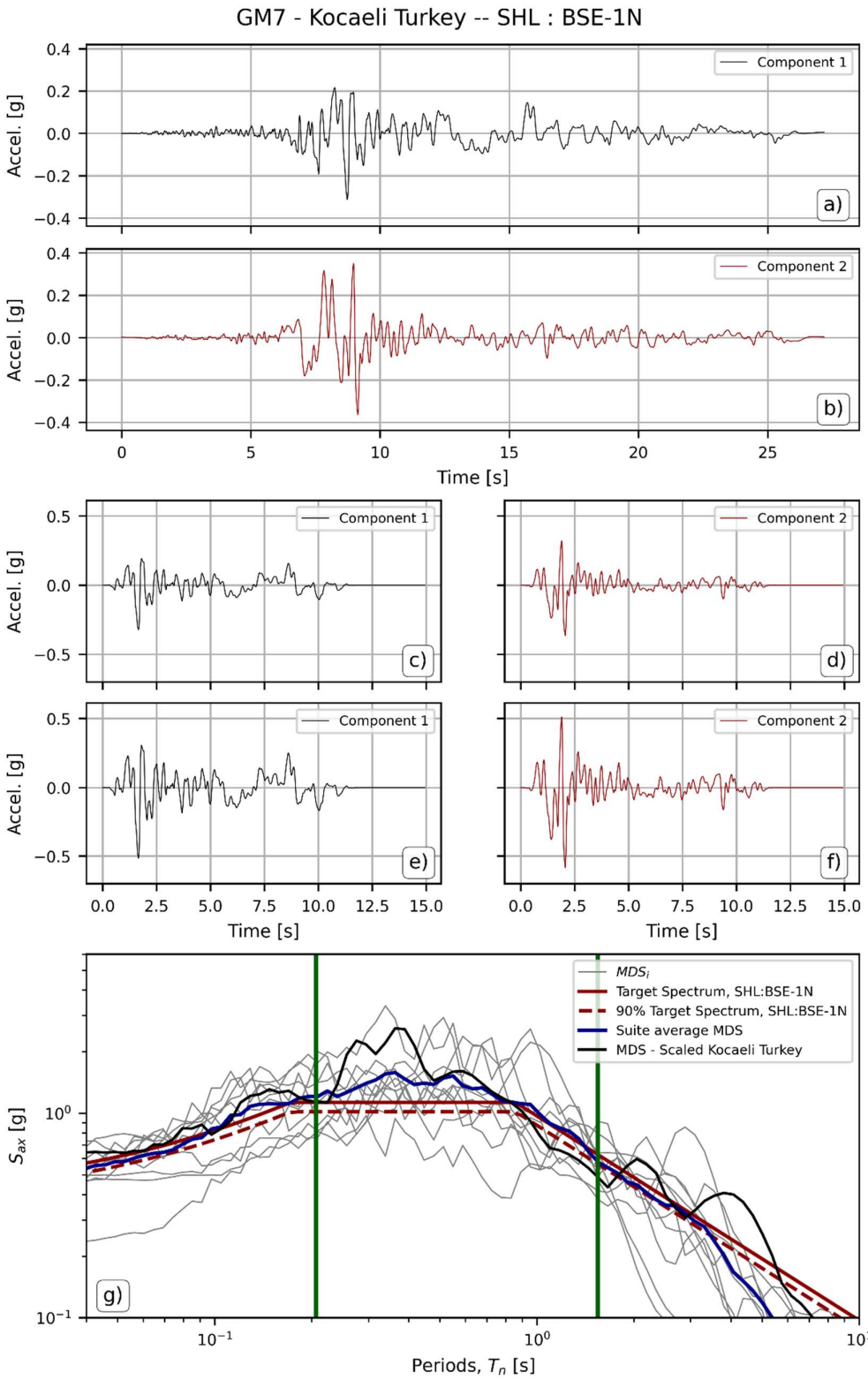

Figure C-7. GM7-Kocaeli Turkey processing and scaling for BSE-1N seismic hazard level. Shown are a) the original signal for component 1; b) the original signal for component 2; c) the trimmed, filtered, and zero-padded signal for component 1; d) the trimmed, filtered, and zero-padded signal for component 2; e) the scaled signal for component 1; f) the scaled signal for component 1; and g) plot depicting the target 3%-damped GRS for SHL=BSE-1N (solid red) along with its 90% representation (dashed red), the MDS obtained from both scaled components of the event (solid black), MDS for all other events in the suite (MDSi – solid gray), and the average MDS for all scaled events in the GMs suite.

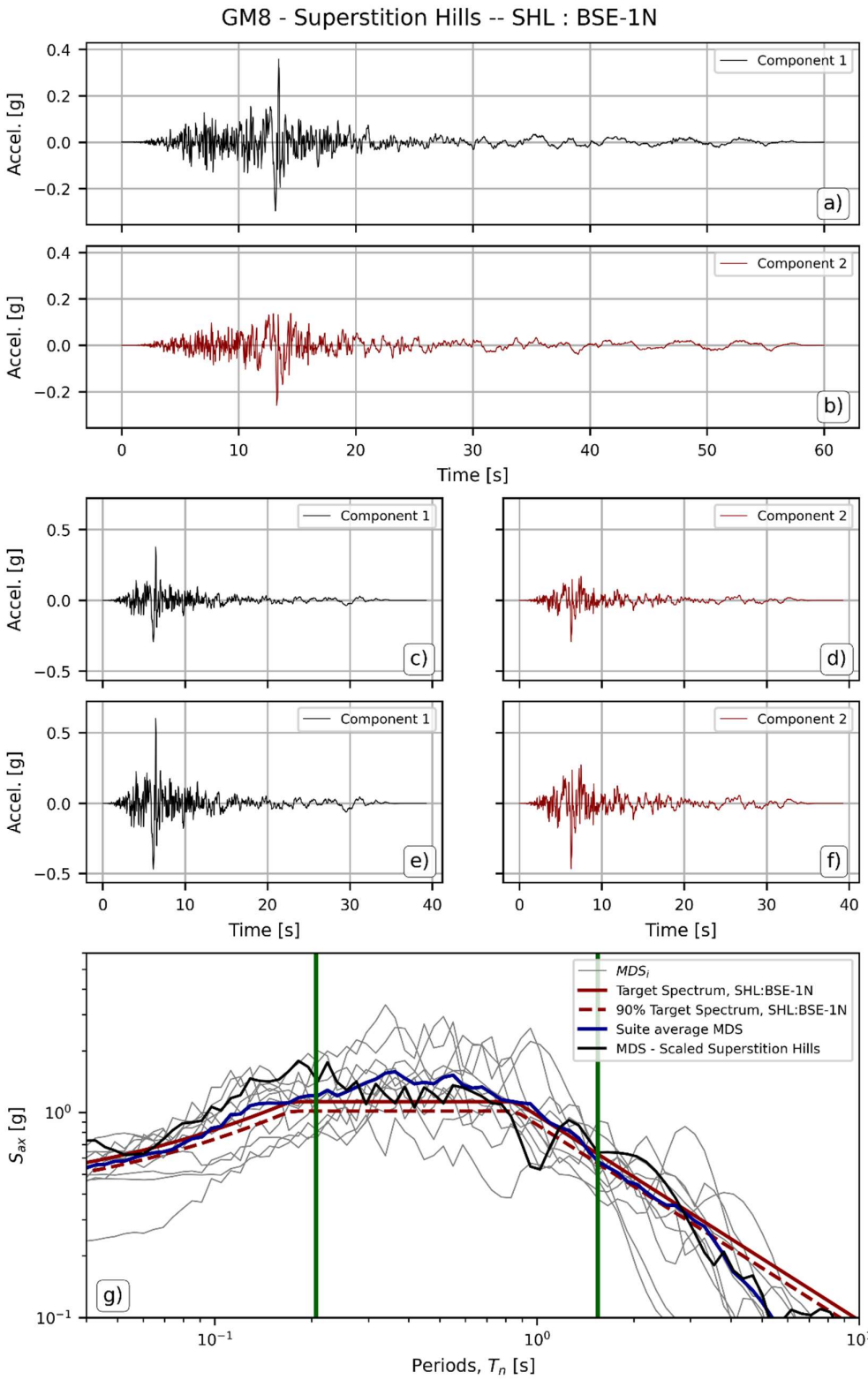

Figure C-8. GM8-Supertition Hills processing and scaling for BSE-1N seismic hazard level. Shown are a) the original signal for component 1; b) the original signal for component 2; c) the trimmed, filtered, and zero-padded signal for component 1; d) the trimmed, filtered, and zero-padded signal for component 2; e) the scaled signal for component 1; f) the scaled signal for component 1; and g) plot depicting the target 3%-damped GRS for SHL=BSE-1N (solid red) along with its 90% representation (dashed red), the MDS obtained from both scaled components of the event (solid black), MDS for all other events in the suite (MDSi – solid gray), and the average MDS for all scaled events in the GMs suite.

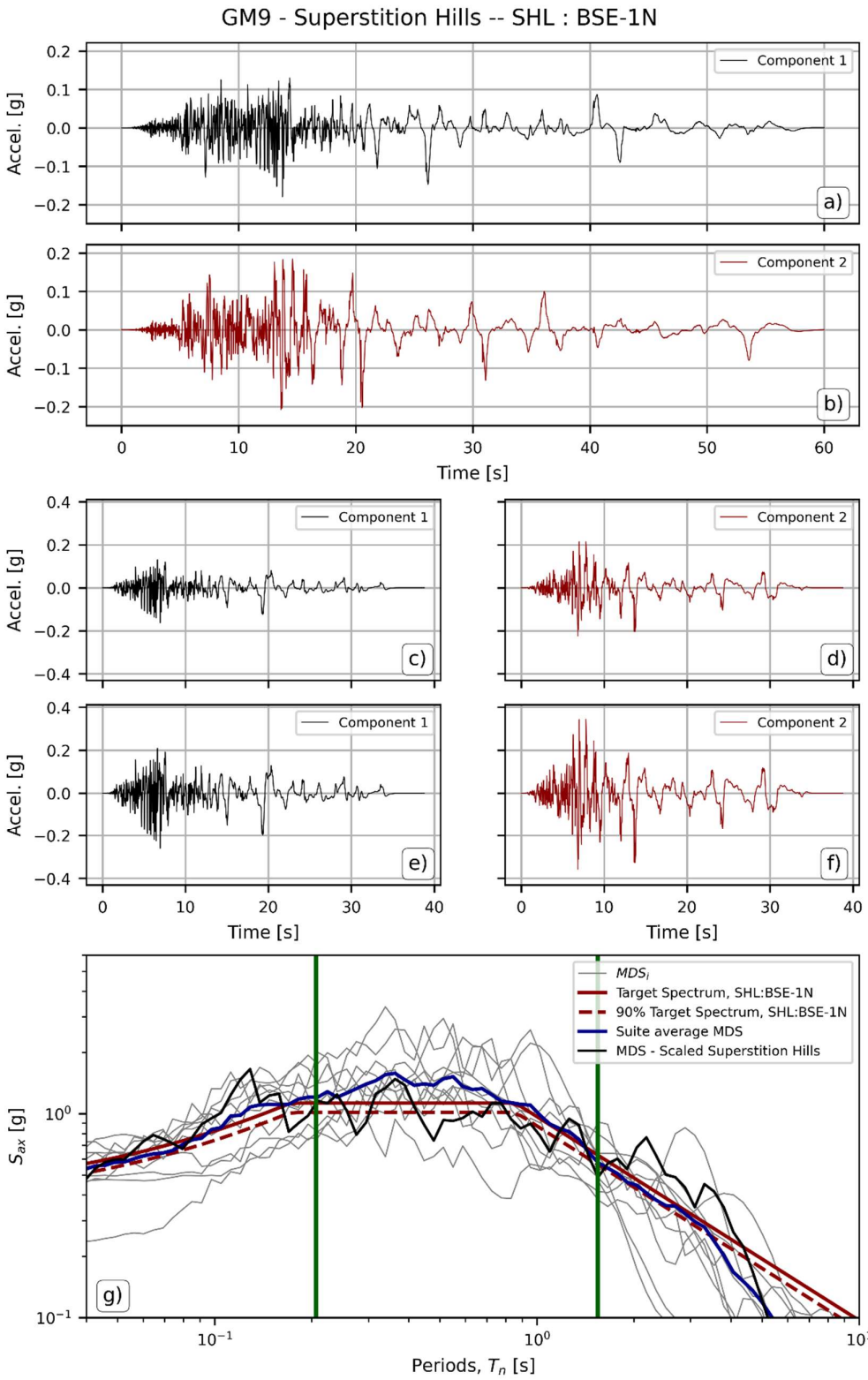

Figure C-9. GM9-Supertition Hills processing and scaling for BSE-1N seismic hazard level. Shown are a) the original signal for component 1; b) the original signal for component 2; c) the trimmed, filtered, and zero-padded signal for component 1; d) the trimmed, filtered, and zero-padded signal for component 2; e) the scaled signal for component 1; f) the scaled signal for component 1; and g) plot depicting the target 3%-damped GRS for SHL=BSE-1N (solid red) along with its 90% representation (dashed red), the MDS obtained from both scaled components of the event (solid black), MDS for all other events in the suite (MDSi – solid gray), and the average MDS for all scaled events in the GMs suite.

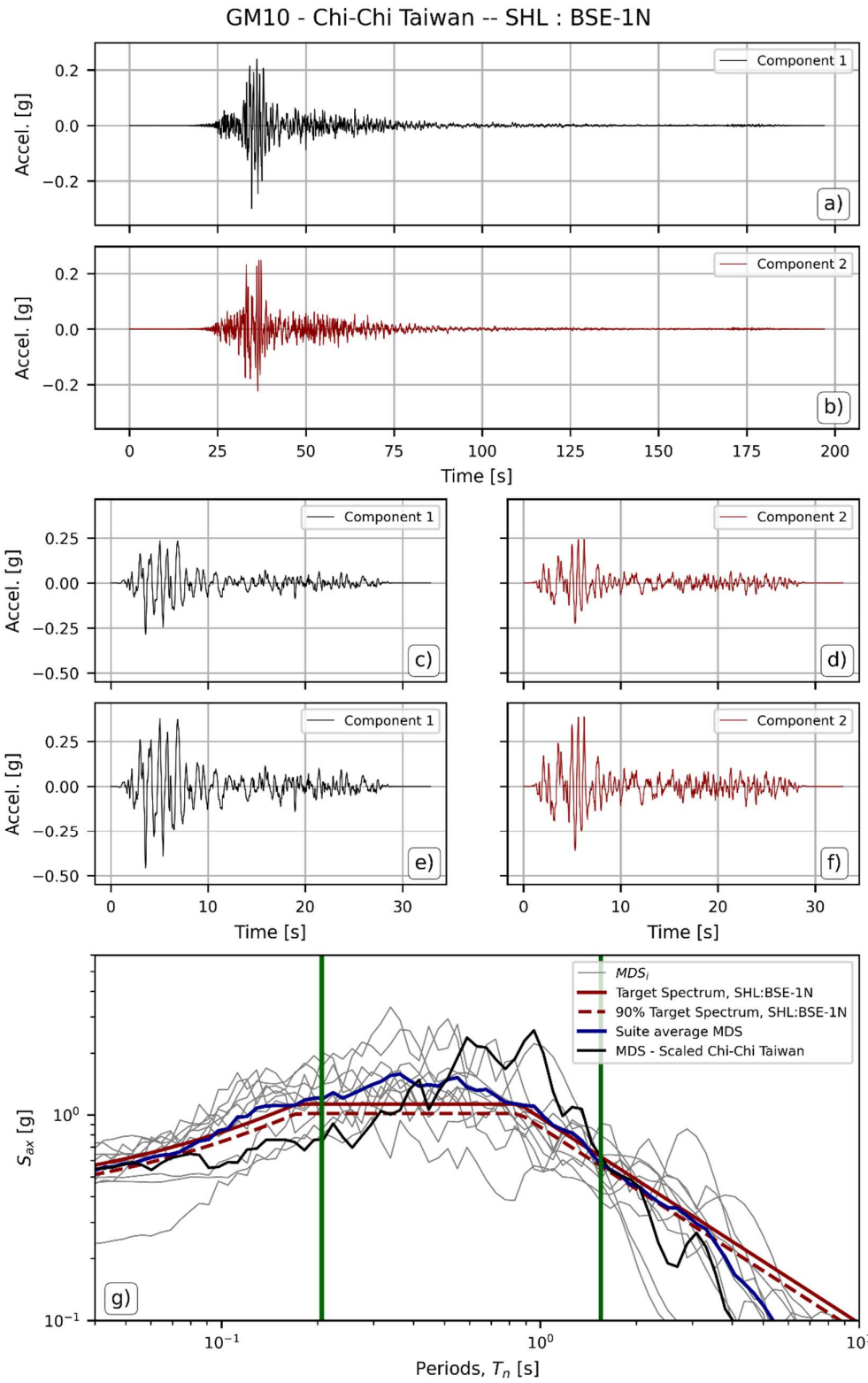

Figure C-10. GM10-Chi-Chi Taiwan processing and scaling for BSE-1N seismic hazard level. Shown are a) the original signal for component 1; b) the original signal for component 2; c) the trimmed, filtered, and zero-padded signal for component 1; d) the trimmed, filtered, and zero-padded signal for component 2; e) the scaled signal for component 1; f) the scaled signal for component 1; and g) plot depicting the target 3%-damped GRS for SHL=BSE-1N (solid red) along with its 90% representation (dashed red), the MDS obtained from both scaled components of the event (solid black), MDS for all other events in the suite (MDSi – solid gray), and the average MDS for all scaled events in the GMs suite.

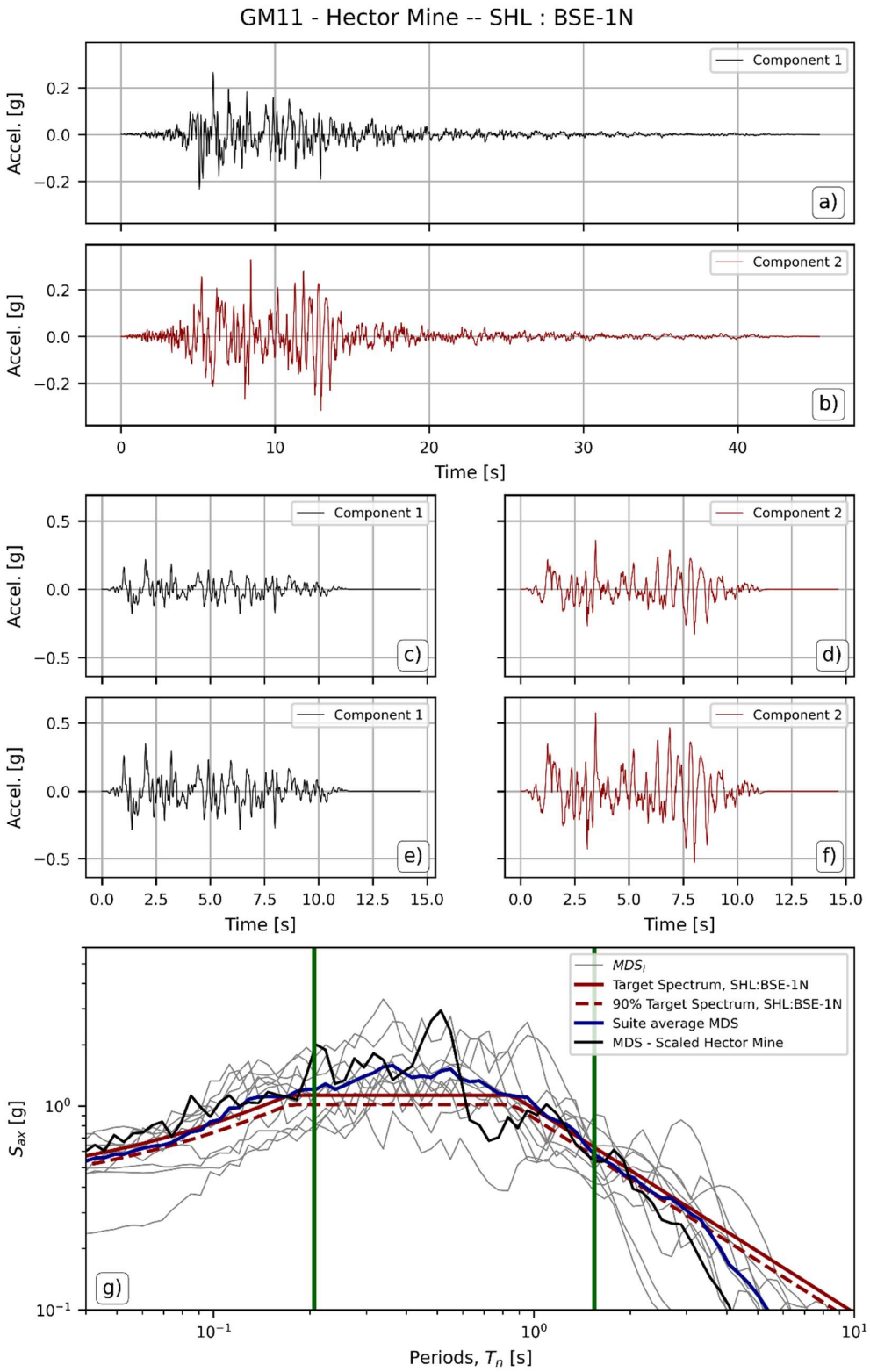

Figure C-11. GM11-Hector Mine processing and scaling for BSE-1N seismic hazard level. Shown are a) the original signal for component 1; b) the original signal for component 2; c) the trimmed, filtered, and zero-padded signal for component 1; d) the trimmed, filtered, and zero-padded signal for component 2; e) the scaled signal for component 1; f) the scaled signal for component 1; and g) plot depicting the target 3%-damped GRS for SHL=BSE-1N (solid red) along with its 90% representation (dashed red), the MDS obtained from both scaled components of the event (solid black), MDS for all other events in the suite (MDSi – solid gray), and the average MDS for all scaled events in the GMs suite.

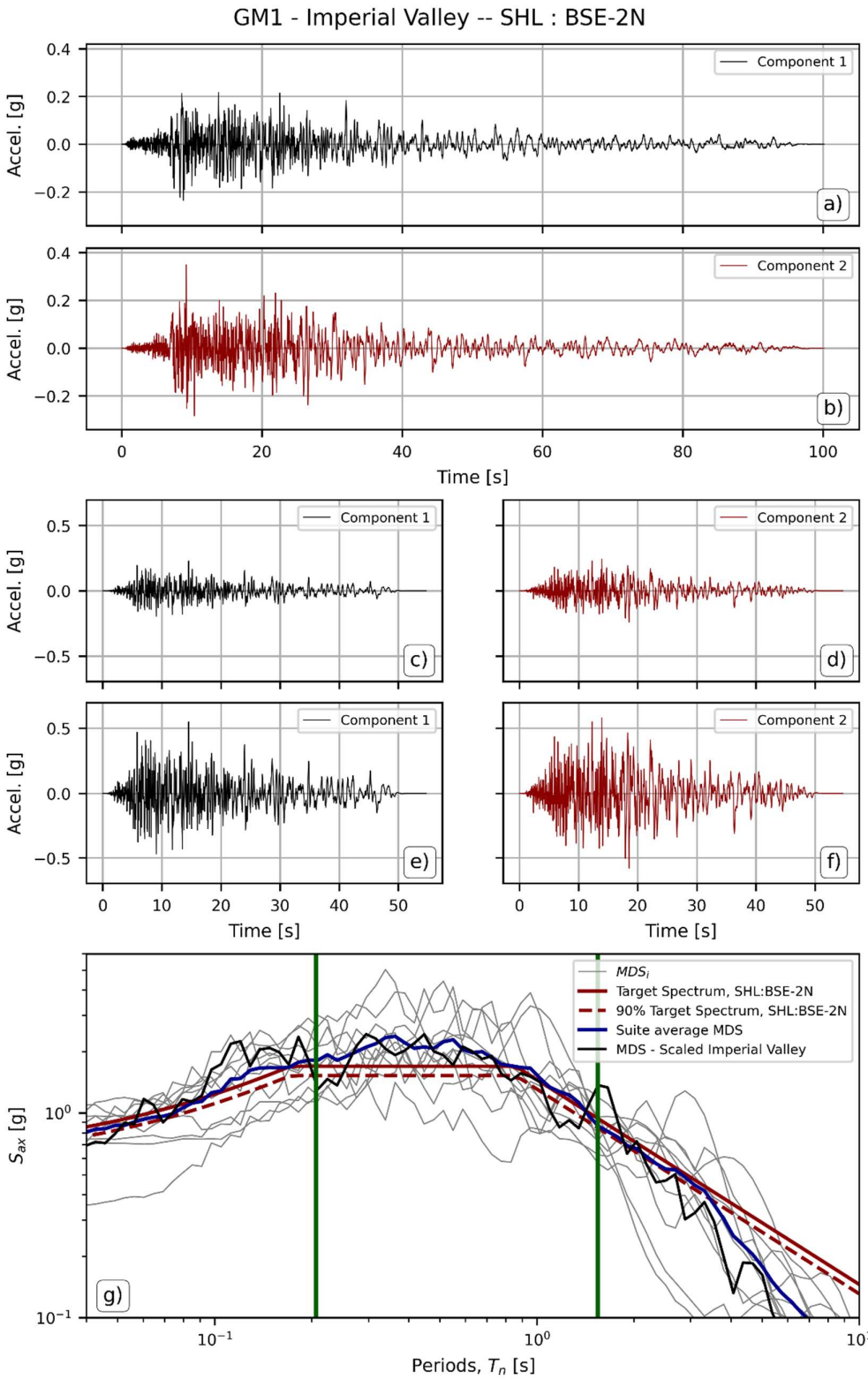

Figure C-12. GM1-Imperial Valley processing and scaling for BSE-2N seismic hazard level. Shown are a) the original signal for component 1; b) the original signal for component 2; c) the trimmed, filtered, and zero-padded signal for component 1; d) the trimmed, filtered, and zero-padded signal for component 2; e) the scaled signal for component 1; f) the scaled signal for component 1; and g) plot depicting the target 3%-damped GRS for SHL=BSE-2N (solid red) along with its 90% representation (dashed red), the MDS obtained from both scaled components of the event (solid black), MDS for all other events in the suite (MDSi – solid gray), and the average MDS for all scaled events in the GMs suite (solid blue).

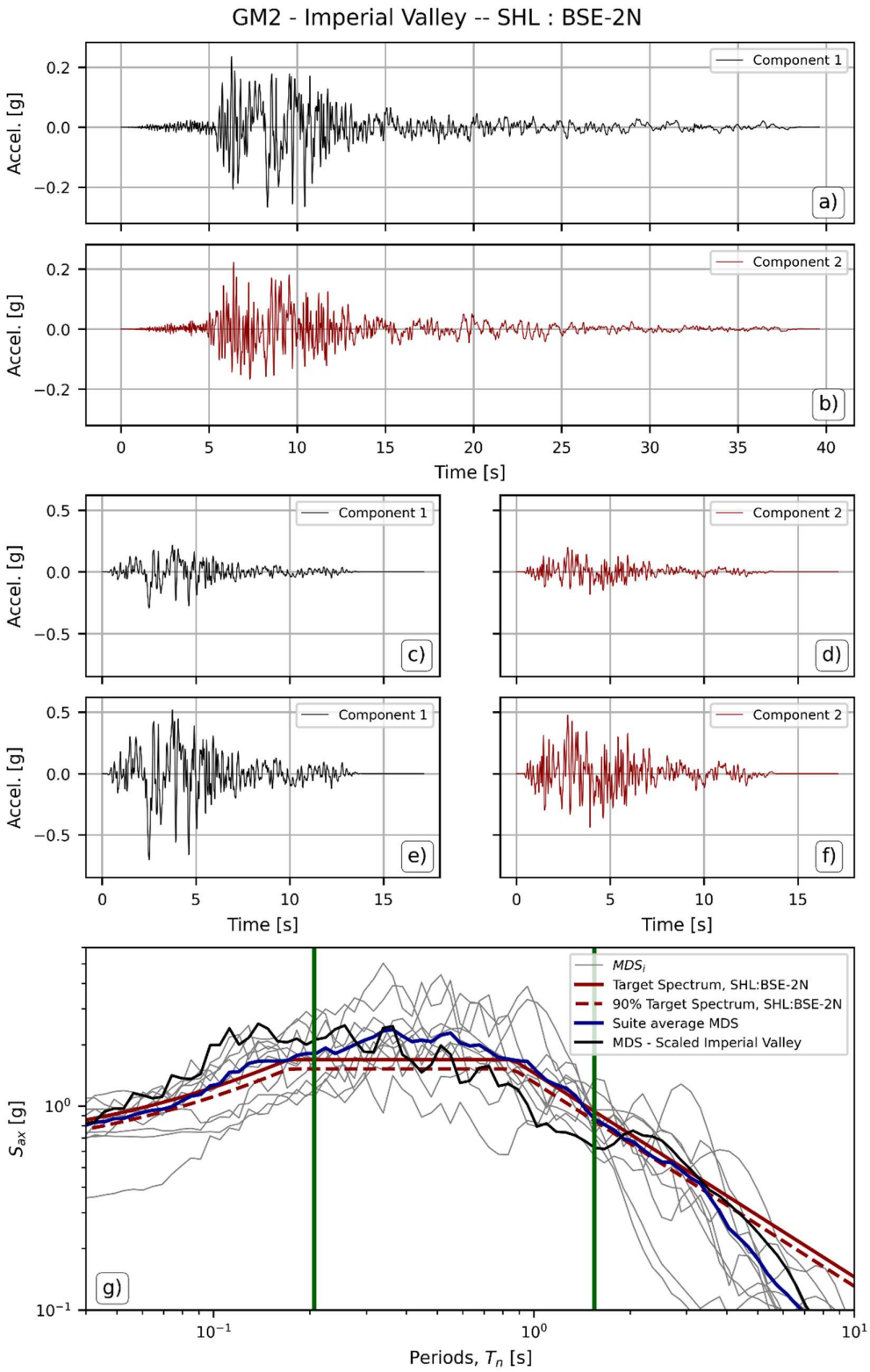

Figure C-13. GM2-Imperial Valley processing and scaling for BSE-2N seismic hazard level. Shown are a) the original signal for component 1; b) the original signal for component 2; c) the trimmed, filtered, and zero-padded signal for component 1; d) the trimmed, filtered, and zero-padded signal for component 2; e) the scaled signal for component 1; f) the scaled signal for component 1; and g) plot depicting the target 3%-damped GRS for SHL=BSE-2N (solid red) along with its 90% representation (dashed red), the MDS obtained from both scaled components of the event (solid black), MDS for all other events in the suite (MDSi – solid gray), and the average MDS for all scaled events in the GMs suite (solid blue).

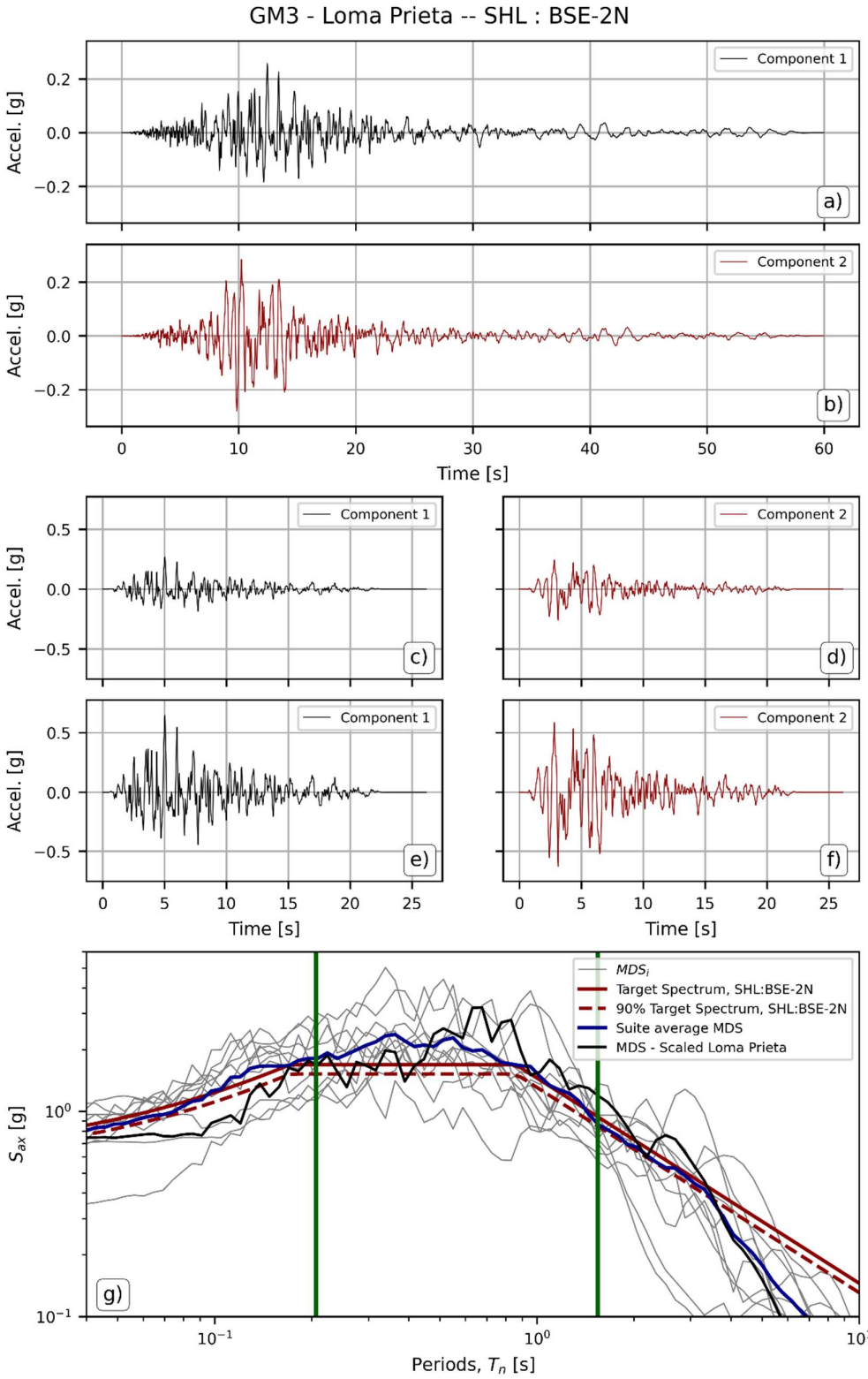

Figure C-14. GM3-Loma Prieta processing and scaling for BSE-2N seismic hazard level. Shown are a) the original signal for component 1; b) the original signal for component 2; c) the trimmed, filtered, and zero-padded signal for component 1; d) the trimmed, filtered, and zero-padded signal for component 2; e) the scaled signal for component 1; f) the scaled signal for component 1; and g) plot depicting the target 3%-damped GRS for SHL=BSE-2N (solid red) along with its 90% representation (dashed red), the MDS obtained from both scaled components of the event (solid black), MDS for all other events in the suite (MDSi – solid gray), and the average MDS for all scaled events in the GMs suite (solid blue).

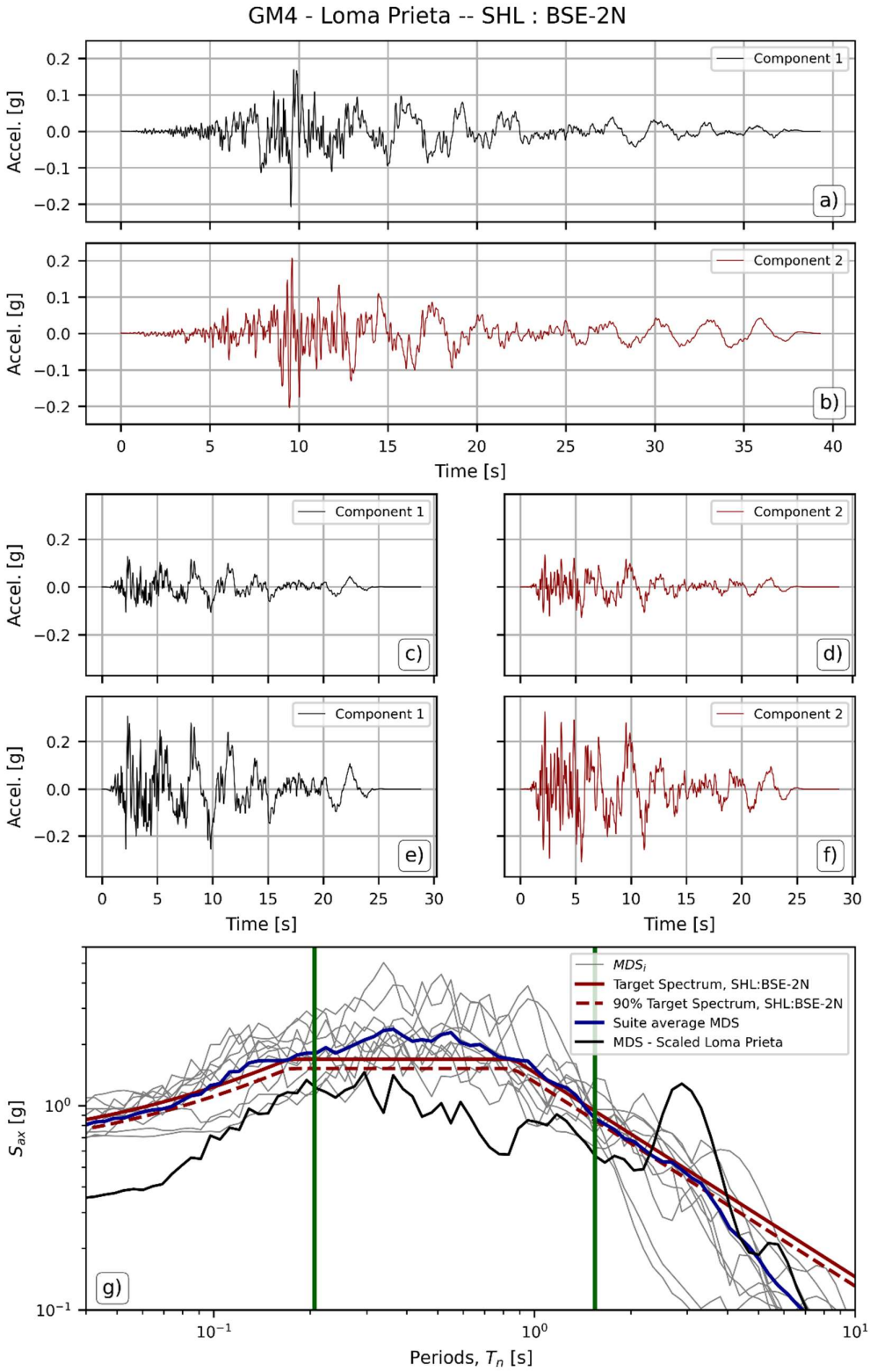

Figure C-15. GM4-Loma Prieta processing and scaling for BSE-2N seismic hazard level. Shown are a) the original signal for component 1; b) the original signal for component 2; c) the trimmed, filtered, and zero-padded signal for component 1; d) the trimmed, filtered, and zero-padded signal for component 2; e) the scaled signal for component 1; f) the scaled signal for component 1; and g) plot depicting the target 3%-damped GRS for SHL=BSE-2N (solid red) along with its 90% representation (dashed red), the MDS obtained from both scaled components of the event (solid black), MDS for all other events in the suite (MDSi – solid gray), and the average MDS for all scaled events in the GMs suite (solid blue).

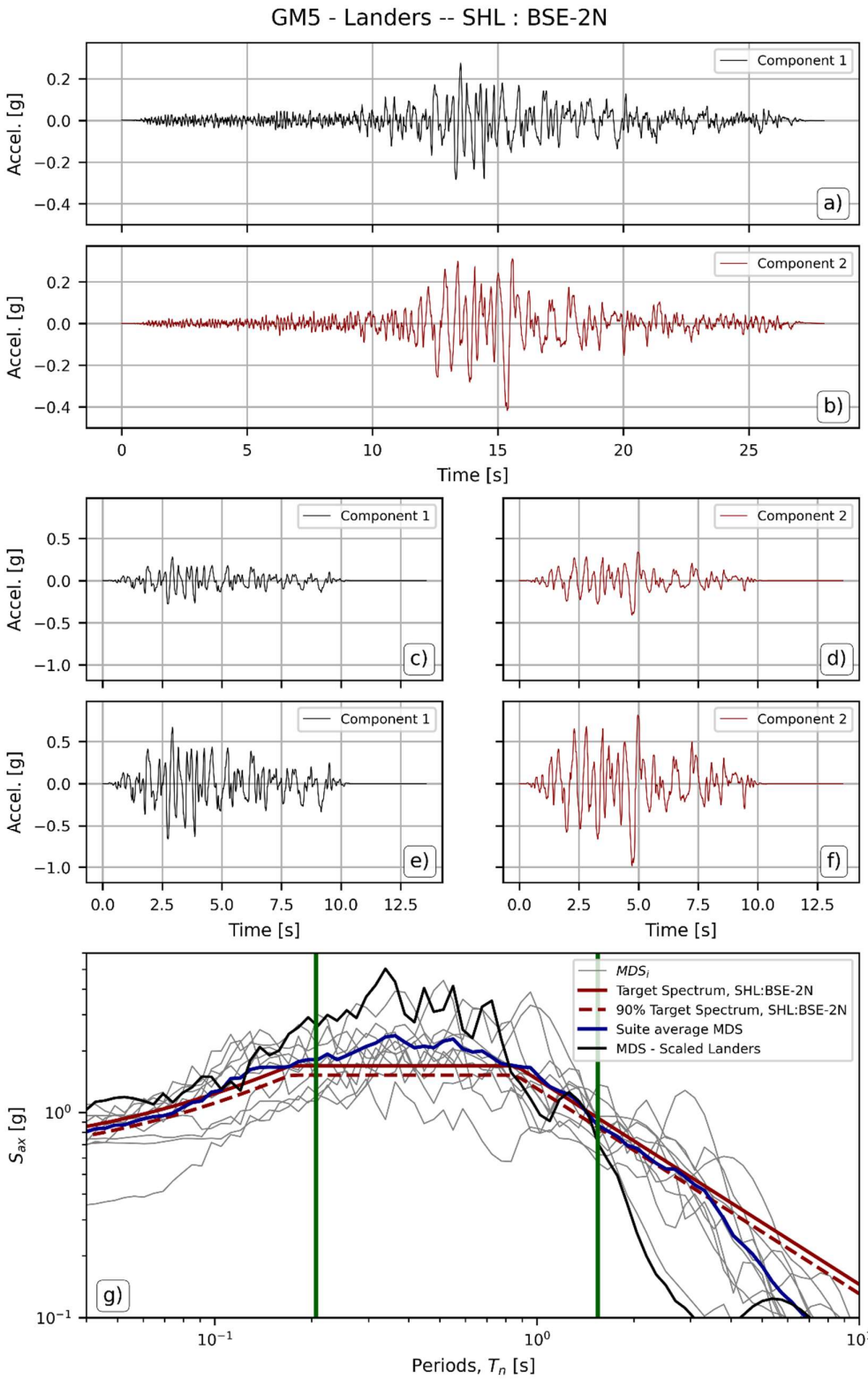

Figure C-16. GM5-Landers processing and scaling for BSE-2N seismic hazard level. Shown are a) the original signal for component 1; b) the original signal for component 2; c) the trimmed, filtered, and zero-padded signal for component 1; d) the trimmed, filtered, and zero-padded signal for component 2; e) the scaled signal for component 1; f) the scaled signal for component 1; and g) plot depicting the target 3%-damped GRS for SHL=BSE-2N (solid red) along with its 90% representation (dashed red), the MDS obtained from both scaled components of the event (solid black), MDS for all other events in the suite (MDSi – solid gray), and the average MDS for all scaled events in the GMs suite (solid blue).

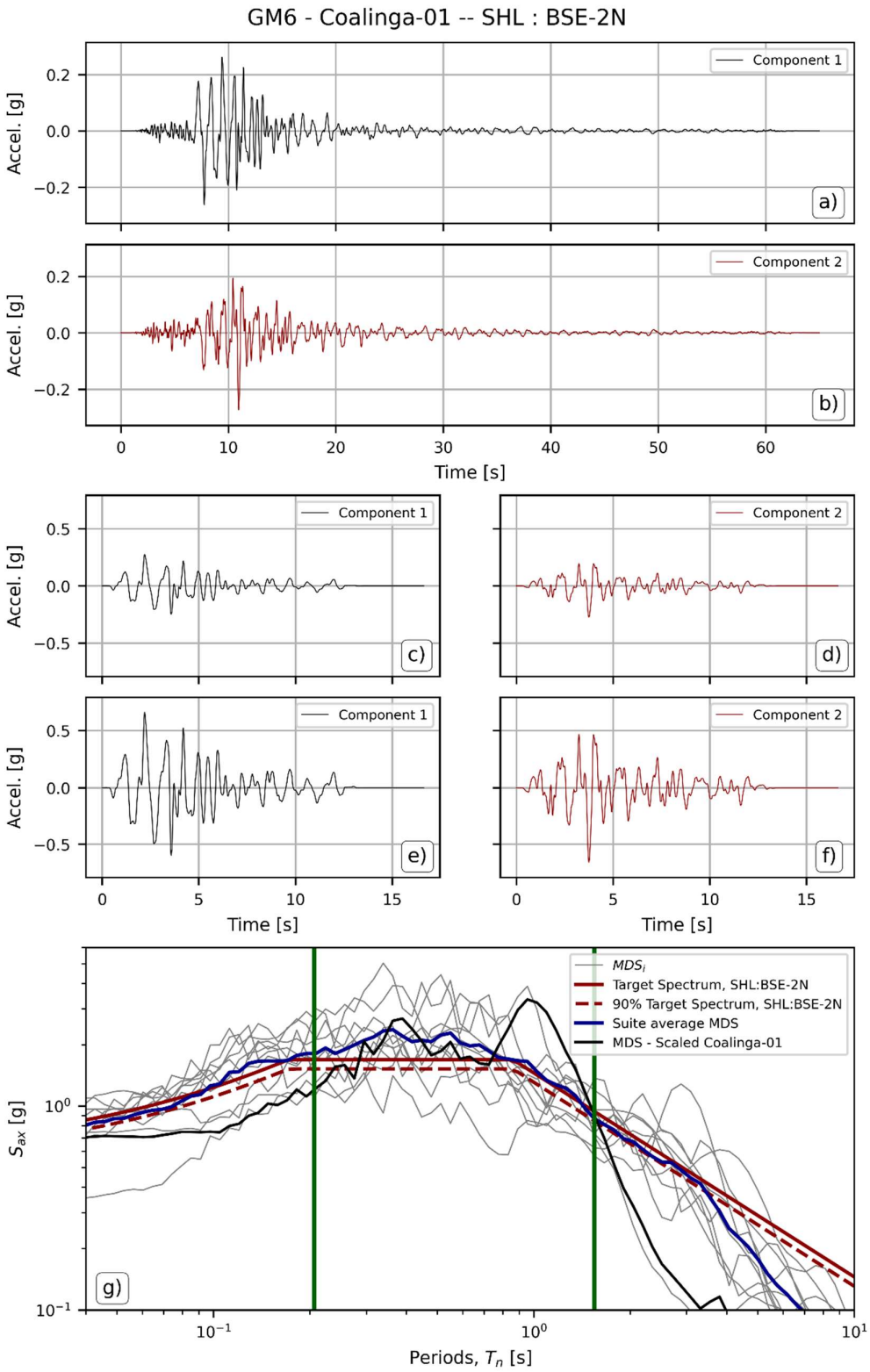

Figure C-17. GM6-Coalinga-01 processing and scaling for BSE-2N seismic hazard level. Shown are a) the original signal for component 1; b) the original signal for component 2; c) the trimmed, filtered, and zero-padded signal for component 1; d) the trimmed, filtered, and zero-padded signal for component 2; e) the scaled signal for component 1; f) the scaled signal for component 1; and g) plot depicting the target 3%-damped GRS for SHL=BSE-2N (solid red) along with its 90% representation (dashed red), the MDS obtained from both scaled components of the event (solid black), MDS for all other events in the suite (MDSi – solid gray), and the average MDS for all scaled events in the GMs suite (solid blue).

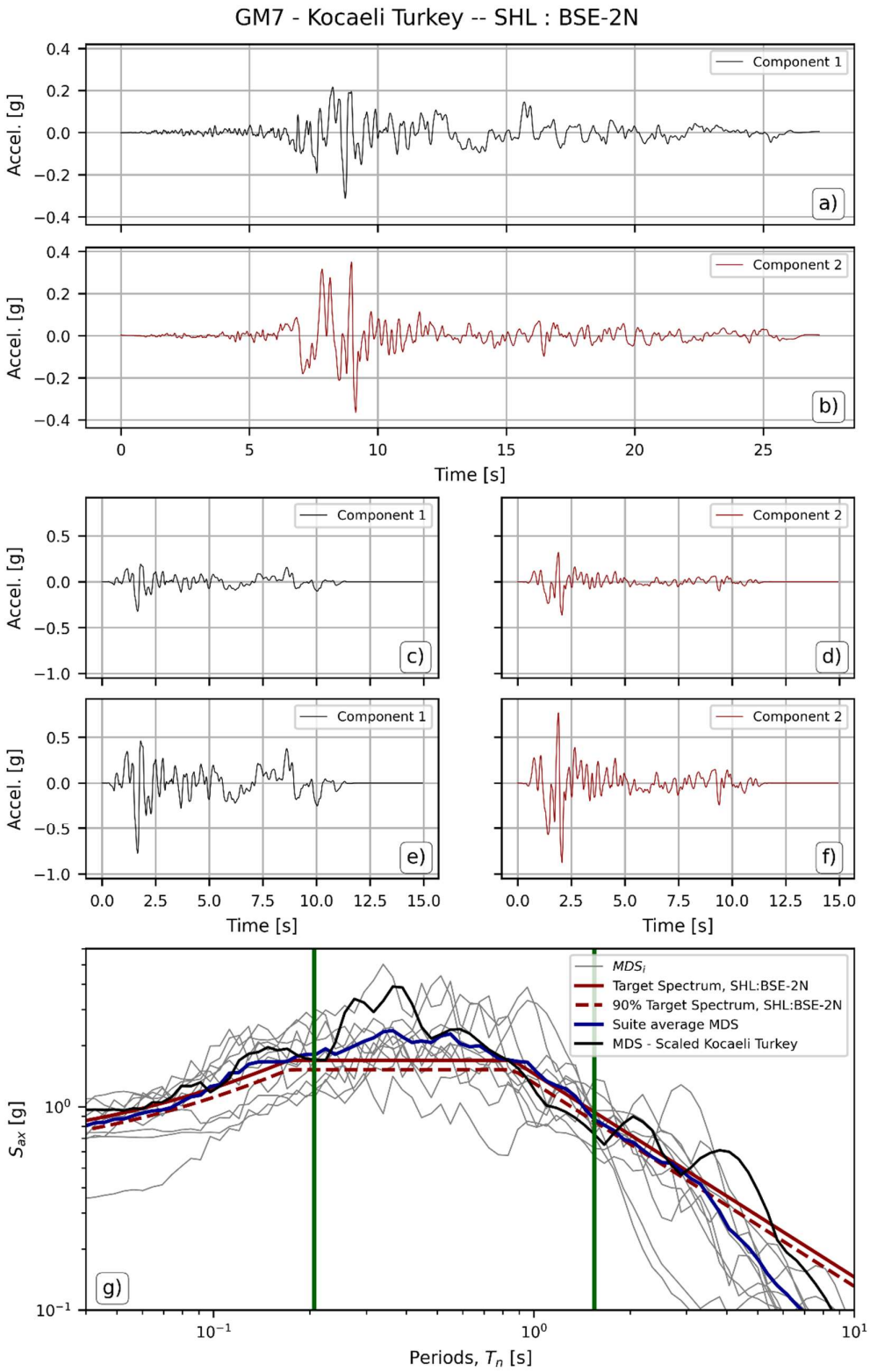

Figure C-18. GM7-Kocaeli Turkey processing and scaling for BSE-2N seismic hazard level. Shown are a) the original signal for component 1; b) the original signal for component 2; c) the trimmed, filtered, and zero-padded signal for component 1; d) the trimmed, filtered, and zero-padded signal for component 2; e) the scaled signal for component 1; f) the scaled signal for component 1; and g) plot depicting the target 3%-damped GRS for SHL=BSE-2N (solid red) along with its 90% representation (dashed red), the MDS obtained from both scaled components of the event (solid black), MDS for all other events in the suite (MDSi – solid gray), and the average MDS for all scaled events in the GMs suite (solid blue).

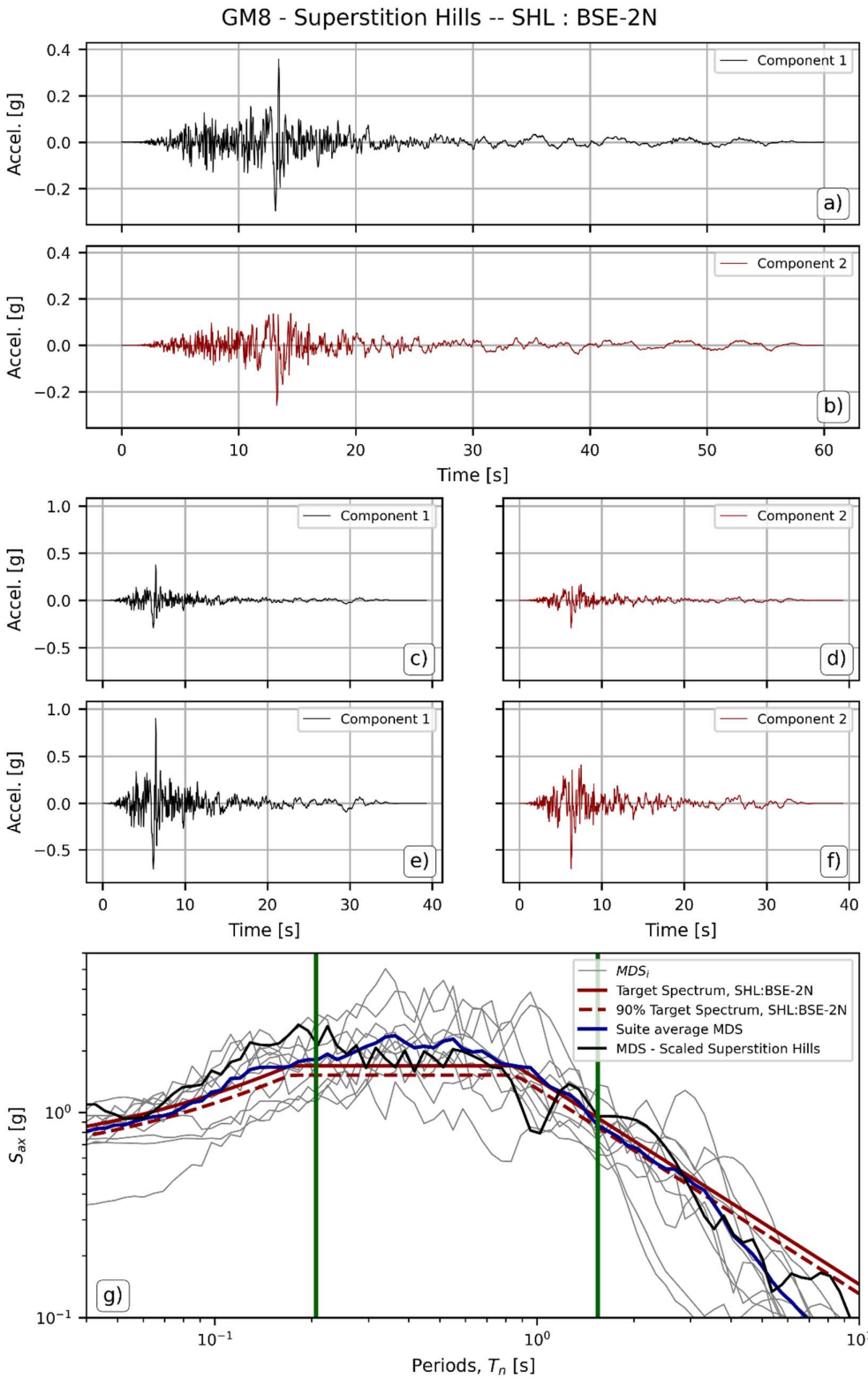

Figure C-19. GM8-Superstition Hills processing and scaling for BSE-2N seismic hazard level. Shown are a) the original signal for component 1; b) the original signal for component 2; c) the trimmed, filtered, and zero-padded signal for component 1; d) the trimmed, filtered, and zero-padded signal for component 2; e) the scaled signal for component 1; f) the scaled signal for component 1; and g) plot depicting the target 3%-damped GRS for SHL=BSE-2N (solid red) along with its 90% representation (dashed red), the MDS obtained from both scaled components of the event (solid black), MDS for all other events in the suite (MDSi – solid gray), and the average MDS for all scaled events in the GMs suite (solid blue).

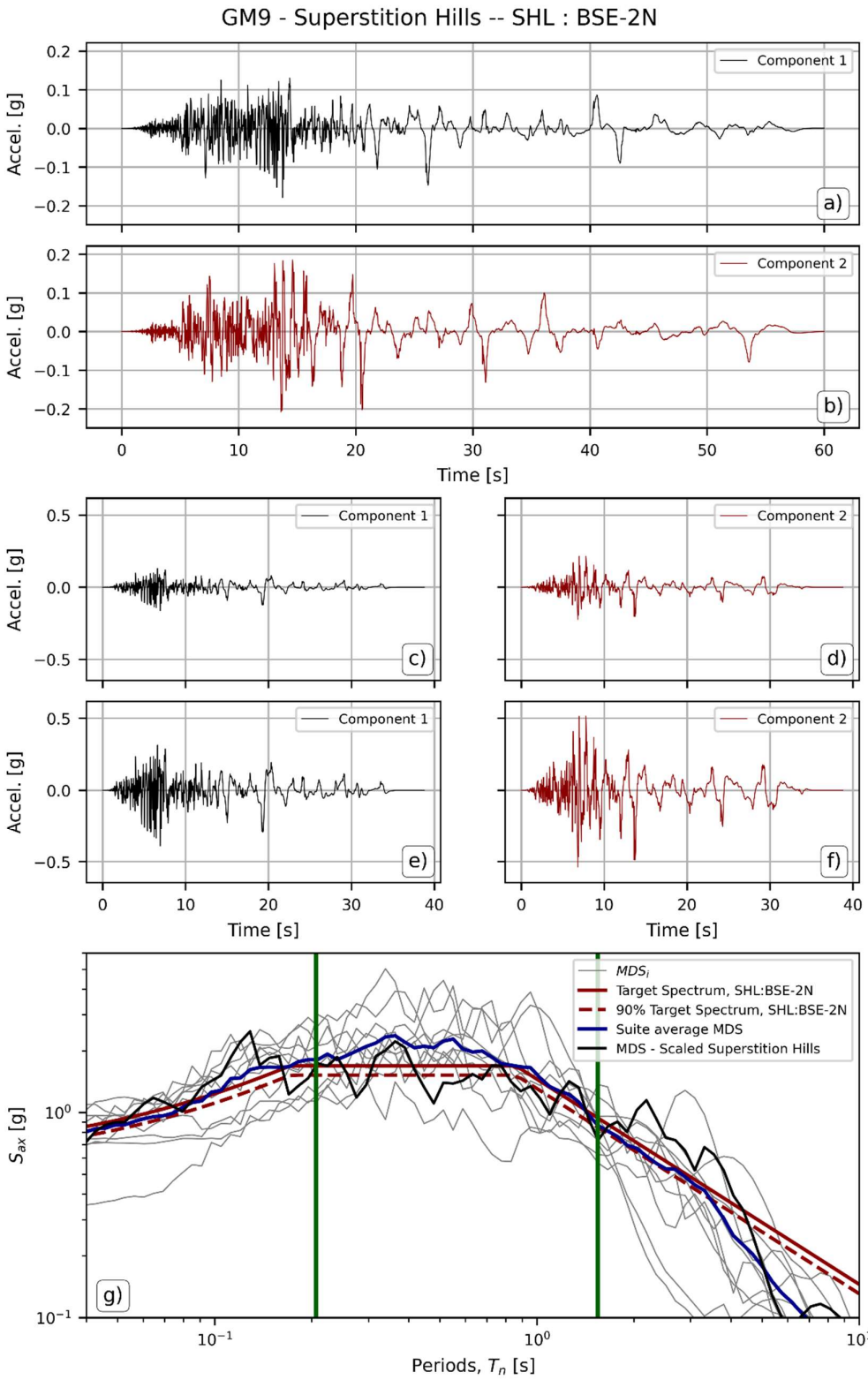

Figure C-20. GM9-Superstition Hills processing and scaling for BSE-2N seismic hazard level. Shown are a) the original signal for component 1; b) the original signal for component 2; c) the trimmed, filtered, and zero-padded signal for component 1; d) the trimmed, filtered, and zero-padded signal for component 2; e) the scaled signal for component 1; f) the scaled signal for component 1; and g) plot depicting the target 3%-damped GRS for SHL=BSE-2N (solid red) along with its 90% representation (dashed red), the MDS obtained from both scaled components of the event (solid black), MDS for all other events in the suite (MDSi – solid gray), and the average MDS for all scaled events in the GMs suite (solid blue).

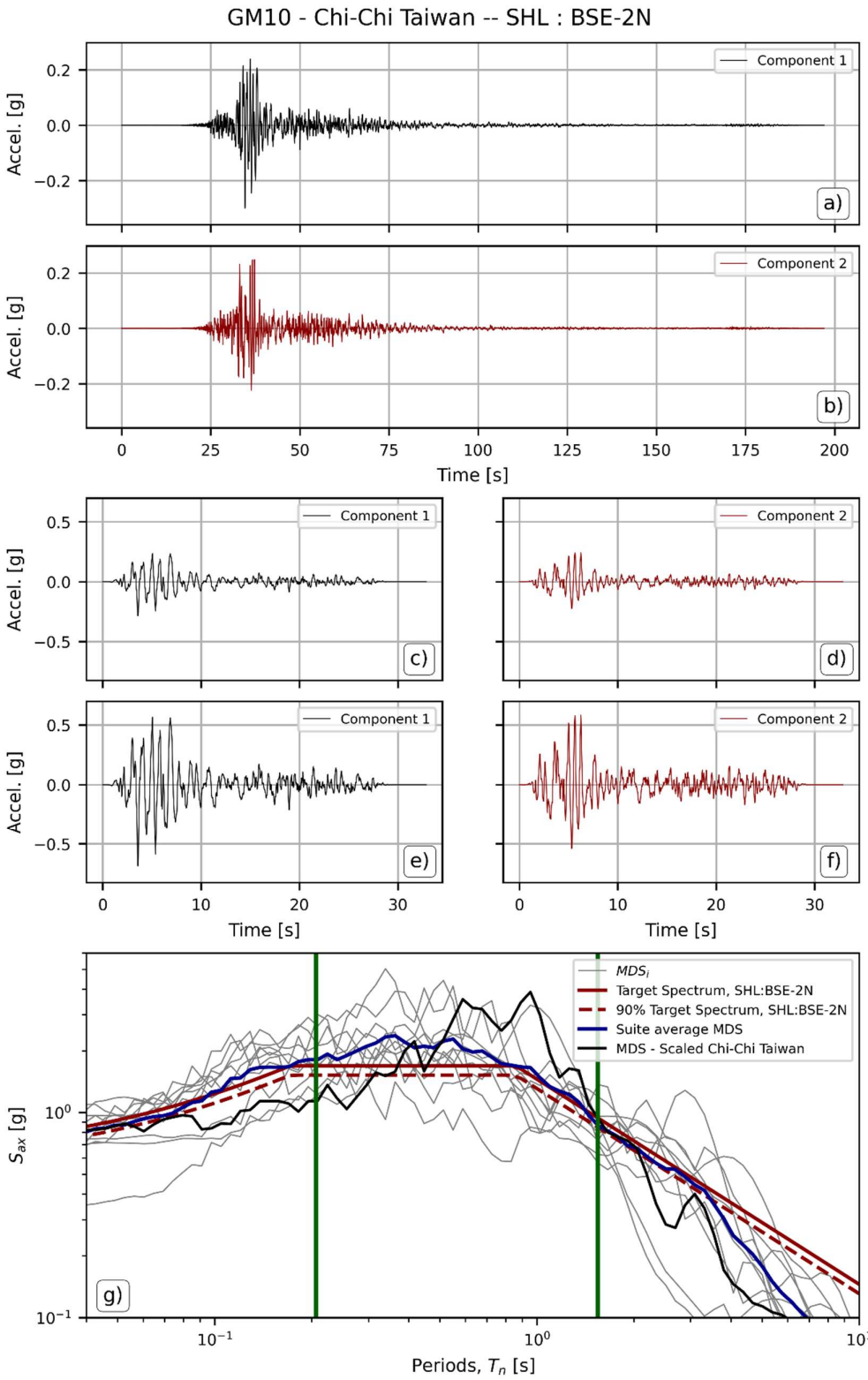

Figure C-21. GM10-Chi-Chi Taiwan processing and scaling for BSE-2N seismic hazard level. Shown are a) the original signal for component 1; b) the original signal for component 2; c) the trimmed, filtered, and zero-padded signal for component 1; d) the trimmed, filtered, and zero-padded signal for component 2; e) the scaled signal for component 1; f) the scaled signal for component 1; and g) plot depicting the target 3%-damped GRS for SHL=BSE-2N (solid red) along with its 90% representation (dashed red), the MDS obtained from both scaled components of the event (solid black), MDS for all other events in the suite (MDSi – solid gray), and the average MDS for all scaled events in the GMs suite (solid blue).

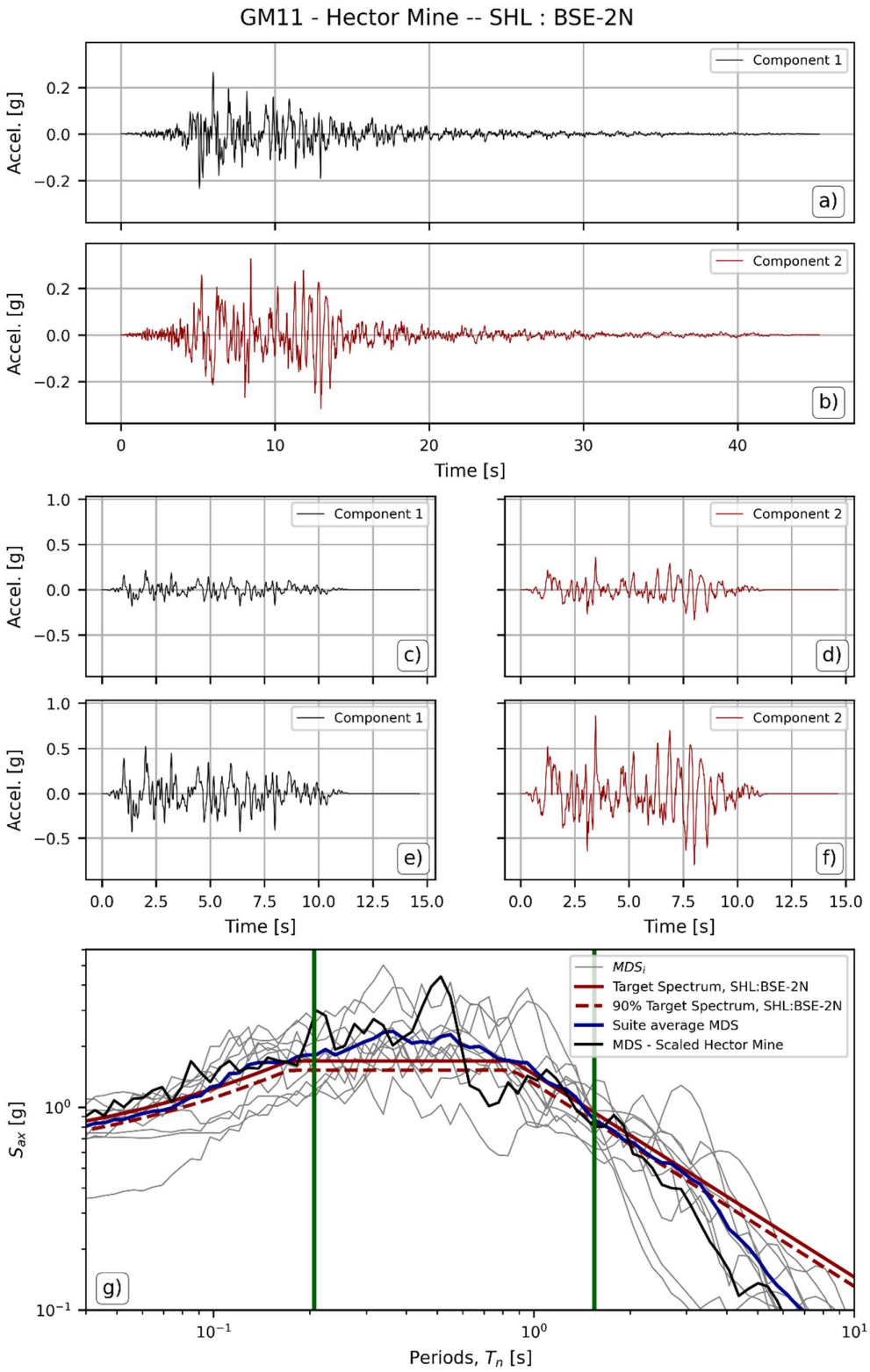

Figure C-22. GM11-Hector Mine processing and scaling for BSE-2N seismic hazard level. Shown are a) the original signal for component 1; b) the original signal for component 2; c) the trimmed, filtered, and zero-padded signal for component 1; d) the trimmed, filtered, and zero-padded signal for component 2; e) the scaled signal for component 1; f) the scaled signal for component 1; and g) plot depicting the target 3%-damped GRS for SHL=BSE-2N (solid red) along with its 90% representation (dashed red), the MDS obtained from both scaled components of the event (solid black), MDS for all other events in the suite (MDSi – solid gray), and the average MDS for all scaled events in the GMs suite (solid blue).

Appendix D. Additional Performance Assessment Results relative to the BSE-2N Seismic Hazard Level

Results from the performance assessment were first introduced in Section 3.5 in a summarized fashion. This appendix shows additional information regarding the effects of subjecting buildings on the BSE-2N structural performance level. In the same section, a discussion of the figures presented in this appendix is also presented.

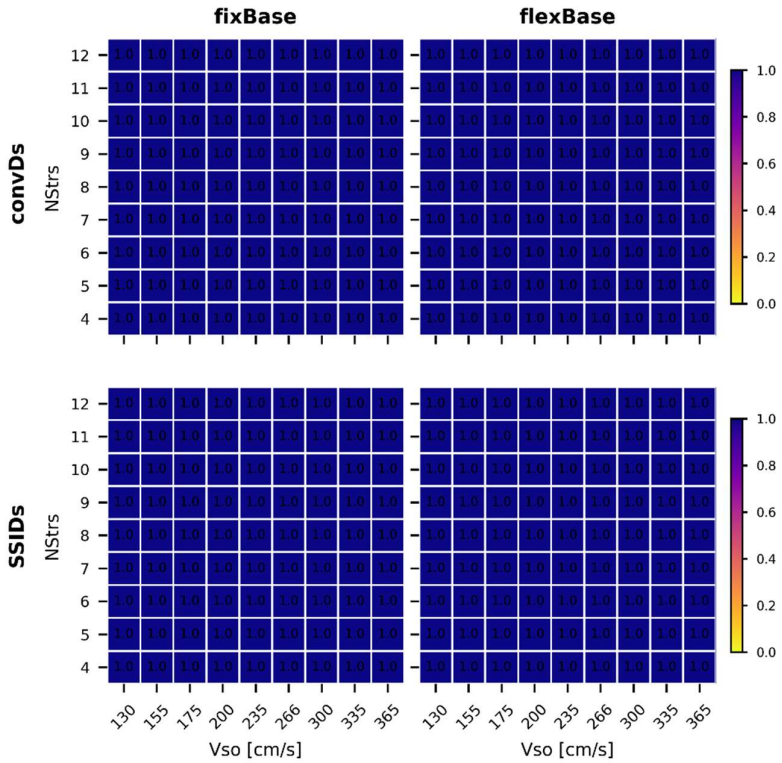

Figure D-1. Percentages of buildings in the database resulting in an unfavorable performance objective achievement through the MRSA procedure. SHL: BSE-2N / SPL: CP.

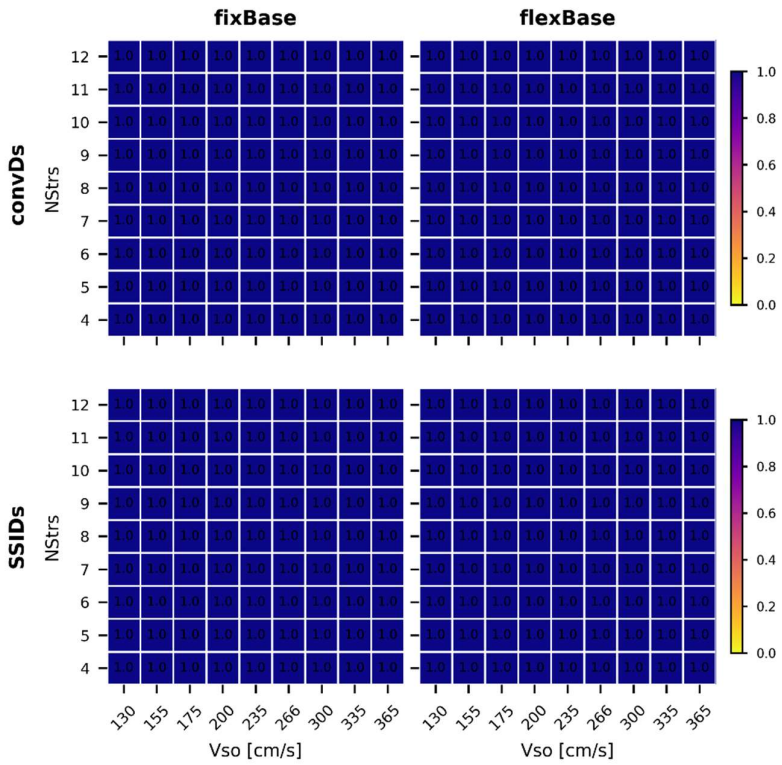

Figure D-2. Percentages of buildings in the database resulting in an unfavorable performance objective achievement through the LTHA procedure. SHL: BSE-2N / SPL: CP.

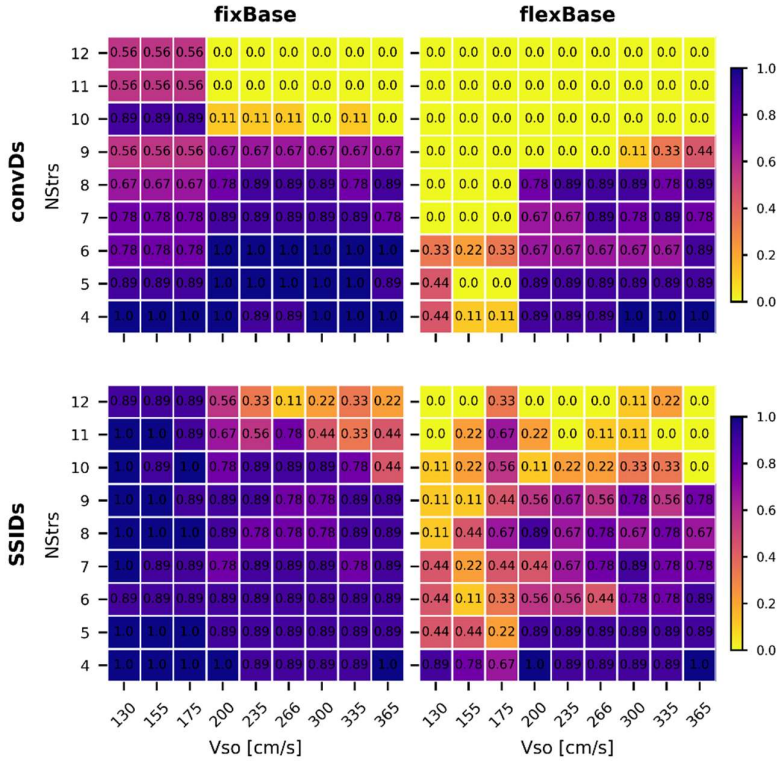

Figure D-3. Percentages of buildings in the database resulting in an unfavorable performance objective achievement through the NSP procedure. SHL: BSE-2N / SPL: CP.

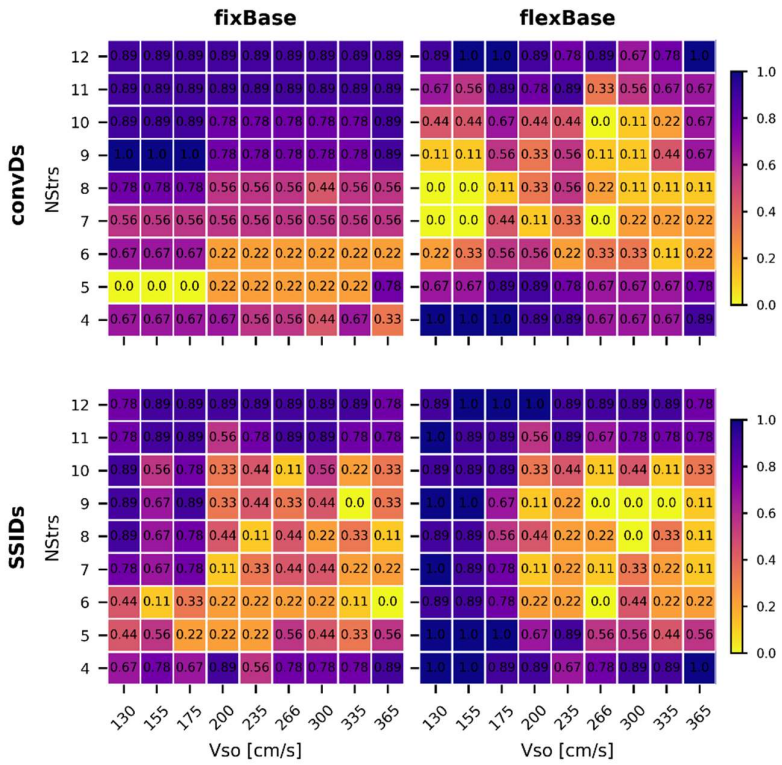

Figure D-4. Percentages of buildings in the database resulting in an unfavorable performance objective achievement through the NLTHA procedure. SHL: BSE-2N / SPL: CP.

Appendix E. Response- and Predictor-Variables

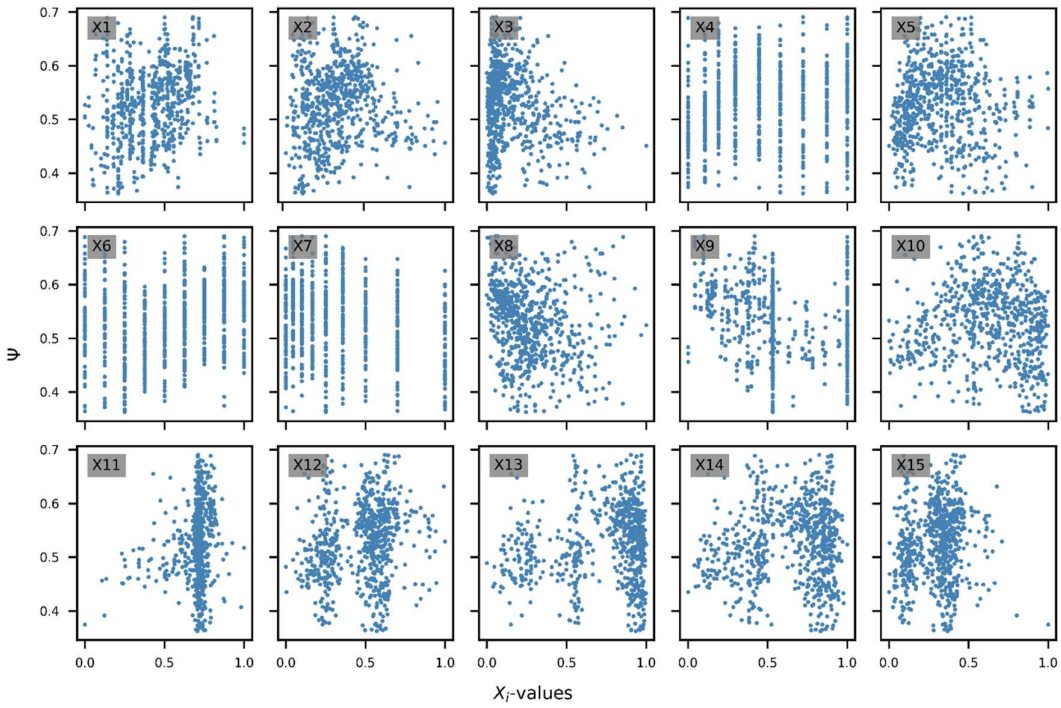

Figure E-1. Scatter plots showing trends between scaled and standardized Xi-predictors and the Ψ-factor. Reference example case, AP: MRSA / DT: *convDs* / BSC: *fixBase* / SPL: LS.

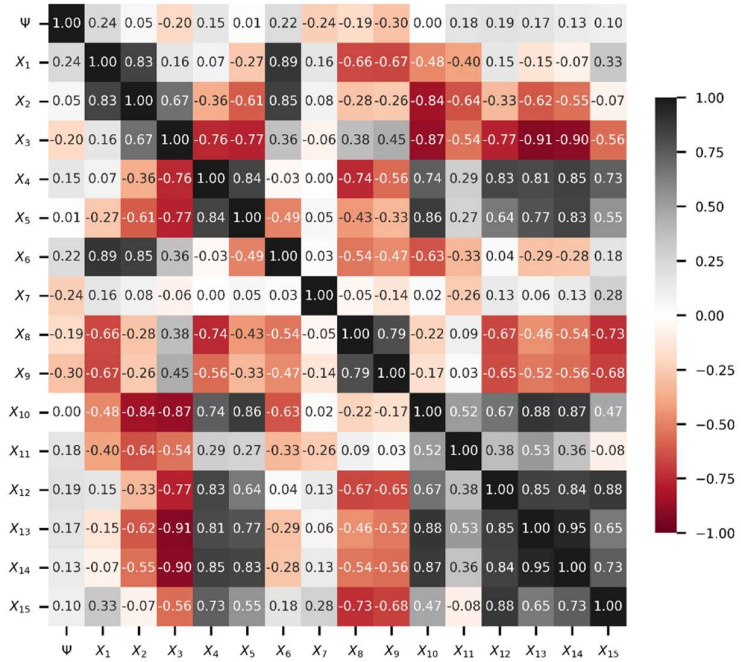

Figure E-2. Heatmap of Pearson correlation coefficients revealing a possible linear correlation between predictors and the Ψ-factor. Reference example case, AP: MRSA / DT: *convDs* / BSC: *fixBase* / SPL: LS.

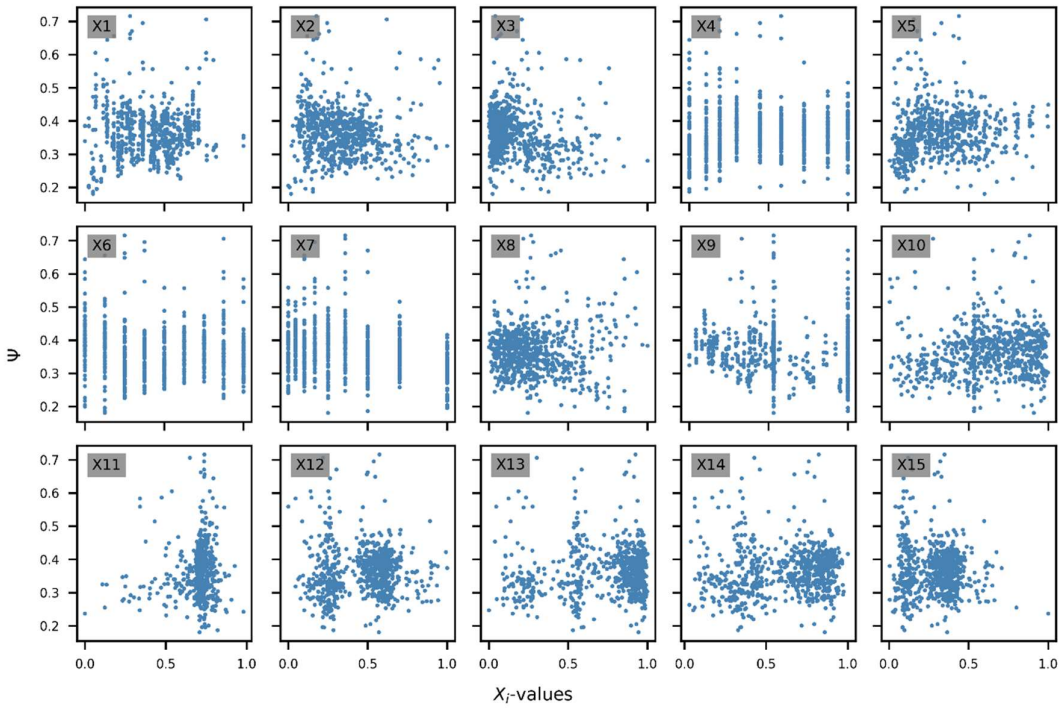

Figure E-3. Scatter plots showing trends between scaled and standardized Xi-predictors and the Ψ-factor. Reference example case, AP: MRSA / DT: *convDs* / BSC: *fixBase* / SPL: CP.

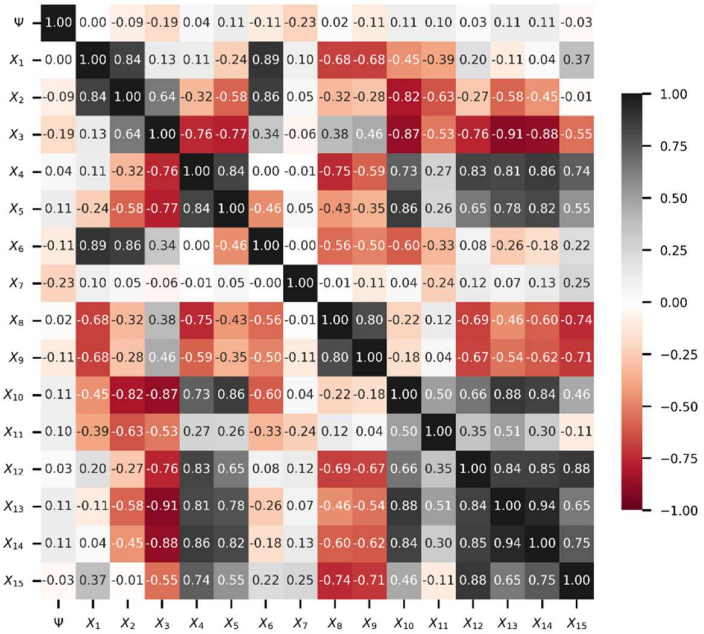

Figure E-4. Heatmap of Pearson correlation coefficients revealing a possible linear correlation between predictors and the Ψ-factor. Reference example case, AP: MRSA / DT: *convDs* / BSC: *fixBase* / SPL: CP.

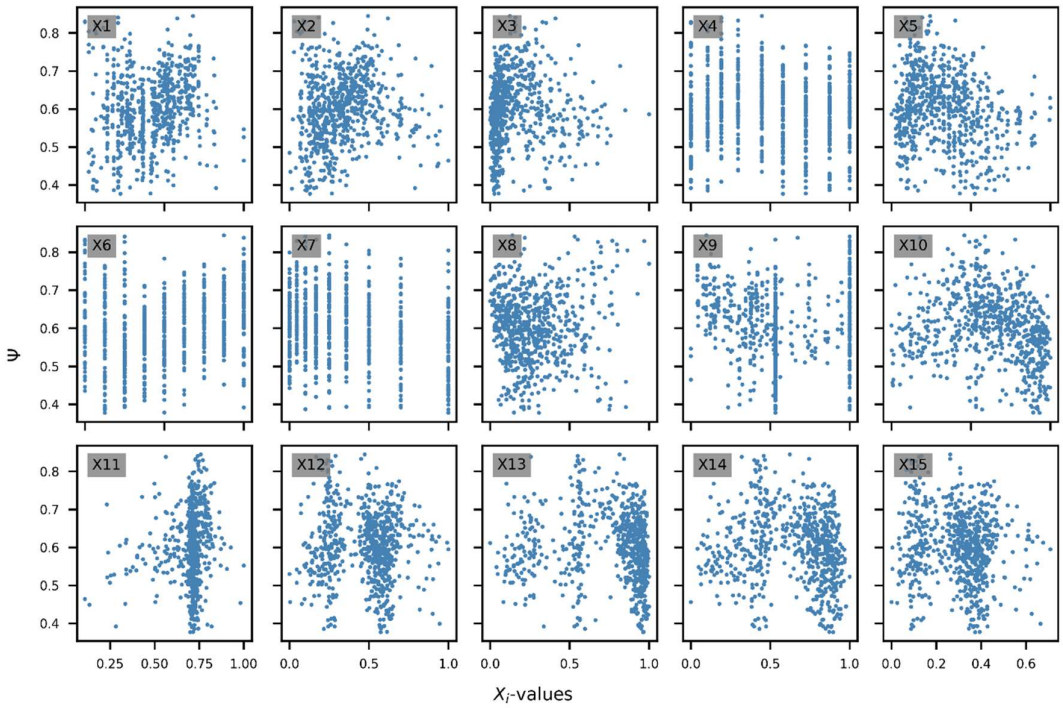

Figure E-5. Scatter plots showing trends between scaled and standardized Xi-predictors and the Ψ-factor. Reference example case, AP: MRSA / DT: *convDs* / BSC: *flexBase* / SPL: LS.

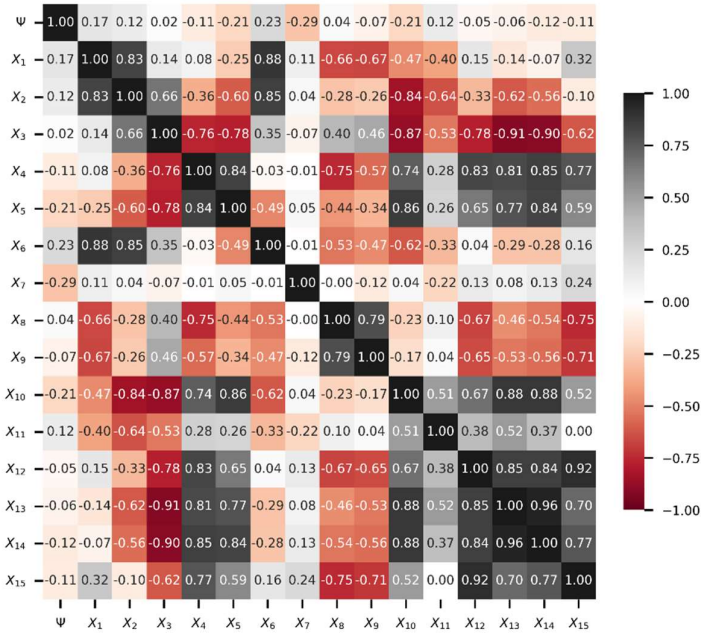

Figure E-6. Heatmap of Pearson correlation coefficients revealing a possible linear correlation between predictors and the Ψ-factor. Reference example case, AP: MRSA / DT: *convDs* / BSC: *flexBase* / SPL: LS.

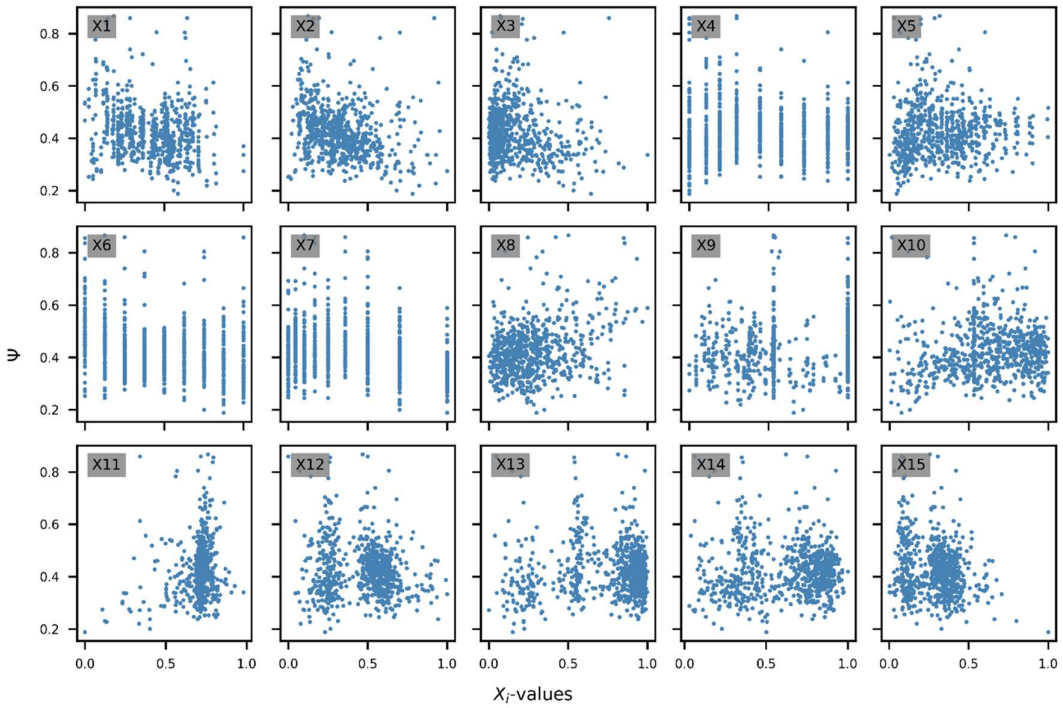

Figure E-7. Scatter plots showing trends between scaled and standardized Xi-predictors and the Ψ-factor. Reference example case, AP: MRSA / DT: *convDs* / BSC: *flexBase* / SPL: CP.

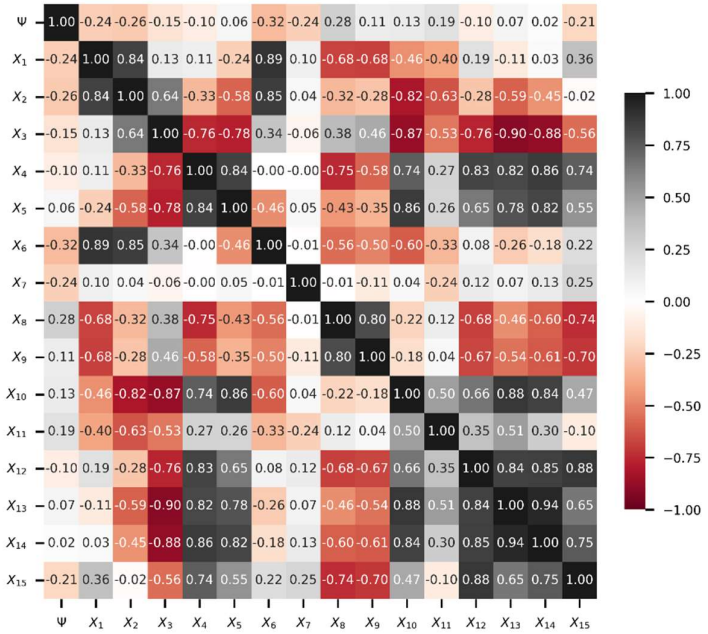

Figure E-8. Heatmap of Pearson correlation coefficients revealing a possible linear correlation between predictors and the Ψ-factor. Reference example case, AP: MRSA / DT: *convDs* / BSC: *flexBase* / SPL: CP.

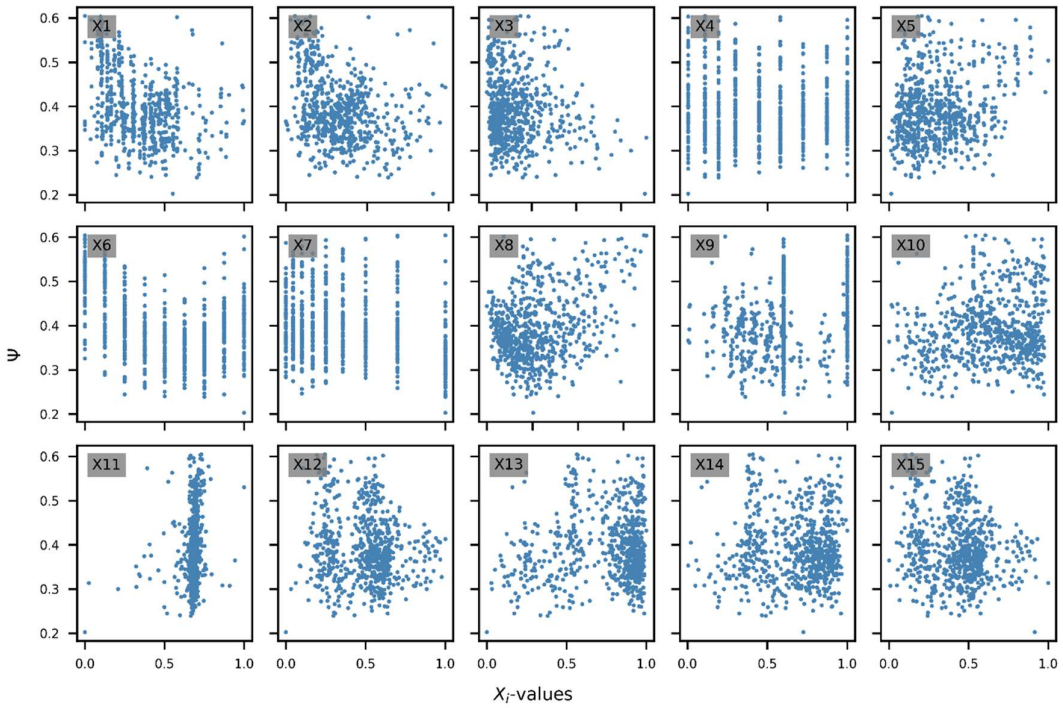

Figure E-9. Scatter plots showing trends between scaled and standardized Xi-predictors and the Ψ-factor. Reference example case, AP: MRSA / DT: *SSIDs* / BSC: *fixBase* / SPL: LS.

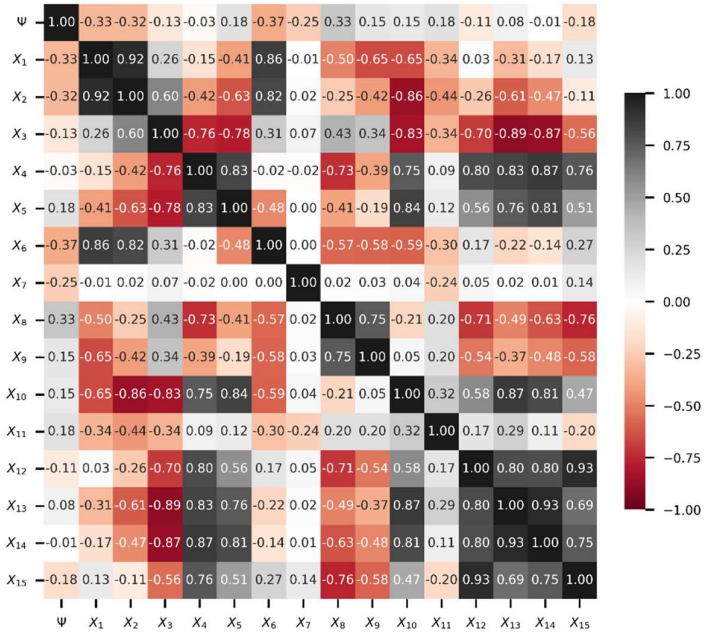

Figure E-10. Heatmap of Pearson correlation coefficients revealing a possible linear correlation between predictors and the Ψ-factor. Reference example case, AP: MRSA / DT: *SSIDs* / BSC: *fixBase* / SPL: LS.

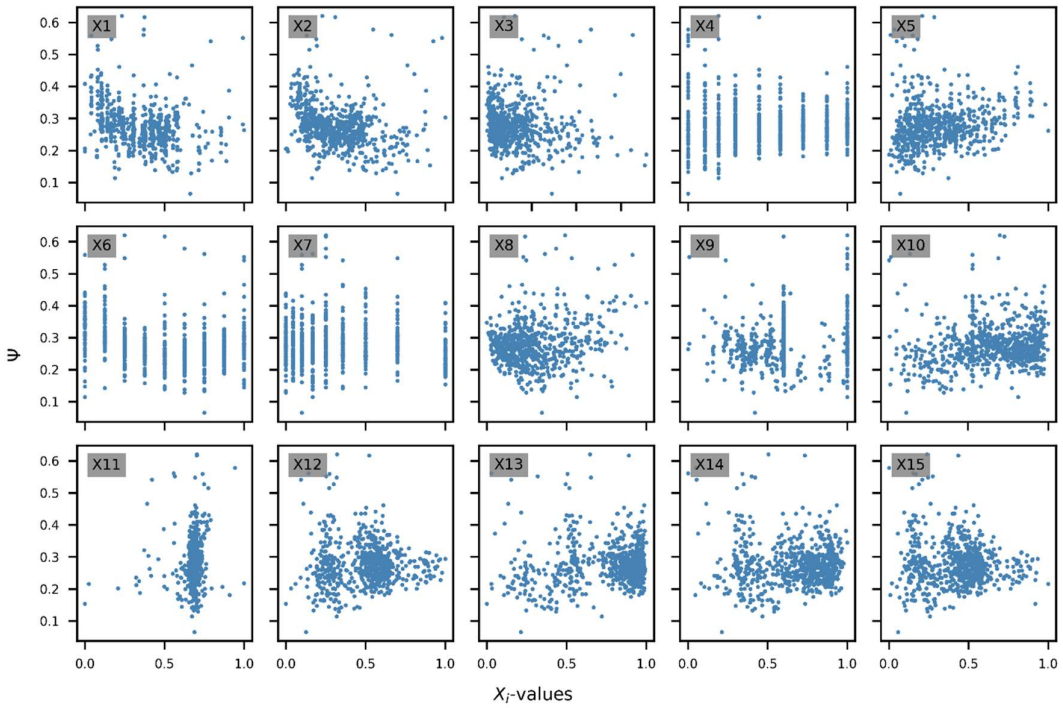

Figure E-11. Scatter plots showing trends between scaled and standardized Xi-predictors and the Ψ-factor. Reference example case, AP: MRSA / DT: *SSIDs* / BSC: *fixBase* / SPL: CP.

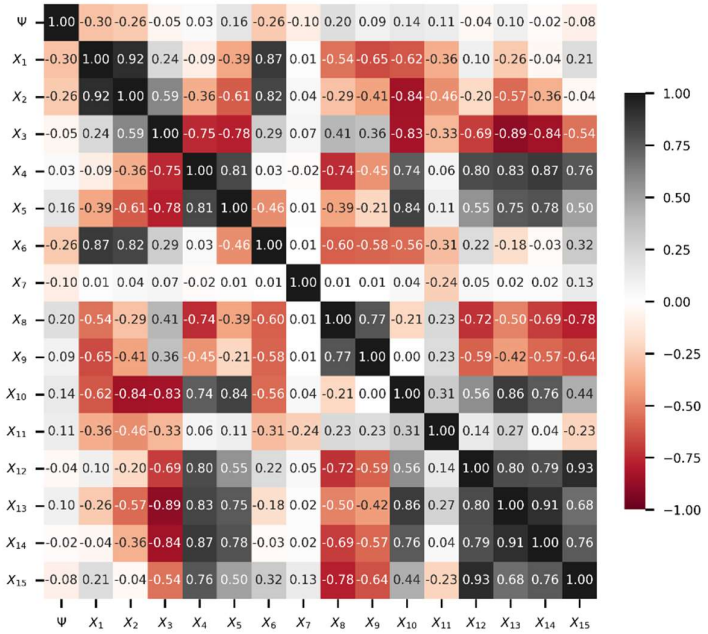

Figure E-12. Heatmap of Pearson correlation coefficients revealing a possible linear correlation between predictors and the Ψ-factor. Reference example case, AP: MRSA / DT: *SSIDs* / BSC: *fixBase* / SPL: CP.

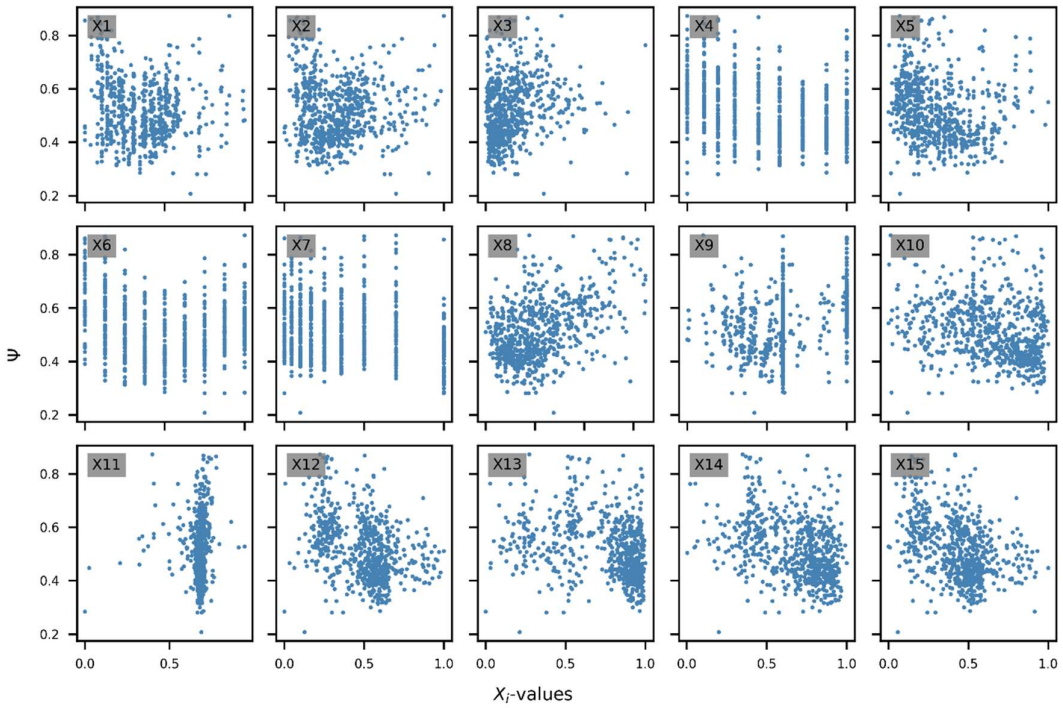

Figure E-13. Scatter plots showing trends between scaled and standardized Xi-predictors and the Ψ-factor. Reference example case, AP: MRSA / DT: *SSIDs* / BSC: *flexBase* / SPL: LS.

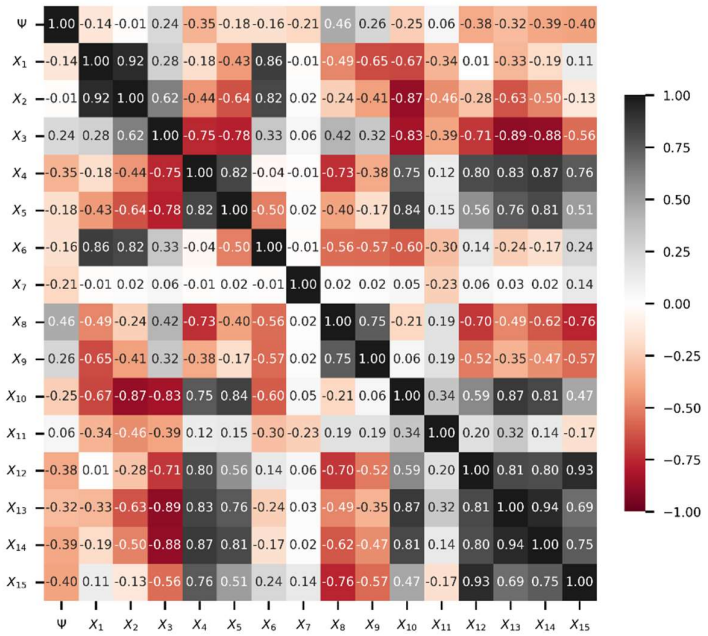

Figure E-14. Heatmap of Pearson correlation coefficients revealing a possible linear correlation between predictors and the Ψ-factor. Reference example case, AP: MRSA / DT: *SSIDs* / BSC: *flexBase* / SPL: LS.

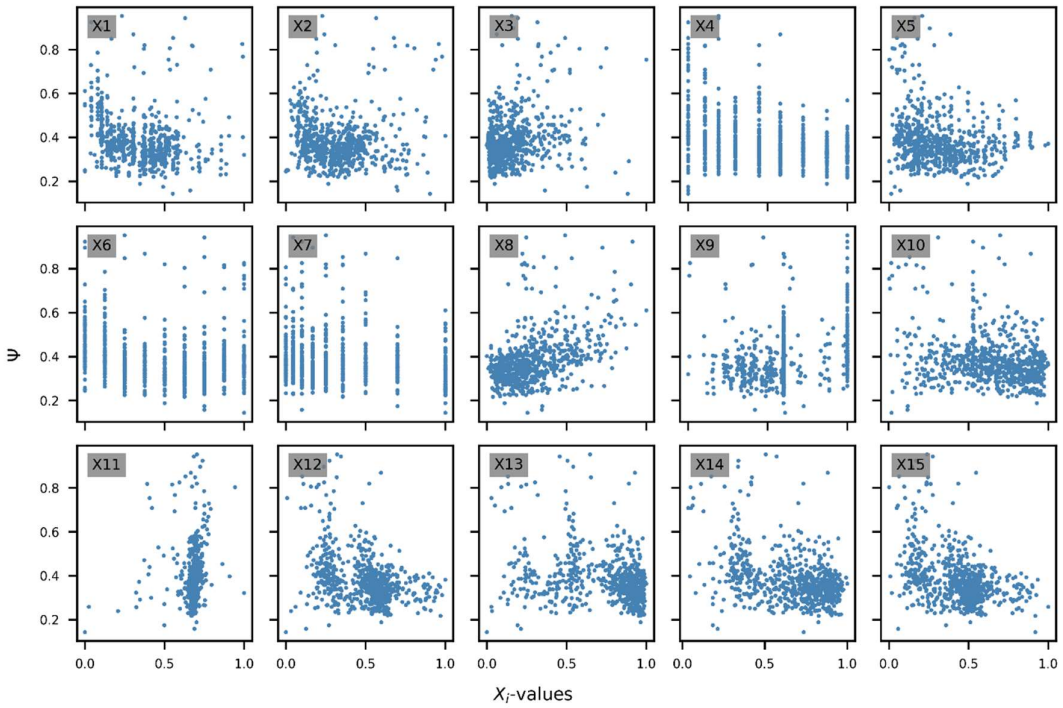

Figure E-15. Scatter plots showing trends between scaled and standardized Xi-predictors and the Ψ-factor. Reference example case, AP: MRSA / DT: *SSIDs* / BSC: *flexBase* / SPL: CP.

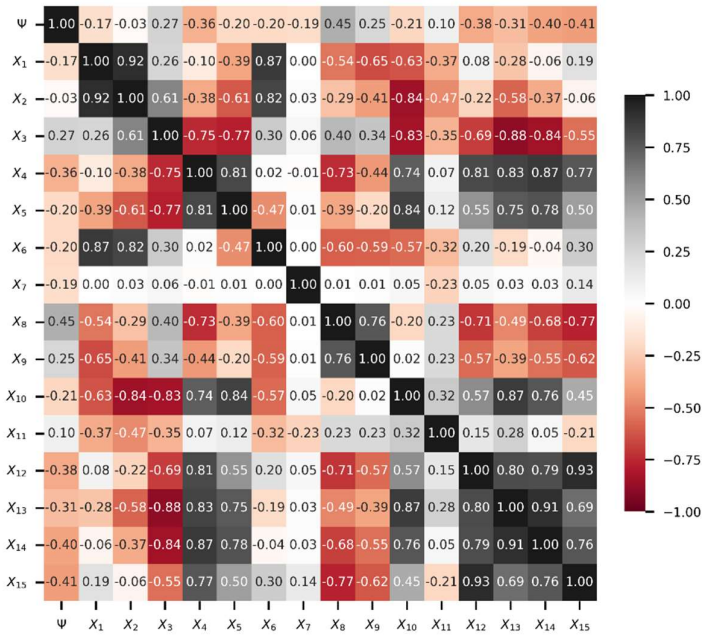

Figure E-16. Heatmap of Pearson correlation coefficients revealing a possible linear correlation between predictors and the Ψ-factor. Reference example case, AP: MRSA / DT: *SSIDs* / BSC: *flexBase* / SPL: CP.

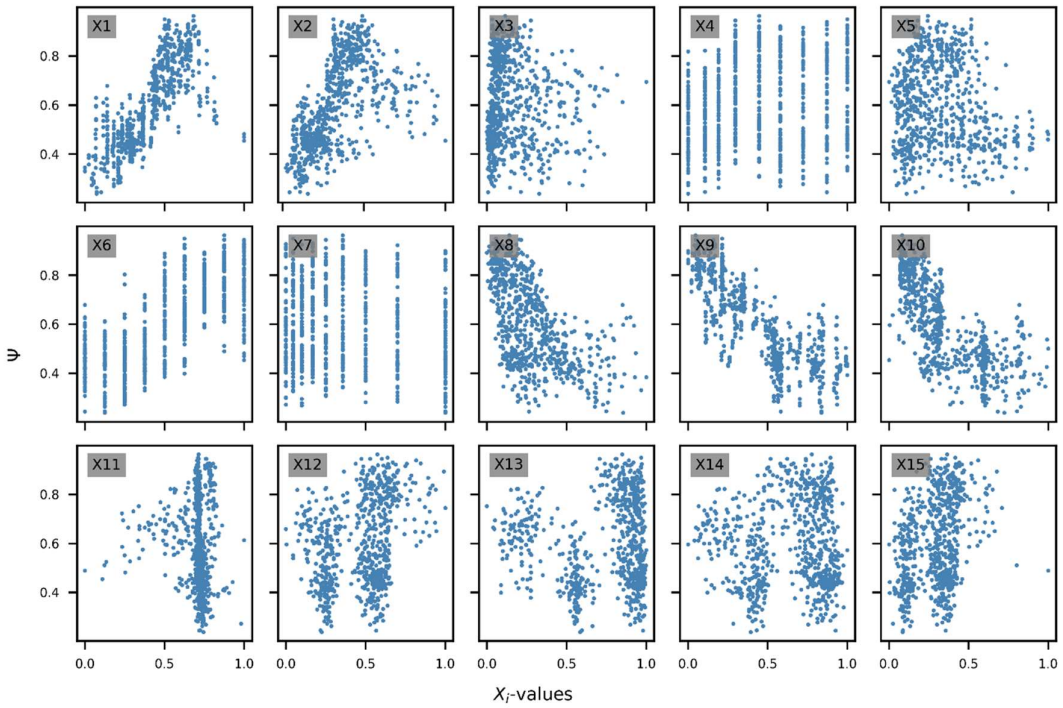

Figure E-17. Scatter plots showing trends between scaled and standardized Xi-predictors and the Ψ-factor. Reference example case, AP: LTHA / DT: *convDs* / BSC: *fixBase* / SPL: LS.

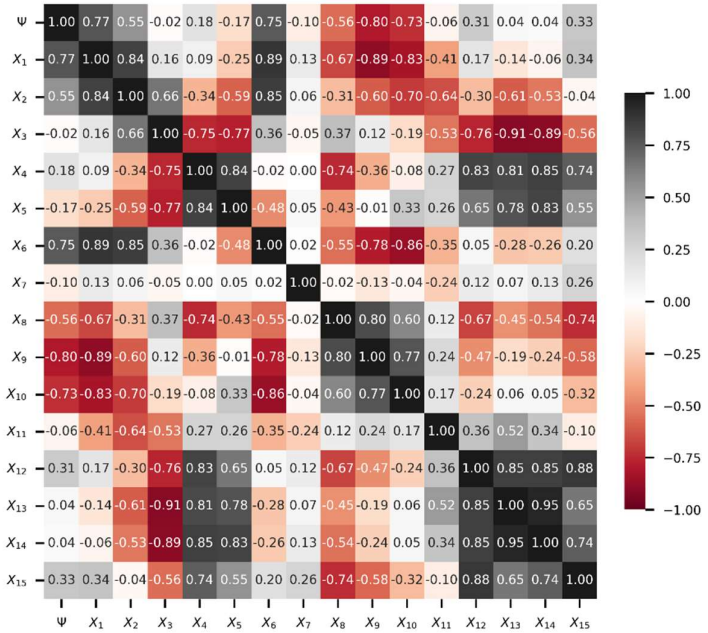

Figure E-18. Heatmap of Pearson correlation coefficients revealing a possible linear correlation between predictors and the Ψ-factor. Reference example case, AP: LTHA / DT: *convDs* / BSC: *fixBase* / SPL: LS.

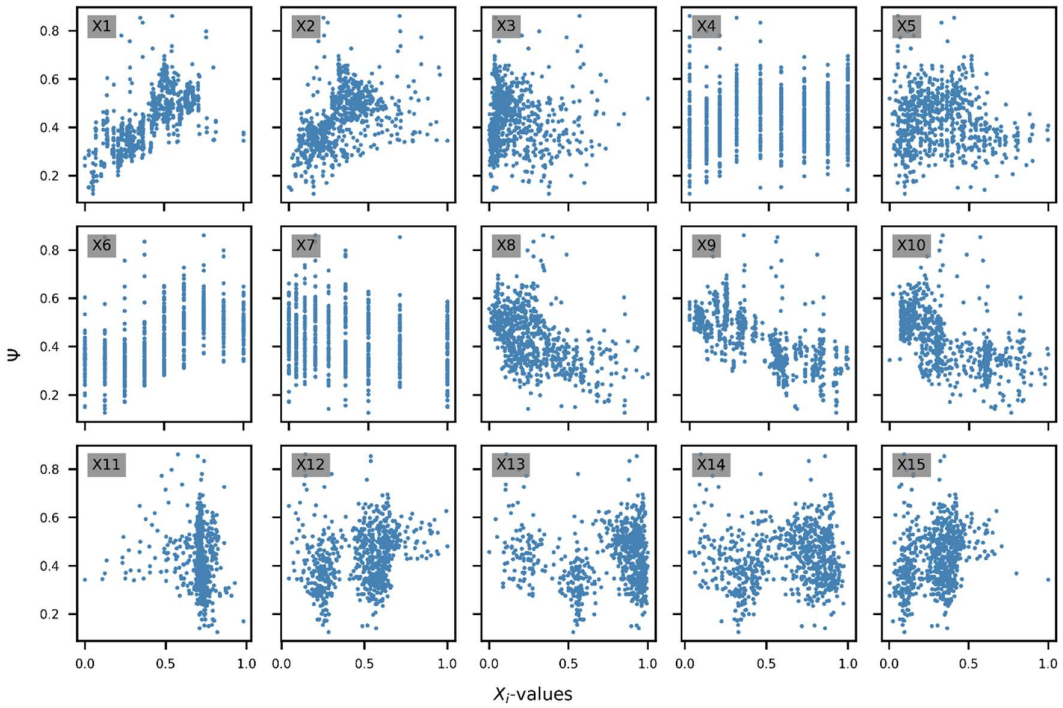

Figure E-19. Scatter plots showing trends between scaled and standardized Xi-predictors and the Ψ-factor. Reference example case, AP: LTHA / DT: *convDs* / BSC: *fixBase* / SPL: CP.

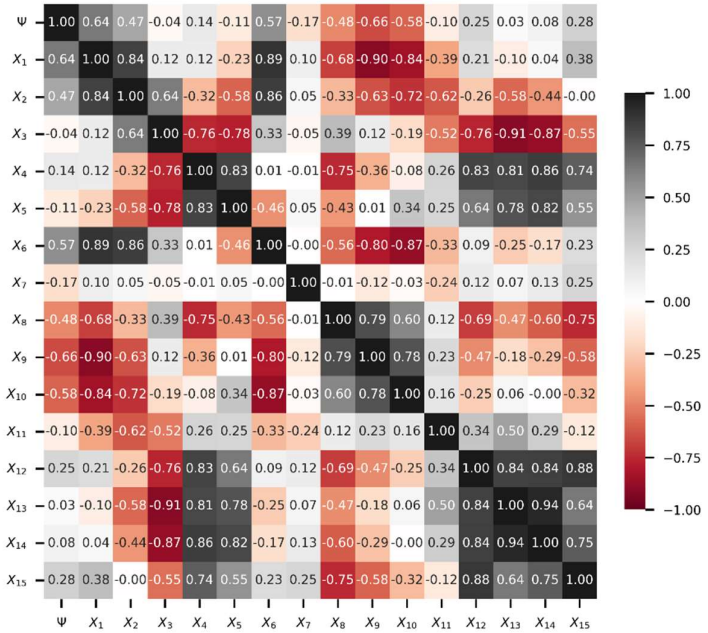

Figure E-20. Heatmap of Pearson correlation coefficients revealing a possible linear correlation between predictors and the Ψ-factor. Reference example case, AP: LTHA / DT: *convDs* / BSC: *fixBase* / SPL: CP.

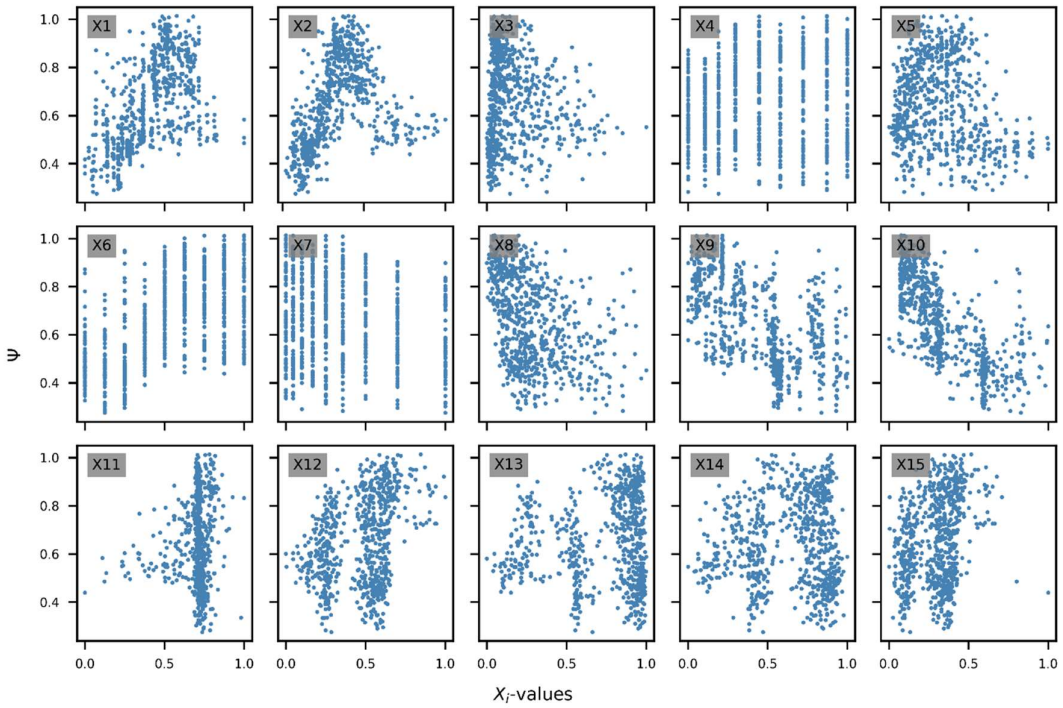

Figure E-21. Scatter plots showing trends between scaled and standardized Xi-predictors and the Ψ-factor. Reference example case, AP: LTHA / DT: *convDs* / BSC: *flexBase* / SPL: LS.

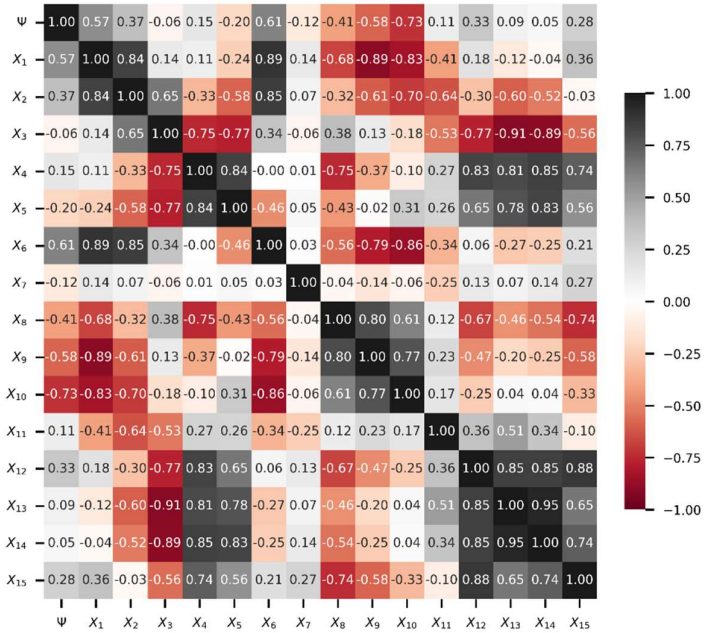

Figure E-22. Heatmap of Pearson correlation coefficients revealing a possible linear correlation between predictors and the Ψ-factor. Reference example case, AP: LTHA / DT: *convDs* / BSC: *flexBase* / SPL: LS.

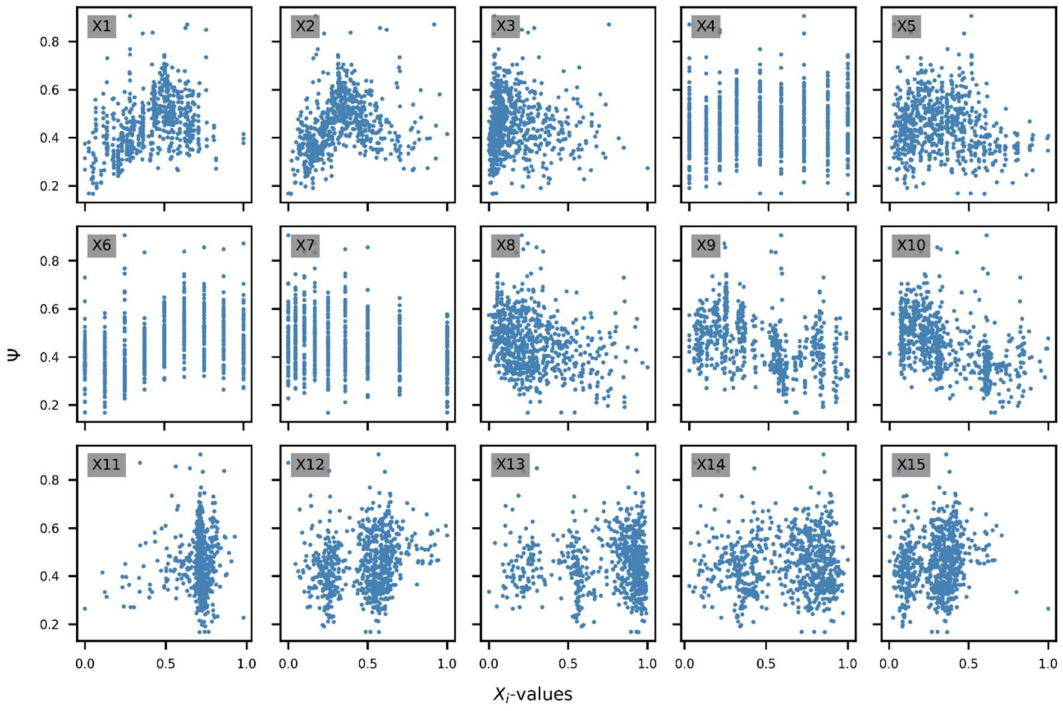

Figure E-23. Scatter plots showing trends between scaled and standardized Xi-predictors and the Ψ-factor. Reference example case, AP: LTHA / DT: *convDs* / BSC: *flexBase* / SPL: CP.

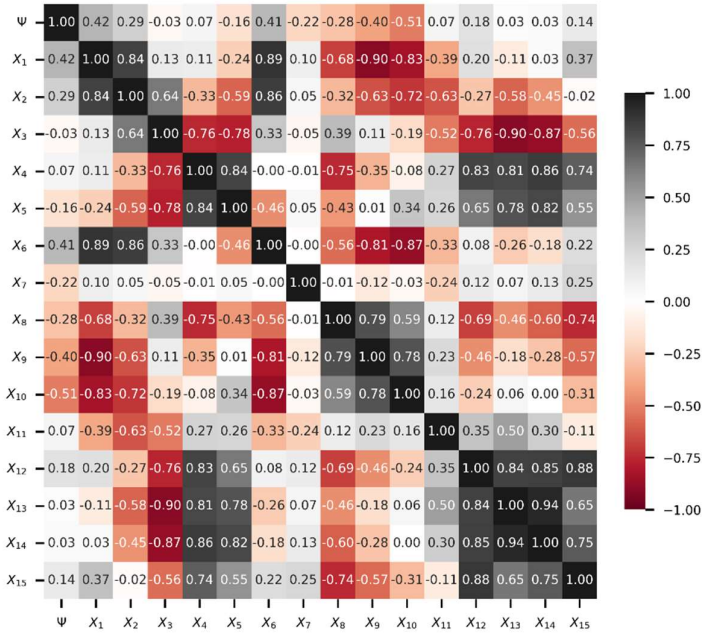

Figure E-24. Heatmap of Pearson correlation coefficients revealing a possible linear correlation between predictors and the Ψ-factor. Reference example case, AP: LTHA / DT: *convDs* / BSC: *flexBase* / SPL: CP.

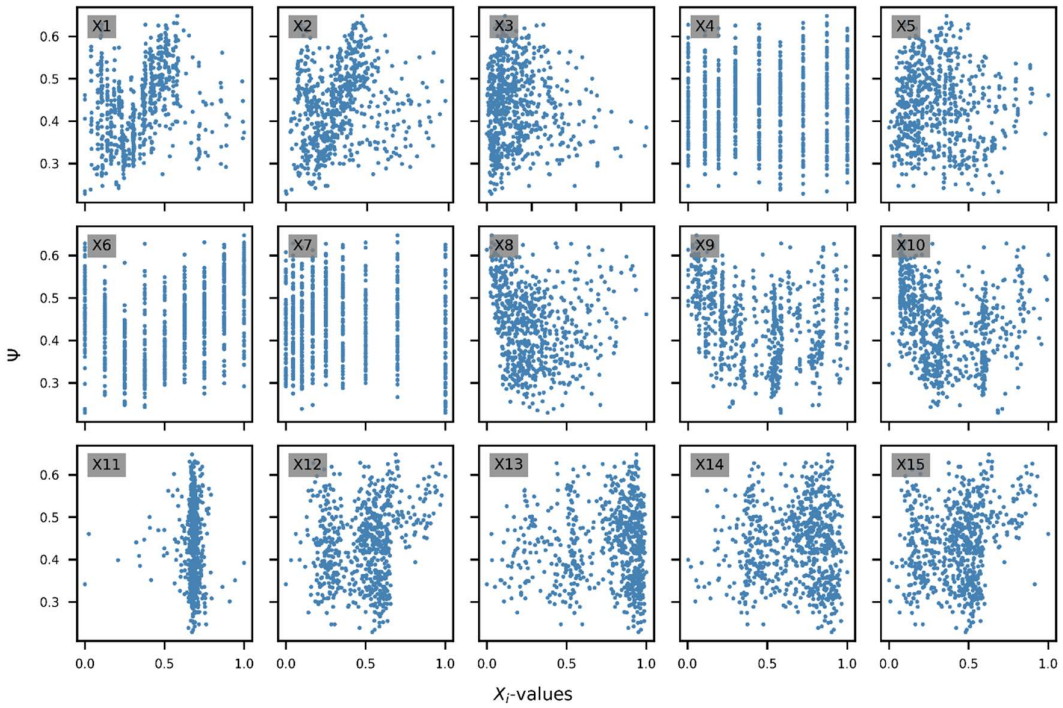

Figure E-25. Scatter plots showing trends between scaled and standardized Xi-predictors and the Ψ-factor. Reference example case, AP: LTHA / DT: *SSIDs* / BSC: *fixBase* / SPL: LS.

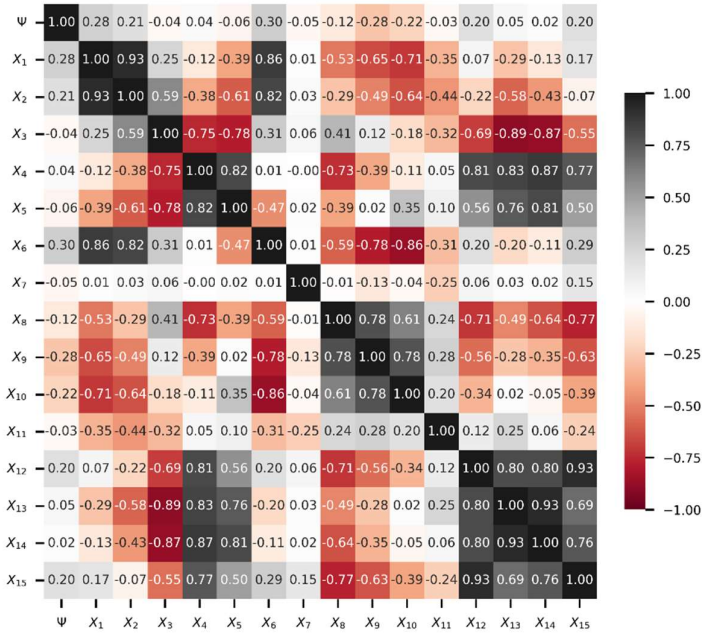

Figure E-26. Heatmap of Pearson correlation coefficients revealing a possible linear correlation between predictors and the Ψ-factor. Reference example case, AP: LTHA / DT: *SSIDs* / BSC: *fixBase* / SPL: LS.

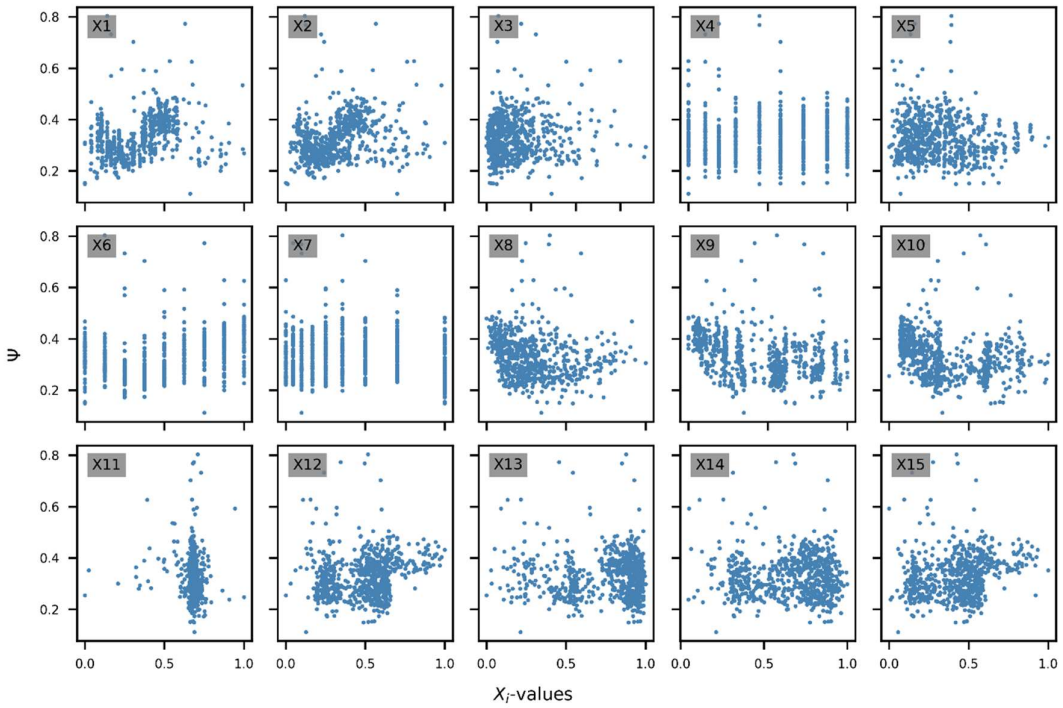

Figure E-27. Scatter plots showing trends between scaled and standardized Xi-predictors and the Ψ-factor. Reference example case, AP: LTHA / DT: *SSIDs* / BSC: *fixBase* / SPL: CP.

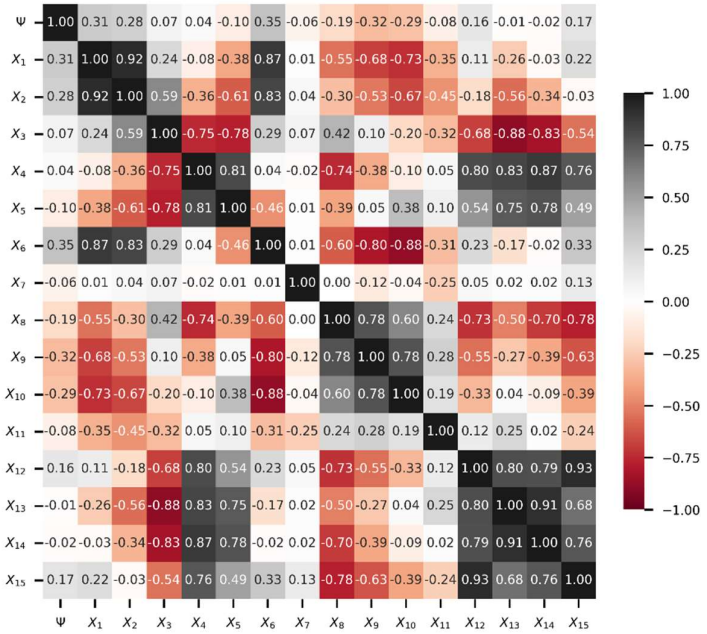

Figure E-28. Heatmap of Pearson correlation coefficients revealing a possible linear correlation between predictors and the Ψ-factor. Reference example case, AP: LTHA / DT: *SSIDs* / BSC: *fixBase* / SPL: CP.

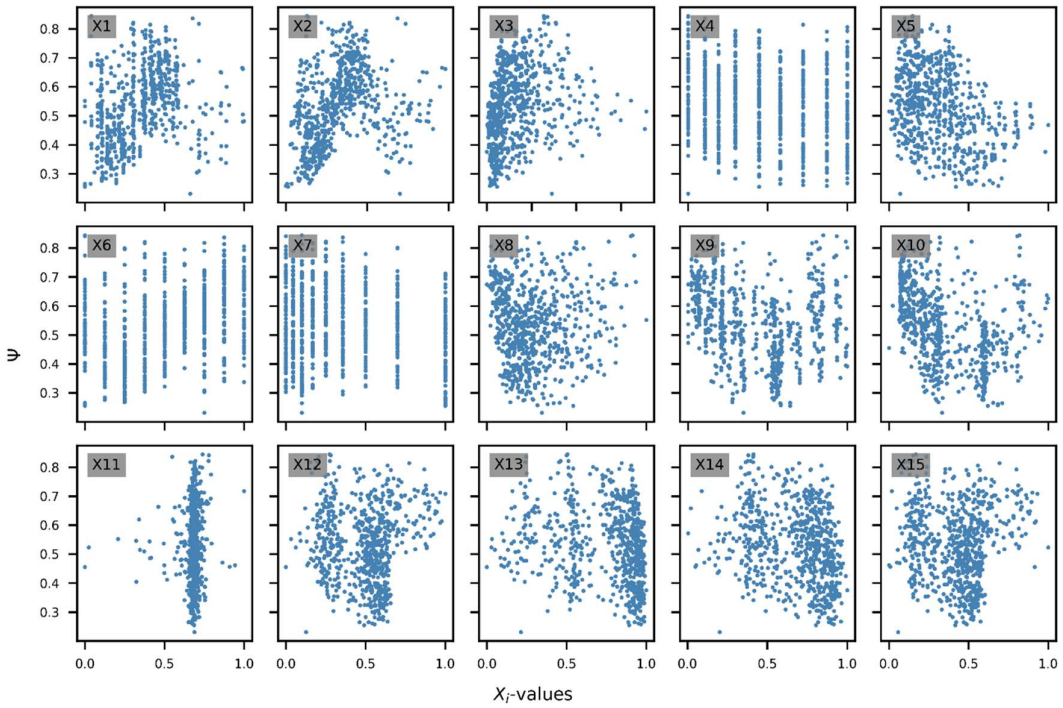

Figure E-29. Scatter plots showing trends between scaled and standardized Xi-predictors and the Ψ-factor. Reference example case, AP: LTHA / DT: *SSIDs* / BSC: *flexBase* / SPL: LS.

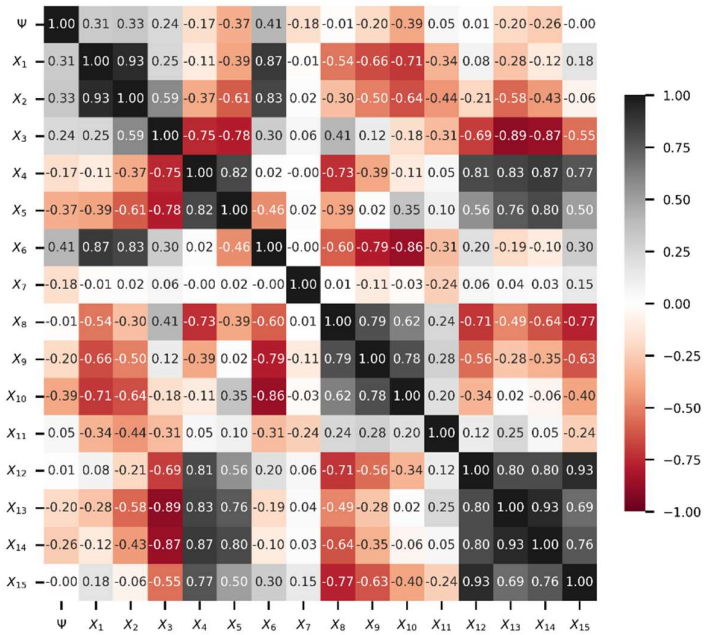

Figure E-30. Heatmap of Pearson correlation coefficients revealing a possible linear correlation between predictors and the Ψ-factor. Reference example case, AP: LTHA / DT: *SSIDs* / BSC: *flexBase* / SPL: LS.

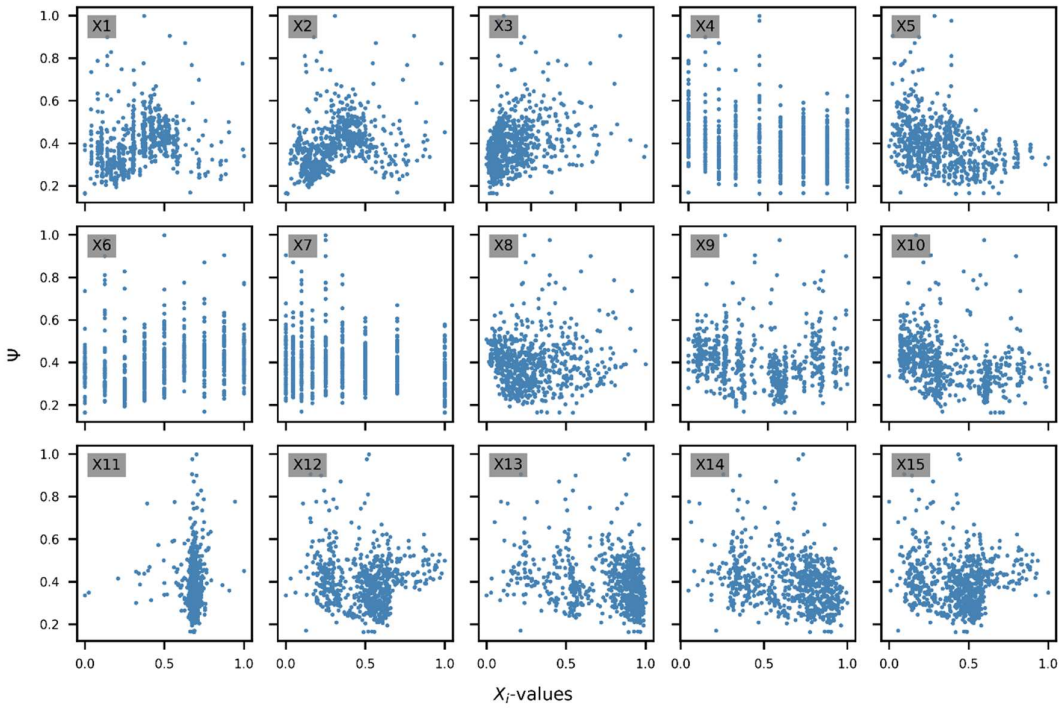

Figure E-31. Scatter plots showing trends between scaled and standardized Xi-predictors and the Ψ-factor. Reference example case, AP: LTHA / DT: *SSIDs* / BSC: *flexBase* / SPL: CP.

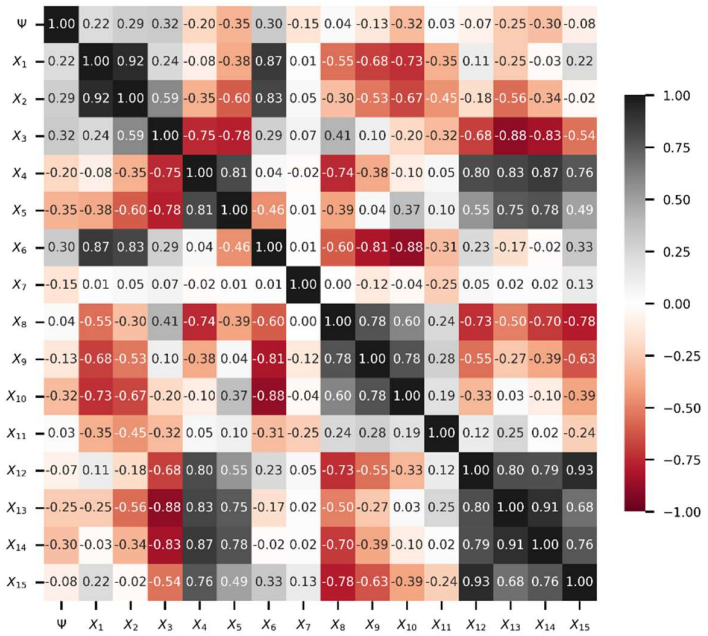

Figure E-32. Heatmap of Pearson correlation coefficients revealing a possible linear correlation between predictors and the Ψ-factor. Reference example case, AP: LTHA / DT: *SSIDs* / BSC: *flexBase* / SPL: CP.

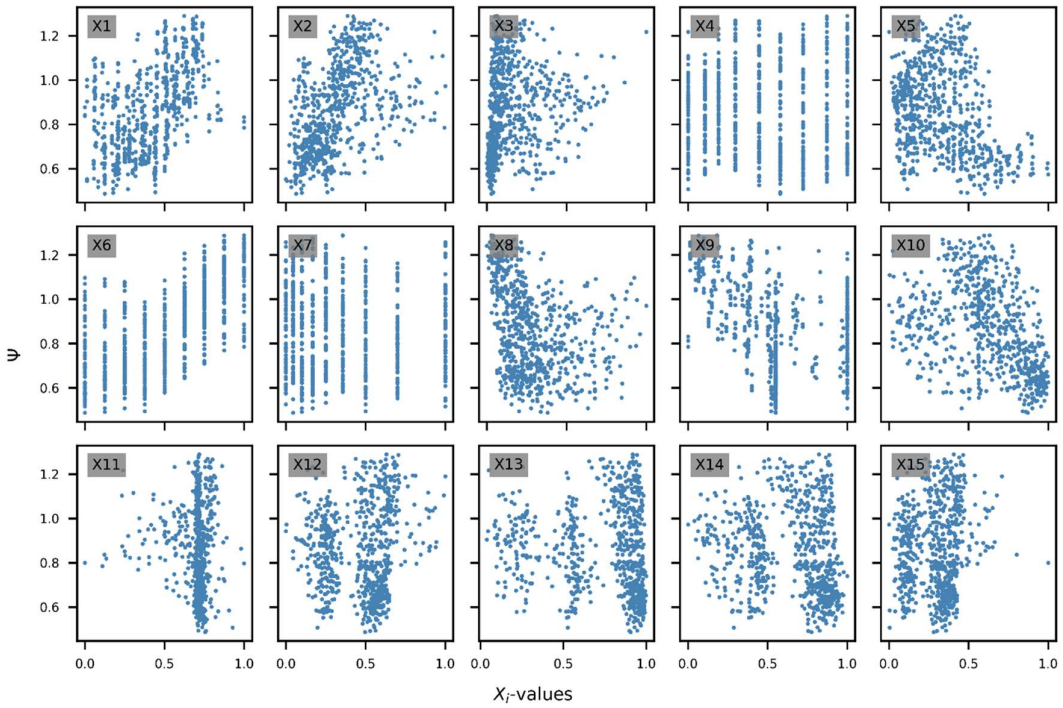

Figure E-33. Scatter plots showing trends between scaled and standardized Xi-predictors and the Ψ-factor. Reference example case, AP: NSP / DT: *convDs* / BSC: *fixBase* / SPL: LS.

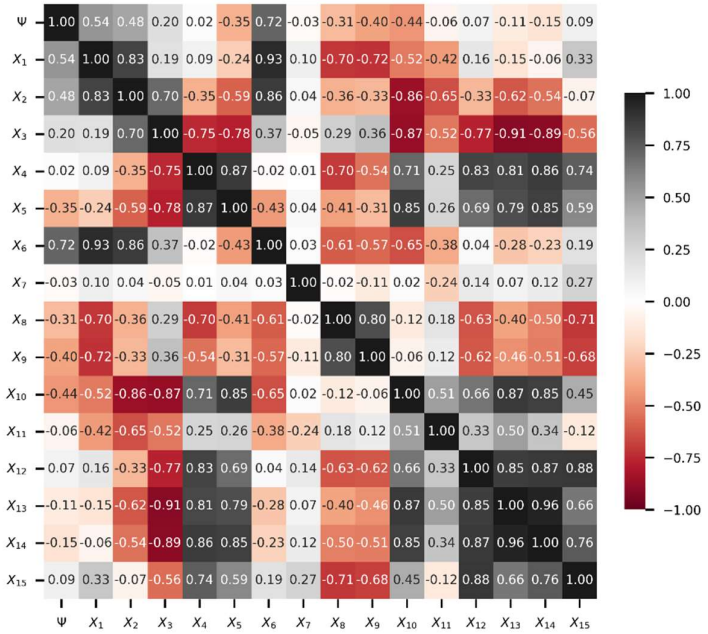

Figure E-34. Heatmap of Pearson correlation coefficients revealing a possible linear correlation between predictors and the Ψ-factor. Reference example case, AP: NSP / DT: *convDs* / BSC: *fixBase* / SPL: LS.

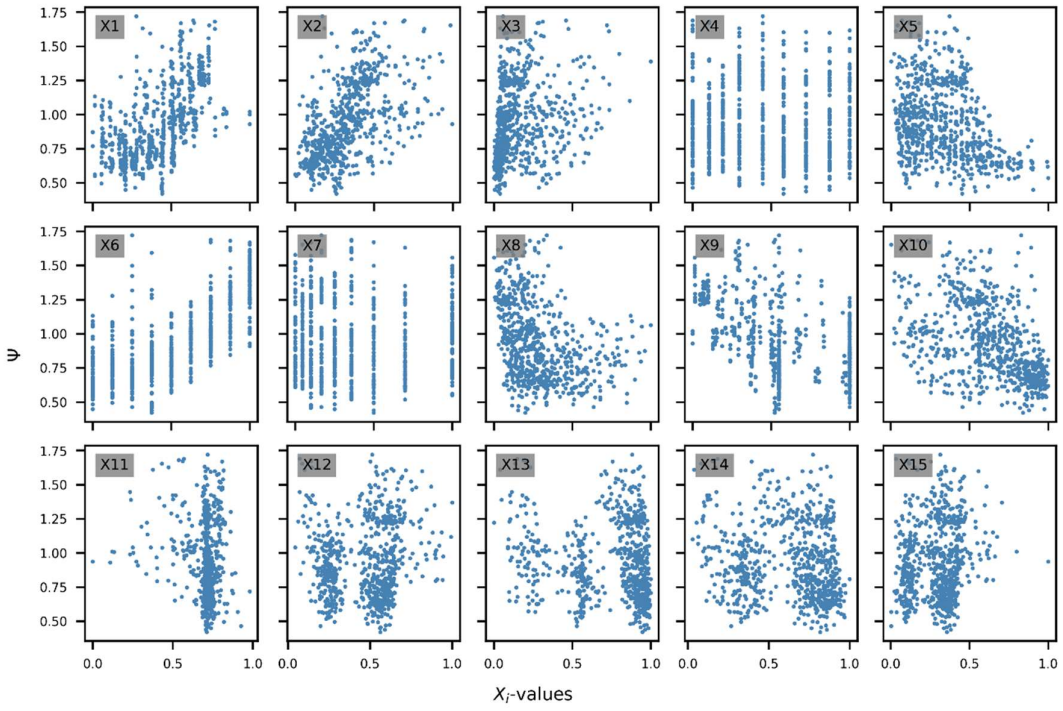

Figure E-35. Scatter plots showing trends between scaled and standardized Xi-predictors and the Ψ-factor. Reference example case, AP: NSP / DT: *convDs* / BSC: *fixBase* / SPL: CP.

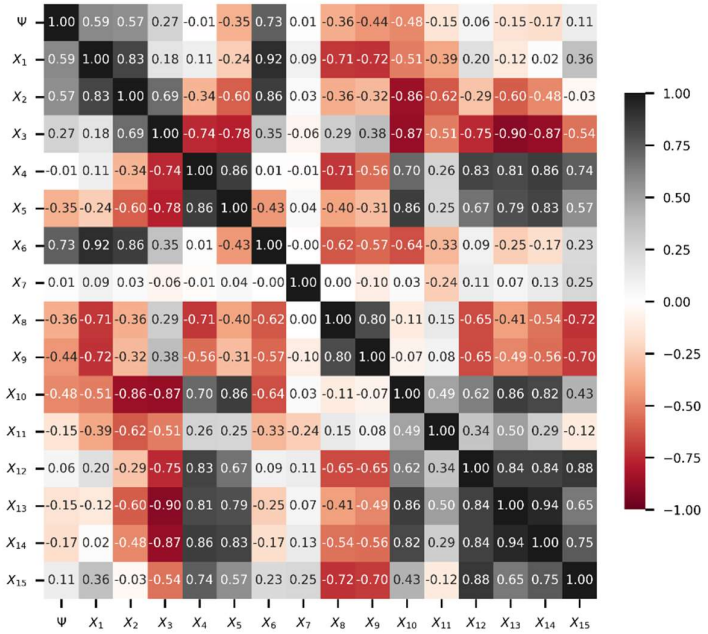

Figure E-36. Heatmap of Pearson correlation coefficients revealing a possible linear correlation between predictors and the Ψ-factor. Reference example case, AP: NSP / DT: *convDs* / BSC: *fixBase* / SPL: CP.

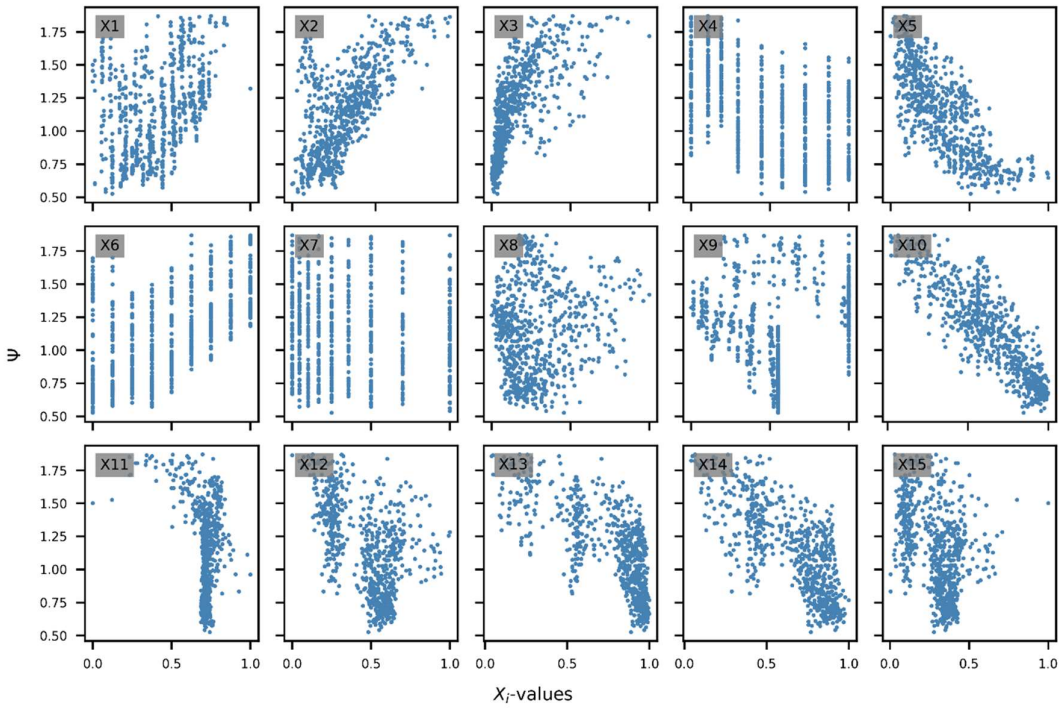

Figure E-37. Scatter plots showing trends between scaled and standardized Xi-predictors and the Ψ-factor. Reference example case, AP: NSP / DT: *convDs* / BSC: *flexBase* / SPL: LS.

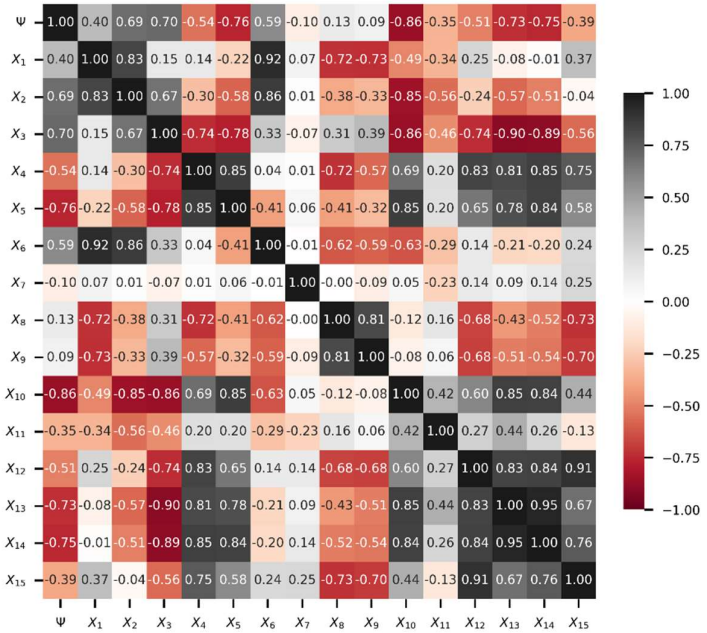

Figure E-38. Heatmap of Pearson correlation coefficients revealing a possible linear correlation between predictors and the Ψ-factor. Reference example case, AP: NSP / DT: *convDs* / BSC: *flexBase* / SPL: LS.

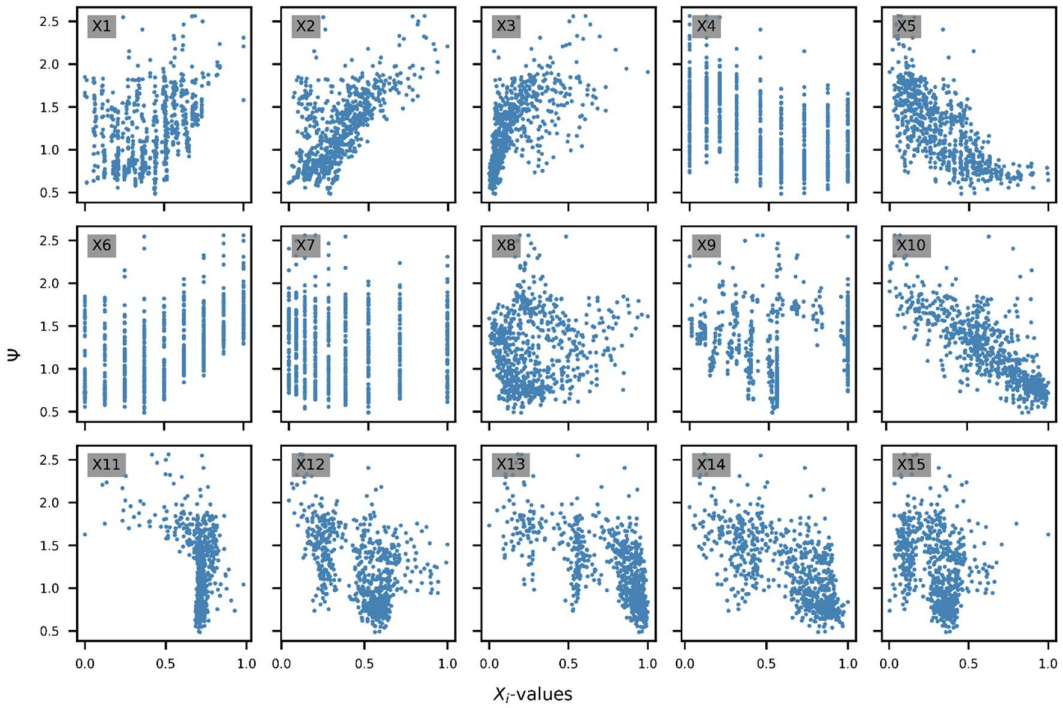

Figure E-39. Scatter plots showing trends between scaled and standardized Xi-predictors and the Ψ-factor. Reference example case, AP: NSP / DT: *convDs* / BSC: *flexBase* / SPL: CP.

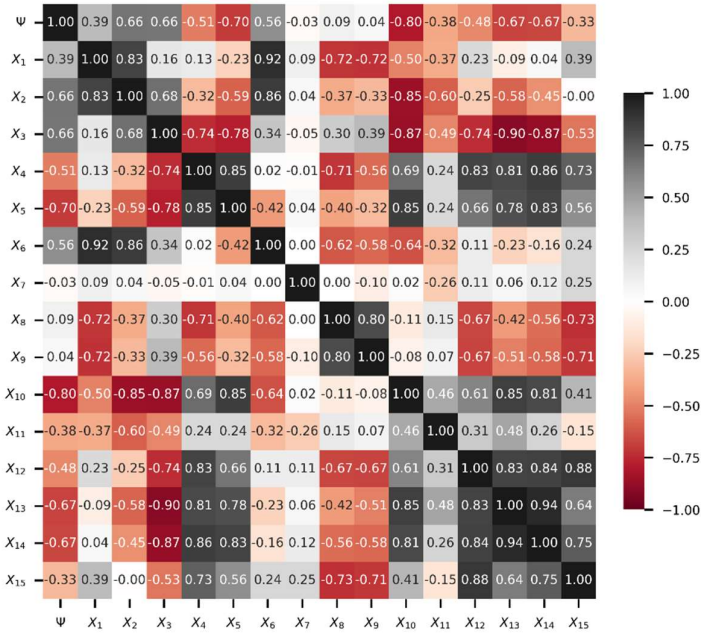

Figure E-40. Heatmap of Pearson correlation coefficients revealing a possible linear correlation between predictors and the Ψ-factor. Reference example case, AP: NSP / DT: *convDs* / BSC: *flexBase* / SPL: CP.

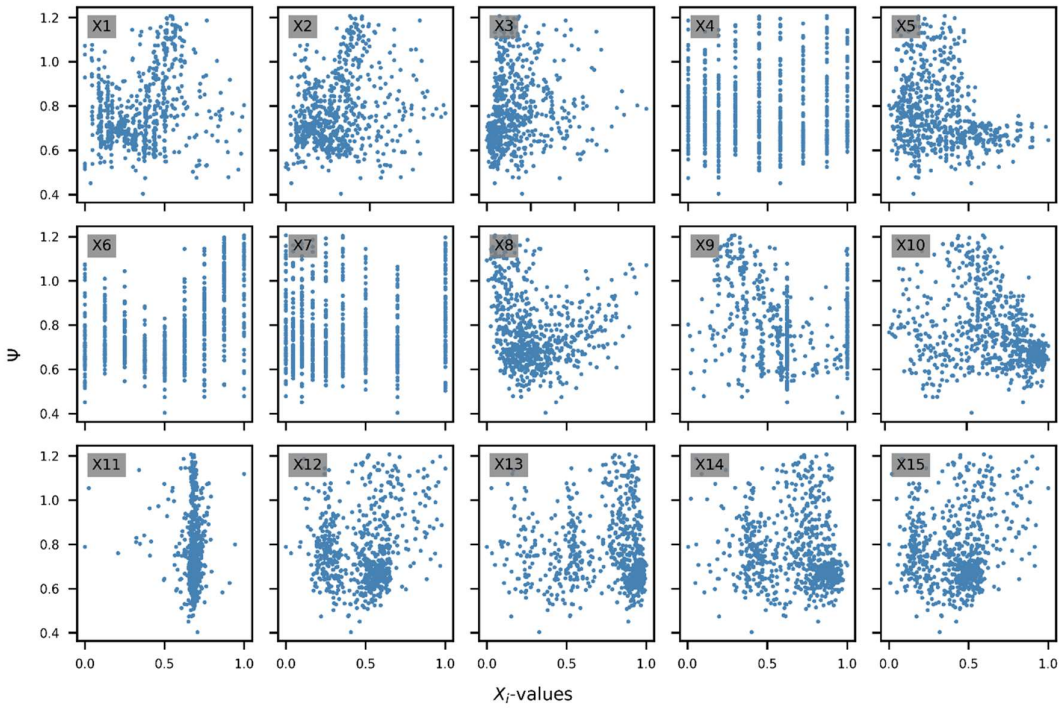

Figure E-41. Scatter plots showing trends between scaled and standardized Xi-predictors and the Ψ-factor. Reference example case, AP: NSP / DT: *SSIDs* / BSC: *fixBase* / SPL: LS.

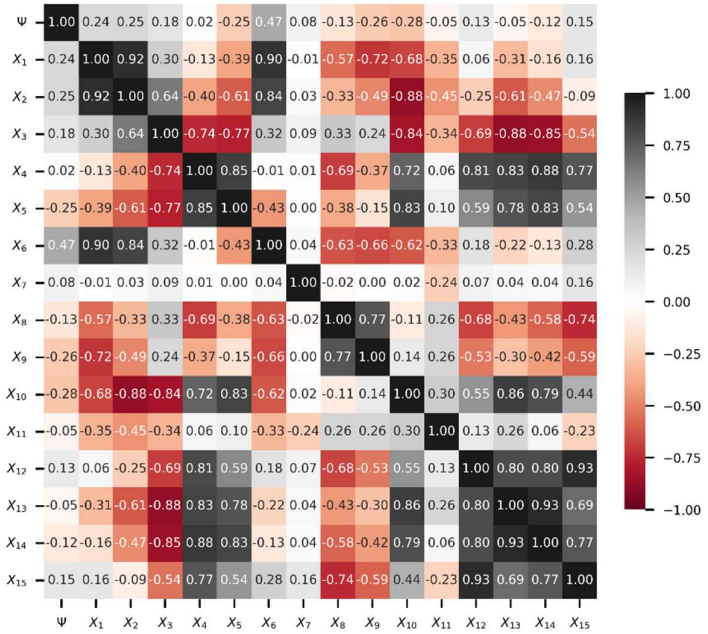

Figure E-42. Heatmap of Pearson correlation coefficients revealing a possible linear correlation between predictors and the Ψ-factor. Reference example case, AP: NSP / DT: *SSIDs* / BSC: *fixBase* / SPL: LS.

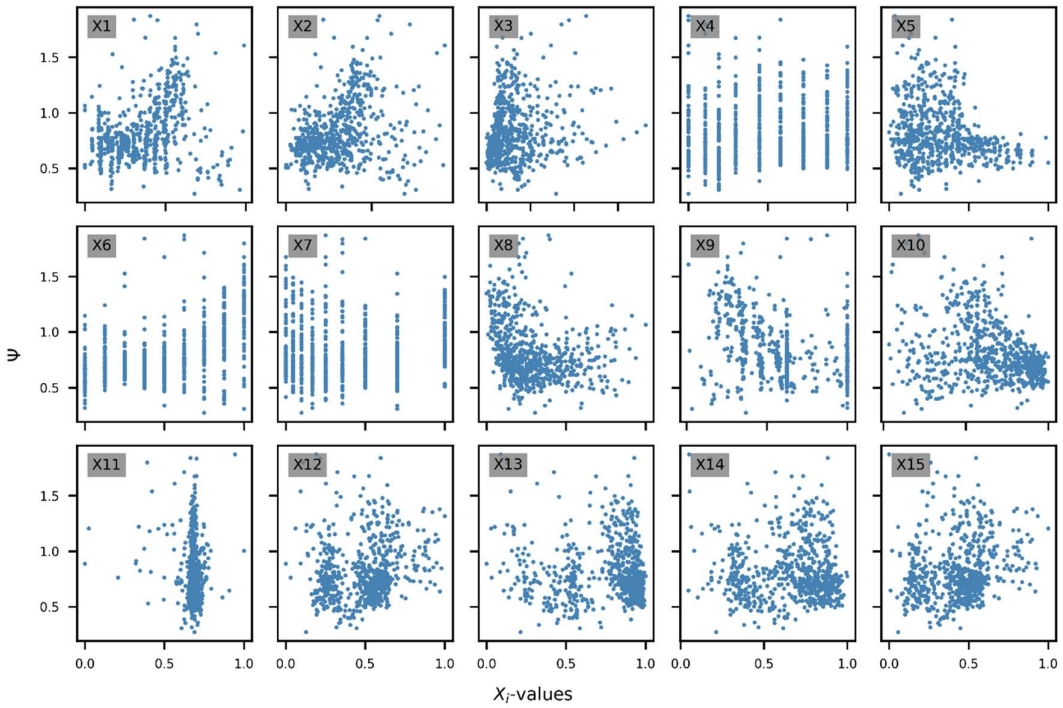

Figure E-43. Scatter plots showing trends between scaled and standardized Xi-predictors and the Ψ-factor. Reference example case, AP: NSP / DT: *SSIDs* / BSC: *fixBase* / SPL: CP.

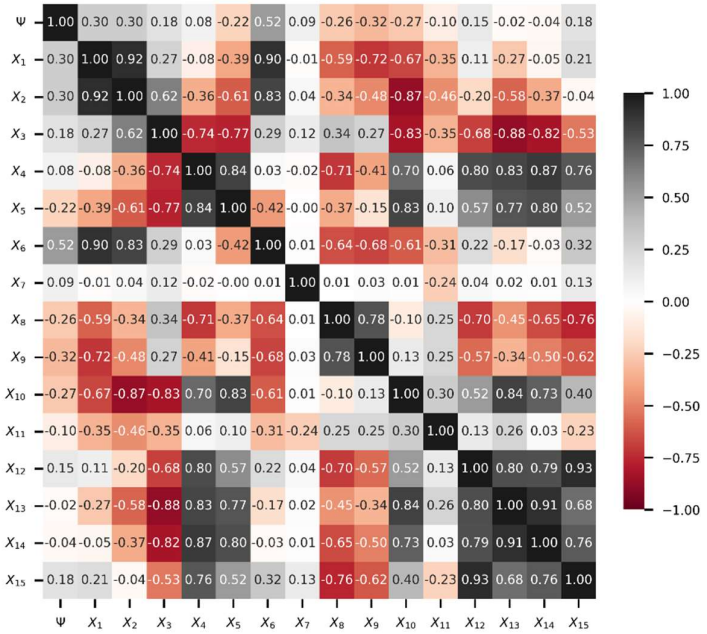

Figure E-44. Heatmap of Pearson correlation coefficients revealing a possible linear correlation between predictors and the Ψ-factor. Reference example case, AP: NSP / DT: *SSIDs* / BSC: *fixBase* / SPL: CP.

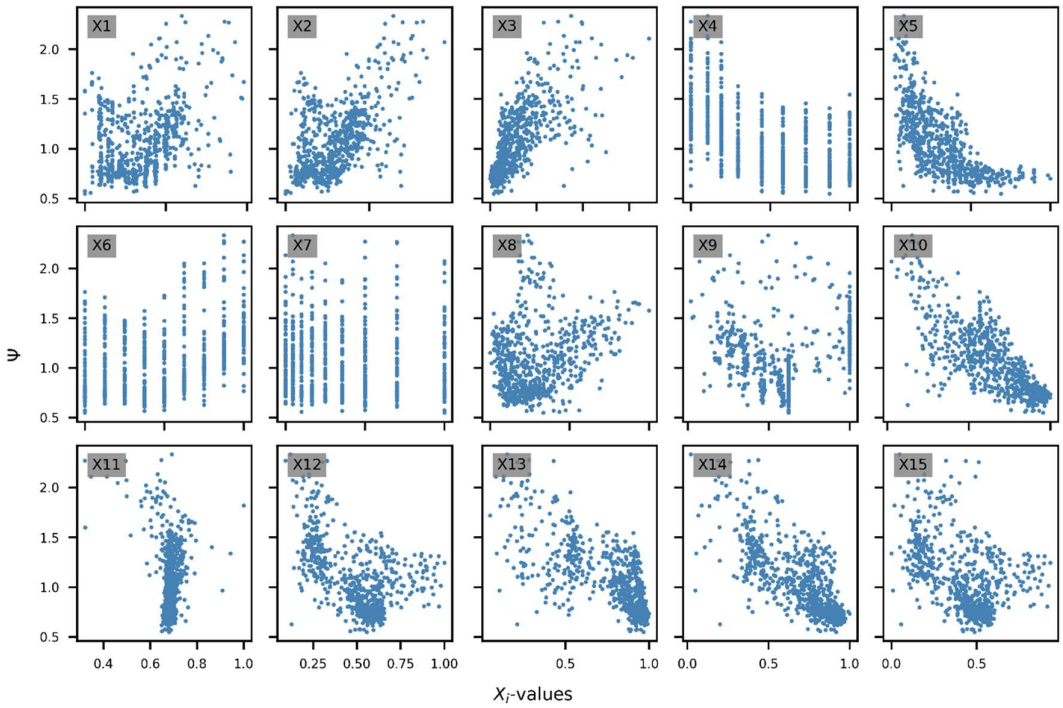

Figure E-45. Scatter plots showing trends between scaled and standardized Xi-predictors and the Ψ-factor. Reference example case, AP: NSP / DT: *SSIDs* / BSC: *flexBase* / SPL: LS.

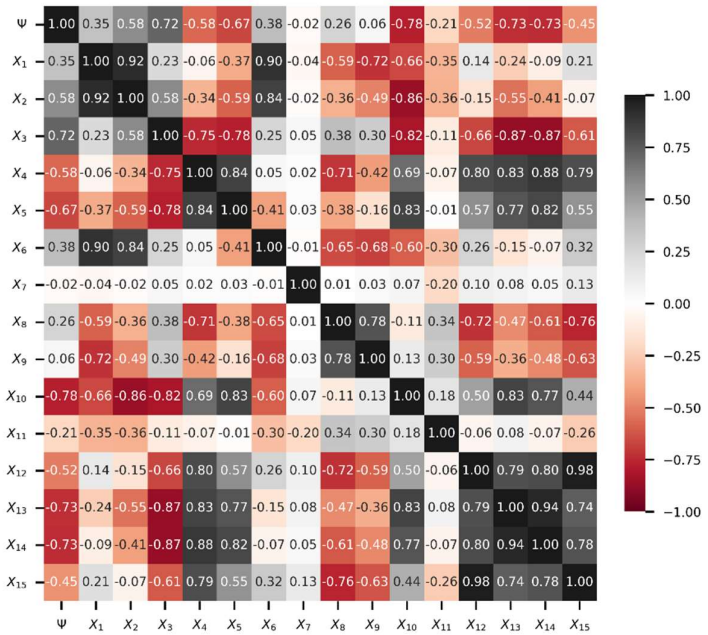

Figure E-46. Heatmap of Pearson correlation coefficients revealing a possible linear correlation between predictors and the Ψ-factor. Reference example case, AP: NSP / DT: *SSIDs* / BSC: *flexBase* / SPL: LS.

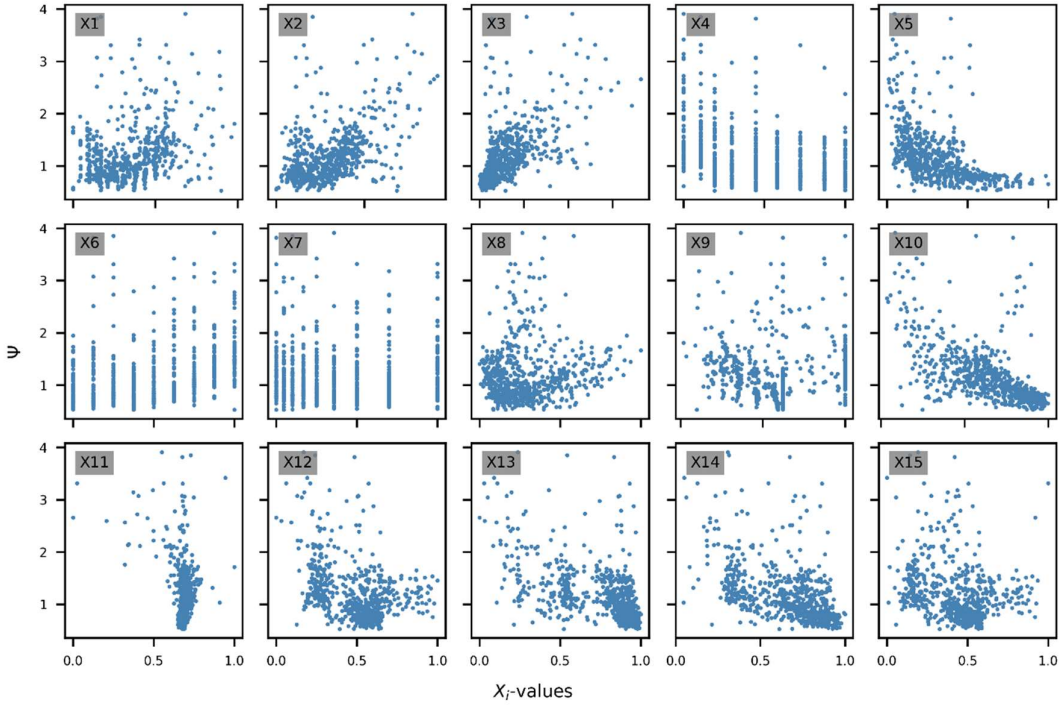

Figure E-47. Scatter plots showing trends between scaled and standardized Xi-predictors and the Ψ-factor. Reference example case, AP: NSP / DT: *SSIDs* / BSC: *flexBase* / SPL: CP.

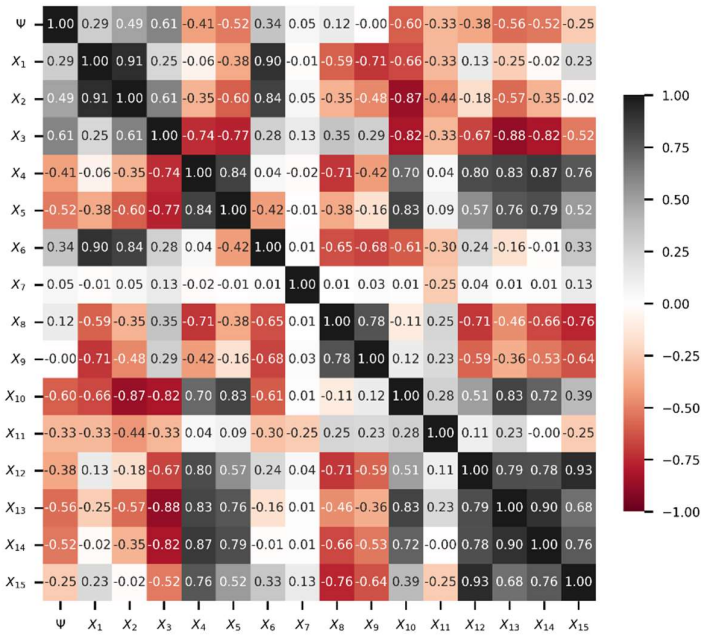

Figure E-48. Heatmap of Pearson correlation coefficients revealing a possible linear correlation between predictors and the Ψ-factor. Reference example case, AP: NSP / DT: *SSIDs* / BSC: *flexBase* / SPL: CP.

Appendix F. A short analysis of the Overstrength Factor, $\widetilde{\Omega}$

Currently, some design requirement documents, such as ASCE-7 Standard, still rely on design criteria based on the determination of forces to establish demands in order to provide adequate structural stiffness and strength. Acknowledging from past seismic events that structures can actually withstand forces of a greater magnitude than that for which they were designed, today's standard practice is to reduce those design forces that one would use to keep the structure's behavior elastic by means of the Response Modification Factor, R. As a result of this reduction, the expected elastic base shear strength, V_e, is reduced to a design base shear strength introduced earlier as V (or $\tilde{V}$ for *SSIDs* and V_{dsgn} in Chapter 5).

Although buildings are provided with a prescribed base shear strength through mathematical models, actual structures can develop higher strengths during seismic events. This increase in structural strength beyond the design forces is called structural overstrength. Analytically, it is expressed as the ratio of the actual developed lateral strength, V_y, and the design shear force V; denominated as *Overstrength Factor,* Ω. Refer to for a graphical description of factors R and Ω.

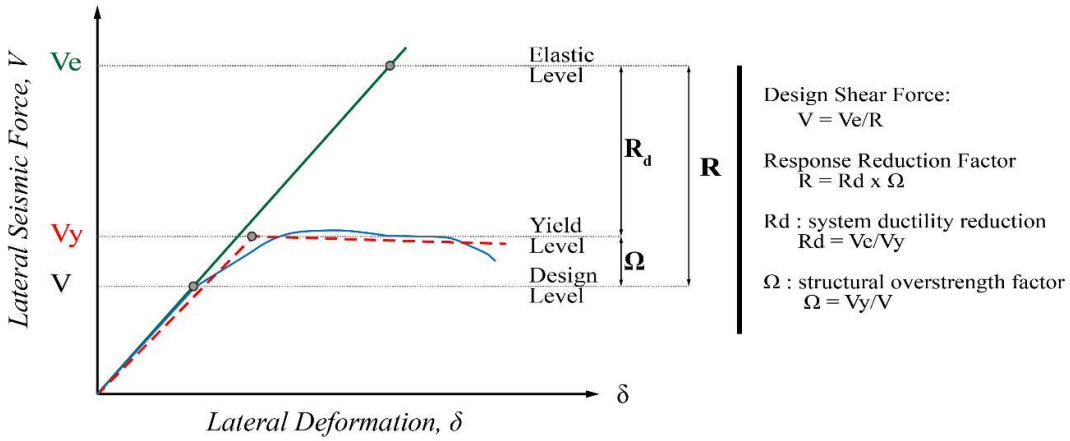

Figure F-1. Illustration of seismic performance (modification) factors for structures in an idealized inelastic force-deformation curve

This figure has been adapted from (FEMA, 2003) and (ATC, 2009). It is worth mentioning that although the seismic modification factors are described in **Figure F-1** as differences of various lateral shear force levels, they actually correspond to ratios of the same values. The way they are graphically represented is merely to ease understanding of their meaning.

From the figure above, factors R and Ω can be defined using Eqs. [F.1] and [F.2], respectively.

$$R = \frac{V_e}{V} \qquad [F.1]$$

$$R = \Omega R_d$$

$$\Omega = \frac{V_y}{V} \quad [F.2]$$

Where another seismic performance factor is introduced, namely, the system ductility reduction factor, R_d. This factor, on the other hand, is defined as the ratio V_e/V_y.

Some studies have focused on the evaluation of these factors, as is the case of (Elnashai & Mwafy, 2002; Fernandez-Sola et al., 2014; Ganjavi et al., 2019; Louzai & Abed, 2015; Tahghighi & Mohammadi, 2020). Authors use models at different levels of sophistication with and without SSI effects considerations and are subjected to seismic actions to evaluate the behavior of R and Ω factors. Special attention deserves the studies carried out in (Muberra Eser Aydemir & Ekiz, 2013) and (Müberra Eser Aydemir & Aydemir, 2016) by Muberra Eser and others, the latter addressing the overstrength factor for *SDOF* and *MDOF* systems considering SSI effects. The authors concluded, among other things, that variation in Ω is related to the vibration period of structures; hence other associated parameters, such as the aspect ratio, λ_{str}, also influence in Ω.

Although it is not the intention of this appendix or this study to focus specifically on the seismic performance factors, the information presented here aims to complement the train of thought introduced earlier in Section 5.3.1 regarding $\widetilde{\Omega}_{(T_n)}$. As mentioned in the referenced section, $\widetilde{\Omega}_{(T_n)}$ was calculated from the Pushover analysis as the ratio of the maximum base-shear capacity of the *flexBase*-BSC building to the design base-shear from the *ConvDs*. Eq. [5.6] was derived from a regression analysis of the 729 building design cases of the database through the following procedures.

The overstrength factor, $\widetilde{\Omega}$, is calculated using Eq. [F.3] as the ratio of the maximum base shear strength obtained from the NSP analysis on a *flexBase*-BSC building, $\tilde{V}_y^{NSP}$, to the prescribed design base shear force calculated for a *convDs* design type, V.

$$\tilde{\Omega} = \frac{\tilde{V}_y^{NSP}}{V} \quad [F.3]$$

This expression intends to determine an overstrength factor that contains the effects of SSI in the leap from the *convDs* design demand to the *flexBase* response.

Once the $\widetilde{\Omega}$ are calculated for buildings in the database, they are used as a response variable and evaluated against the same predictor variables established in Section 5.4 and shown in **Figure F-2** for convenience.

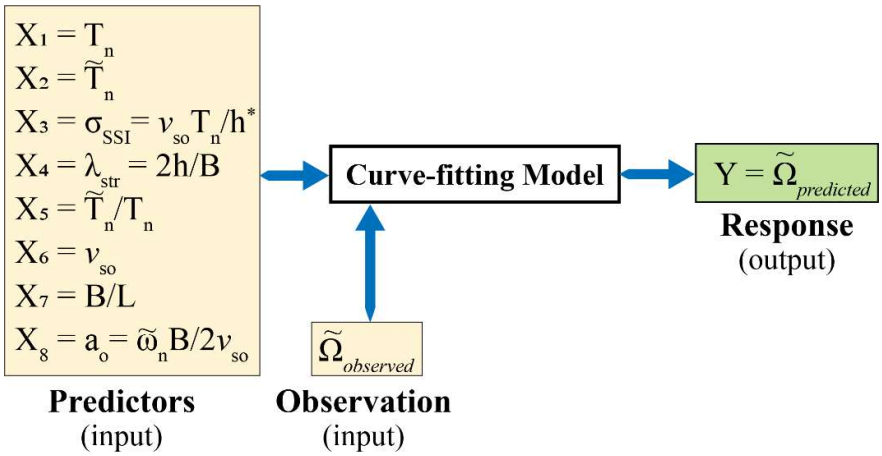

Figure F-2. Schematization of selected predictors and responses for estimation of $\tilde{\Omega}$.

A Pearson correlation coefficient matrix is built to grasp how the predictor values X_i and $\tilde{\Omega}$ are correlated if they are so. The matrix is shown in **Figure F-3**. Notice that the predictors with a higher correlation to $\tilde{\Omega}$ are X_1, X_2, and X_4, in that order. These predictors correspond to parameters T_n, $\tilde{T}_n$ and λ_{str}, but it is worth observing that they show a strong correlation with each other (Pearson correlation coefficient higher than 0.90). The other parameters are of less significance in terms of linear correlation.

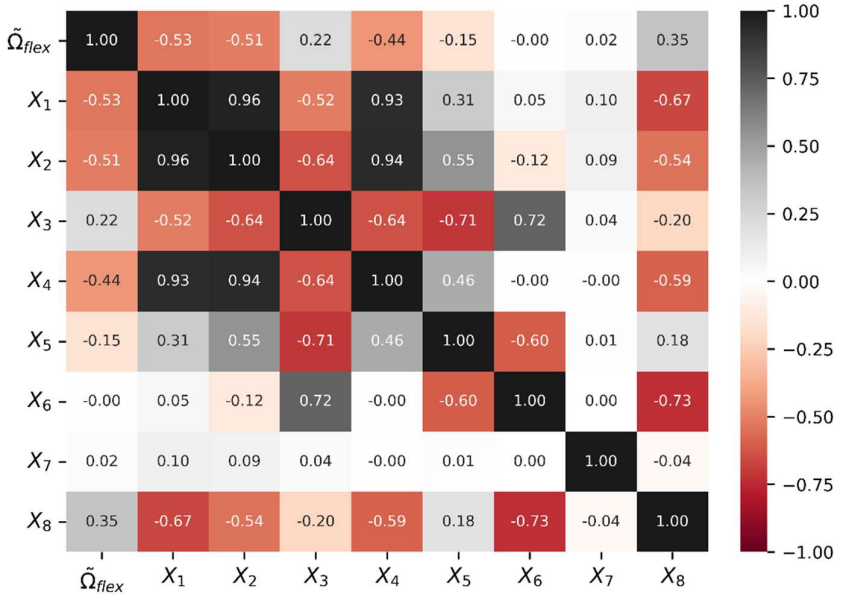

Figure F-3. Pearson-correlation coefficients matrix for representative predictors against $\tilde{\Omega}$.

Additional to the Pearson correlation matrix, scatter plots are presented in **Figure F-4** to appreciate any relation between the selected predictors X_i and $\tilde{\Omega}$. This figure can draw similar conclusions to what was observed from the Pearson correlation matrix; that is, the parameters showing a trend in the scatter plots relative to the overstrength factor are X_1, X_2, and X_4. However, the trend seems to

be nonlinear; hence the medium correlation observed in the Pearson matrix above. Notice, on the other hand, that $\widetilde{\Omega}$ appears invariant relative to the rest of the predictors.

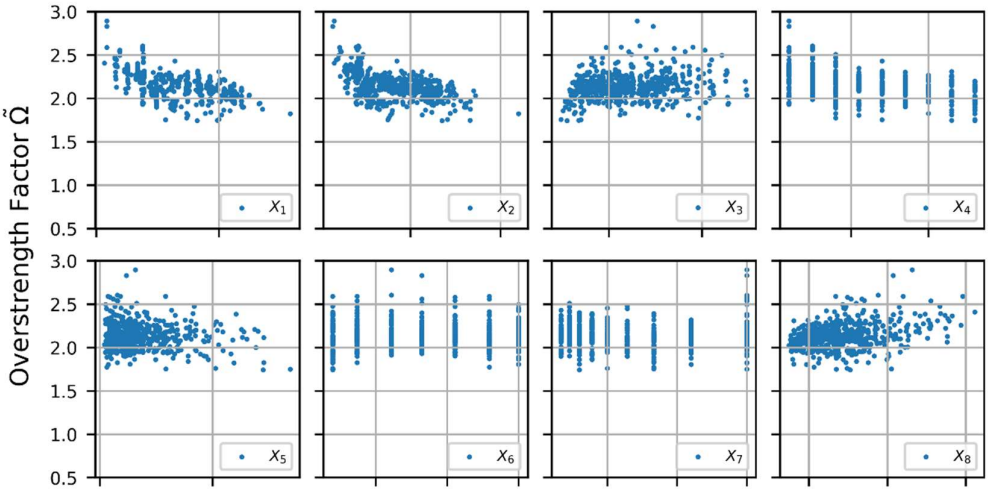

Figure F-4. Scatter plots of Predictors X_i vs $\widetilde{\Omega}$.

Recall that from evaluating **Figure F-3**, a strong correlation between X_1, X_2, and X_4 was found. For this reason, only one of these predictors was selected to accommodate a model that lets us predict the value of $\widetilde{\Omega}$. A couple of fitted equations were obtained through the *optimize.curve_fit* curve-fitting module of the ***scipy*** Python package using the form of Eq. [F.4].

$$\tilde{\Omega}_{(X_i)} = \frac{C_1 X_i - C_2}{X_i - C_3} \qquad [F.4]$$

Where C_1, C_2, and C_3 are fitting coefficients resulting from the curve-fitting process. Having selected this form, $X_1 = T_n$ and $X_2 = \tilde{T}_n$ are used in fitting the curves to the observed data. Results from the curve-fitting process are shown in **Table F-1**.

Table F-1. Curve-fitting coefficient for predictors X_1 and X_2.

Predictors	**Fitting Coefficients**		
$\boldsymbol{X_i}$	$\boldsymbol{C_1}$	$\boldsymbol{C_2}$	$\boldsymbol{C_3}$
T_n	1.969	0.841	0.456
$\tilde{T}_n$	2.006	0.995	0.516

Coefficients obtained from the curve-fitting are used in Eq. [F.4] to generate the prediction model expression for estimating $\widetilde{\Omega}_{(X_i)}$ as depicted in **Figure F-5**. In the figure, it can be appreciated how $\widetilde{\Omega}_{(X_i)}$ seems to be constant for values of T_n and $\tilde{T}_n$ greater than $1.20s$ adopting values $\widetilde{\Omega}_{(X_i)} \approx 2.0$. This indicates that for structures having periods of vibration below $1.20s$, the actual maximum strength increases relative to the design strength that would be provided during *convDs,* suggesting a possible better structural behavior in buildings with lower aspect ratios, λ_{str}.

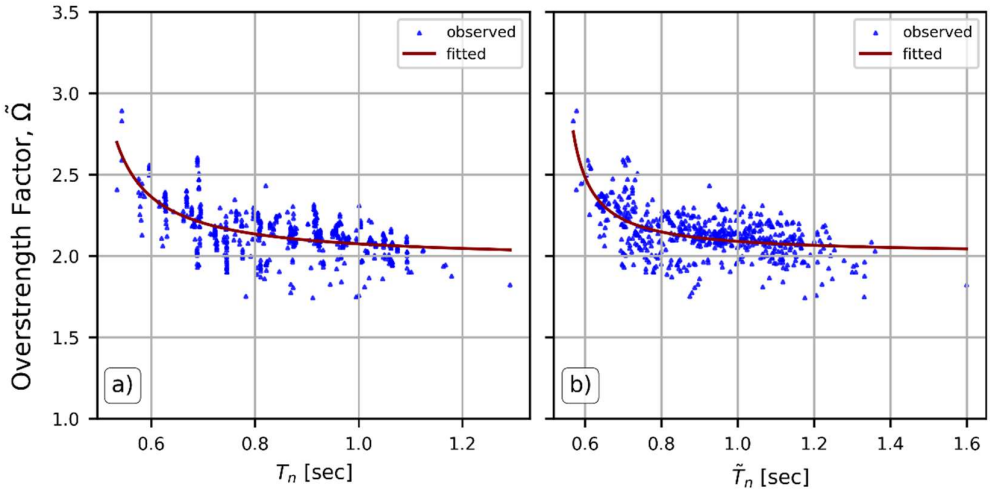

Figure F-5. Observed scatter plot and fitting curve for $\tilde{\Omega}$ versus T_n -plot a)- and $\tilde{\Omega}$ versus T_n -plot b)-.

Finally, the predictor $X_1 = T_n$ has been selected as the unique parameter to ease the use of a single expression for estimating $\tilde{\Omega}_{(X_1)}$ since the *fixBase* vibration period T_n would be easier to determine than its *flexBase* counterpart. Eq. [F.5] is then assembled in the form of Eq. [F.4] and coefficients from **Table F-1**.

$$\tilde{\Omega}_{(T_n)} = \frac{1.969T_n - 0.841}{T_n - 0.456} \qquad [F.5]$$

Which is the same as Eq. [5.6] introduced in Section 5.3.1.